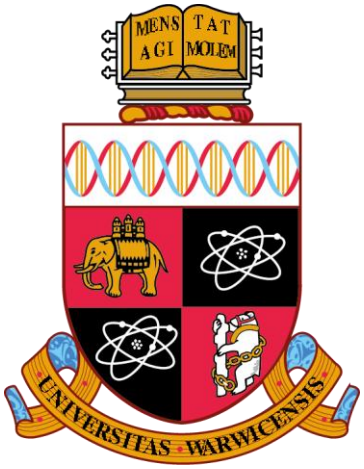

Methods for the Determination of the Structures and Dynamics of Proteins by Solid-State NMR Spectroscopy

by

Jonathan Mark Lamley

Thesis

Submitted to the University of Warwick

for the degree of

Doctor of Philosophy

Supervised by Dr. Józef R. Lewandowski

Department of Chemistry

August 2015

THE UNIVERSITY OF WARWICK

CONTENTS

LIST OF TABLES

LIST OF FIGURES

ACKNOWLEDGEMENTS

The undertaking of this project would not have been possible without the help of a number of important people. First and foremost, I must thank my supervisor, Dr. Józef Lewandowski, for the endless guidance and support he has given me throughout. I am enormously grateful for all of the time he has dedicated to teaching me over the last four years, and I will miss his infectious (often coffee-augmented) enthusiasm. I also owe a great deal to Dr. Dinu Iuga, Dr. Andy Howes and Dr. Tom Kemp for their frequent technical assistance, and to Prof. Steven Brown for introducing me to the field of NMR around five years ago. I am also grateful to Carl Öster and Becky Stevens for their assistance in conducting experiments.

Huge thanks must go to the collaborators I have had the fortune to work with, in particular Prof. Dr. Stephan Grzesiek, Dr. Hans Jürgen Sass and Marco Rogowski for supplying our group with high quality protein samples and for their advice and input on manuscripts for publication, and also Ago Samoson for sharing with us his revolutionary 0.8 mm probe and the skills for its use (and of course the refreshments he supplied at times of need). I am also indebted to Dr. Yusuke Nishiyama, Dr. Michal Malon and Dr. Manoj Pandey for inviting me to Japan and helping me to conduct such exciting research there in collaboration with Jeol Resonance.

This project was funded by the EPSRC, and I am also extremely thankful to the 850 MHz Solid-State NMR Facility for their generous grants that have enabled me to travel and share my research with a global audience.

Finally, special thanks must go to all of my good friends and colleagues in the NMR department (and of course the NMR football team) for keeping me (mostly) sane, and to Chloe for putting up with me even when I wasn't.

DECLARATIONS

This thesis, **Methods for the Determination of the Structures and Dynamics of Proteins by Solid-State NMR Spectroscopy**, is original work based on my research at the University of Warwick under the supervision of Dr. Józef Lewandowski, and no part of it has been submitted for any degree at any other university.

A number of the results presented in this work were obtained in collaboration with others. All solid-state NMR spectra, measurements, spectral assignments and data analyses were recorded or carried out by myself, except for the following: the spectra shown in Figures 4.3 and 4.4 were recorded by Józef Lewandowski, the spectrum shown in Figure 9.1a was recorded by Carl Öster, and the spectra shown in Figure 9.4 were recorded by Józef Lewandowski and Rebecca Stevens. Subsequent processing was completed by myself.

The simulations of TSAR polarisation transfer shown in Figure 4.2 were conducted by Józef Lewandowski, as were the modelling of the GB1-IgG complex shown in Figure B.5, the simulations of ^{15}N $R_{1\rho}$ rates in Figure C.2, and the simulations of spectral densities and the model-free fitting in Chapter 10. The model-free analysis in Chapter 9 was conducted by myself. The solution-state NMR spectrum of GB1 in Figure B.4 was recorded by Hans Jürgen Sass.

All GB1 protein samples were expressed at Biozentrum, Basel, Switzerland by Hans Jürgen Sass, Marco Rogowski and Stephan Grzesiek, and subsequently prepared into crystalline or complex form by myself. The results obtained using the 0.8 mm MAS probe for Chapters 6 and 9 were obtained in collaboration with Dinu Iuga and Ago Samoson (Tallin, Estonia).

Results from other authors' publications, where quoted, are referenced in the text. As indicated in the text, the results of Chapters 4, 5, 8 and 10 have been published in *Journal of Magnetic Resonance*, *Journal of the American Chemical Society*, *Angewandte Chemie* and *Physical Chemistry Chemical Physics* respectively. Much of the content of Chapter 7 has been accepted for publication in the *Encyclopedia of Magnetic Resonance*.

ABSTRACT

Protein molecules perform a vast array of functions in living organisms and the characterisation of their structures and dynamics is a key step towards a full understanding of many biological processes. Magic angle spinning (MAS) solid-state NMR (SSNMR) spectroscopy has emerged as a uniquely powerful technique for the extraction of such information at atomic resolution, with mounting successes founded on continual developments in methodology and technology. In this thesis, a number of new approaches for probing the structures and dynamics of proteins are presented, towards the aim of overcoming current challenges regarding sensitivity, spectral resolution and a shortage of quantitative experimental observables.

A streamlined method for simultaneously obtaining long-distance homonuclear (^{13}C-^{13}C) and heteronuclear (^{15}N-^{13}C) contacts is introduced that relies on the third spin-assisted recoupling (TSAR) mechanism. The experiment, dubbed "time-shared TSAR" (TSTSAR), effectively doubles the information content of spectra and reduces the required experimental time to that needed for just one of the equivalent PAR or PAIN-CP experiments.

An approach for the quantitative study of large proteins and complexes is presented, relying on a combination of proton detection at "ultrafast" (≥55 kHz) MAS frequencies, sample deuteration and optional paramagnetic doping. This is successfully employed for the characterisation of a >300 kDa precipitated complex of the protein GB1 with full length human immunoglobulin (IgG), with only a few nanomoles of sample.

Recent advances in MAS technology have enabled spinning frequencies of 100 kHz and above to be obtained. Using the dipeptide *β*-Asp-Ala, it is found that under such conditions, protons lines are narrowed to an extent similar to that achievable using contemporary homonuclear decoupling methods, leading to a time-efficient method for obtaining resolved spectra of small, natural-abundance molecules. Similar experiments with a GB1-IgG complex sample confirm the technology's applicability to non-model biological systems, despite the tiny rotor volume of 0.7 μL (≤3 nanomoles of complex).

^{15}N $R_{1\rho}$ relaxation rates are measured for the same complex and compared with identical measurements in crystalline GB1, allowing for a direct comparison between the slow (ns-ms) dynamics of the protein in different molecular environments. Motions on this time scale are found to be more prevalent in the complex, possibly evidence of an overall collective molecular motion.

An approach for the measurement of aliphatic ^{13}C relaxation rates in fully protonated samples is presented, based on a combination of ultrafast MAS rates and alternately labelled samples. Sample spinning at ≥80 kHz enables resolved $^{13}C^{\alpha}$-^{1}H correlations, forming a base for $^{13}C^{\alpha}$ relaxation experiments that are subsequently performed on crystalline [1,3-^{13}C,^{15}N]GB1 and analysed using a simple model-free (SMF) treatment. It is noted that without further data, this analysis is likely inadequate for an accurate description of the dynamics of the protein.

The measurement of ^{13}C' $R_{1\rho}$ relaxation rates at ultrafast MAS rates is introduced as a probe of backbone protein dynamics in fully protonated samples. ^{13}C and ^{15}N R_1 and $R_{1\rho}$ relaxation rates are measured in crystalline [U-^{13}C,^{15}N]GB1 and analysed using the SMF formalism. An examination of simulated spectral densities rationalises the apparent inconsistencies that arise from this and reveals that motions in GB1 occur on at least two time scales. A combined ^{15}N/^{13}C extended model-free (EMF) analysis is conducted for peptide plane motions in GB1, whereupon it is found that the addition of ^{13}C data helps to remove fitting artefacts present in a ^{15}N-only analysis.

ABBREVIATIONS

2D (*n*D)	Two-Dimensional (*n*-Dimensional)
COSY	COrrelation SpectroscopY
CP	Cross-Polarisation
CRAMPS	Combined Rotation And Multiple Pulse Spectroscopy
CSA	Chemical Shift Anisotropy
CSP	Chemical Shift Perturbation
CW	Continuous Wave
DARR	Dipolar Assisted Rotary Resonance
DREAM	Dipolar Recoupling Enhanced by Amplitude Modulation
DSS	4,4-dimethyl-4-silapentane-1-sulfonic acid
EDTA	Ethylenediaminetetraacetic acid
EMF	Extended Model-Free
FID	Free Induction Decay
FT	Fourier Transform
GAF	Gaussian Axial Fluctuation
GB1	The B1 domain of Protein G
HORROR	HOmonucleaR ROtary Resonance
IgG	Immunoglobulin G
INEPT	Insensitive Nuclei Enhanced by Polarisation Transfer
IUPAC	International Union of Pure and Applied Chemistry
MAS	Magic Angle Spinning
NOE	Nuclear Overhauser Effect
NOESY	Nuclear Overhauser Effect SpectroscopY
NMR	Nuclear Magnetic Resonance
PAIN-CP	Proton-Assisted Insensitive Nuclei – Cross Polarisation
PAR	Proton-Assisted Recoupling
PAS	Principle Axis System
PDB	Protein Data Bank
PDSD	Proton-Driven Spin Diffusion
ppm	Parts Per Million
r.f.	Radio Frequency
R^2	Rotational Resonance
R^3	Rotary Resonance Recoupling
REDOR	Rotational Echo DOuble Resonance
RFDR	Radio Frequency-driven Dipolar Recoupling
S/N	Signal to Noise
S^3E	Spin State Selective Excitation
slpTPPM	Swept Low-Power Two Pulse Phase Modulation
SMF	Simple Model-Free
SPINAL	Small Phase INcremental ALternation decoupling
SSNMR	Solid-State Nuclear Magnetic Resonance
TMS	Tetramethylsilane
TPPI	Time-Proportional Phase Incrementation
TPPM	Two Pulse Phase Modulation
TSAR	Third Spin-Assisted Recoupling
TSTSAR	Time-Shared Third Spin-Assisted Recoupling
WALTZ	Wideband, Alternating phase, Low-power Technique for Zero-residual splitting
XiX	X-Inverse-X

1

INTRODUCTION

In the past few decades, solid-state nuclear magnetic resonance (SSNMR) spectroscopy has emerged as a powerful technique for the characterisation of molecular structures and dynamics. Such is the richness and diversity of information available from SSNMR spectroscopy that it is now integral to a huge range of disciplines across the fields of chemistry, physics, biology, materials science, engineering and medicine.

Although historically some of the first NMR experiments were performed on solid samples,[1] the wider field of NMR is today dominated by experiments on samples in solution, where the free tumbling of molecules brings about significant advantages for the implementation of experiments as well as the interpretation of spectra. Because of this key difference in the way in which samples behave in each state, the areas of solution-state and solid-state NMR have over time diverged and become somewhat distinct, and though both are based on the same underlying physical concepts, the methodology associated with each is often appreciably different. Despite the overwhelming prevalence of solution-state NMR as an analytical tool, SSNMR remains arguably the more general technique, as the ability to dissolve a sample (or at least obtain it in liquid form) is not a prerequisite for experimental success. Indeed, the only basic requirement for the latter is a presence of local order within the sample, a fact that also renders SSNMR a practical alternative to x-ray diffraction for structural studies of samples that do not exist in a crystalline form.

Among the most successful of the applications of SSNMR has been the study of biological macromolecules, and in particular proteins. Protein molecules perform a tremendous range of functions in living cells, from enzymatic catalysis and signal transduction to molecular recognition and transport, and as such a key aspiration of biophysical science is the elucidation of detailed structure-dynamics-function relationships that can shed light on the mechanisms that control life processes. At a basic level, a protein is merely a polymer comprising a unique sequence of amino acids, of which twenty different types are genetically coded for. However, further layers of structural complexity are imparted by a capacity to fold into unique three-dimensional

shapes, stabilised by inter-residual interactions (*e.g.* hydrogen bonds, Van der Waals interactions). Locally, secondary structure elements such as α-helices and β-sheets can form, while globally a protein folds into a complex (but specific) structure that determines its ability to interact with other molecules and hence perform its specific function. Moreover, the flexibility of the amino acid chain permits extensive molecular dynamics, and indeed this ability to sample different conformations is often equally important to a protein's function.[2,3] Governed by an exceedingly complex energy landscape, protein dynamics occur across a vast range of time scales, extending from small-scale (ps-range) bond librations, through (ns-range) side chain rotations to large scale events such as collective domain motions and folding (ns-s). A true, comprehensive description of a protein must therefore reflect not only the average molecular structure, but its evolution through time.

The essentially infinite scope for variation in the length and sequence of amino acid chains enables living organisms to manufacture a vast array of macromolecules of bewildering diversity, each one bespoke to its individual task. Whilst there has been great progress in *ab initio* structure prediction methods,[4] it is generally unfeasible to predict a protein's complex fold and behaviour simply from its composition, and so understanding of these aspects must be derived from experimental data. At present, the only methods capable of finding the structures of proteins with atomic resolution are NMR and x-ray diffraction (though state of the art cryo-electron microscopy is rapidly approaching atomic resolution[5]). For the site-specific study of protein dynamics, the former of these offers the distinct advantage that the depth and breadth of information available allows it to distinguish between static disorder and motions occurring on different time scales. Because of these facts, solution-state NMR has been widely used for the study of the structures and dynamics of soluble proteins, the first *de novo* structure being solved by Wüthrich and co-workers in 1985 (a feat that would go towards him being jointly awarded a Nobel Prize in 2002).[6] A huge number of important proteins, however, including membrane proteins and amyloid fibrils, are not amenable to study in solution on account of their insolubility. While membrane proteins are known to comprise between 20% and 30% of the human proteome,[7] and are the targets of over 50% of all modern medicinal drugs,[8] they currently account for only around 1% of those proteins whose entire structure is known.[9] Amyloid protein aggregates are known to be implicit in the pathology of several serious diseases such as Alzheimer's and Parkinson's.[10,11] Furthermore, the study of any soluble protein above a certain molecular weight is

hindered by their slow rotational diffusion rates, which may in the future practically limit the utility of solution NMR for the investigation of larger supramolecular protein complexes. Since all these types of systems are also often notoriously difficult or impossible to crystallise, SSNMR is unique in its ability to probe their structures and dynamics at atomic resolution.[12-16]

Ever since the very first Nobel Prize-winning observations of NMR signals by Bloch *et al.* and Purcell *et al.* in December 1945,[1,17] the progression of NMR experimental methodology has been marked by a number of revolutionary breakthroughs that continue to underpin experiments in the field today. In the years immediately following, the potential utility of NMR spectroscopy as a tool for chemical investigation began to be revealed with the discovery of chemical shift[18-20] as well as the observation of internuclear dipolar interactions[21] that encode information about internal molecular structure. It was also realised early on that NMR observables, in particular nuclear relaxation times, were influenced by thermal dynamics within a sample.[22-24] Continual improvements in magnet design led to the attainment of ever greater field strengths and homogeneities, the former of which was boosted significantly by a move from permanent magnets and electromagnets to superconducting magnets starting in 1964.[25] Benefitting from concurrent advances in electronics and computing, the pulsed-Fourier transform (FT) NMR method that continues to be used almost exclusively in modern spectrometers was developed by Ernst and co-workers in 1966.[26] Pulsed-FT NMR would go on to almost completely supplant the "continuous wave" method employed up to that point thanks to its ability to far more rapidly acquire data.

The very first published NMR spectrum of a protein was in 1957 by Saunders *et al.*[27] Because of their relatively large molecular size and the large number of distinct resonances, NMR of proteins has always been limited by low inherent sensitivity and the complexity of the resulting spectra. A crucial advance, first suggested by Jean Jeener in 1971 and subsequently developed by the Ernst group, was two-dimensional (2D) NMR, in which resonances are dispersed across two frequency dimensions and correlated with those of neighbouring nuclei.[28-30] The resulting "correlation spectroscopy" (COSY) experiment, in which resonances are correlated via scalar couplings between nuclei, continues to be a staple in the NMR arsenal, both for helping to resolve crowded spectra and for resonance assignment. This pivotal breakthrough was followed by the introduction of a similar method ("nuclear Overhauser spectroscopy", or "NOESY") that made use of the dipolar coupling-based nuclear Overhauser effect (NOE),[31] enabling

the quantitative measurement of internuclear distances that was to become key to protein structure determination protocols in solution. Quantitative, widespread site-specific study of the dynamics of proteins by NMR relaxation can be largely traced back to work in the solution state by the Bax group in the late 1980s,[32] with quantitative analysis of dynamics data aided significantly by the successful "model-free" formalism introduced by Lipari and Szabo.[33,34]

For SSNMR, the broadening of resonances due to a lack of motional averaging from overall molecular tumbling has traditionally represented its greatest hurdle, and has thus been a major factor in experimental method development in the field. The invention of magic angle spinning (MAS) in the late 1950's by Andrew *et al.* and Lowe *et al.* to counter this broadening has had a monumental impact.[35,36] MAS, which involves the mechanical rotation of the sample about an axis oriented at 54.7° with respect to the external magnetic field, lies at the heart of nearly all modern protein SSNMR experiments (and indeed the majority of all SSNMR experiments), and achieving ever-greater spinning frequencies in the quest for narrower lines remains an extremely worthwhile ambition. That radio frequency (r.f.) irradiation can also be used to narrow lines by averaging spin interactions ("decoupling") has proven to be similarly indispensable in this capacity.[37-41] The characteristically broader lines encountered in the solid state lead to particularly severe difficulties in observing protons (see Chapter 6), and so most protein SSNMR has conventionally relied on the relatively insensitive direct detection of (unless enriched, dilute) ^{13}C or ^{15}N nuclei, compounding the natural insensitivity of the technique. The "cross-polarisation" (CP) method, pioneered in 1962 by Hartmann and Hahn,[42] brings about an essential enhancement in sensitivity by transferring polarisation to the observed spins from abundant protons, and for this reason has (in combination with decoupling and MAS)[43,44] become a foundation of the bulk of protein SSNMR experiments.

The explosive growth in structural protein SSNMR that continues to this day can in large part be traced back to the development of dipolar recoupling schemes starting in the late 1980's, which enable the reintroduction of dipolar couplings (that are otherwise averaged by MAS) and hence facilitate the measurement of internuclear distances. This growth was, and continues to be, sustained by continual development of experimental methodology, including new recoupling schemes and pulse sequences, improved assignment and data analysis techniques, and novel sample preparation methods. These innovations have been achieved in parallel with (and often facilitated by) rapid advances in technology – in the last three decades, the highest commercially available magnetic

field has risen from around 600 MHz to over 1 GHz,[45] while the maximum MAS frequencies attainable have increased tenfold to over 100 kHz.[15,46-48] By 2002, the field was mature enough to determine the complete 3D structure of a protein (the SH3 domain by Castellani *et al.*[49]). Many more, and larger, structures have since been solved, including those of other crystalline proteins,[50-56] membrane proteins[57-65] and fibrils[66-78]. Whereas solution NMR studies are generally limited to targets of less than approximately 40 kDa (although a few special cases greatly surpass this[79-82]), no such ceiling exists for solids – recently complexes of 1 MDa and above have been studied by SSNMR.[83,84] Contemporary advances such as proton detection[85], dynamic nuclear polarisation (DNP)[86], non-uniform sampling (NUS)[87] and sample sedimentation[13,88] (to name but a few) promise to pave the way for further progress.

Comparable growth is currently being seen in SSNMR dynamics studies thanks to the development of a range of different probes of molecular motion, which offer site-specific and quantitative information over the entire range of protein time scales. Though many of these are derived from solution methods, it is becoming apparent that solid state dynamics studies hold many advantages over solution investigations (see Chapters 7-10). Above all, the lack of tumbling, which is so often a hindrance, actually allows the observation of a broader window of motional time scales.

Despite the Herculean efforts outlined above, the field of SSNMR is still in its relative infancy in comparison with its solution-state cousin. Thanks to its unique capabilities, however, SSNMR is poised to become an equally indispensable technique for the detailed characterisation of proteins and other biomolecules. In order for its growth to continue to accelerate, new and improved tools are required to tap further into the wealth of structural and dynamical information that exists, as well as to overcome persistent difficulties associated with sensitivity and resolution. The work contained within this thesis therefore aims to address this need, by focussing on the development of methods for characterising the structures and dynamics of proteins in the solid state. It is split into several sections: the physical theory relevant to the experiments presented is outlined in Chapter 2. This is followed in Chapter 3 by an examination of contemporary methods that are specific to SSNMR spectroscopy of proteins, in particular for structure determination purposes. Chapters 4-6 contain the results of investigations with this latter theme: (4) a streamlined method for obtaining long-range distance constraints in solids, (5) an approach for the characterisation of large protein complexes, and (6) an exploration into the application of newly-developed MAS

technology to organic and biological molecules. The focus subsequently shifts to the development and application of SSNMR methods for the characterisation of protein dynamics. Chapter 7 outlines current techniques employed in this role, concentrating predominantly on relaxation methods, providing further context for the final three results chapters: (8) the application of relaxation experiments to a large (>300 kDa) protein complex, (9) the introduction of new $^{13}C^{\alpha}$ relaxation probes for fully protonated proteins, and finally (10) a quantitative study of the dynamics of microcrystalline GB1 which includes a new $^{13}C'$ relaxation probe.

2

Nuclear Magnetic Resonance Theory

The theory of NMR is remarkably involved, and there exist numerous volumes concerned with its various intricacies. In contrast with many areas of physical science, the magnetic resonance phenomenon that underpins even the most basic NMR experiment is poorly explained by anything other than quantum mechanics. An exhaustive review of each and every facet of NMR theory is clearly inappropriate here, but below are outlined the main concepts necessary for a full understanding of the work in this thesis, including a review of the basic quantum mechanics of NMR and interaction Hamiltonians, details of the pulsed-FT NMR experiment, and finally a more in-depth examination of NMR relaxation phenomena. The following is largely based on content from the following texts: (a) Duer, M. J. *Introduction to Solid-State NMR Spectroscopy*;[89] Wiley-Blackwell, 2005; (b) Luginbühl, P.; Wüthrich, K. *Progress in Nuclear Magnetic Resonance Spectroscopy* **2002**, *40*, 199;[90] (c) Keeler, J. *Understanding NMR Spectroscopy*; John Wiley & Sons, 2011;[91] (d) Hore, P. J.; Jones, J. A.; Wimperis, S. *NMR: The Toolkit*; Oxford University Press Oxford, 2000; Vol. 92;[92] (e) Levitt, M. H. *Spin Dynamics: Basics of Nuclear Magnetic Resonance*; John Wiley & Sons, 2001;[93] (f) McDermott, A. E.; Polenova, T. *Solid State NMR Studies of Biopolymers*; John Wiley & Sons, 2012;[94] (g) Abragam, A. *The Principles of Nuclear Magnetic Resonance*; Clarendon, Oxford, 1961.[95]

2.1 Theoretical Foundations of Magnetic Resonance

2.1.1 The Zeeman Interaction

The nuclear magnetic resonance phenomenon arises from spin angular momentum, which, like mass or electric charge, is an intrinsic property of subatomic particles. The spin quantum number, I, of an atomic nucleus is dependent on its makeup of protons and neutrons and can take a zero, positive integer or positive half-integer value. The magnitude of the total spin angular momentum, $\hat{\boldsymbol{I}}$, of a nucleus with spin quantum number I is equal to $\hbar\sqrt{I(I+1)}$, while its projection (along an arbitrary z-axis), $\hat{I}_z$, is

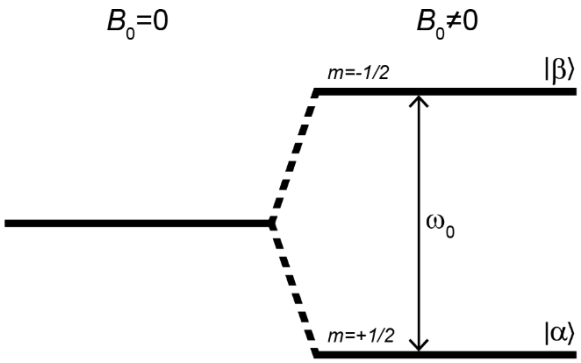

Figure 2.1. Energy levels for a single spin-½ nucleus, with and without an applied magnetic field, B_0. States α and β (with magnetic quantum numbers $\pm$½) have energies that differ by an amount equivalent to the Larmor frequency (in rad s^{-1}), which is proportional to the magnitude of the applied magnetic field.

also quantised in units of ħ by the magnetic quantum number, m, which can take values of $-I, -I+1 \ldots +I$.

Nuclei for which I is non-zero possess a magnetic moment given by

$$\hat{\boldsymbol{\mu}} = \gamma \hat{\boldsymbol{I}} \tag{2.1}$$

where the constant γ is the gyromagnetic ratio, whose value is specific to each nuclear species. In the presence of a static magnetic field, $\boldsymbol{B_0}$, this magnetic moment will interact with the field with the resulting interaction Hamiltonian

$$\hat{H}_Z = -\hat{\boldsymbol{\mu}} \cdot \boldsymbol{B_0} = -\gamma \hat{\boldsymbol{I}} \cdot \boldsymbol{B_0}. \tag{2.2}$$

This is the Zeeman interaction. If the magnetic field vector is taken to define the z-axis ($\boldsymbol{B_0} = (0, 0, B_0)$), the Zeeman Hamiltonian is

$$\hat{H}_Z = -\gamma \hat{I}_z B_0 = \omega_0 \hat{I}_z \tag{2.3}$$

where we define the *Larmor frequency* as $\omega_0 = -\gamma B_0$.[i] In the classical view of magnetic resonance, the nuclear magnetic moment vector nutates about the field axis at ω_0.[22]

In the simple case of an isolated spin-½ nucleus, $m = \pm 1/2$ and so the Hamiltonian has two eigenstates, denoted $|\alpha\rangle$ and $|\beta\rangle$ ("aligned" and "anti-aligned", or "spin-up" and "spin-down"), with energies

[i] In NMR spectroscopy, the strength of the applied magnetic field, B_0, is commonly given in terms of the Larmor frequency (in Hz) of the ^{1}H nucleus at that field (e.g. 14.1 T ≡ 600 MHz).

$$E_{\alpha,\beta} = \mp\frac{1}{2}\hbar\gamma B_0 = \pm\frac{1}{2}\hbar\omega_0. \tag{2.4}$$

Without a magnetic field, these energy levels are degenerate. In general, upon application of a magnetic field to a nucleus with spin I, a total of $2I + 1$ energy levels are formed, each separated by an energy equivalent to ω_0. This is called Zeeman splitting (Figure 2.1). At equilibrium, the populations of the energy levels are determined by the Boltzmann distribution, with the result that a population difference (and hence a net magnetisation) is induced that scales with B_0. Transitions between energy levels of a system may be stimulated by applying radio frequency (r.f.) irradiation (see section 2.2.1).

2.1.2 The Density Operator

Quantum mechanically, the physical state of a system can be represented in the bra-ket notation by a state vector, $|\psi\rangle$, a linear superposition of $|\alpha\rangle$ and $|\beta\rangle$ states, *i.e.* $|\psi\rangle = c_\alpha|\alpha\rangle + c_\beta|\beta\rangle$.[ii] A convenient approach for describing the state of an ensemble of spins is to define a density operator, $\hat{\rho}$:

$$\hat{\rho} = \overline{|\psi\rangle\langle\psi|} \tag{2.5}$$

where the overscore indicates an ensemble average. In matrix form, the density matrix has elements $\rho_{rs} = \langle r|\hat{\rho}|s\rangle = c_r c_s^*$, which, for a single spin-½ nucleus is

$$\rho_{\alpha\beta} = \begin{pmatrix} c_\alpha c_\alpha^* & c_\alpha c_\beta^* \\ c_\beta c_\alpha^* & c_\beta c_\beta^* \end{pmatrix}. \tag{2.6}$$

With increasing numbers of spins, N, the size of this matrix scales as 2^N. The diagonal elements correspond to populations of eigenstates, while the off-diagonal elements represent coherences between the eigenstates. Non-zero off-diagonal elements indicate that the phases of the involved states evolve not randomly, but to some extent in a coherent manner on average. At equilibrium in a static magnetic field, only the diagonal elements of the density matrix are non-zero. The *order* of coherence between two states, 1 and 2, is defined as $p_{1,2} = |m_1 - m_2|$, with m the total magnetic quantum number of each state. In an NMR experiment, r.f. radiation is applied to the spin system with the aim of generating and manipulating coherences between states.

[ii] Or more generally, $|\psi\rangle = \sum_i c_i|\phi_i\rangle$.

For any observable Q, it can be shown[96] that the expectation value of its corresponding operator, $\hat{Q}$, is simply

$$\langle \hat{Q} \rangle = \mathrm{Tr}[\rho(t)\boldsymbol{Q}] \tag{2.7}$$

with information about the sample and relating to the measurement being contained within ρ and $\boldsymbol{Q}$ respectively. $\rho(t)$ is as a function of time, as the spin system evolves under the influence of the Hamiltonian, and it is this behaviour that we observe in an NMR experiment. The evolution of pure quantum mechanical states is described by the time-dependent Schrodinger equation. Derived[96] from this is the Liouville von-Neumann equation, which describes how the density operator evolves in time:

$$\frac{\mathrm{d}}{\mathrm{d}t}\hat{\rho}(t) = -i[\hat{\mathcal{H}}, \hat{\rho}]. \tag{2.8}$$

The solution to this equation is

$$\hat{\rho}(t) = e^{-i\hat{\mathcal{H}}t}\hat{\rho}(0)e^{i\hat{\mathcal{H}}t} \tag{2.9}$$

where $\hat{\mathcal{H}}$ is the total Hamiltonian, a sum of contributions that each arise from different interactions of spins with their environment. To fully understand the result of an NMR experiment, we must therefore consider these different contributions. Indeed, the true power of NMR spectroscopy lies in its ability to probe, and derive useful information from, the unique multitude of interactions present in a given sample.

2.1.3 Interaction Hamiltonians

When placed in a magnetic field, the total Hamiltonian that acts on a system of spins is

$$\hat{\mathcal{H}} = \hat{\mathcal{H}}_Z + \hat{\mathcal{H}}_{CS} + \hat{\mathcal{H}}_D + \hat{\mathcal{H}}_J + \hat{\mathcal{H}}_Q + \hat{\mathcal{H}}_P + \hat{\mathcal{H}}_K. \tag{2.10}$$

The first of these terms is the Zeeman Hamiltonian, which we have already discussed ($\hat{\mathcal{H}}_Z = \omega_0 \hat{I}_z$). Even with the high magnetic fields commonly used for NMR spectroscopy experiments, this constitutes only a very small energy compared to those encountered in other spectroscopic techniques. The remaining terms, which represent internal interactions present within the sample, are further orders of magnitude smaller still and as such are usually treated as first order perturbations to the Zeeman Hamiltonian. These interactions are specific to the chemical environments of the nuclei themselves, giving rise to different energies for different nuclei even within the same

molecule. Respectively, $\hat{\mathcal{H}}_{CS}$, $\hat{\mathcal{H}}_{D}$, $\hat{\mathcal{H}}_{J}$, $\hat{\mathcal{H}}_{Q}$, $\hat{\mathcal{H}}_{P}$ and $\hat{\mathcal{H}}_{K}$ are Hamiltonians for the chemical shielding, the dipolar interaction, J-coupling, the quadrupolar interaction, the paramagnetic interaction and the Knight shift, and the details of each of which will be discussed below.

The Hamiltonian for each internal interaction can be written as a Cartesian tensor:

$$\hat{\mathcal{H}}_{A} = \hat{I} \cdot \tilde{A} \cdot \hat{S} = [I_x \; I_y \; I_z] \begin{pmatrix} A_{xx} & A_{xy} & A_{xz} \\ A_{yx} & A_{yy} & A_{yz} \\ A_{zx} & A_{zy} & A_{zz} \end{pmatrix} \begin{bmatrix} S_x \\ S_y \\ S_z \end{bmatrix} \tag{2.11}$$

where $\tilde{A}$ is a second rank tensor representing the interaction (with elements dependent on the coordinate frame). $\hat{I}$ is the spin operator for one spin, while $\hat{S}$ is either the spin operator for a second spin or the external field, depending on the interaction.

In order to consider each of the interactions, it is most straightforward to deal with them in their principal axis system (PAS), a coordinate frame in which the interaction tensor $\tilde{A}$ is diagonal:

$$\hat{\mathcal{H}}_{A}^{P} = \hat{I} \cdot A^{P} \cdot \hat{S} = I_x A_{xx}^{P} S_x + I_y A_{yy}^{P} S_y + I_z A_{zz}^{P} S_z. \tag{2.12}$$

However, since NMR measurements are conducted in the laboratory frame (in which the dominant Zeeman interaction lies, by convention, in the z-direction), it is necessary to rotate each interaction tensor to this frame from its individual PAS. In order that we can more easily accomplish this, we can express the interaction Hamiltonians in spherical, rather than Cartesian, tensor form:

$$\hat{\mathcal{H}}_{A} = \sum_{j=0}^{2} \sum_{m=-j}^{+j} (-1)^{m} \Lambda_{j,m} \hat{T}_{j,-m}. \tag{2.13}$$

The Hamiltonian is hence expressed as a sum of a number of terms with different rank j and order m (which can take $2j$+1 values). Each term in this expansion is made up of an irreducible spherical tensor component (*i.e.* spatial component), $\Lambda_{j,m}$, which represents the direction and magnitude of the interaction, and a spin operator, $\hat{T}_{j,-m}$, representing the quantum mechanical operator. Under spatial rotations, only $\Lambda_{j,m}$ is affected. The spin operators for each rank and order, as well as the correspondence between the Cartesian and spherical tensor components is given in Appendix A. In the PAS, because only the

diagonal elements of the Cartesian tensors are non-zero, the above expression reduces to only four terms (all others are zero):

$$\hat{\mathcal{H}}_A^P = \Lambda_{00}^P \hat{T}_{00} + \Lambda_{20}^P \hat{T}_{20} + \Lambda_{22}^P \hat{T}_{2-2} + \Lambda_{2-2}^P \hat{T}_{22}. \tag{2.14}$$

The first of these terms is isotropic (rank 0, *i.e.* a scalar), while the next three terms are anisotropic (rank 2 tensors). Of these, only select terms will be non-zero depending on the interaction type, leading to further possible simplifications (see below for specific interactions). The spin operators and irreducible tensor components for the chemical shift and dipolar interactions are given in Appendix A.

The PASs for each interaction (and for each spin within a sample) are not coincident, and as such rotation of the interaction tensors in three dimensions to the laboratory frame must be through a general set of "Euler angles", (α,β,γ). By common convention (and it should be noted that more than one convention is used in the literature[89]), rotation is firstly applied about the z-axis by an angle α, which shifts the x- and y-axes. A second rotation is then applied about the "new" y-axis by an angle β, shifting the x- and z-axes. This is followed finally by a rotation about the new z-axis by an angle γ. This set of rotations is illustrated in Figure 2.2 and can be written

$$\hat{R}(\alpha, \beta, \gamma) = \hat{R}_z(\alpha)\hat{R}_y(\beta)\hat{R}_z(\gamma). \tag{2.15}$$

A spherical tensor component, Λ_{jm}, is converted by rotation into a sum of components with the same rank, j (*i.e.* a scalar will remain a scalar, while a second rank tensor will remain as such) but different order, m. For a rotation from the PAS to the laboratory frame, this is given by

$$\Lambda_{jm'}^L = \sum_{m=-j}^{+j} \Lambda_{jm}^P D_{mm'}^j(\alpha_{PL}, \beta_{PL}, \gamma_{PL}) \tag{2.16}$$

where $D_{mm'}^j(\alpha_{PL}, \beta_{PL}, \gamma_{PL})$ is the rotation matrix, defined as

$$D_{mm'}^j(\alpha_{PL}, \beta_{PL}, \gamma_{PL}) = e^{-im\alpha_{PL}} \cdot d_{mm'}^j(\beta_{PL}) \cdot e^{-im'\gamma_{PL}} \tag{2.17}$$

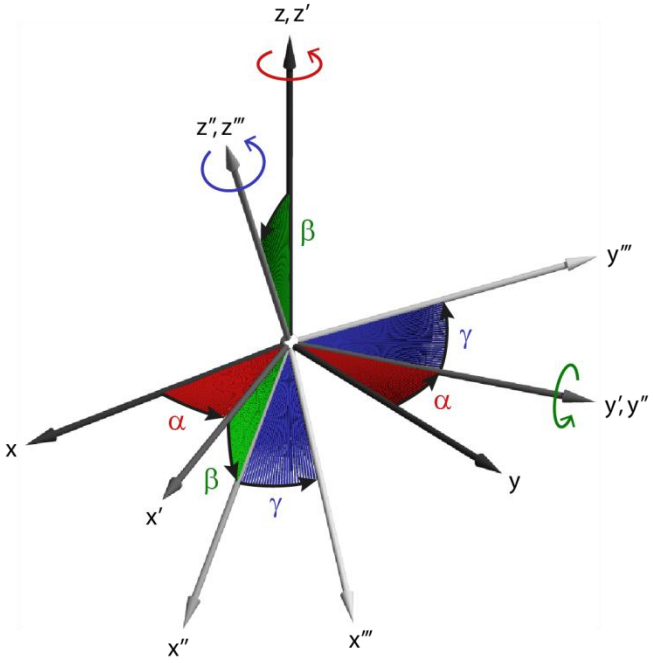

Figure 2.2. Illustration of the rotation between frames using Euler angles. The set of rotations represented by $\hat{R}(\alpha, \beta, \gamma)$ corresponds to (i) a rotation about the z-axis by an angle α, (ii) a rotation about the y-axis by an angle β, and finally (iii) a rotation about the z-axis by an angle γ.

and α_{PL}, β_{PL} and γ_{PL} are the Euler angles describing the relative orientation between the two frames. $d^{j}_{mm'}(\beta)$ are elements of what are known as the reduced Wigner rotation matrices, which can be found in Appendix A.

As mentioned, the interactions discussed here are much smaller than Zeeman interaction and as such can be considered as first order perturbations to the Zeeman Hamiltonian. As a consequence of this, an approximation can be made whereby in rotating to the laboratory frame only spin terms that commute with the Zeeman interaction, $\hat{I}_z$, are retained. This is known as the secular, or high-field, approximation. The commutator is $[\hat{I}_z, \hat{T}_{jm}] = m\hat{T}_{jm}$, which is only equal to zero when m=0. Therefore, in the laboratory frame,

$$\hat{\mathcal{H}}_A^L = \Lambda_{00}^L \hat{T}_{00} + \Lambda_{20}^L \hat{T}_{20}. \tag{2.18}$$

Only a single isotropic component and a single anisotropic component remain. The magnitude of an anisotropic interaction depends on its orientation with respect to the magnetic field, while isotropic interactions are orientation-independent. In the solution state, the overall tumbling of molecules ensures that the nuclei within them experience effectively all possible orientations over a short time scale (*e.g.* ns, depending on the size

of the molecule), and so an average of each interaction is observed. Anisotropic interactions are said to be "averaged", and only the effects of isotropic chemical shift and J-coupling are observed.

2.1.4 Chemical Shielding

Perhaps the most valuable interaction for the majority of NMR experiments carried out is chemical shielding. Within a molecule, an applied static magnetic field ($\boldsymbol{B_0}$) induces currents in electron orbitals, generating an opposing field. The total effective field at the site of the nucleus is therefore modified:

$$\boldsymbol{B_{eff}} = (1 - \tilde{\sigma})\boldsymbol{B_0} \tag{2.19}$$

where $\tilde{\sigma}$ is the chemical shielding tensor. Because the electron density surrounding a nucleus varies depending on the local environment of that site (*e.g.* its location within a molecule), the strength of the chemical shielding interaction is different for each unique nuclear environment in a molecule, leading to measurable differences in the Larmor frequencies of those nuclei. This effect is called *chemical shift*, and the ability to measure it and hence differentiate between nuclei that are of the same species but located in different chemical environments is one of the most powerful tools in experimental NMR.

In Cartesian form the Hamiltonian for the chemical shift interaction is

$$\hat{\mathcal{H}}_{cs} = \gamma \hat{\boldsymbol{I}} \cdot \tilde{\sigma} \cdot \boldsymbol{B_0}. \tag{2.20}$$

Because the electron density is three-dimensional and in general not isotropic, $\tilde{\sigma}$ is a second rank tensor. In general, the chemical shift has both an isotropic and anisotropic contributions (see Appendix A). In the PAS, $\tilde{\sigma}$ is diagonal, with the terms σ_{xx}^P, σ_{yy}^P and σ_{zz}^P known as the principal components (where superscript P denotes PAS). The isotropic chemical shift, which is invariant under rotations, can be written as the mean of these components:

$$\sigma_{iso} = \frac{1}{3}\left(\sigma_{xx}^P + \sigma_{yy}^P + \sigma_{zz}^P\right). \tag{2.21}$$

To describe the anisotropy of the chemical shift tensor, rather than quoting the three principal components it is common to parameterise the tensor with, in addition to σ_{iso}, the so-called anisotropy (Δ) and asymmetry (η). These are defined as[iii]

$$\Delta = \sigma_{zz}^{P} - \sigma_{iso} \tag{2.22}$$

$$\eta = \frac{\sigma_{xx}^{P} - \sigma_{yy}^{P}}{\Delta}. \tag{2.23}$$

In liquids, averaging by isotropic molecular tumbling averages the anisotropic component of chemical shift, so only the isotropic interaction is observed. In this case, each resonance is observed at a different location on the spectrum depending on the isotropic chemical shift (often shortened to simply the "chemical shift"), itself dependent on the local nuclear environment. Because the chemical shift interaction strength is directly proportional to the external magnetic field, in order to directly compare chemical shifts across different fields they are usually quoted with respect to the Larmor frequency of a reference compound:

$$\delta_{iso} = \frac{\omega_0^{sample} - \omega_0^{ref}}{\omega_0^{ref}} \times 10^6 = \frac{\sigma^{ref} - \sigma^{sample}}{1 - \sigma^{ref}} \times 10^6 \tag{2.24}$$

where we have used equations 2.3 and 2.19 to convert between Larmor frequencies and shielding tensors, and δ_{iso} is in units of parts per million (ppm) owing to the relatively small magnitude of the shift when compared to the Zeeman interaction (the difference in Larmor frequencies that is due to the chemical shift is small compared to the overall Larmor frequencies). Because δ_{iso} is now field-independent, it reflects purely the local electronic environment of the nucleus. For ^{1}H and ^{13}C (and ^{29}Si), the standard reference compound for most applications is tetramethylsilane (TMS), although 4,4-dimethyl-4-silapentane-1-sulfonic acid (DSS) is often used for proteins as it is soluble in water and may therefore be packed along with a hydrated sample.[97,98]

In static solids, the lack of molecular tumbling means that the interaction is not averaged, and for different orientations the interaction strength (and hence chemical shift observed) is different. At a given angle defined by (θ, ϕ) (polar and azimuthal angles

[iii] σ_{iso}, Δ and η roughly correspond to the spherical tensor components Λ_{00}, Λ_{20} and $\Lambda_{2\pm2}$ in the PAS, respectively (see Appendix).

between the chemical shielding PAS and the laboratory frame – see Ref. 89), the first order interaction strength is given by:[89]

$$\omega_{CS}(\theta,\phi) = -\omega_0\sigma_{iso} - \frac{1}{2}\omega_0\Delta[(3\cos^2\theta - 1) - \eta\sin^2\theta\cos 2\phi]. \quad (2.25)$$

In a static powdered sample, effectively all the possible orientations are present and sum to give rise to a distinctive "powder pattern".

2.1.5 Dipolar Coupling

As described earlier, nuclei with non-zero spin possess a magnetic moment. In a multi-spin system, these will interact with one another through space. The strength of this interaction, which is known as the direct dipole-dipole interaction (or dipolar coupling), depends on the gyromagnetic ratios of the two nuclei, the distance between them and the orientation of the dipolar vector with respect to the magnetic field (see Figure 2.3a). For coupled spins I and S,

$$\hat{\mathcal{H}}_D = d_{IS}(\hat{\boldsymbol{I}}\cdot\hat{\boldsymbol{S}} - \frac{3(\hat{\boldsymbol{I}}\cdot\hat{r})(\hat{\boldsymbol{S}}\cdot\hat{r})}{r^2}) \quad (2.26)$$

where $\hat{r}$ and r are, respectively, the unit vector and the magnitude of the vector between the two spins, and d_{IS} the dipolar coupling constant:

$$d_{IS} = -\frac{\mu_0\hbar}{4\pi}\frac{\gamma_I\gamma_S}{r^3} \quad (2.27)$$

in units of rad·s^{-1} Note that the inverse-cubed dependence of the interaction on the separation means that measurements of dipolar couplings can provide distance measurements between pairs of nuclei, which can ultimately lead to methods for determining molecular structures. Note also that the dipolar coupling is, unlike the chemical shift, independent of the B_0 field. For neighbouring nuclei within a molecule, dipolar couplings usually lie in the range of kHz to tens of kHz (*e.g.* a ^{13}C-^{1}H coupling at a one-bond distance of 1.09 Å has a strength of ~23 kHz). The energy levels resulting from a system of two coupled spins are shown diagrammatically in Figure 2.3b. In such a system, double-quantum ("flip-flip") transitions ($|\alpha\alpha\rangle \leftrightarrow |\beta\beta\rangle$) and zero-quantum ("flip-flop") transitions ($|\alpha\beta\rangle \leftrightarrow |\beta\alpha\rangle$) are possible in addition to the single-quantum transitions that were possible for a single spin-½, two level system (one spin "flips").

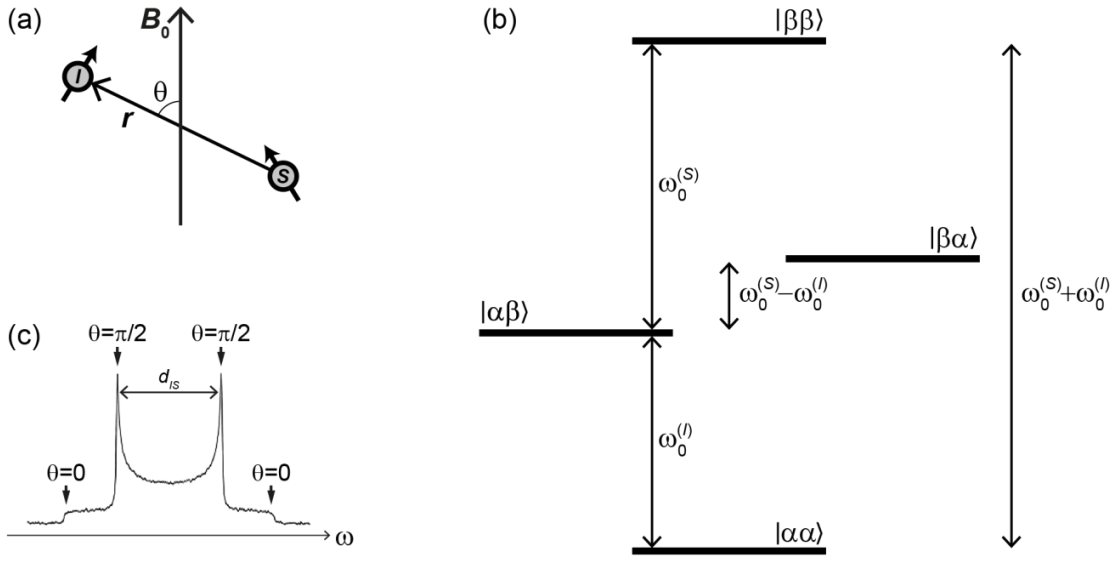

Figure 2.3. (a) Representation of the dipolar interaction between two nuclei (I and S), where the interaction strength is dependent on the angle, θ, subtended by the internuclear vector, $\boldsymbol{r}$, and the magnetic field vector, $\boldsymbol{B_0}$. (b) Energy levels for two dipolar-coupled spin-½ nuclei, I and S, with corresponding Larmor frequencies ω_I and ω_S. (c) Pake doublet line shape of a static powdered sample that is due to the $(3\cos^2\theta - 1)$ dependence of dipolar coupling. For each distinct value of θ, the line is split into a doublet with separation d_{IS}. When the $(3\cos^2\theta - 1)$ dependence is integrated over a sphere, the line shape is a superposition of two mirror-image powder patterns corresponding to each of the doublet resonances. Features arising from different values of θ are marked. The separation between the two maxima is d_{IS} (or $3d_{IS}/2$ for a homonuclear coupling[99]), the dipolar coupling constant as defined in the main text of §2.1.5.

In Cartesian tensor form, the dipolar coupling Hamiltonian is

$$\hat{\mathcal{H}}_D = -2\hat{\boldsymbol{I}} \cdot \tilde{D} \cdot \hat{\boldsymbol{S}}. \tag{2.28}$$

In spherical tensor notation, in the PAS, this is

$$\hat{\mathcal{H}}_D^P = \Lambda_{20}^P \hat{T}_{20} \tag{2.29}$$

where the rank 0 term (see equation 2.14) is zero because the dipolar tensor, $\tilde{D}$, is traceless ($D_{xx} + D_{yy} + D_{zz} = 0$) and the terms with rank 2, order ±2 are zero because $\tilde{D}$ is axially symmetric ($D_{xx} = D_{yy}$).

Rotating A_{20}^P into the laboratory frame gives (ignoring the Λ^L terms for which $m \neq 0$ by using the secular approximation[iv])

[iv] The full expressions for $\hat{T}_{2,\pm1,2}$ are given in Appendix A. In some cases, such as for the treatment of relaxation, all terms need to be considered.

$$\Lambda_{20}^{L} = \Lambda_{20}^{P} D_{00}^{2} = \sqrt{6} d_{IS} \frac{1}{2} (3\cos^2\theta - 1) \tag{2.30}$$

where we have substituted $A_{20}^{P} = \sqrt{6} d_{IS}$ and looked up the relevant reduced Wigner rotation matrix element.

The $\hat{T}_{20}$ spin term is given by (see Appendix A)

$$\hat{T}_{20} = \frac{1}{\sqrt{6}} (3\hat{I}_z\hat{S}_z - \hat{\boldsymbol{I}} \cdot \hat{\boldsymbol{S}}) = \frac{1}{\sqrt{6}} (2\hat{I}_z\hat{S}_z - (\hat{I}_x\hat{S}_x + \hat{I}_y\hat{S}_y)) \tag{2.31}$$

where $\hat{\boldsymbol{I}} \cdot \hat{\boldsymbol{S}} = \hat{I}_x\hat{S}_x + \hat{I}_y\hat{S}_y + \hat{I}_z\hat{S}_z$. For the heteronuclear case (where the two coupled nuclei are of different species), the $(\hat{I}_x\hat{S}_x + \hat{I}_y\hat{S}_y)$ term is absent and the dipolar Hamiltonian constitutes a first order shift to the Zeeman interaction (the eigenfunctions of the $\hat{I}_z\hat{S}_z$ operator are simply the Zeeman states, $|\alpha\alpha\rangle$ *etc.*). For the homonuclear case, the presence of this latter term has some interesting effects. In particular, the degenerate spin states (*e.g.* $|\alpha\beta\rangle$ and $|\beta\alpha\rangle$ states in a two-spin system) are "mixed", so that the eigenfunctions of the spin system are linear combinations of degenerate Zeeman levels. This leads to a range of transition frequencies, resulting in Gaussian broadening of the observed lineshape.[89] In addition, it leads to a phenomenon whereby the Hamiltonian does not necessarily commute with itself at different time points (the "observed" spin state of each spin varies between α and β), a consequence of which is that magic angle spinning (see below) proves less efficient than in the heteronuclear case.

In the heteronuclear case, there is no degeneracy and hence only two transitions are possible. For a static powdered sample, integrating the $(3\cos^2\theta - 1)$ dependence of each of these transitions over all orientations results in a so-called *Pake doublet* lineshape (Figure 2.3c).[21]

2.1.6 J-Coupling

A second mechanism through which nuclei can couple is J-coupling, which, in contrast to the through-space direct dipole-dipole interaction, is an indirect coupling mediated by electrons. The spin of the first nucleus perturbs the spin of the electrons, which in turn perturb the energy levels of the second nucleus. The Hamiltonian for this type of interaction is

$$\hat{\mathcal{H}}_J = \hat{\boldsymbol{I}} \cdot \tilde{J} \cdot \hat{\boldsymbol{S}} \tag{2.32}$$

where $\tilde{J}$ is the J-coupling tensor. $\tilde{J}$ is not traceless and as such has an isotropic (scalar) component, but while anisotropic J-coupling terms can exist[100] they are almost always ignored owing to their small magnitude. The J-coupling tensor is therefore normally written as $\tilde{J} = \frac{1}{3}(J_{xx} + J_{yy} + J_{zz})$.

The isotropic J-coupling interaction is field-independent and causes splitting of resonances in the NMR spectrum, with the components separated by an energy, given by J (in units of Hz), of usually only a few Hz to hundreds of Hz (*e.g.* ~120-130 Hz for a ^{13}C-^{1}H one-bond J-coupling). This splitting is readily observed in solution NMR (molecular tumbling does not average the isotropic interaction) and is a valuable tool in determining the structures of soluble molecules[101], but such a small coupling strength often renders it unobservable by solid state NMR, where other interactions dominate and mask its effect. Nevertheless, in many biological samples in the solid-state, line widths (*e.g.* of ^{13}C resonances) are narrow enough under favourable conditions for J-couplings to be observed.

2.1.7 Other Interactions

Nuclear species with spin >½ possess, in addition to a magnetic dipole moment, an electric quadrupole moment due to a non-spherical charge distribution at the nucleus. The interaction of this moment with electric field gradients across the nucleus is known as the quadrupolar interaction. This effect can often lead to extremely broad resonances of several MHz. For biological samples, the nuclei of interest (*e.g.* ^{1}H,^{13}C, ^{15}N) are mostly spin-½ only and therefore do not exhibit quadrupolar couplings. Deuterium (^{2}H, spin-1) is used reasonably often in biological solid-state NMR (*e.g.* in observation of the narrowing of the lineshape by dynamics[102] but for the purposes of this work is only used in the context of dilution of proton dipolar networks, and as such the details of the quadrupolar interaction will not be discussed further.

Materials with unpaired electrons exhibit the paramagnetic interaction, where couplings exist between the unpaired electrons and nuclei. In the context of proteins, paramagnetic ions can be added to a sample in order to induce resonance shifts and/or enhanced relaxation (see §2.3). Because the couplings depend on the distances between the paramagnetic centre and the nuclei, distance information may be extracted from

paramagnetic shifts.[103-105] In addition, relaxation enhancements can be used as a tool to reduce the recycle time of an experiment (see §2.2.4).

Finally, the Knight shift interaction arises in metals when shielding from conduction electrons leads to an additional effective field at the nucleus. As the Knight shift only occurs in metals, it is not relevant to any of the results in this thesis.

2.1.8 Magic Angle Spinning

As has been described, many of the interactions discussed above are anisotropic in nature, meaning that their strength depends on their orientation with respect to the external magnetic field. In solution, the overall tumbling of molecules ensures anisotropic interactions are averaged. In the solid state, however, this natural averaging does not occur, and so anisotropic interactions remain directly observable. In a solid sample, where typically many (or indeed effectively all) orientations are present, NMR lines are broadened as a result of summing the resonances from each of the individual orientations. This broadening is often undesirable, as although many potentially valuable sources of information are encoded within it, excessive broadening can easily lead to poor spectral resolution and hence difficulties in extracting that information.

A common and often indispensable technique to counteract this broadening in solid-state NMR is *magic angle spinning* (MAS), in which samples are placed inside a "rotor" that is mechanically rotated rapidly about an axis that is oriented at the so-called "magic angle" (θ =54.7°) with respect to the external magnetic field (see Figure 2.4). This method effectively attempts to emulate the molecular tumbling that occurs in liquids.

To explain how MAS works, we return to our discussion of frame transformations and rotation operators. There, we dealt with rotations of spherical tensors using Euler angles between the PAS and laboratory frames. Including MAS into this treatment necessitates the use of two rotations: firstly from the PAS to the rotor frame, with Euler angles $\Omega_{PR} = (\alpha_{PR}, \beta_{PR}, \gamma_{PR})$, and secondly from the rotor frame to the laboratory frame, with Euler angles $\Omega_{RL} = (\alpha_{RL}, \beta_{RL}, \gamma_{RL})$. Of the latter, α_{RL} is the time-dependent angle through which the rotor rotates (equal to $-\omega_r t$ where ω_r is the sample spinning frequency), β_{RL} is the angle of the rotor axis with respect to the field, and γ_{RL} is essentially arbitrary and can be set to zero. For the two rotations, the spatial component of the anisotropic interaction tensor can be written

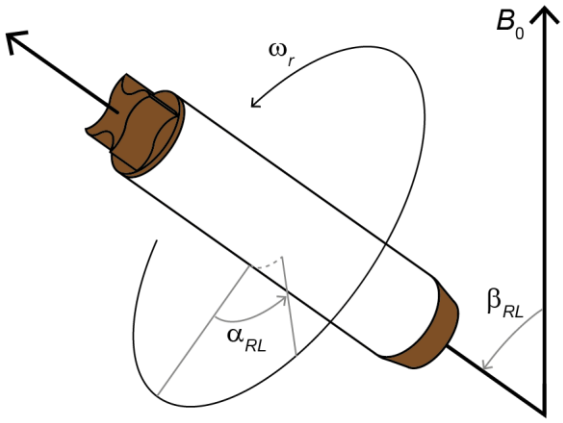

Figure 2.4. Magic angle spinning. The sample is packed into a rotor that is mechanically rotated (through the time-dependent angle α_{RL}) at a frequency ω_r about an axis oriented at an angle β_{RL} with respect to the applied magnetic field, $\boldsymbol{B_0}$. For effective averaging of first order anisotropic interactions, β_{RL} is set by the experimentalist to 54.7°.

$$\Lambda_{20}^{L} = \sum_{m=-2}^{2} \Lambda_{2m}^{P} D_{m0}^{2}(\Omega_{RL}) D_{0m}^{2}(\Omega_{PR}) \tag{2.33}$$

recalling that, owing to the secular approximation, Λ_{20}^{L} is the only relevant non-scalar term in the laboratory frame. The Wigner rotation matrix for the rotation from the rotor frame to the laboratory frame is

$$D_{m0}^{2}(\Omega_{RL}) = e^{im\omega_r t} d_{m0}^{2}(\beta_{RL}). \tag{2.34}$$

For one rotation of the rotor over a time $2\pi/\omega_r$,

$$\int_{0}^{2\pi/\omega_r} e^{im\omega_r t} = \begin{cases} 1 \text{ for } m = 0 \\ 0 \text{ for } m \neq 0 \end{cases}. \tag{2.35}$$

Therefore, for $m \neq 0$, $D_{m0}^{2}(\Omega_{RL})$ and hence Λ_{20}^{L} average to zero over one complete rotor period.

For the $m = 0$ case,

$$\Lambda_{20}^{L} = \Lambda_{20}^{P} D_{00}^{2}(\Omega_{RL}) D_{00}^{2}(\Omega_{PR}) = \Lambda_{20}^{P} d_{00}^{2}(\beta_{RL}) d_{00}^{2}(\beta_{PR}) \tag{2.36}$$

where the reduced Wigner rotation matrix $d_{00}^{2}(\beta_{RL}) = \frac{1}{2}(3\cos^2\beta_{RL} - 1)$. By setting the rotor axis, β_{RL}, to 54.7°, this term and hence A_{20}^{L} are zero.

MAS experiments therefore aim to reduce the anisotropic components of interactions by employing sample rotation about an axis that lies at this angle with

respect to the magnetic field. In simple terms, all components of anisotropic interactions that are parallel with the rotor axis are zero at 54.7°, while all those perpendicular are averaged to zero over a full rotor period. The faster the spinning frequency, the better this averaging. As a rule of thumb, the sample must be spun at a frequency much greater than the interaction strength (in Hz) for fully effective averaging of the interaction (for homogeneous interactions, for reasons discussed in §2.1.5, the requirements are even greater). At lower spinning frequencies, where averaging is not complete, the $m \neq 0$ terms of equation 2.33 must be considered. Full calculation involving the Wigner rotation matrices for $m = \pm 1,2$ (and taking β_{RL}=54.7°) yields

$$\Lambda_{20}^{L} = \Lambda_{20}^{P}\left[\frac{1}{2}\sin^2(\beta_{PR})\cos(2\gamma_{PR} - 2\omega_r t) - \sqrt{2}\sin(2\beta_{PR})\cos(\gamma_{PR} - \omega_r t)\right]. \qquad (2.37)$$

This expression contains terms oscillating at frequencies of ω_r and $2\omega_r$, which give rise to so-called "spinning side bands". The lineshape arising from an anisotropic interaction is split into a number of resonances, separated, in Hz, by integer multiples of the spinning frequency. These sidebands decrease in intensity as the spinning frequency is increased, eventually leaving only a single resonance at the isotropic chemical shift, which remains observable (as do J-couplings, which are also scalar) as in liquid-state NMR. Modern MAS technology can routinely spin samples up to frequencies of tens of kHz. Many of the experiments in this piece of work rely of state-of-the-art probes that enable spinning frequencies of up to 67 kHz (1.3 mm diameter rotors) or even 100 kHz (0.8 mm rotors). Such fast spinning can cause a large amount of frictional heating of the rotor and hence sample, an important consideration when dealing with biological samples. Additionally, the necessarily small diameters of rotors used can limit the volume of sample that can be studied, impacting negatively on experimental sensitivity.

2.2 The Pulsed-FT NMR Experiment

The NMR experiment allows an experimental scientist to probe a sample, at the molecular level, by observing the behaviour of spins over time and hence obtaining information about the various interaction Hamiltonians active in the system. In order to accomplish this, the experimentalist must perturb the system. This is achieved through the application of r.f. radiation. The total Hamiltonian becomes

$$\hat{\mathcal{H}} = \hat{\mathcal{H}}_Z + \hat{\mathcal{H}}_{int} + \hat{\mathcal{H}}_{rf} \qquad (2.38)$$

where $\hat{\mathcal{H}}_{int}$ is the Hamiltonian representing all internal interactions (see Equation 2.10) and $\hat{\mathcal{H}}_{rf}$ is the Hamiltonian for the r.f. irradiation.

Before exploring the various details of the NMR experiment, it is useful at this stage to outline its basic form. The first NMR experiments involved the simultaneous application of r.f. irradiation and a "sweeping" of the B_0 field strength through the resonance condition. Modern experiments, however, are almost exclusively performed in a pulsed manner, whereby the B_0 field is held static and r.f. irradiation is applied in short pulses. This fact, combined with the Fourier transform that is applied to the final signal, gives the technique its name – *pulsed-Fourier transform* (pulsed-FT) *NMR*.

In the simplest terms, the basic pulsed-FT NMR experiment (in its most common form) can be broken down as follows. The sample is placed into a large (*e.g.* several Tesla) static magnetic field, B_0, by packing it into an NMR tube (liquid-state) or rotor (solid-state MAS), loading this into a probe, then inserting this probe into the bore of a superconducting electromagnet. Through interacting with the nuclear magnetic moments within the sample, the magnetic field generates a net magnetisation (M) along the axis of the field (taken to be z) that is proportional to the population difference (between aligned and anti-aligned states) induced. Each of the individual magnetic moment vectors in the sample precesses about the field axis at a frequency ω_0, but because of an isotropic distribution of phases the bulk magnetisation is stationary. Without further intervention, however, the magnetisation of the nuclei is dwarfed by, and cannot be isolated from, the diamagnetism of paired electrons.

In a "one-pulse" experiment, the spectrometer generates an r.f. signal (B_1, orders of magnitude weaker than B_0) that is applied in the form of electromagnetic radiation along an axis perpendicular to B_0, with the effect that each of the individual nuclear magnetic moment vectors, and hence the bulk magnetisation, rotates about the axis of the pulse. The irradiation can be turned off when the bulk nuclear magnetisation lies in the x-y plane. The spins and hence bulk magnetisation continue to precess about the z-axis, an effect that is measurable through electromagnetic induction in a coil wrapped around the sample (the same coil administers the r.f. irradiation). The resulting signal, now isolated from the effect of electron pairs, is returned to the spectrometer for processing.

The above describes the simplest of all NMR experiments. While much information may already be gleaned from such an experiment, more complex methods allow the spectroscopist to probe deeper into the structures, dynamics and behaviour of

a range of samples. Below the various details of NMR experiments are explored in more detail, with a focus where necessary on those methods that are common in protein NMR.

2.2.1 The B_1 Field

The transverse magnetisation that is required for detection is a first order coherence ($p = 1$, see §2.1.2)[v], generated by applying an oscillating magnetic field, referred to as B_1. This has the form

$$\boldsymbol{B}_1 = 2|B_1|\big(\cos\omega_{rf}t + \phi\big)\boldsymbol{i} = |B_1|\big(e^{i(\omega_{rf}t+\phi)} + e^{-i(\omega_{rf}t+\phi)}\big)\boldsymbol{i} \tag{2.39}$$

where $|B_1|$ is the amplitude of the field, ω_{rf} is the frequency of oscillation (and where $\omega_{rf} \approx \omega_0$ to ensure resonance is achieved – see below) and ϕ is the initial phase.

Based on the above expression, the B_1 field can be viewed as two counter-rotating fields with frequencies $+\omega_{rf}$ and $-\omega_{rf}$. Because $-\omega_{rf}$ is far from the Larmor frequency, the component oscillating at this frequency is far off-resonance and so can be neglected. For a field $\boldsymbol{B}$, $\hat{\mathcal{H}} = -\gamma\hat{\boldsymbol{I}}\cdot\boldsymbol{B}$ (as in equation 2.2). The B_1 Hamiltonian is therefore

$$\hat{\mathcal{H}}_{rf} = -\gamma B_1\big[\hat{I}_x\cos(\omega_{rf}t + \phi) + \hat{I}_y\sin(\omega_{rf}t + \phi)\big]. \tag{2.40}$$

By transforming to a second frame that rotates about the z-axis at ω_{rf} (known as the *rotating frame*), the B_1 field appears stationary:

$$\hat{\mathcal{H}}_{rf}^{rot} = -\gamma B_1\big[\hat{I}_x\cos\phi + \hat{I}_y\sin\phi\big]. \tag{2.41}$$

Choosing $\phi = 0$ gives

$$\hat{H}_{rf}^{rot} = \omega_1\hat{I}_x \tag{2.42}$$

i.e. a static field along the x-axis in the rotating frame. We can also define a *nutation frequency*:

$$\omega_1 = -\gamma B_1. \tag{2.43}$$

[v] Coherence is often simply referred to as "magnetisation".

The effect of applying an on-resonance oscillating field to a spin-½ nucleus (starting at equilibrium, $\hat{\rho}(0) = \hat{I}_z$) can be demonstrated by substituting equation 2.42 into the solution to the Liouville von Neumann equation (equation 2.9):

$$\hat{\rho}(t) = e^{-i\omega_1 t\hat{I}_x}\hat{\rho}(0)e^{i\omega_1 t\hat{I}_x} = \frac{1}{2}\begin{pmatrix} \cos(\omega_1 t) & i\sin(\omega_1 t) \\ -i\sin(\omega_1 t) & -\cos(\omega_1 t) \end{pmatrix} \tag{2.44}$$

where for the final step the derivation of the exponential matrix representation of $\hat{I}_x$ can be found in Ref. 92 (see Appendix A for the $\hat{I}_x$, $\hat{I}_y$ and $\hat{I}_z$ spin matrices). Using equation 2.7, the expectation values can be calculated:

$$\begin{aligned} \langle \hat{I}_x \rangle &= Tr[\rho I_x] = 0 \\ \langle \hat{I}_y \rangle &= Tr[\rho I_y] = -i\tfrac{1}{2}\sin(\omega_1 t) \\ \langle \hat{I}_z \rangle &= Tr[\rho I_z] = \tfrac{1}{2}\cos(\omega_1 t). \end{aligned} \tag{2.45}$$

Therefore, applying a pulse with phase ϕ=0 causes oscillations in the y and z components of the spin angular momentum; the "spin vector" rotates about the x axis at the nutation frequency. Changing the phase varies the axis about which the pulse rotates the spin vector. The quantity $\omega_1 t$ is called the *flip angle* of the pulse. When this is equal to $\pi/2$, pure transverse magnetisation is generated: the magnitude of $\hat{I}_y$ is at a maximum and a pure coherence state, where only off-diagonal elements of the density matrix (equation 2.44) are non-zero, is achieved. At $\omega_1 t = \pi$, the transverse magnetisation is zero and the populations in the density matrix are inverted.

The Zeeman Hamiltonian can also be expressed in the rotating frame, where it becomes

$$\hat{H}_Z^{rot} = \Omega\hat{I}_x \tag{2.46}$$

where Ω is the *resonance offset*, equal to $\omega_0 - \omega_{\mathrm{rf}}$. We can therefore define a "reduced field", equal to $-\Omega/\gamma$, that represents the apparent strength of B_0 field in the rotating frame. In the presence of a B_1 field, the effective field experienced in the rotating frame is

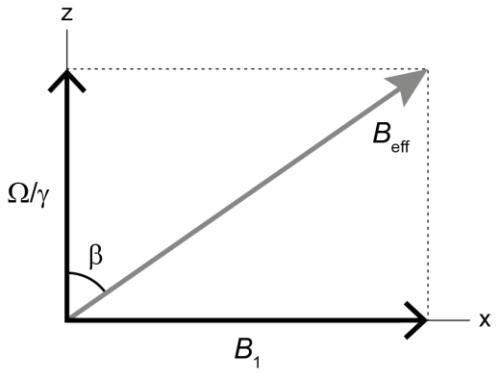

Figure 2.5. Graphic illustration of the effective field, B_{eff}, which in the rotating frame is equal to $\sqrt{{B_1}^2 + (\Omega/\gamma)^2}$.

$$B_{eff} = \sqrt{{B_1}^2 + (\Omega/\gamma)^2} \tag{2.47}$$

as shown diagrammatically in Figure 2.5. For an on-resonance B_1 field ($\omega_{rf} = \omega_0$), $B_{eff} = B_1$. For severely off-resonance r.f. irradiation, the reduced field may be comparable to or larger than the B_1 field and the B_{eff} vector will lie far from the intended axis of the pulse, resulting in an inefficient pulse with a nutation frequency of

$$\omega_{eff} = \sqrt{{\omega_1}^2 + \Omega^2}. \tag{2.48}$$

The "tilt angle" is defined as

$$\tan\beta = \omega_1/\Omega. \tag{2.49}$$

For relatively high values of ω_1 (a "hard" pulse, *e.g.* ~100 kHz), the tilt angle is $\sim\pi/2$ for a wider range of offsets, Ω, than for lower ω_1 (a "soft" pulse, *e.g.* a few kHz). Hard pulses are therefore generally used to excite resonances over the chemical shift range of a given isotope, while soft pulses can be used to selectively excite resonances in a much narrower band. The extremely large offset between nuclei of different nuclear species (usually tens or hundreds of MHz) ensures that any pulse applied on-resonance to one species (*e.g.* ^{1}H) will have essentially no effect on spins of other species (*e.g.* ^{13}C).

2.2.2 The NMR Signal

From here, we turn our attention to detection of the signal, which in the laboratory frame oscillates at ω_0. In practical terms, frequencies on the order of the resonance

offset are much more manageable and so the raw signal is "mixed down" with the r.f. frequency generated by the spectrometer (ω_{rf}). The observed transverse magnetisation therefore evolves under the Zeeman Hamiltonian according to

$$\hat{\rho}(t) = e^{-i\Omega t\hat{I}_z}\hat{\rho}(0)e^{i\Omega t\hat{I}_z} = \begin{pmatrix} 0 & \frac{1}{2}e^{-i\Omega t} \\ \frac{1}{2}e^{i\Omega t} & 0 \end{pmatrix} \tag{2.50}$$

where we have started with $\hat{\rho}(0) = \hat{I}_x$. The operator corresponding to the measured transverse magnetisation is the lowering operator[vi] (in this case its complex conjugate, *i.e.* the raising operator, $\hat{I}_+ = \hat{I}_x + i\hat{I}_y$; see Appendix A). The measured signal is simply the expectation value, given by

$$s(t) = Tr\left[\hat{\rho}(t)\hat{I}_+\right] = \frac{1}{2}e^{i\Omega t} = \frac{1}{2}[\cos(\Omega t) + i\sin(\Omega t)]. \tag{2.51}$$

The signal that is detected therefore has two components, real and imaginary, oscillating at the resonance offset. This corresponds to measuring two signals $\pi/2$ out of phase with each other, which enables the discrimination of the sense of precession when detected in the coil.

In reality, the signal does not continue interminably, but rather its envelope decays exponentially until it effectively vanishes. The origin of this damping is "spin-spin", or T_2, relaxation, which may be understood in terms of individual precessing magnetic moment vectors. Because of small inhomogeneities in the local magnetic fields experienced by the spins (due to different chemical environments, for example), they each precess at slightly different frequencies. As precession continues, the spins lose coherence with one another as the phases between them grow. In this way, the magnitude of the overall precessing bulk magnetisation, and hence signal, decays:

$$s(t) = e^{i\Omega t}e^{-\frac{t}{T_2}} \tag{2.52}$$

where T_2 is the transverse relaxation time (and we have dropped the factor of ½ from the previous expression). When this is detected in the coil, the resulting signal is known as the *free induction decay* (FID).

[vi] Transverse magnetisation is coherence of $p = \pm 1$. By convention, $p = -1$ is measured (with corresponding operator $\hat{I}_-$).

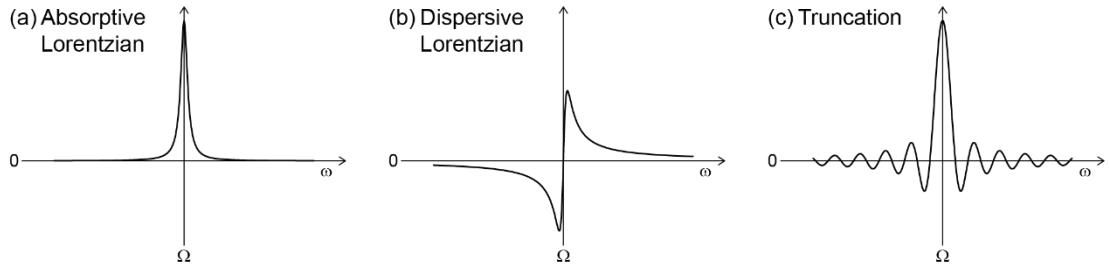

Figure 2.6. (a) Absorptive and (b) dispersive Lorentzian line shapes that result from applying a Fourier transform to a raw NMR signal. If acquisition stops before the signal fully decays, the resulting line shape (c) displays oscillations that are characteristic of a sinc function ($f(x) = x/\sin(x)$).

2.2.3 The Fourier Transform

In an NMR experiment, we observe the behaviour of spins in a variety of different chemical environments, often at the same time. The signal from each of these will oscillate at a unique frequency defined by not only the Hamiltonian of the Zeeman interaction, but those of the various internal interactions the nuclei are subject to. In a protein, for example, there are often hundreds of ^{13}C nuclei, with varying chemical shifts resulting from their different local electronic environments. The total NMR signal measured will be a sum of the individual signals from all of these. To separate the signal into its different frequency components, a Fourier transform is applied to convert the time-domain signal into a function of frequency (ω):

$$s(\omega) = \int_0^\infty [e^{i\Omega t} e^{-t/T_2}] e^{-i\omega t} = A(\omega - \Omega) - iD(\omega - \Omega) \tag{2.53}$$

where

$$A = \frac{1/T_2}{(1/T_2)^2 + (\omega - \Omega)^2} \tag{2.54}$$

$$D = \frac{(\omega - \Omega)}{(1/T_2)^2 + (\omega - \Omega)^2}. \tag{2.55}$$

The Fourier transform therefore yields real and imaginary lineshapes that are absorptive and dispersive Lorentzian curves, respectively (see Figures 2.6a,b). Usually, only the absorptive line shape is displayed as the imaginary part is broader, although in practice the real part is often not purely absorptive due to phase imperfections in the magnetisation detected. In order to counteract this, a linear combination of the real and

imaginary parts can be taken to recover a purely absorptive lineshape in a procedure known as "phasing".

The line width (at half height) of the absorptive Lorentzian is, in Hz, $1/\pi T_2$, meaning that the longer the transverse relaxation time, the narrower the lines observable and hence the greater the spectral resolution obtainable. This is influenced by a number of factors, including field and sample inhomogeneities, internuclear interactions and dynamics.

In practice, the FID is sampled at discrete time points by the spectrometer. The time period between these points, called the "dwell time", must be short enough to effectively sample the rapidly oscillating signal, and defines the width (in Hz) of the observed spectrum by the relation $SW = \frac{1}{\tau_D}$, where SW is the spectral width (or "sweep width") and τ_D is the dwell time. The spectral window is centred at the resonance offset, Ω. An important note is that the total length (in time) of the FID defines the minimum line width observable – the shorter the acquisition time, the narrower the minimum line width that can be measured. Ceasing acquisition before a signal has relaxed fully results in truncation effects, whereby lines appear broader than their true line width. Extreme truncation leads to spectral distortions known "sinc wiggles" either side of resonances (Figure 2.6c). Usually, a longer acquisition is desirable for avoiding such effects, although if too long excess noise can be introduced. The total acquisition time may also be limited by powerful decoupling (see §2.2.6), which can be damaging to the probe and/or the sample.

2.2.4 Experimental Sensitivity

The overall sensitivity of an NMR experiment is determined by the amplitude of the signal detected in the coil. This is governed by a number of factors, in particular the number of spins, N, the gyromagnetic ratio of the observed nuclear species, the magnetic field and the temperature, T:

$$S \propto \frac{N\gamma^3 {B_0}^2}{T}. \tag{2.56}$$

Note that because the signal intensity is proportional to N, NMR is a quantitative technique. N is defined not only by the size of the sample, but also the relative abundance of the relevant nuclear isotope. The natural abundances of the most commonly observed species in biological NMR are listed in Table 2.1. The most

abundant form of carbon is ^{12}C, but as this has a spin of zero it does not possess a magnetic moment and is therefore "invisible" to NMR. The isotope ^{13}C, which has a spin of ½, is instead used for NMR, but this only has a natural abundance of 1.1%, leading to relatively poor sensitivity. In order to maximise the sensitivity available, it is common to enrich samples with the preferred isotope. The ^{1}H nucleus is almost 100% naturally abundant and also has the highest gyromagnetic ratio of any nucleus type (bar ^{3}H), leading to relatively high sensitivity. Note that the apparent sensitivity of an experiment is also affected by line widths of the resonances observed – the broader the lines, the less intense they are at their maxima.

Although an incredibly powerful technique in terms of the depth and breadth of information available, NMR spectroscopy is in fact inherently insensitive. At the root of this is the fact that the Zeeman interaction itself constitutes an extremely small energy, leading to a small population difference. This can often be so small that the spectral intensity, once Fourier transformed, is on the same order as random noise that is also acquired. To increase the signal to noise (S/N) ratio, it is common to run an experiment

Table 2.1. List of nuclei common in biological molecules, along with spin quantum numbers (I), natural abundances, gyromagnetic ratios (γ) and resultant Larmor frequencies ($\omega_0/2\pi$) at a magnetic field of 14.1 T.[93] The most naturally abundant forms of carbon and oxygen are spin 0 and hence NMR "silent". ^{2}H, ^{14}N and ^{17}O have $I > 1/2$ and so are quadrupolar. ^{1}H, ^{13}C and ^{15}N are spin-½, although the latter two have gyromagnetic ratios of ~1/4 and ~1/10 that of ^{1}H and are of much lower natural abundance, leading to poorer experimental sensitivity. Note that γ is negative for ^{15}N and ^{17}O, leading to negative Larmor frequencies (*i.e.* precession in the opposite direction), a fact that the spectrometer must take into account.

Isotope	Spin, I	Natural abundance (%)	Gyromagnetic ratio, γ (rad s^{-1} T^{-1} × 10^6)	Larmor frequency, $\omega_0/2\pi$, at 14.1 T (MHz)
^{1}H	1/2	~100	267.522	600.00
^{2}H	1	0.015	41.066	92.10
^{12}C	0	98.9		
^{13}C	1/2	1.1	67.283	150.87
^{14}N	1	99.6	19.338	43.36
^{15}N	1/2	0.37	-27.126	-60.82
^{16}O	0	~100		
^{17}O	5/2	0.04	-36.281	-81.34

a number of times and sum the resulting FIDs. The peak intensity obtained is directly proportional to the number of so-called co-added transients (or, commonly, "scans"), n, while the noise is only proportional to the $\sqrt{n}$, resulting in the overall S/N ratio growing as $\sqrt{n}$.

Each scan of an experiment must be separated by a length of time, the *recycle delay*, that permits the spin system to return to equilibrium before repeating it. The process by which this return occurs is "spin-lattice" (T_1) relaxation, and can be viewed as a regaining of z-magnetisation (*c.f.* T_2 relaxation, the loss of x-y magnetisation). The T_1 relaxation time of a nucleus depends on several parameters (see §2.3), but can lie anywhere between μs and minutes or even hours. In practice, the recycle delay should be at least a few times longer than the T_1 time (a multiple of five is often quoted[09]), which can result in experiments needing to be run for anywhere from seconds to days or even weeks to achieve the desired signal to noise.

Clearly the latter case is less than ideal, and as such in many cases the FID is multiplied by a so-called "window function" to improve signal to noise post-Fourier transform. In the simplest case this takes the form of a decaying exponential, which has the effect of suppressing contributions from points recorded later in the FID (where noise constitutes a larger fraction of the recorded intensity) compared to those closer to the beginning of the signal. Unfortunately, this improvement in signal to noise comes at the expense of resolution, as the decay of the signal is effectively enhanced, leading to larger line widths. Because of this, the application of window functions is often termed "line broadening". While exponential broadening is common, Gaussian, sine-squared and other functions are all routinely employed to achieve an effective balance between signal to noise and resolution.

2.2.5 Cross-Polarisation

Because of aforementioned insensitivity of NMR (and especially in the solid state where lines are often broader than in solution), signal intensity is invariably at a premium and much effort must be invested in maximising the efficiency and sensitivity of experiments. An invaluable technique in NMR in the solid state is *cross-polarisation* (CP), whereby after transverse magnetisation is initially generated on one spin species (*e.g.* ^{1}H), it is transferred via dipolar couplings to another by the action of suitably applied r.f. pulses.[42,44]

In the case of CP from protons to a nuclear species X (which is usually a rare or low-γ species such as ^{13}C or ^{15}N), the technique can deliver gains in experimental S/N in two ways. Firstly, a direct sensitivity enhancement is achieved that, maximally, is equal to the ratio of gyromagnetic ratios (γ_H/γ_X). Secondly, because each scan of the experiment begins with the excitation of ^{1}H coherence, the required recycle delay depends on the T_1 relaxation of the ^{1}H rather than that of the X spin. The T_1 times of protons are often far shorter than those of rare spins owing to the larger dipolar couplings ^{1}H are subject to, meaning that more scans can be taken and summed in the same experimental time.

Figure 2.7a shows a simple pulse sequence for CP from ^{1}H to X spins in the form of a pulse diagram, where the horizontal axis represents time (though not quantitatively) and pulses are shown as rectangles upon separate lines that correspond to the nuclei they are being applied on-resonance with. After an initial $\pi/2$ pulse on resonance with protons with phase x ($[\pi/2]_x$), a *spin-lock* pulse is applied to ^{1}H along –y, which acts to maintain ^{1}H magnetisation along –y. A second spin-lock pulse is simultaneously applied to the X spins.

For the general case of species A and B spins in a static sample, for CP to occur the nutation frequencies of the two spin-lock pulses must satisfy the *Hartmann-Hahn condition*:[42]

$$\nu_{1A} = \nu_{1B} \tag{2.57}$$

where $\nu_1 = \omega_1/2\pi$. In order to understand the phenomenon further, it is useful to transform into a "doubly-rotating" frame. In such a system, the A spins are considered in a frame where all the magnetic fields due to A pulses appear static. The B spins are similarly considered in a frame where all the magnetic fields due to B pulses are static. Setting the nutation frequencies of the spin-lock pulses to match the Hartmann-Hahn condition essentially ensures that in the doubly-rotating frame, the energy gaps between the spin states of A and B spin species are equal. The dipolar coupling between the two species allows redistribution of energy between A and B spins whilst maintaining the overall energy of the system, via zero-quantum transitions (see Figure 2.3b). As an A spin flips states (*e.g.* from $|\alpha\rangle$ to $|\beta\rangle$), a B spin flips (or "flops") in the opposite manner (*e.g.* from $|\beta\rangle$ to $|\alpha\rangle$), conserving overall energy. In this way, the B spins can gain polarisation at the expense of A polarisation, which is initially high owing to the initial $[\pi/2]_x$ pulse, but decreases as it cannot be sustained by the weaker spin-lock pulse. This view omits

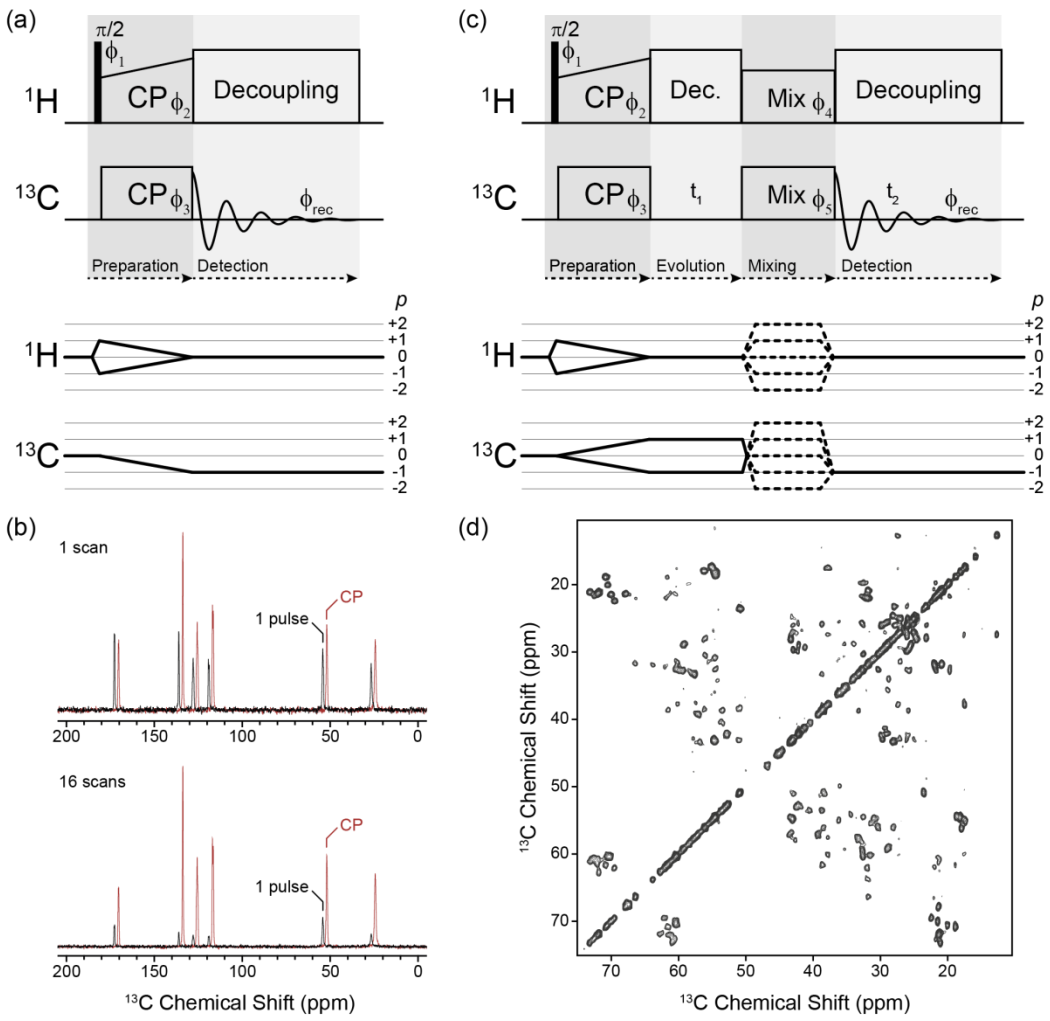

Figure 2.7. (a) Pulse sequence diagram for a ^{1}H-^{13}C cross-polarisation (CP) experiment. t_2 is the acquisition time. The phases of pulses, marked ϕ_n, are cycled over consecutive scans in such a manner that the desired coherence pathway, shown beneath, is followed exclusively. (b) Comparison of 1D ^{13}C spectra of [U-^{13}C,^{15}N]histidine obtained using one-pulse (black spectra) and ^{1}H-^{13}C CP (red spectra) pulse sequences, at a magnetic field of 600 MHz and an MAS frequency of 60 kHz. The red spectra are offset by -3 ppm for ease of comparison. For the CP (1.8 ms), nutation frequencies of 50 kHz and 10 kHz were used for ^{1}H and ^{13}C respectively in order to satisfy the double-quantum Hartmann-Hahn condition. The upper panel shows the spectra resulting from a single scan of each type of experiment – the signal intensities are larger for the CP experiment because of the higher gyromagnetic ratio of ^{1}H (except for the ^{13}C', which lies further from a proton – the CP contact time is unlikely to have been optimal for this site). The lower panel shows the spectra (scaled differently to the upper panel) resulting from 16 scans of the same experiment, with a recycle delay of 2 s – the signal intensity for the one-pulse experiment is even lower relative to the CP experiment because the recycle delay used was far shorter than the T_1 relaxation time of the ^{13}C nuclei (on the order of a minute) but suitably long for protons. (c) Pulse sequence diagram for a generic homonuclear ^{13}C-^{13}C 2D correlation experiment, with the preparation, evolution, mixing and detection stages marked (preparation and detection stages of the CP sequence are marked for comparison in (a)). The blocks marked "Mix" are placeholders for the chosen recoupling scheme, which may excite coherences of various order (as indicated in the coherence pathway diagram) depending on the desired experimental outcome. t_1 is the evolution time. *(Cont'd)*

(d) Example homonuclear 2D correlation experiment on a sample of hydrated fully protonated crystalline [1,3-^{13}C,^{15}N]GB1 protein at a magnetic field of 600 MHz and an MAS frequency of 10 kHz. The general sequence outlined in (c) was used, with a radio frequency driven recoupling (RFDR) recoupling scheme (see §3.2) during the mixing period (1.83 ms). Note the diagonal that is characteristic of homonuclear correlation spectra and results from magnetisation that is not transferred between nuclei during mixing. For both (a) and (c), blocks marked "Decoupling" or "Dec" represent heteronuclear decoupling, applied during evolution and direct detection.

the effects of homonuclear dipolar couplings between the A spins (usually protons). An in-depth treatment is offered in Ref. 89, but, briefly, the primary consequence is that as magnetisation is transferred from protons to the X spins, the proton magnetisation within the ^{1}H network is redistributed accordingly.

The length of time for which the spin-lock pulses are applied during CP is known as the *contact time*, and is typically in the region of ms. The longer the contact time, the more magnetisation can be transferred between spins and the larger the sensitivity enhancement, until the point at which the effects of relaxation begin to dominate. Relaxation in the presence of a spin-lock field is called $T_{1\rho}$ relaxation, or "spin-lattice relaxation in the rotating frame". Longer contact times allow for transfers across larger distances, allowing the experimentalist to control the range of the transfer and potentially to select the nuclei within a molecule that are subject to enhancement. It should be noted, however, that because the enhancement is dependent on this and other factors (*e.g.* resonance offset, dipolar coupling strength, sample dynamics), CP experiments are no longer quantitative.

When MAS is introduced, the fixed time-dependence of the dipolar coupling has the effect of altering the energy gap between the high and low energy spin states by multiples of the spinning frequency. The single CP condition is split into several bands:

$$\nu_{1A} = \nu_{1B} + n\nu_r \tag{2.58}$$

where ν_r is the sample spinning frequency in Hz ($\omega_r/2\pi$) and n is an integer.[44] Efficient polarisation transfer is achieved for $n = 1, 2$. Another matching condition is found at $\nu_{1A} + \nu_{1B} = \nu_r$, *i.e.* where the sum of the spin-lock nutation frequencies is equal to the spinning frequency. This is especially useful at higher spinning frequencies, as it allows spin-lock fields of moderate strength to be applied, avoiding damage to the probe and/or sample. CP of this type is called double-quantum CP, as it relies on double-quantum, rather than zero-quantum, coherence. For either condition, it is common practice to "ramp" at least one of the CP spin-lock pulses across a range of nutation frequencies to

ensure that the condition is more closely matched, if only transiently.[106] A linear ramp is frequently used, although greater efficiency can often be found with more complex shapes. For the majority of experiments in this thesis, a tangent shape is used for double-quantum CP at high MAS frequencies.[107]

For biological SSNMR, in which ^{13}C and ^{15}N act as the most commonly detected nuclei, CP is usually essential and often acts as the first building block in more complex pulse sequences, such as those for two- and three-dimensional experiments. In this context, a useful feature of CP is that it may be performed either in a broadband or a selective manner (for a limited chemical shift range), depending on the offset and nutation frequency of the spin-lock irradiation. For transfer from ^{1}H and ^{13}C, for example, selective CP can be used to excite either the carbonyl ($^{13}C'$) or the aliphatic ($^{13}C^{\alpha,\beta,\cdots}$) carbon resonances, thus affording a measure of control over the "flow" of magnetisation throughout the system.

2.2.6 Decoupling

In §2.1.8, the details of, and the motivation behind, the use of MAS in the solid state to average anisotropic interactions were discussed. Such averaging may be sufficient for interactions of low strength, but the maximum frequency of mechanical rotation attainable is limited by engineering considerations and MAS alone cannot always fully average the stronger dipolar couplings found in proton-rich organic systems. Averaging of these couplings may also be achieved in spin space by use of decoupling pulses applied during the acquisition period (and evolution period – see §2.2.7). We focus here on heteronuclear decoupling, as unfortunately[vii] the requirements for effective homonuclear decoupling (*e.g.* high nutation frequencies that can induce severe sample heating) in many cases preclude their use on protein samples. Heteronuclear decoupling, however, is common in protein experiments and is used for all of the experiments contained within this thesis.

A myriad of heteronuclear decoupling pulse schemes have been developed, varying in their complexity and effectiveness under different experimental conditions, but all have the common aim of suppressing the effects of dipolar couplings between protons and rare spins and hence narrowing spectral line widths. In order to accomplish this, irradiation applied on-resonance with protons reintroduces homonuclear couplings

[vii] Before recent developments in MAS technology and sample deuteration methods, proton detection in proteins in the solid state was severely hampered by the extreme line broadening caused by strong ^{1}H-^{1}H dipolar couplings.

between them, inducing rapid transitions. The result is that an average of the heteronuclear dipolar Hamiltonian is observed (*i.e.* zero), and the coupling is effectively removed.

The simplest form of decoupling is continuous wave (CW) irradiation.[108] Generally, the greater the amplitude of the decoupling, the more effective the averaging is. With MAS of increasing frequency (*e.g.* to remove a larger chemical shift anisotropy at a higher magnetic field), however, the averaging effect becomes less effective. Commonly used heteronuclear decoupling schemes designed to offset this degradation of performance include TPPM[109], SPINAL-64[110] and XiX[111,112], each of which involves trains of pulses of various flip angles and phases. Nevertheless, increased MAS frequencies still require higher nutation frequencies for decoupling, and such strong B_1 fields are undesirable as again they can prove detrimental to sample (and indeed probe) integrity. At MAS frequencies of >40 kHz, it is possible to employ low-power decoupling schemes such as WALTZ-16[113] (often used in solution experiments), slpTPPM[114] and low-power XiX[115], which are efficient at nutation frequencies well below the MAS frequency.

2.2.7 Two-Dimensional Correlation NMR Spectroscopy

In most cases, for useful and reliable information to be extracted from NMR spectra, the individual resonances must be resolved. In one-dimensional (1D) NMR (direct detection only), the resolution of resonances relies on their chemical shift separation being larger than their line widths, which, for many types of samples, cannot always be the case. For proteins, it is common for hundreds of resonances of a given nuclear species (*e.g.* ^{1}H, ^{13}C, ^{15}N) to be present, leading to crowded spectra in which many resonances are likely to overlap. An indispensable tool for studying such samples is the two dimensional (2D) correlation experiment, in which resonances are dispersed across two frequency dimensions.[28,116] Depending on the choice of frequency dimensions, this has the effect of decreasing the likelihood that resonances overlap, as well as, as we shall discuss, offering additional information compared to a 1D experiment.

A 2D correlation experiment consists of a minimum of 4 basic stages: preparation, evolution, mixing and detection (see Figure 2.7c). In the first instance, magnetisation (*i.e.* coherence) is generated on the nuclear species of interest, usually by either a single $\pi/2$ pulse or (more commonly for ^{13}C or ^{15}N) via CP from protons. During the evolution period, the coherence generated is allowed to evolve under the

influence of isotropic chemical shift for a time t_1, before the mixing period where this magnetisation is transferred to different nuclei. This may be to nuclei of a different species (*e.g.* by CP) or to others of the same species, and is achieved by using r.f. pulses and delays to reintroduce interactions such as dipolar couplings (which have been averaged by MAS) in a process called *recoupling*. This transfer of magnetisation can to some extent be controlled by careful choice of the recoupling scheme (see §3.2), but will in general occur between nuclei close in space. The final signal is detected in the same manner as in a 1D experiment, and the entire sequence is repeated for increasing values of t_1 that sample the oscillatory behaviour during evolution. In this way the detected signal is amplitude-modulated by the evolution earlier in the pulse sequence and therefore contains chemical shift information about both nuclear sites:

$$s(t_1, t_2) = (e^{+i\Omega t_1} + e^{-i\Omega t_1}) e^{-t_1/T_2^{(1)}} e^{i\Omega t_2} e^{-t_2/T_2^{(2)}}$$

$$= 2\cos(\Omega t_1)\, e^{-t_1/T_2^{(1)}} e^{i\Omega t_2} e^{-t_2/T_2^{(2)}} \qquad (2.59)$$

where $T_2^{(1)}$ and $T_2^{(2)}$ are the transverse relaxation times for the t_1 (evolution/indirect detection) and t_2 (direct detection) periods respectively.

2D experiments that correlate the chemical shifts of different nuclear sites in this manner are a staple of biological NMR, often forming the basis for more elaborate experiments, and as such this technique is used often throughout this thesis. Depending on the recoupling method employed, an experiment can be designed to correlate chosen nuclei that neighbour each other, giving information about molecular structure and for peak assignment.[94] Note that because the coherence that evolves during t_1 does not necessarily have to be single-quantum coherence (whereas detection during t_2 requires single-quantum coherence), the 2D method also offers the ability to observe multiple-quantum coherences. Experiments that excite and correlate double- (or higher) with single-quantum coherences for the same nuclei are a common and powerful tool in many fields of SSNMR because of their ability to help resolve broad resonances,[117-119] although the efficiency of exciting higher-order coherences can be relatively low.

For a 1D experiment, the total experimental time is simply the length of the pulse sequence (including recycle delay) multiplied by the number of scans. Because acquisition of 2D data requires the repetition of the entire pulse sequence for multiple values of t_1, the total time scale for a 2D experiment is many times longer than an equivalent 1D experiment. The experimental time scales with the spectral width in the indirect

dimension, as this is inversely proportional to the time separation between t_1 increments (resulting in more t_1 increments over the same total t_1 time). The spectral width is often defined by the chemical shift range of observed resonances. Choosing the number of t_1 increments for a given spectral width is then often a balance between the experimental time and the resolution required (as the maximum t_1 time defines the minimum line width observable in the corresponding Fourier-transformed F_1 dimension). The overall sensitivity of an experiment is also impacted by the efficiency of the mixing step – depending on the mixing scheme used and the experimental conditions, only a fraction of the original polarisation may be recovered at the end, so many more scans may be required to offset these losses. Because losses are cumulative, in general the more steps in a pulse sequence, the lower its overall efficiency and the lower the final signal to noise.

To produce a spectrum (with dimensions F_1 and F_2 for the indirect and direct dimensions respectively), Fourier transforms are performed in each dimension. A Fourier transform in the t_2 dimension gives

$$s(t_1, \omega_2) = (e^{+i\Omega t_1} + e^{-i\Omega t_1})e^{-t_1/T_2^{(1)}}(A_2^+ - iD_2^+) \,. \tag{2.60}$$

Here and in all that follows, $A_n^{\pm}$ and $D_n^{\pm}$ represent the absorptive and dispersive lineshapes, respectively, centred at frequencies $\pm\Omega$ in the Fn dimension. To ensure absorptive lineshapes are obtained, a so-called *hypercomplex Fourier transform* is performed, whereby the signal is separated into its real and imaginary parts prior to performing the Fourier transform in F_1. For the real part,

$$\begin{aligned} s^{Re}(\omega_1, \omega_2) &= [(A_1^- - iD_1^-) + (A_1^+ - iD_1^+)]A_2^+ \\ &= (A_1^+ + A_1^-)A_2^+ - i(D_1^+ + D_1^-)A_2^+ \,. \end{aligned} \tag{2.61}$$

For the imaginary part,

$$\begin{aligned} s^{Im}(\omega_1, \omega_2) &= -[(A_1^- - iD_1^-) + (A_1^+ - iD_1^+)]D_2^+ \\ &= -(A_1^+ + A_1^-)D_2^+ + i(D_1^+ + D_1^-)D_2^+ \,. \end{aligned} \tag{2.62}$$

This process therefore yields four different lineshapes – absorptive in both dimensions, dispersive in F_1 only, dispersive in F_2 only and dispersive in both dimensions. However, there is no sign discrimination for Ω in the F_1 dimension – each of the four terms contain lineshapes centred at both $+\Omega$ and $-\Omega$.

A commonly-employed technique to restore this discrimination is the "States" method[120]. In this scheme, two experiments are performed per t_1 increment, with appropriate pulse phases (during the preparation stage) such that during evolution, the signals in each instance are $\pi/2$ out of phase with each other. Two signals are therefore recorded: one with sine modulation and the other with cosine modulation. As above, we first apply Fourier transforms in the t_2 dimension:

$$\begin{aligned} s_{sin}(t_1, \omega_2) &= 2\sin(\Omega t_1)\, e^{-\frac{t_1}{T_2^{(1)}}}(A_2^+ - iD_2^+) \\ &= i(e^{-i\Omega t_1} - e^{+i\Omega t_1})e^{-\frac{t_1}{T_2^{(1)}}}(A_2^+ - iD_2^+) \end{aligned} \tag{2.63}$$

$$\begin{aligned} s_{cos}(t_1, \omega_2) &= 2\cos(\Omega t_1)\, e^{-\frac{t_1}{T_2^{(1)}}}(A_2^+ - iD_2^+) \\ &= (e^{+i\Omega t_1} + e^{-i\Omega t_1})e^{-\frac{t_1}{T_2^{(1)}}}(A_2^+ - iD_2^+)\,. \end{aligned} \tag{2.64}$$

Taking the real parts only and applying Fourier transforms in the t_1 dimension gives

$$\begin{aligned} s_{sin}^{Re}(\omega_1, \omega_2) &= i[(A_1^- - iD_1^-) - (A_1^+ - iD_1^+)]A_2^+ \\ &= [(D_1^- - D_1^+)A_2^+ + i(A_1^- - A_1^+)]A_2^+ \end{aligned} \tag{2.65}$$

$$\begin{aligned} s_{cos}^{Re}(\omega_1, \omega_2) &= [(A_1^- - iD_1^-) + (A_1^+ - iD_1^+)]A_2^+ \\ &= [(A_1^- + A_1^+)A_2^+ + i(D_1^- + D_1^+)]A_2^+\,. \end{aligned} \tag{2.66}$$

Finally, taking the difference of the real part of $s_{cos}^{Re}(\omega_1, \omega_2)$ and the imaginary part of $s_{sin}^{Re}(\omega_1, \omega_2)$ gives

$$\mathrm{Re}[s_{cos}^{Re}(\omega_1, \omega_2)] - \mathrm{Im}[s_{sin}^{Re}(\omega_1, \omega_2)] = 2A_1^+A_2^+ \tag{2.67}$$

i.e. the desired absorptive lineshape at (+Ω, +Ω) only. Peaks are found at the chemical shift of the first nucleus in the F_1 dimension, and the second nucleus (due to mixing) in the F_2 dimension, leading to correlations.

A second popular method for returning sign discrimination, known as "time-proportional phase incrementation" (TPPI)[121], relies on linearly incrementing the phase of the preparation stage by $\pi/2$ every t_1 slice, with the t_1 increment halved. For many of the experiments performed for this thesis, a hybrid method known as "States-TPPI"[122] was used. This is based on the States method outlined above but instead of resetting the phase after every two experiments (*i.e.* 0, $\pi/2$, 0, $\pi/2$...), the phase is incremented linearly

(*i.e.* 0, π/2, π, 3π/2...) as in the TPPI method. This has the result that every other t_1 point is negative, but traditionally this method was much simpler to programme a spectrometer to carry out.

2.2.8 Three-Dimensional Experiments

In the above it was explained how 2D methods can improve experimental resolution by dispersing resonances across a second frequency dimension. A natural extension to this is the three-dimensional (3D) experiment,[123] where a third frequency dimension is introduced by inserting another incremented evolution period and another mixing block or CP step into the pulse sequence.

3D experiments are commonplace in protein NMR owing to their utility in assigning the often large numbers of resonances present.[124,125] Their ability to correlate 3 different types of nuclei (*e.g.* $^{13}C/^{15}N/^{1}H$, backbone or aliphatic *etc.*) for each residue in the chain of a protein is particularly powerful, and frequently multiple complementary 3D experiments are carried out to assign resonances via a sequential process (see §3.3).[125-127]

Naturally, the inclusion of the additional incremented delay again multiplies the experimental time by the number of increments for the third dimension. In addition, the extra homo- or heteronuclear transfer step introduces further losses. Whilst four- (and higher) dimensional experiments are possible,[128-131] in the solid state at least their use is not yet common because of prohibitive experimental time scales. For longer pulse sequences, the action of relaxation means that coherence lifetimes also become a necessary consideration.

2.2.9 Phase Cycling

The idea of coherence relating to off-diagonal elements of the density operator matrix was introduced in §2.1.2. At the beginning of an experiment, at equilibrium, there is no coherence ($\hat{I}_z$) and p=0 (p=0 also represents zero-order coherence, $\hat{I}_+\hat{S}_-$). At the end of an experiment, in-phase transverse magnetisation is detected via electromagnetic induction. This is first order, or single-quantum, coherence: p=±1 ($\hat{I}_\pm$). Through quadrature detection, only one of these is detected, which by convention is p=-1.

In §2.2.1, it was shown how, for a single-spin system, applying a π/2 r.f. pulse can create this single-quantum coherence. For more complicated pulse sequences, additional pulses allow the experimentalist to manipulate coherences further. The

coherence pathway diagrams shown in Figures 2.7a and 2.7c illustrate the desired behaviour of the coherences throughout the sequence. In reality, however, for a more complex system of spins, additional, unwanted coherence orders are excited during pulses. These can be filtered out by *phase cycling*, whereby the experiment in question is repeated a number of times and upon each iteration the phases of the pulses and the receiver (*i.e.* the phase of detection) in the sequence are cycled. Matching the phase of the receiver to that of the desired coherence ensures selection of that coherence, while over a whole cycle, when the FIDs are added, the contributions from unwanted coherences destructively interfere and are hence suppressed.

2.3 Nuclear Relaxation

When perturbed by an applied r.f. field, a system of spins will return to its equilibrium state by relaxation processes. The basic concepts of T_1 and T_2 relaxation were described in §2.2. At its heart, nuclear relaxation is caused by modulation of interactions by molecular motions. Many of the interactions that are relevant to NMR (*e.g.* chemical shift, dipolar and quadrupolar couplings) are anisotropic in nature. Within a molecule, thermal motions will lead to rotations of nuclei (whose configurations define the interactions) and consequently modulation of the magnitudes of these interactions. The resulting fluctuations in the local magnetic fields, if at suitable frequencies, will lead to transitions between energy levels for different spin states and hence allow relaxation of spins back to their equilibrium states. Observation of this behaviour can therefore give insights into the internal motions of molecules, including proteins, where the flexibility and time-evolution of a structure may often be crucial to its function. The details of the complex relationships between relaxation and dynamics are therefore explored in more detail below.

2.3.1 Spin-Lattice (T_1) Relaxation

T_1, or *spin-lattice* relaxation refers to relaxation of a perturbed system back to equilibrium through exchange of energy with a thermal bath, or "lattice". For relaxation to happen, transitions must occur between energy levels to return to the equilibrium state. In proteins, the primary sources of relaxation for ^{13}C and ^{15}N spins are modulation of dipolar couplings and chemical shift anisotropy (CSA) tensors by molecular motions. For a single spin-½ nucleus, spin-lattice relaxation due to modulation of the CSA interaction can be described in terms of transitions between two energy levels (Figure 2.8a).

Assuming that the rate of transitions is proportional to how far from equilibrium the system is, we can write

$$\frac{dn_\alpha}{dt} = W\left(n_\beta - n_\beta^0\right) - W(n_\alpha - n_\alpha^0) = -\frac{dn_\beta}{dt} \tag{2.68}$$

where W is the transition probability (or equivalently transition rate) and multiplies $(n_{\alpha,\beta} - n_{\alpha,\beta}^0)$, the deviation of the population $n_{\alpha,\beta}$ from its equilibrium value, $n_{\alpha,\beta}^0$. At equilibrium, $n_{\alpha,\beta} = n_{\alpha,\beta}^0$ and the rates are zero. The overall z-magnetisation, M_z, is proportional to the population difference. The rate of change of M_z is therefore[132]

$$\frac{dM_z}{dt} = \frac{dn_\alpha}{dt} - \frac{dn_\beta}{dt} = -2W\left[\left(n_\alpha - n_\beta\right) - \left(n_\alpha^0 - n_{\alpha\beta}^0\right)\right] = -2W(M_z - M_z^0) \tag{2.69}$$

where M_z^0 is the equilibrium magnetisation and for simplicity we have taken $M_z = (n_\alpha - n_\beta)$. The above is usually written $\frac{dM_z(t)}{dt} = -\frac{1}{T_1}[M_z(t) - M_z^0]$,[22] where T_1 is the longitudinal (spin-lattice) relaxation time, with the solution

$$M_z(t) = [M_z(0) - M_z^0]e^{-R_1 t} + M_z^0 \tag{2.70}$$

where we have used the relaxation rate, $R_1 = 1/T_1$. It is possible to measure this constant by performing an "inversion recovery" experiment, whereby after an initial π pulse, an incremented delay (τ) is used to follow the return of z-magnetisation due to T_1 relaxation. At the end of the delay, a final $\pi/2$ pulse converts whatever z-magnetisation has been regained by that point into transverse magnetisation for detection. With varying values of τ, the signal intensity I recorded at the end follows the function $I(\tau) = I_0[1 - 2e^{-R_1\tau}]$, which can hence be fitted to the data to extract the constant R_1. Because the energy difference between the energy levels is ω_0, the rate of transitions and hence relaxation will be related to the amount of motion occurring at that frequency.

For the ^{15}N and ^{13}C nuclei that are commonly observed in biological SSNMR studies, inversion recovery is not usually practical as sensitivity often dictates that excitation must take the form of CP from neighbouring protons. Directly following this, the magnetisation lies in the x-y plane, but is of far larger amplitude than it would have been had it been generated simply by a $\pi/2$ pulse. In order to measure R_1, at this point a $[\pi/2]_{-x}$ pulse is used to flip the magnetisation vector back to the +z direction, followed by a delay τ, and finally a $[\pi/2]_x$ to return it back to the x-y plane. By incrementing τ while

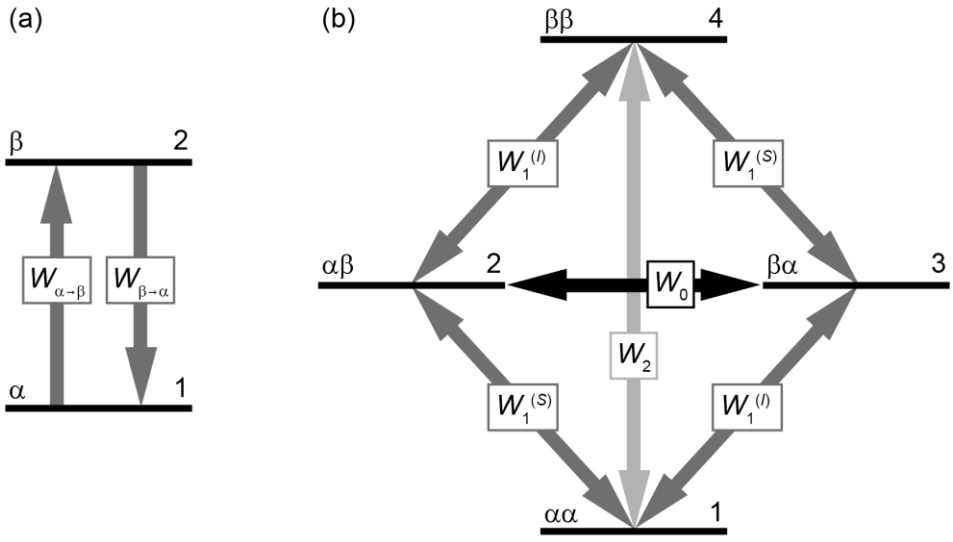

Figure 2.8. Energy level diagrams for (a) a single spin-½ nucleus and (b) two (alike) dipolar-coupled spin-½ nuclei, with transition rates W shown. In (b), a homonuclear case is depicted (*i.e.* $\omega_0^I - \omega_0^S = 0$) but the system is general.

the vector lies in the +z direction, the return of z-magnetisation to its (comparatively tiny) equilibrium value can be tracked as it decays exponentially via the T_1 mechanism.

For relaxation occurring via reorientation of the dipolar coupling between two spins I and S, the situation is complicated by the possibility of transitions at multiple frequencies. This is illustrated in Figure 2.8b, where rates of transition are labelled as $W_{\Delta m}$ (where Δm is the total change in magnetic quantum number) with a superscript denoting which spin is undergoing a transition. The rate of change of the population of level 1 is

$$\frac{dn_1}{dt} = -W_1^{(S)}(n_1 - n_1^0) - W_1^{(I)}(n_1 - n_1^0) - W_2(n_1 - n_1^0) + W_1^{(S)}(n_2 - n_2^0) + W_1^{(I)}(n_3 - n_3^0) + W_0(n_4 - n_4^0) \tag{2.71}$$

where the first three terms represent losses from level 1 and the last three terms account for gains from the other three energy levels. Similar expressions can be written for the other three levels. Both population differences $(n_1 - n_3)$ and $(n_2 - n_4)$ contribute to the z-magnetisation of spin I:

$$I_z = (n_1 - n_3) + (n_2 - n_4) \tag{2.72}$$

while for spin S,

$$S_z = (n_1 - n_2) + (n_3 - n_4) \tag{2.73}$$

After much algebra[133], the rate equations for the populations of each spin can be written in as

$$\frac{dI_z}{dt} = -R_{DD}^{(I)}(I_z - I_z^0) - \sigma^{(IS)}(S_z - S_z^0) \tag{2.74}$$

$$\frac{dS_z}{dt} = -R_{DD}^{(S)}(S_z - S_z^0) - \sigma^{(IS)}(I_z - I_z^0) \tag{2.75}$$

where

$$R_{DD}^{(I)} = 2W_1^{(I)} + W_2 + W_0 \tag{2.76}$$

$$R_{DD}^{(2)} = 2W_1^{(S)} + W_2 + W_0 \tag{2.77}$$

$$\sigma^{(IS)} = W_2 - W_0\,. \tag{2.78}$$

These are known as the *Solomon equations* for the relaxation of spins *I* and *S*, for which the general solution is biexponential. $R_{DD}^{(I)}$ and $R_{DD}^{(S)}$ are the *autorelaxation* rates of spins 1 and 2, respectively, determined without the involvement of the magnetisation of the other spin in each case (analogous to equation 2.69, for a two level system). In equation 2.74, for spin I, a second term exists that depends on the z-magnetisation of spin S (S_z), and vice-versa for equation 2.75, with the rate constant $\sigma^{(IS)}$. This can be interpreted as $\sigma^{(IS)}$ describing the rate at which magnetisation in transferred between spins I and S by the dipolar relaxation process. This is called *cross-relaxation*, and is responsible for the nuclear Overhauser effect (NOE)[134,135], a phenomenon that is routinely exploited in solution NMR for structural studies of molecules owing to its dependence on the dipolar coupling.[31,136-138] The rates W_0, W_1 and W_2 are related to the amount of motion occurring at frequencies corresponding the energies of those transitions, *i.e.* $(\omega_S - \omega_I)$, (ω_S) or (ω_I), and $(\omega_S + \omega_I)$ respectively. The expression of these in terms of motions is explored in §§2.3.3–2.3.5.

2.3.2 Spin-Spin (T_2) relaxation

The dephasing of precessing spin vectors due to motionally-induced variations in the local *B*-field in the z-direction, discussed in §2.2.2, is known as the secular contribution

to transverse (T_2, or "spin-spin") relaxation. A second, non-secular contribution to the decay of transverse magnetisation comes from variations in local fields directly affecting the x- and y-components of the magnetic moments. This contribution is simply half the longitudinal autorelaxation rate constant.[91] The decay of transverse magnetisation by T_2 relaxation can be described by

$$\frac{dM_{xy}(t)}{dt} = -R_2 M_{xy}(t) \tag{2.79}$$

with the solution $M_{xy}(t) = M_{xy}(0)e^{-R_2 t}$, where R_2 is the relaxation rate constant ($R_2 = 1/T_2$) and $M_{xy} = \sqrt{{M_x}^2 + {M_y}^2}$.

In §2.2.3 it was noted that the line width of a resonance is proportional to the rate of transverse decay; line broadening due to pure R_2 processes is known as *homogeneous broadening*. When recording an FID at the end of an experiment, however, the detected signal usually decays much more rapidly than would be expected from the homogeneous R_2 rate alone. This extra dephasing stems from inhomogeneities in the external magnetic field as well as in the sample itself, and leads to *inhomogeneous broadening*. The overall decay of the signal therefore goes as $e^{-R_2^* t}$ where R_2^* is the sum of the homogeneous and inhomogeneous decay rates, and for this reason simply measuring the rate of decay of the FID is not useful (*e.g.* for extracting dynamical information). Instead, a "spin-echo" experiment can be conducted, whereby after an initial $[\pi/2]_x$ pulse an incremented delay τ is inserted before detection. In the centre of this delay is a $[\pi]_y$ pulse, which serves to refocus the precessing spin vectors. Those spins that are precessing faster (because they are in a region of slightly higher magnetic field) travel through a larger angle during the first period $\tau/2$, but after the refocusing pulse have to "catch up" during the second period $\tau/2$. At the end of this period an "echo"[139] is formed (which can be detected), as the spin vectors are once again in phase and any resonance offsets (including those due to chemical shift as well as inhomogeneities) are cancelled out. Tracking the decay of the signal intensity of the echo therefore yields the transverse relaxation rate without inhomogeneous contributions. A spin-echo element within a pulse sequence will refocus not only inhomogeneous broadening and chemical shift, but also heteronuclear couplings.

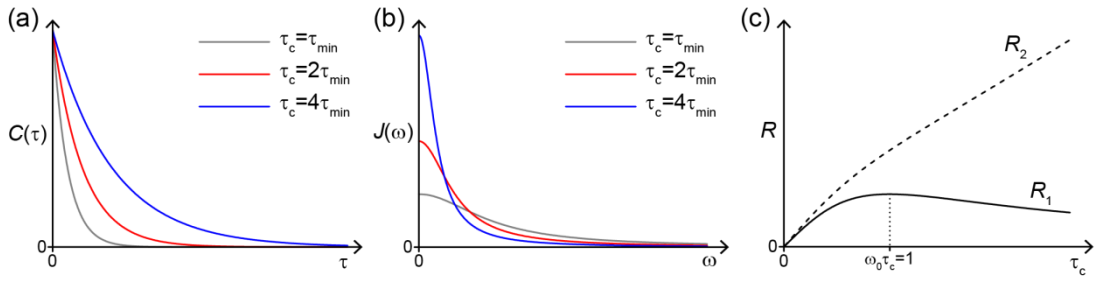

Figure 2.9. (a) Exponential correlation functions ($C(\tau)$) and (b) corresponding Lorentzian spectral density functions ($J(\omega)$) for three different motional correlation times, τ_c. (c) The behaviour of R_1 and R_2 relaxation rates as a function of the motional correlation time. As τ_c increases, R_2 increases, but R_1 reaches a maximum when $\tau_c = 1/\omega_0$. This point is often described as the "T_1 minimum" ($T_1 = 1/R_1$). The relaxation here was assumed to be driven by CSA reorientation, but the behaviour is similar for the dipolar coupling mechanism.

2.3.3 The Spectral Density Function

As was alluded to, the relaxation phenomena described above result from stochastic modulation of anisotropic interactions by molecular motions. A description of the rates of relaxation in terms of the motions that caused them can be calculated from semi-classical relaxation theory (see below), leading to a powerful tool for probing the dynamics of samples through experimental NMR spectroscopy. Assuming that the motions are thermally driven and therefore random in nature, the fluctuations of a local field $B(t)$ can be described by defining a correlation function,

$$C(\tau) = C(t_2 - t_1) = \overline{B(t_1)B(t_2)} \tag{2.80}$$

where the overscore indicates an ensemble average over the entire sample.[94] In general this function will decay with increasing τ, as at longer values of τ the likelihood of $B(t_2)$ changing sign increases, leading to a smaller average. The slower the fluctuation, the slower the decay of $C(\tau)$ (see Figure 2.9a). In general, the form of the correlation function is model-dependent, but in the simplest case we can assume that it can be described as a single exponential:

$$C(\tau) = C(0)\mathrm{e}^{-|\tau|/\tau_c} \tag{2.81}$$

where τ_c is the correlation time, which describes the time scale of the fluctuation and hence molecular motion (the slower the motion, the larger τ_c) and $C(0)$ relates to the amplitude of the fluctuation.

The Fourier transform of the correlation function is the spectral density function,

$$J(\omega) = 2\int_0^\infty C(\tau)\mathrm{e}^{-i\omega\tau}d\tau \tag{2.82}$$

which essentially maps out the "amount of motion" at different frequencies, ω. The spectral density for a single-exponential correlation function is a Lorentzian,

$$J(\omega) = 2C(0)\frac{\tau_c}{1+\omega^2{\tau_c}^2} \tag{2.83}$$

with a maximum centred at $\omega = 0$. Figure 2.9b shows how the form of the spectral density changes with varying values of τ_c. For smaller τ_c (faster motions), the spectral density becomes more spread out, while the intensity at zero frequency is diminished. Multiple uncoupled motions occurring on different time scales can be described by multiple superposed Lorentzian functions. As will be shown below, relaxation rates are related to spectral densities evaluated at frequencies that correspond to those of transitions through which the system can return to equilibrium. These spectral densities are themselves dependent on both the time scales and amplitudes of motions, meaning that measurements of relaxation can give access to comprehensive dynamic information. These ideas are key to many of the experiments carried out in this work (Chapters 9,10).

2.3.4 Semi-Classical Relaxation Theory

To calculate the measurable relaxation rates in terms of spectral densities, we begin by writing the total Hamiltonian as a sum of a static part, $\widehat{\mathcal{H}}_0$, and time-dependent part, $\widehat{\mathcal{H}}_1(t)$:

$$\widehat{\mathcal{H}} = \widehat{\mathcal{H}}_0 + \widehat{\mathcal{H}}_1(t). \tag{2.84}$$

We can switch to the so-called *interaction frame* in which only the $\widehat{\mathcal{H}}_1(t)$ part is active and $\widehat{\mathcal{H}}_0$ vanishes. For laboratory frame relaxation, $\widehat{\mathcal{H}}_0$ is simply the Zeeman Hamiltonian, $\widehat{\mathcal{H}}_Z$, and the interaction frame is the rotating frame (see §2.2.1). For rotating frame relaxation, $\widehat{\mathcal{H}}_0$ is equal to a sum of the $\widehat{\mathcal{H}}_Z$ and $\widehat{\mathcal{H}}_{rf}$ and the interaction frame is the doubly-rotating frame (see §2.2.5). $\widehat{\mathcal{H}}_1(t)$ is purely due to the anisotropic interactions (*e.g.* dipolar coupling, CSA) whose modulation causes relaxation. In solution, under conditions of isotropic molecular tumbling, $\widehat{\mathcal{H}}_1(t)$ is purely stochastic in nature. In the solid state, if anisotropic interactions are not completely averaged (*e.g.* by MAS), $\widehat{\mathcal{H}}_1(t)$

has not only stochastic ("incoherent") contributions, but also "coherent" contributions that are not random in nature[viii]. These processes cause additional magnetisation decay but as this is not caused by motions, their presence often only serves to mask the dynamical information available from relaxation measurements. For example, the T_2 relaxation rate as measured in proteins by a spin-echo experiment is dominated by coherent contributions (and is heavily dependent on the MAS frequency). In this thesis and other works, a distinction is therefore made between pure T_2 relaxation times due to motions only and those measured with a spin-echo, referred to as T_2'.

Assuming perfect averaging of the coherent contributions (*e.g.* in solution or under conditions of suitably fast MAS), $\hat{\mathcal{H}}_1(t)$ can be written as a sum of products of spin operators, $\hat{T}_{j,m}$, and stochastic functions, $F_m(t)$:

$$\hat{\mathcal{H}}_1(t) = \sum_j \sum_m \hat{T}_{j,m} F_m(t)\,. \tag{2.85}$$

$\hat{T}_{j,m}$ are the same as in equation 2.13 (also see Appendix A), with rank j and order m, and correspond to transitions between energy levels of the spin system that are associated with a change of the total magnetic quantum number by m. The eigenvalues, $\omega_{j,m}$, of these operators correspond to the energy that is dissipated into the lattice by these transitions (*i.e.* the differences between the energy levels).

Relaxation rates are obtained by measuring a change of magnetisation over time. Recalling equation 2.7, the expectation value of an observable Q is

$$\langle \hat{Q} \rangle^{int} = \mathrm{Tr}\left[\rho^{int}(t) Q\right] \tag{2.86}$$

where the superscript "int" indicates that the quantity is considered in the interaction frame (and therefore ρ^{int} evolves under $\hat{\mathcal{H}}_1(t)$ only). The Liouville von-Neumann equation can be used to derive[140,141] the macroscopic differential equation for this:

$$\frac{d}{dt}\langle \hat{Q} \rangle^{int} = -\left(\mathrm{Tr}\left(\hat{\Gamma}\{Q\}\rho^{int}(t)\right) - \mathrm{Tr}\left(\hat{\Gamma}\{Q\}\rho_0\right)\right) \tag{2.87}$$

where

[viii] Coherent processes are in principle (although not necessarily experimentally) reversible, as opposed to incoherent processes which are random and therefore irreversible.

$$\hat{\Gamma}\{Q\} = \sum_{j,m} (-1)^m J_m(\omega_{j,m}) \left[\hat{T}_{j,m}, \left[\hat{T}_{j,-m}, Q\right]\right]. \tag{2.88}$$

The change in expectation value (*i.e.* measured value) can therefore be expressed using spectral density functions, J_m, evaluated at the eigenvalues (*e.g.* Larmor frequencies), $\omega_{j,m}$, of the Zeeman Hamiltonian, and the double commutator of spin operators, $\hat{T}_{j,m}$, with the observable Q. In this way, relaxation rates can be expressed in terms of the motions that cause the relaxation process (through spectral densities). Depending on the interaction implicit in causing the relaxation, $\hat{\mathcal{H}}_1(t)$ and therefore the spin operator ($T_{j,m}$) terms will be different (equation 2.85), leading to different expressions for the relaxation rates.

2.3.5 The T_1 Relaxation Rate

T_1 relaxation is the regaining of z-magnetisation (I_z), so the quantity that must be calculated is $\frac{d}{dt}\langle I_z\rangle(t)$. For CSA-induced T_1 relaxation (full details of the calculation, including CSA can be found in Ref. 90; chemical shift $T_{j,m}$ terms can be found in Appendix A),

$$\frac{d}{dt}\langle I_z\rangle(t) = -\left(\mathrm{Tr}\left(\hat{\Gamma}\{I_z\}\rho(t)\right) - \mathrm{Tr}\left(\hat{\Gamma}\{I_z\}\rho_0\right)\right) = -R^{(I)}_{1,CSA}(\langle I_z\rangle(t) - I_0) \tag{2.89}$$

where

$$R^{(I)}_{1,CSA} = \frac{2}{15}(\gamma_I B_0)^2(\sigma_{xx}{}^2 + \sigma_{yy}{}^2 + \sigma_{zz}{}^2 - \sigma_{xx}\sigma_{yy} - \sigma_{xx}\sigma_{zz} - \sigma_{yy}\sigma_{zz})J_1(\omega_I) \tag{2.90}$$

and the superscript "int" has been dropped (because in this case the expression is identical in the laboratory frame). σ_{xx}, σ_{yy} and σ_{zz} are the components of the chemical shift tensor in the PAS. As expected, the rate of relaxation depends on the spectral density evaluated at the Larmor frequency (meaning T_1 relaxation is most sensitive to motions occurring at ω_0 – see Figure 2.9c). Note that owing to the factor of $B_0{}^2$, relaxation due to CSA is much stronger at higher magnetic fields.

For dipolar relaxation between spins I and S, the spin operators are different, leading to different decay constants:

$$\frac{d}{dt}\langle I_z\rangle(t) = -\Big(\mathrm{Tr}\left(\hat{\Gamma}\{I_z\}\rho(t)\right) - \mathrm{Tr}\left(\hat{\Gamma}\{I_z\}\rho_0\right)\Big)$$
$$= -R_{DD}^{(I)}(\langle I_z\rangle(t) - I_0) - \sigma^{(IS)}(\langle S_z\rangle(t) - S_0) \tag{2.91}$$

where

$$R_{DD}^{(I)} = \frac{1}{10}\left(\frac{\mu_0}{2\pi}\frac{\gamma_I\gamma_S}{\hbar r^3}\right)^2 [J_0(\omega_S - \omega_I) + 3J_1(\omega_I) + 6J_2(\omega_I + \omega_S)] \tag{2.92}$$

$$\sigma^{(IS)} = \frac{1}{10}\left(\frac{\mu_0}{2\pi}\frac{\gamma_I\gamma_S}{\hbar r^3}\right)^2 \left[-\frac{1}{3}J_0(\omega_S - \omega_I) + 2J_2(\omega_I + \omega_S)\right] \tag{2.93}$$

and the bracketed superscripts signify which spin the relaxation involves. r is the separation between the two nuclei. For both spins,

$$\frac{d}{dt}\begin{pmatrix}\langle I_z\rangle(t)\\ \langle S_z\rangle(t)\end{pmatrix} = -\begin{pmatrix}R_{DD}^{(I)} & \sigma^{(IS)}\\ \sigma^{(IS)} & R_{DD}^{(S)}\end{pmatrix}\begin{pmatrix}\langle I_z\rangle(t) - I_0\\ \langle S_z\rangle(t) - S_0\end{pmatrix} \tag{2.94}$$

which are the Solomon equations. Again, as expected, the relaxation rates depend on the spectral density at the frequencies of the transitions involved. This reflects the fact that the rate of single-quantum transitions depends on the amount of motion at the Larmor frequencies of spins I and S ($J(\omega_I)$ and $J(\omega_S)$ respectively), while the rate at which the double-quantum transition occurs is dependent on $J(\omega_I + \omega_S)$. The zero-quantum transition rate constant depends on $J(\omega_I - \omega_S)$. Note that the rates of relaxation depend on the distance between the coupled nuclei and their gyromagnetic ratios (*i.e.* the dipolar coupling constant).[ix]

In solids, cross-relaxation is small enough that it can be considered negligible in most practical circumstances in the solid state (although the fast rotations of CH_3 groups can lead to the observation of appreciable methyl ^{13}C NOEs in deuterated samples[142]). The measured change in longitudinal magnetisation can therefore often be approximated as a single exponential, with the rate of direct-dipolar relaxation, $R_{1,DD}$ equal to R_{DD}.

Assuming the sources of relaxation are independent, the total relaxation rate for a given nucleus is simply the sum of the individual relaxation rates due to each source, *e.g.* $R_{1,total} = R_{1,CSA} + R_{1,DD(NH)}$ for CSA and direct N-H dipole-dipole contributions. In

[ix] In paramagnetic materials, strong couplings between unpaired electrons and nuclei generate extremely efficient relaxation in a similar manner.

some cases, however, this assumption is not valid. For example, a ^{15}N nucleus in an NH group in a protein relaxes through both dipolar and CSA mechanisms, but the motions causing the relaxation in each case are the same. The fluctuations in the local fields arising from reorientations of the ^{15}N CSA and N-H dipolar interactions are therefore correlated. If we consider the relaxation behaviour of the dipolar-coupled system of spins in equations 2.71–2.78, the result is that the rate of single-quantum transitions (W_1) depends on the state of the second (non-transitioning) spin in each case: $W_1^{\alpha\alpha\leftrightarrow\beta\alpha} \neq W_1^{\alpha\beta\leftrightarrow\beta\beta}$. This introduces a third term in the expression for dI_z/dt. This interference of relaxation mechanisms, known as *cross-correlation* (not to be confused with cross-relaxation), is readily observable in solution in the form of different relaxation times for individual j-doublet components,[143,144] but in the solid state its effect is usually suppressed by spin diffusion effects (see §3.2).[145,146]

2.3.6 The T_2 Relaxation Rate

For transverse CSA relaxation, the appropriate observable is I_+:

$$\frac{d}{dt}\langle I_+\rangle^{int}(t) = -\Big(\mathrm{Tr}\left(\hat{\Gamma}\{I_+\}\rho^{int}(t)\right) - \mathrm{Tr}\big(\hat{\Gamma}\{I_+\}\rho_0\big)\Big) = -R_{2,CSA}^{(I)}\langle I_+\rangle^{int}(t) \tag{2.95}$$

where

$$R_{2,CSA}^{(I)} = \frac{2}{15}(\gamma_I B_0)^2(\sigma_{xx}{}^2 + \sigma_{yy}{}^2 + \sigma_{zz}{}^2 - \sigma_{xx}\sigma_{yy} - \sigma_{xx}\sigma_{zz} - \sigma_{yy}\sigma_{zz})\left[\frac{2}{3}J_0(0) + \frac{1}{2}J_1(\omega_I)\right]. \tag{2.96}$$

For transverse dipolar relaxation,

$$\frac{d}{dt}\langle I_+\rangle^{int}(t) = -\Big(\mathrm{Tr}\left(\hat{\Gamma}\{I_+\}\rho^{int}(t)\right) - \mathrm{Tr}\big(\hat{\Gamma}\{I_+\}\rho_0\big)\Big) = -R_{2,DD}^{(I)}\langle I_+\rangle^{int}(t) \tag{2.97}$$

where

$$R_{2,DD}^{(I)} = \frac{1}{10}\Big(\frac{\mu_0}{2\pi}\frac{\gamma_I\gamma_S}{\hbar r^3}\Big)^2\left[2J_0(0) + \frac{1}{2}J_0(\omega_S - \omega_I) + \frac{3}{2}J_1(\omega_I) + 3J_1(\omega_S) + 3J_2(\omega_I + \omega_S)\right]. \tag{2.98}$$

Note that $R_{2,DD}^{(I)}$ depends on the Larmor frequency of the second spin through $J_1(\omega_S)$. Significantly, the presence of $J_0(0)$ in these expressions means that R_2 relaxation rates are much more sensitive to slower motions than R_1 rates (see Figure 2.9c). The $\frac{1}{2}J_1(\omega_I)$ term of equation 2.96 and terms 2, 4 and 5 in the square brackets of equation 2.98 are equal to the non-secular contributions to transverse relaxation, *i.e.* half of the longitudinal autorelaxation rates (see equations 2.90 & 2.92). The total transverse relaxation rate is $R_{2,DD}^{(I)} + R_{2,CSA}^{(I)}$ (assuming only incoherent motionally-induced contributions).

2.3.7 Spin-Lattice Relaxation in the Rotating Frame

As mentioned in §2.2.5, relaxation in the presence of a spin-lock field is known as $T_{1\rho}$ relaxation. Such an r.f. field that is applied along an axis perpendicular to B_0 has the effect of modifying $\widehat{\mathcal{H}}_0$ to a sum of the Zeeman and r.f. Hamiltonians. The frame in which it is static is the doubly-rotating frame. Treatment of this type of relaxation is the same as spin-lattice relaxation but the eigenvectors of the Zeeman Hamiltonian (T_n^m) used to calculate $\frac{d}{dt}\langle I_z\rangle(t)$ are first transformed to the doubly-rotating frame[90], ultimately leading to different relaxation rates.

For rotating frame relaxation caused by CSA,

$$\frac{d}{dt}\langle I_z\rangle^{int}(t) = -R_{1\rho,CSA}^{(I)}\left(\langle I_z\rangle^{int}(t) - I_0\right) \tag{2.99}$$

where

$$\begin{aligned} R_{1\rho,CSA}^{(I)} = \frac{2}{15}(\gamma_I B_0)^2\big(&{\sigma_{xx}}^2 + {\sigma_{yy}}^2 + {\sigma_{zz}}^2 - \sigma_{xx}\sigma_{yy} - \sigma_{xx}\sigma_{zz} \\ &- \sigma_{yy}\sigma_{zz}\big)\left[\frac{2}{3}\sin^2(\beta)J_0(\omega_{eff})\right. \\ &+ \frac{1}{4}(\cos^2(\beta)+1)^2 J_1(\omega_I + \omega_{eff}) \\ &\left. + \frac{1}{4}(\cos^2(\beta)-1)^2 J_1(\omega_I - \omega_{eff})\right]. \end{aligned} \tag{2.100}$$

ω_{eff} and β are the effective nutation frequency and tilt angle of the spin-lock pulse as defined in equations 2.48 and 2.49.

For $\omega_1 \ll \omega_I$ in the on-resonance limit ($\omega_{rf} = \omega_S,\ \omega_{eff} = \omega_1,\ \beta = \pi/2$), equation 2.100 simplifies to

$$R_{1\rho,CSA}^{(I)} = \frac{2}{15}(\gamma_I B_0)^2\left(\sigma_{xx}{}^2 + \sigma_{yy}{}^2 + \sigma_{zz}{}^2 - \sigma_{xx}\sigma_{yy} - \sigma_{xx}\sigma_{zz} - \sigma_{yy}\sigma_{zz}\right)\left[\frac{2}{3}J_0(\omega_1) + \frac{1}{2}J_1(\omega_I)\right]. \tag{2.101}$$

The measured rotating frame relaxation rate, $R_{1\rho}$ is equal to $1/T_{1\rho}$ where $T_{1\rho}$ is the rotating frame relaxation time. This constant can be measured for a nucleus by using a spin-lock pulse after transverse magnetisation has first been generated (*e.g.* by CP or a $\pi/2$ pulse). Variation of the length of this spin lock pulse will enable capture of the rate of decay of magnetisation by $T_{1\rho}$ relaxation.

For dipolar relaxation, assuming that the spin-lock field is selectively applied to only one spin, *e.g.* the ^{15}N in an NH group,

$$\frac{d}{dt}\langle I_z\rangle^{int}(t) = -\left(\mathrm{Tr}\left(\hat{\Gamma}\{I_z\}\rho^{int}(t)\right) - \mathrm{Tr}\left(\hat{\Gamma}\{I_z\}\rho_0\right)\right) \tag{2.102}$$

$$= -R_{\rho,DD}^{(I)}\left(\langle I_z\rangle^{int}(t) - I_0\right) - \sigma^{(IS)}\left(\langle S_z\rangle^{int}(t) - S_0\right) \tag{2.103}$$

where (*overleaf*)

$$
\begin{aligned}
R_{\rho,DD}^{(I)} = \frac{1}{10}\left(\frac{\mu_0}{2\pi}\frac{\gamma_I\gamma_S}{\hbar r^3}\right)^2 \Bigg[& 2\sin^2(\beta)J_0(\omega_{eff}) \\
& + \left(\sin^4\left(\frac{\beta}{2}\right)J_0(\omega_S - \omega_I + \omega_{eff})\right. \\
& \left. + \cos^4\left(\frac{\beta}{2}\right)J_0(\omega_S - \omega_I - \omega_{eff})\right) \\
& + 3\left(\cos^4\left(\frac{\beta}{2}\right)J_1(\omega_I + \omega_{eff}) + \sin^4\left(\frac{\beta}{2}\right)J_1(\omega_I - \omega_{eff})\right) \\
& + \frac{3}{2}\left(\sin^2(\beta)J_1(\omega_S + \omega_{eff}) + \sin^2(\beta)J_1(\omega_S - \omega_{eff})\right) \\
& + 6\left(\cos^4\left(\frac{\beta}{2}\right)J_2(\omega_I + \omega_S + \omega_{eff})\right. \\
& \left. + \sin^4\left(\frac{\beta}{2}\right)J_2(\omega_I + \omega_S - \omega_{eff})\right)\Bigg]
\end{aligned}
\tag{2.104}
$$

and

$$
\begin{aligned}
\sigma^{(IS)} = \frac{1}{10}\left(\frac{\mu_0}{2\pi}\frac{\gamma_I\gamma_S}{\hbar r^3}\right)^2 \Bigg[& \left(\sin^4\left(\frac{\beta}{2}\right)J_0(\omega_S - \omega_I + \omega_{eff})\right. \\
& \left. - \cos^4\left(\frac{\beta}{2}\right)J_0(\omega_S - \omega_I - \omega_{eff})\right) \\
& + \frac{3}{2}\left(\sin^2(\beta)J_1(\omega_S + \omega_{eff}) + \sin^2(\beta)J_1(\omega_S - \omega_{eff})\right) \\
& + 6\left(\cos^4\left(\frac{\beta}{2}\right)J_2(\omega_I + \omega_S + \omega_{eff})\right. \\
& \left. + \sin^4\left(\frac{\beta}{2}\right)J_2(\omega_I + \omega_S - \omega_{eff})\right)\Bigg].
\end{aligned}
\tag{2.105}
$$

For an on-resonance spin-lock pulse ($\omega_{rf} = \omega_S,\ \omega_{eff} = \omega_1,\ \beta = \pi/2$) that satisfies the condition $\omega_1 \ll \omega_I, \omega_S, \omega_I \pm \omega_S$, equations 2.104 and 2.105 simplify to

$$R_{\rho,DD}^{(I)} = \frac{1}{10}\left(\frac{\mu_0}{2\pi}\frac{\gamma_I\gamma_S}{\hbar r^3}\right)^2\left[2J_0(\omega_1) + \frac{1}{2}J_0(\omega_S - \omega_I) + \frac{3}{2}J_1(\omega_I) + 3J_1(\omega_S) + 3J_2(\omega_I + \omega_S)\right] \quad (2.106)$$

$$= R_{1\rho,DD}^{(I)}$$

and

$$\sigma^{(IS)} = 0. \quad (2.107)$$

Under these conditions, therefore, the measured rate of rotating frame relaxation, $R_{1\rho,DD}^{(I)} = R_{\rho,DD}^{(I)}$.

In the limit of a weak on-resonance spin-lock pulse ($\omega_1 \to 0$), equations 2.101 and 2.106 reduce to the expressions for the transverse relaxation rate due to dipolar coupling and CSA in the laboratory frame (equations 2.96 and 2.98). This can prove especially valuable for investigations of protein dynamics in the solid state, where measurements of T_2 relaxation are dominated by coherent (rather than dynamic) contributions. Note that the above expressions can be modified to include the influence of MAS, although this only becomes important when considering relatively slow motions in the μs–ms regime.[147]

As a final remark, because the relaxation rates depend upon motions occurring at specific combinations of Larmor frequencies, measurement of these parameters at different magnetic field strengths can be used to attempt to "map out" more of the spectral densities. If enough of these constraints can be acquired, the data can be used in a fit to a motional model in order to extract quantitative information about molecular dynamics (see §7.6).

3

SSNMR FOR STRUCTURAL STUDIES OF PROTEINS

Although SSNMR offers a wide range of structural information at atomic resolution, its routine use for solving biomolecular structures has always faced significant challenges, many of which have been rooted in a persistent need for better sensitivity and spectral resolution. These factors have therefore largely defined many aspects of biomolecular SSNMR experimental design, and continue to drive development in the area. Sensitivity is more limited in the case of proteins (*e.g.* compared to small organic molecules) because of their large molecular size, with a potentially enormous number of resonances but an overall smaller number of molecules within a sample. The same abundance of resonances, while representing a rich source of information, also limits resolution as they begin to overlap, especially if line widths are broadened by anisotropic interactions. Obviously, the experiments that can be performed are also restricted by the types of nuclei that are present within a system. In addition, experimental design must take into account the potential instability of biological samples, in particular with respect to the range of temperatures across which they are subjected to.

Given the above considerations, biological SSNMR experiments are unique in many respects compared to those in other fields within SSNMR. Solid-state protein studies are typified by extensive use of multidimensional experiments on spin-½ nuclei under conditions of MAS. The use of high magnetic fields (*e.g.* ≥500 MHz) for proteins is almost universal. It is also common to control the temperature of the sample to prevent its degradation in the presence of heating effects induced by MAS and/or r.f. irradiation. The chief aspects of SSNMR methods for studying proteins are detailed below, along with widely-used techniques used for the extraction of structural information.

3.1 Protein Samples for SSNMR

Protein samples for NMR are usually produced via expression in bacteria such as *E.coli*.[148] The most numerous species within a protein are hydrogen, carbon, nitrogen and oxygen. Of these, the most abundant isotopes of carbon and oxygen (^{12}C and ^{16}O) are spin-zero and hence do not possess a magnetic moment, so cannot be used for NMR studies. The most common form of nitrogen, ^{14}N, is quadrupolar (spin-1) and so gives broad lines that, when combined with the high numbers of resonances within a protein, are not immediately conducive to high resolution studies. The same is true of the ^{17}O (spin-5/2), which is additionally a decidedly expensive isotope to incorporate. In solution, protons are an ideal nucleus for NMR as they are abundant, have a high gyromagnetic ratio and are spin-½, but until recently (see below) proton-detected experiments in the solid state have been hampered by impractically broad resonances caused by strong ^{1}H-^{1}H dipolar couplings. Because of this, solid-state protein NMR experiments have traditionally been ^{13}C- or ^{15}N-detected. Both of these nuclei are spin-½ but their natural abundances are low (see Table 2.1), leading to low experimental sensitivity. Protein studies therefore usually rely on enriched (or "labelled") samples, which can be produced by using ^{13}C- and ^{15}N-enriched carbon and nitrogen sources during expression of the proteins.[149] The resulting proteins then contain ^{13}C and/or ^{15}N nuclei instead of ^{12}C/^{14}N. Although it comes at greater expense and commonly a lower yield, isotopic labelling of proteins provides a vital enhancement in sensitivity for NMR studies.

Samples with complete isotopic enrichment of carbon or nitrogen sites are "uniformly labelled", and offer a large amount of information per spectrum. Often, labelled and unlabelled protein may be mixed to a specific ratio in order to prevent the appearance of intermolecular cross-peaks and thus avoid assignment difficulties that may consequently arise.[49] If specific distance constraints are required, select individual residues can be labelled,[150] with the result that any cross-peaks observed are far less ambiguous in their origin. In some cases, more elaborate labelling schemes are desirable. For example, by using [2-^{13}C]- or [1,3-^{13}C]-labelled glycerol as carbon sources in expression, alternately labelled samples can be produced in which effectively every other carbon site is labelled (the exact pattern depends on the residue type – see Figure 3.1).[151] Such a strategy therefore removes many of the peaks in the carbon spectrum, alleviating crowding whilst also eliminating the effect of one-bond ^{13}C-^{13}C J-couplings (~30-50 Hz) and hence improving resolution. Such a strategy was used for the first determination of a complete protein structure by NMR by Castellani *et al.*[49] Significantly, dipolar truncation

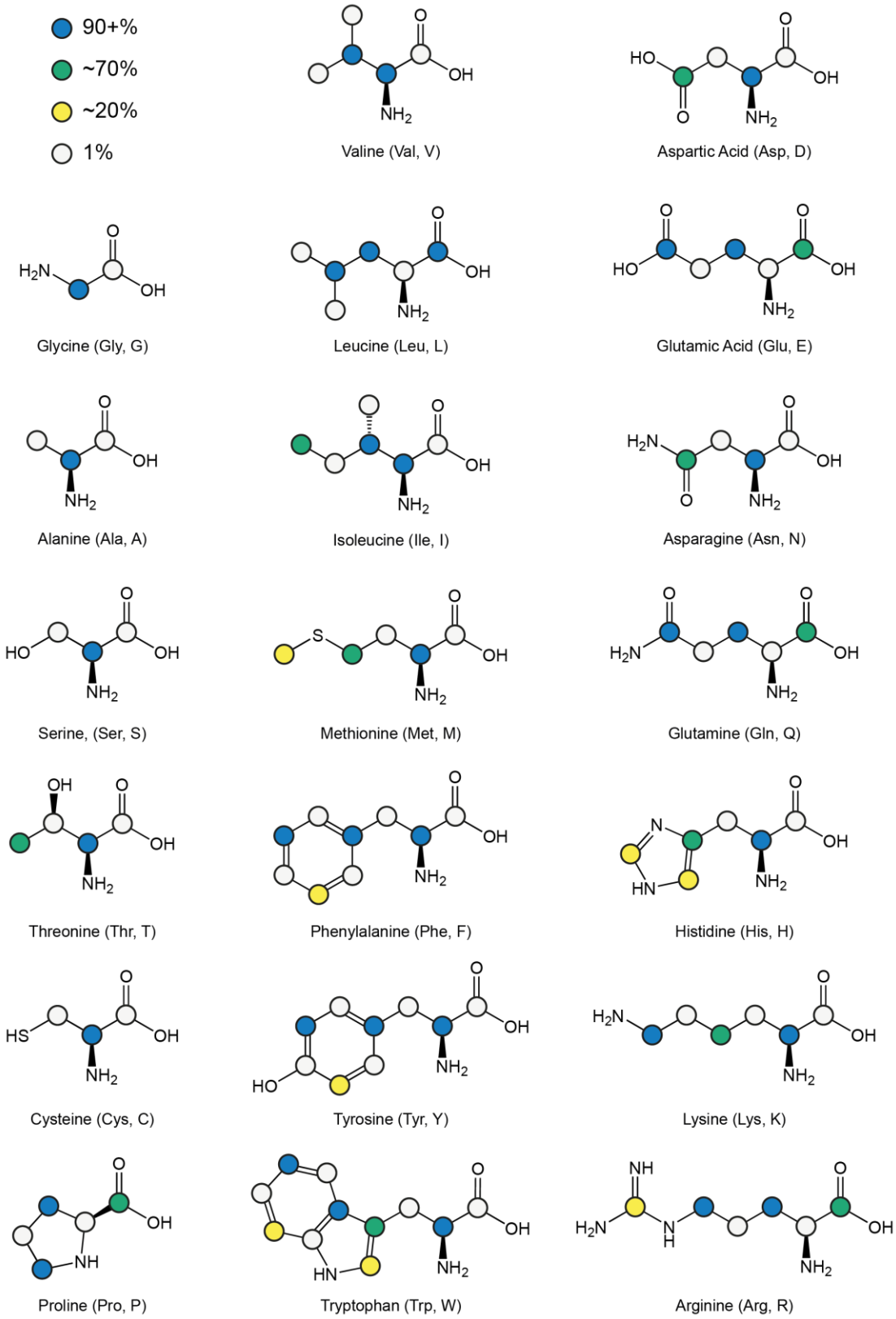

Figure 3.1. ^{13}C enrichment pattern for amino acids of proteins expressed using [2-^{13}C]glycerol. The opposite labelling pattern is obtained with [1,3-^{13}C]glycerol. Adapted from Ref. 151.

effects (see below) were reduced, allowing for longer-range contacts between nuclei to be established for structural constraints. Samples expressed using [1-^{13}C]- and [2-^{13}C]-labelled glucose can also been used to give similar benefits.[152] In general, the choice of labelling strategy is guided by the specific experimental goals and the challenges of a particular system, and the ability to engineer different labelling schemes and combine them with complementary experimental NMR approaches is a powerful tool for the determination of protein structures. A given approach may utilise multiple samples with different labelling patterns. Generally, however, more sophisticated labelling strategies are more expensive to achieve. There is, therefore, a strong case for the development of advanced experimental NMR methods that can take full advantage of cheaper, uniformly labelled samples so as to reduce the need for producing multiple, expensive site-directed labelled samples.

Besides enrichment of carbon and nitrogen sites, protons (^{1}H) may also be replaced by deuterons (^{2}H, spin-1) by using deuterated glucose and D_2O during expression of the protein.[153] This may be done specifically in order to conduct ^{2}H experiments (*e.g.* for line shape analysis in dynamics studies[154,155]), or in an effort to dilute the proton network within a protein and thus remove much of the line broadening that stems from strong ^{1}H dipolar couplings (Figure 3.2).[156-160] After expression of a deuterated protein, protons can be reintroduced at exchangeable (amide) sites by

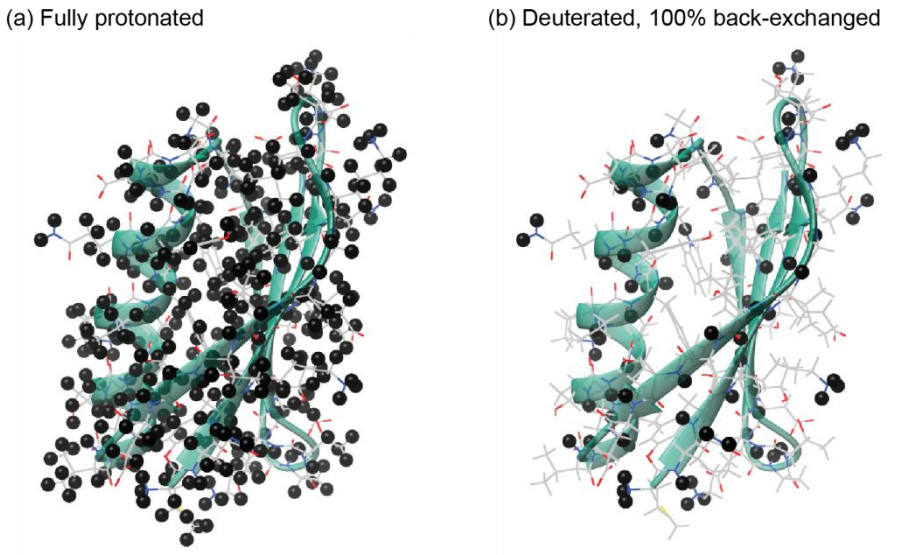

Figure 3.2. Visualisation of the effect of deuteration on the concentration of protons in a protein sample (shown is the protein GB1). Protons are shown as black spheres. (a) Fully protonated sample. (b) Deuterated sample with 100% back-exchanged protons. The concentration of protons within a sample can be further reduced by back-exchange using a H_2O/D_2O mix.

preparing the sample in a H_2O/D_2O mixture of variable ratio, depending on the desired final concentration of protons. Alternatively, by expressing a protein with only ~97 % deuterium-enriched glucose, protons may be incorporated at certain methyl sites to allow for high-resolution methyl ^{13}C-^{1}H spectra.[161] Crucially, the extent of line-narrowing provided by deuteration, in combination with advances in MAS technology, has enabled the introduction of proton-detected experiments in peptides and proteins in the solid state, which are far more sensitive than corresponding ^{13}C- or ^{15}N-detected experiments.[158,159,162] The optimum level of deuteration for this purpose varies as a function of the MAS frequency: at $\omega_r/2\pi$ ~60 kHz or more, 100% back-exchange of protons provides the best balance between sensitivity and resolution, while at lower spinning frequencies, a higher level dilution is preferable.[83,163-165] Despite this breakthrough and other advantages of deuteration (*e.g.* longer coherence lifetimes[163]) it should be noted that for some studies it may be less effective as a lower concentration of protons naturally reduces the absolute polarisation that can be attained from CP, as well as the efficiency of second-order dipolar recoupling techniques involving protons (see below). Deuteration is also expensive to implement, and so in many cases alternatives such as using fully protonated samples at higher MAS frequencies may be desirable.

Local order is a prerequisite for obtaining high-resolution spectra and is highly dependent on the homogeneity of a sample. Whilst this condition is less limiting than the requirement for long-range order in x-ray diffraction studies, it is nevertheless an important consideration for SSNMR sample preparation (and one that is frequently more of an obstacle than in solution experiments). A total lack of local order leads to spectra with lines dominated by inhomogeneous broadening, with the resulting lack of resolution and low peak intensities hampering extraction of structural or dynamical information. Much success has been had with microcrystalline preparations of proteins.[49-56,166,167] The excellent resolution and sensitivity afforded in small microcrystalline proteins make them ideal benchmarks for method development. In some cases, such as in fibrils, a presence of local order might be to a certain extent inherent to their form. Recently, sedimentation by ultracentrifugation was introduced as a sample preparation method for large proteins, yielding high sample homogeneity and accordingly high-quality SSNMR spectra rivalling those obtained with crystalline preparations.[13,16,88,168] Samples of sufficient molecular size can be sedimented from a highly concentrated solution, either inside the NMR rotor (*in situ*) by its rotation under MAS ("freezing rotational diffusion of protein solutions at low temperature and high viscosity", or FROSTY),[88,169] or into the rotor prior to MAS (*ex*

situ) using custom-made tools.[16,170] Importantly, this methodology provides an option for the preparation of large protein complex samples, where other preparations may produce amorphous samples and/or co-crystallisation may not be trivial. On the other hand, it has been found that at least in some cases, excellent resolution may be obtained for large protein complexes that are simply precipitated upon mixing their constituent proteins in solution (see Chapter 5).[15]

Whilst not dissolved, the protein samples used in SSNMR experiments must still be hydrated in order for internal dynamic processes to occur. Motions of nuclei within protein molecules have a substantial averaging effect on the anisotropic interactions that cause line broadening, and so narrower lines can be observed than would be possible through averaging by MAS and decoupling alone. Without hydrating water, protein dynamics are to a large extent limited, and hence dry protein samples typically give broad and unresolved spectra. Because of the viscous nature of hydrated protein samples, packing them into MAS rotors can often prove challenging, although for many samples good results can be consistently achieved by centrifugation (though this procedure becomes more difficult as MAS rotors continually decrease in size in the pursuit of ever-higher spinning frequencies). In proton-detected experiments, the presence of a large water signal may mask other features within the spectrum, and for this reason a variety of methods have been developed in solution to suppress it, many of which rely on field gradients generated by dedicated coils within the probe.[171] Whilst similar methods can be applied in solids,[158] this capability is not yet commonly built into SSNMR probes, and so (for the experiments presented here at least) water suppression must be based simply on r.f. irradiation, which acts to dephase the water signal prior to ^{1}H-detection.[172]

3.2 Recoupling Techniques

Because of the challenge of crowding in protein spectra (especially in uniformly enriched samples), 2D (and higher-dimensional) experiments are typically necessary to achieve resolution of resonances. This is the case even in solution, where lines are generally of much narrower width owing to molecular tumbling. In §2.2.7, the basic stages of a multidimensional correlation experiment were outlined. During the mixing stage, transfer of polarisation, mediated by couplings between nuclei, occurs between nuclei between the evolution and detection steps. J-coupling-based methods for polarisation transfer are common in solution, as employed in 2D COSY[28] (homonuclear) and "heteronuclear single-quantum correlation" (HSQC; heteronuclear)[173] experiments, which reveal

through-bond correlations. The averaging by overall tumbling dictates that dipolar interactions may not be exploited directly, but transfer via NOEs (caused by relaxation by dipolar mechanisms) is used in NOESY experiments,[31] which correlate nuclei close in space. In solids, whilst similar experiments are possible,[94] efficient transfers may be facilitated directly by strong dipolar couplings, which are not averaged in the absence of molecular tumbling. However, the requirement for MAS to overcome line broadening for spectral resolution also leads to the attenuation of dipolar transfer between neighbouring nuclei. Fortunately, carefully-designed "dipolar recoupling" techniques may be used to selectively reintroduce dipolar couplings by ensuring that over an integral rotor period, the average of the dipolar Hamiltonian is no longer zero in the interaction frame, thus inducing the transfer of magnetisation between spins.[94] Besides offering correlations between nuclei near to each other in space, dipolar recoupling methods can also offer the ability to measure dipolar couplings in a quantitative manner and hence extract valuable information for structure determination such as distances and torsion angles. A selection of common recoupling techniques are described below (with focus on those that are most relevant to this work), although the list should by no means be taken as exhaustive – a huge array of techniques have been developed in the quest for efficient and selective recoupling under various experimental conditions.[94,174] The way in which each of the methods described accomplishes recoupling in terms of average Hamiltonian theory (AHT) is not covered in detail here, but can be found in Refs.[94,175,176].

Often, dipolar couplings can be reintroduced when the relationships between the sample spinning frequency and other frequencies involved meet specific resonant conditions. For example, the rotational resonance (R^2) effect, first observed by Andrew *et al.* in 1966, reintroduces the homonuclear dipolar coupling between a pair of spins when the chemical shift difference (in Hz) between their resonances is matched by an integral multiple of the spinning frequency.[177] Since then, this technique has been refined as a magnetisation transfer tool[178] and has most notably been exploited in proteins for the measurement of dipolar couplings between labelled spin pairs,[179] although use of R^2 to solve complete protein structures is limited by the requirement for selective labelling of residues.

Further resonance conditions can be found when irradiation is applied. Depending on the condition, homonuclear and/or heteronuclear couplings can be reintroduced in the rotating frame (allowing for homonuclear or heteronuclear correlation experiments). Rotary resonance recoupling (R^3) reintroduces heteronuclear

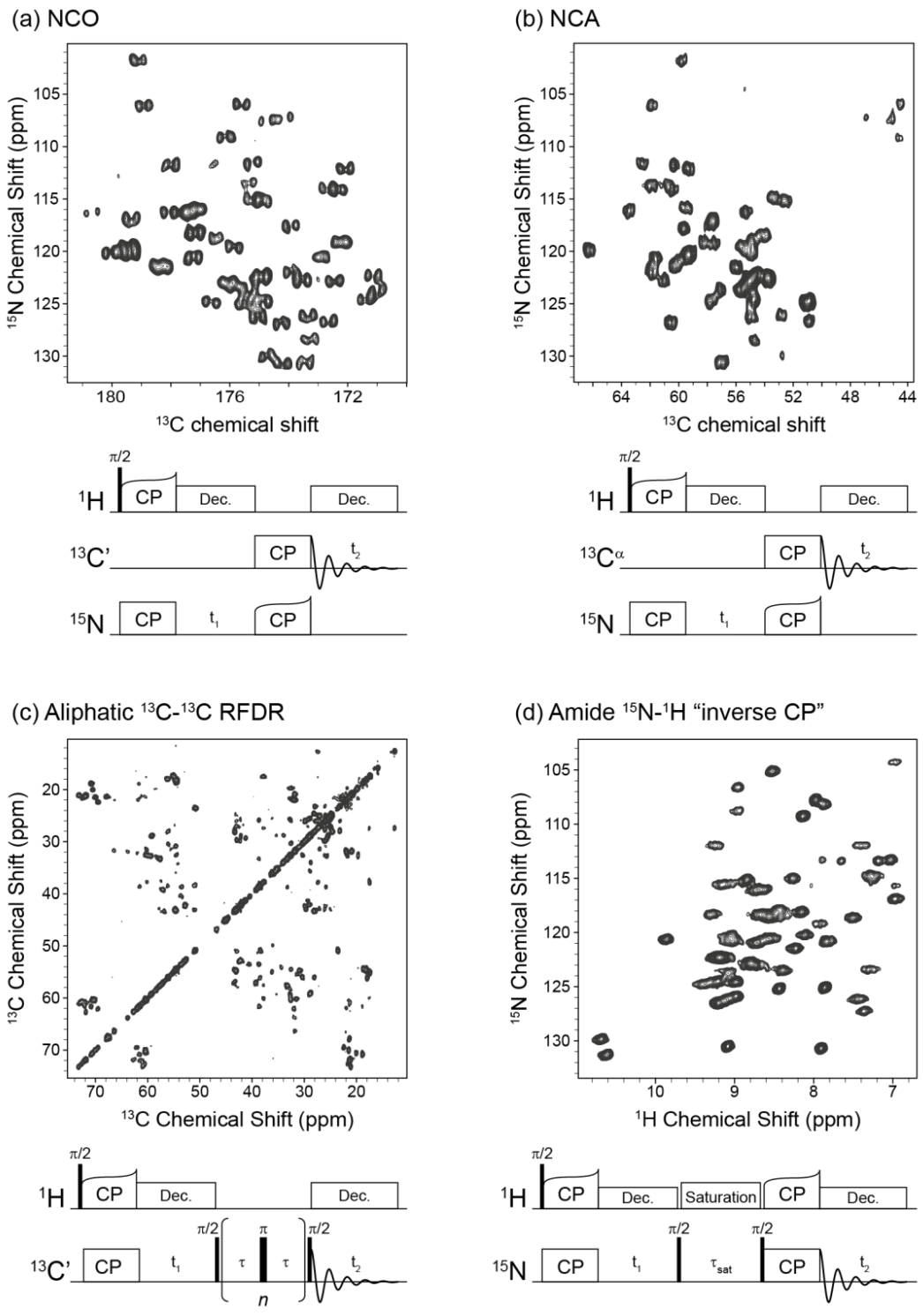

Figure 3.3. Example spectra and pulse sequences for various recoupling techniques: (a) NCO double CP, (b) NCA double CP, (c) homonuclear ^{13}C-^{13}C RFDR and (d) proton-detected "inverse CP", all conducted at 60 kHz MAS and at 600 MHz ^{1}H Larmor frequency. The sample used in (a), (b) and (c) was fully protonated [U-^{13}C,^{15}N]GB1, while that used in (d) was 100% back-exchanged [U-^{2}H,^{13}C,^{15}N]GB1 (necessary to achieve narrow proton line widths at this spinning frequency).

dipolar couplings (and CSA) when CW irradiation, set to a nutation frequency that is a small integer multiple of the spinning frequency (*i.e.* $\omega_1 = n\omega_r$ where $n = 1,2$), is applied to one of the spin species.[180,181] Homonuclear rotary resonance (HORROR), on the other hand, occurs when the nutation frequency is equal to half of the spinning frequency ($\omega_1 = \omega_r/2$).[182] Whereas R^2 and R^3 reintroduce zero-quantum "flip-flop" dipolar terms, HORROR produces pure double-quantum dipolar recoupling. The efficiency of this technique can be enhanced by sweeping the nutation frequency through the HORROR condition for adiabatic dipolar recoupling.[183,184] This is known as "dipolar recoupling enhanced by amplitude modulation" (DREAM), and the exact shape of the pulse (*i.e.* how the amplitude is modulated) can be chosen to optimise transfer between spins across different chemical shift differences.[185]

Cross-polarisation between nuclei was described in §2.2.5. Irradiation at the Hartmann-Hahn condition (accounting for MAS) has the effect of reintroducing dipolar couplings between heteronuclei, enabling transfer of magnetisation between them. This effect may be used to enhance the polarisation of rare/low-γ spins from protons, but in general it can be used to transfer polarisation between heteronuclei in order to correlate their chemical shifts in multidimensional experiments. In the simplest case, a ^{1}H-^{13}C or ^{1}H-^{15}N heteronuclear correlation (HETCOR) experiment can correlate protons with carbon/nitrogen nuclei by implementing proton evolution prior to CP to ^{13}C/^{15}N and detecting the latter spins, although sensitivity can be further enhanced by the addition of a ^{13}C/^{15}N-^{1}H step and proton detection (Figure 3.3d). ^{13}C and ^{15}N spins themselves are commonly correlated in a "double CP" (DCP) experiment,[186] whereby after initial polarisation of nitrogen spins through ^{1}H-^{15}N CP, evolution encodes the ^{15}N chemical shift. A further CP step to ^{13}C is then employed prior to ^{13}C detection.[x] Furthermore, the selectivity of the ^{15}N-^{13}C CP step can be used to enable the recording of separate "NCO" and "NCA" DCP experiments, which correlate amide ^{15}N resonances with neighbouring ^{13}C' or ^{13}C$^{\alpha}$ nuclei, respectively (Figures 3.3a & 3.3b). As with any recoupling technique, these may be used as "building blocks" within more elaborate pulse sequences for experiments of higher dimensionality. In this way, experiments can be designed to

[x] The experiment can be carried out the other way around, i.e. ^{13}C evolution and ^{15}N direct detection, although the sensitivity of direct ^{15}N detection is more limited owing to its lower gyromagnetic ratio. In addition, ^{13}C chemical shift ranges are often larger, necessitating the use of a larger spectral width and hence lengthening the experimental time scale. Such considerations are important when designing an experiment, as experimental time is often at a premium.

correlate chosen nucleus types within a protein for assignment or for optimal chemical shift dispersion (and hence resolution).

Resonant recoupling may also be achieved in the laboratory frame via discrete pulses of r.f. irradiation. Representative of this approach is "radio frequency-driven recoupling" (RFDR) recoupling, which consists of rotor-synchronised π-pulses that reintroduce homonuclear dipolar couplings (Figure 3.3c).[187] "Rotational-echo double resonance NMR" (REDOR), introduced earlier by Gullion and Schaefer, consists of a series of rotor-synchronised π-pulses applied in order to reintroduce heteronuclear dipolar couplings (in addition to homonuclear dipolar couplings).[188] Typically, after polarisation of ^{13}C spins, two π-pulses are applied every rotor period to the ^{15}N spins, for a total mixing time τ_{mix}, in order to reintroduce the ^{13}C-^{15}N dipolar coupling. If τ_{mix} is varied, the measured ^{13}C peak intensities are modulated according to the strength of the ^{13}C-^{15}N dipolar coupling, and hence (after comparison with a reference experiment to account for relaxation effects) distance information can be obtained (or alternatively, for a known distance, dynamics information – see Chapter 7).[189] Since the introduction of these techniques, Levitt and co-workers have developed a generalised approach for designing rotor-synchronised recoupling sequences that rely on symmetry properties of the pulses, for selective reintroduction of interactions.[190-192]

The above methods work by reintroducing first-order dipolar coupling terms directly between nuclei. A number of other popular approaches rely on second-order recoupling, where although to the first order the average Hamiltonian is still zero under MAS, the next-order corrections (which are generally cross-terms between different dipolar couplings) are not. These methods can be particularly effective in a protein, where there exists an abundance of protons. Methods that use second-order recoupling include those based on spin diffusion or the "third spin-assisted recoupling" (TSAR) mechanism, which both induce zero-quantum dipolar transfer. The basic proton-driven spin diffusion (PDSD) experiment (for ^{13}C-^{13}C homonuclear correlations) involves the insertion of a delay during the pulse sequence, during which magnetisation can "diffuse" throughout the system using cross-terms between ^{13}C-^{13}C and ^{13}C-^{1}H dipolar couplings.[193,194] Based on the spin diffusion principle are CHHC and NHHC experiments,[195,196] which yield contacts between ^{13}C nuclei or between ^{13}C and ^{15}N nuclei indirectly via a three-step process consisting of CP to directly-bonded protons, spin diffusion amongst protons, and finally CP back to ^{13}C. In "dipolar-assisted rotational resonance" (DARR, alternatively called "r.f.-assisted diffusion", RAD), the spin diffusion

is accelerated by applying r.f. irradiation to protons at the condition $\omega_1 = \omega_r$, which broadens ^{13}C lines and recouples both ^{1}H-^{1}H and ^{1}H-^{13}C dipolar couplings.[197,198]

Because of the straightforwardness of experimental setup and the abundance of cross-peaks obtained, spin diffusion-based experiments are very popular and remain a principal tool for the determination of 3D structures in the solid state. However, at higher MAS frequencies, which can be required to average large CSAs at high fields or strong ^{1}H-^{1}H dipolar couplings for proton detection, spin diffusion efficiency rapidly degrades as the second order terms involved are averaged. The TSAR mechanism, however, differs with regard to spin dynamics and functions relatively well in the fast-spinning regime. TSAR experiments circumvent the problem of dipolar truncation, whereby the presence of strong (short distance) dipolar couplings acts to attenuate magnetisation transfer via weaker (long distance) couplings, and are hence particularly valued for their ability to yield relatively long-range contacts. The homonuclear version of the experiment is known as "proton-assisted recoupling" (PAR),[175] while the heteronuclear version is called "proton-assisted insensitive nuclei – cross polarisation" (PAIN-CP).[176,199] A detailed description of the homonuclear PAR mechanism in terms of average Hamiltonian theory is given in Ref. 175, but, briefly, r.f. fields are applied to both ^{1}H and ^{13}C (or ^{15}N) to induce second order cross-terms between ^{13}C-^{1}H dipolar couplings. The r.f. field amplitudes are chosen to minimise the contributions of ^{13}C-^{13}C autocross terms (which lead to lower transfer efficiency), whilst also deliberately avoiding direct recoupling conditions. The PAIN-CP experiment is conducted in a similar manner, with irradiation applied on all three (^{1}H, ^{13}C, ^{15}N) channels.

With any dipolar recoupling scheme, those nuclei closer in space (*e.g.* a few Å) will be most strongly recoupled owing to the r^{-3} dependence of the interaction (as well as the potential effects of dipolar truncation, depending on the recoupling scheme). Generally, the longer the mixing time (or contact time), the further the transfer of magnetisation (directly or by relayed transfer) and the longer the range of the contacts that can be established for structure determination. As mentioned, longer-range contacts may often be difficult to obtain because these relatively weak couplings can, in the presence of stronger couplings (*e.g.* to nuclei closer in space), suffer from dipolar truncation. The intensities of cross peaks may also be influenced by other factors such as dynamics. For many first order techniques, the r.f. field strength has to be a number of times higher than the MAS frequency for efficient transfer. For fast spinning experiments (*e.g.* ω_r >30 kHz), CW (or even pulsed) irradiation at this strength can be impractical

owing to heating effects and the risk of probe damage. As mentioned, the efficiency of spin diffusion is also dramatically reduced at higher MAS frequencies. For these reasons, the choice of recoupling scheme in a given experiment is restricted – RFDR, DREAM (and HORROR), PAR/PAIN-CP and double-quantum CP stand out as practical and robust methods for dipolar transfer in non-selectively labelled samples at high MAS rates.

3.3 Spectral Assignment

Ultimately, the majority of methods for detailed, widespread structure and dynamics determination rely on a requisite ability to obtain well-resolved spectra with sufficient signal to noise. If this feat can be achieved, a spectroscopist can fully take advantage of the wealth of atomic-resolution information available through NMR. After obtaining a spectrum, it is not always immediately obvious which resonances correspond to which nuclei within the protein. Within the spectrum of each nuclear species, each type of nuclear site will generally appear within a certain range of chemical shifts because of the various shielding effects of neighbouring nuclei. For the example of a ^{13}C spectrum of a protein, carbonyl sites will appear at ~170-180 ppm, while aliphatic sites will generally populate the ~10-70 ppm range. Of the latter, $^{13}C^{\alpha}$ sites (which are mostly CH groups) will occupy the upper end of that range, with generally lower chemical shifts for sites with a greater number of directly-bonded protons. Aromatic carbon resonances lie between ~100 ppm and the carbonyl region. This general "grouping" of chemical shifts allows for selective coherence transfers based on chemical shifts (*e.g.* selective CP). The type of amino acid also has an influence on the chemical shifts of each of the nuclei within it. For example, glycine $^{13}C^{\alpha}$ chemical shifts are generally much lower than for other amino acids (in this case because there are two directly-bonded protons).

Before any information can be extracted, each of the individual resonances must be assigned to nuclei within the sample. Evidently, the sequence of a protein must first be known before assignment can be attempted. Assignment strategies are based on using known assignments[xi] and following correlations in multidimensional correlation spectra. For example, in a 2D ^{13}C-^{13}C one-bond correlation experiment with a short mixing time in a uniformly ^{13}C-labelled protein, cross peaks may be observed for neighbouring ^{13}C sites within the same residue. If the assignment of one of the resonances within that

[xi] These may be resonances whose assignments are unambiguous based on distinctively high or low chemical shifts, or else based on some other recognisable pattern of shifts, e.g. of a certain amino acid type.

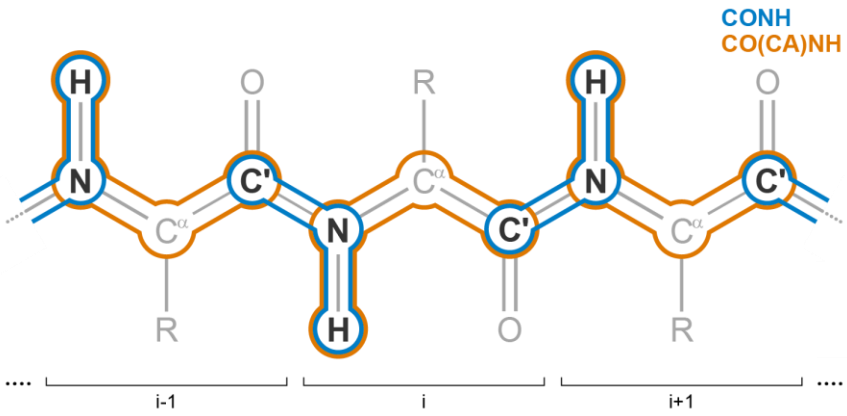

Figure 3.4. Representation of a sequential assignment strategy for a protein backbone, using complementary CONH and CO(CA)NH 3D experiments.

residue is known, the remainder can therefore be assigned. A long-mixing time experiment can yield correlations between different residues (either neighbouring or close in space owing to the fold of the protein). In general, the observation of a cross peak from a dipolar-based experiment reveals a proximity in space, whether that be within the same molecule or between two molecules close to each other. NMR is therefore a powerful tool for not only characterising protein molecules, but also for probing molecular interfaces and the interactions between those molecules.

3D or higher-dimensional methods can assist with assignment by correlating the chemical shifts of three or more nuclei. In particular, 3D experiments facilitate sequential assignment, whereby multiple complementary experiments are used to assign the resonances of a protein using a systematic, iterative routine. As an example, a CONH experiment can be used to correlate the chemical shifts of amide ^{1}H with those of their neighbouring ^{15}N and of the ^{13}C' of the previous residue (see Figure 3.4). In theory, if it is known that the ^{1}H and/or ^{15}N chemical shifts of a certain peak correspond to the sites $^{1}H_{i}$ /$^{15}N_{i}$ (in residue number *i*), then the chemical shift at which that peak lies in the ^{13}C dimension can be assigned to $^{13}C_{i-1}$. A second experiment can be performed to correlate ^{13}C' with ^{15}N and ^{1}H of the same residue (which would likely direct magnetisation via the connecting $^{13}C^{\alpha}$ – a CO(CA)NH experiment). The assignments of $^{1}H_{i-1}$ and $^{15}N_{i-1}$ can then be deduced from the assignment of $^{13}C_{i-1}$. This process can be repeated, revealing ^{1}H, ^{15}N and ^{13}C' assignments along the backbone of the protein.

Of course, spectral resolution dictates whether or not assignments can be made unambiguously. In solids, a high degree of assignment ambiguity that stems from broad lines is the main obstacle for adapting automated assignment routines from the field of solution NMR.[131,200-204] The assignment process can be fraught with uncertainties caused

by overlapping resonances, in addition to the possibility of "missing" peaks (that may be broadened beyond detection because of dynamics or inhomogeneity) or multiple populations, and it is therefore frequently highly challenging and time-consuming. Despite these difficulties, new sets of assignments for proteins are nowadays fairly regularly published. Moreover, several generalised SSNMR assignment strategies have been proposed,[127,131,205-210] although the use of these have not yet been "standardised" within the field to the extent that they have in solution, where complete protocols exist for the entire experiment-to-structure process.[211] Note, however, that each specific system (in the solution- or solid-state) will present unique difficulties (*e.g.* crowded areas of spectra, mobile regions) and so adaptation of any chosen method, or indeed use of several methods, may often be necessary.

3.4 Structural Information

Once assignments can be found for the resonances that appear in the spectra of a sample, information can be extracted that can give deep insights into the structures and behaviours of a system. Even from a single spectrum, an estimate of the secondary structure of a protein can be obtained via secondary chemical shifts. Depending on whether the residue in which a $^{13}C^{\alpha}$ nucleus resides is part of an α-helix or a β-sheet, its chemical shift is more likely to be higher or lower (respectively) than if that residue were in a random coil conformation. Therefore, defining the secondary chemical shift as $\delta_{\text{observed}} - \delta_{\text{random coil}}$, multiple positive values for a row of adjacent residues indicate the presence of an α-helix, while a number of consecutive negative values signify a β-strand.[212] The same analysis can be performed with $^{13}C^{\beta}$ chemical shifts, which have the opposite dependence compared with random coil shifts.[212]

One of the most powerful aspects of NMR is that information can be obtained at the level of individual nuclei. As mentioned above, dipolar coupling measurements (using, *e.g.*, REDOR) can be used to measure distances between pairs of nuclei. This is most practical in selectively labelled samples, as the analysis is complicated in the presence of additional (*e.g.* homonuclear) dipolar couplings, as in a uniformly-labelled sample.[174] For this reason, in the solid state it is currently more common to rely on the collection of semi-quantitative distance constraints that are gathered from a range of experiments with a variety of mixing times, using samples with widespread isotopic labelling schemes (as described in Ref. 49). At each given mixing time of a particular recoupling experiment, an approximate range of distances for which cross peaks will

appear can be estimated, and hence the observed cross peaks can be classed accordingly and used as distance constraints. Torsion angles between neighbouring nuclei may also be measured directly,[213-215] but for the backbone they may be predicted with some accuracy by comparing secondary chemical shifts, which have been found to correlate with ϕ and ψ torsion angles, with values from an empirical database.[216]

The procedure of solving of a structure culminates in inputting the experimentally-derived distance and/or torsion angle constraints into a structure calculation routine,[217] with the resulting lowest-energy structures corresponding to those most likely to be physical given the available data. Generally, the more constraints that can be used, the more reliable and accurate the output (with a smaller RMSD between predicted structures), although the constraints that are of highest value are those corresponding to longer distances. These help determine the global fold of the protein but are often scarce because of the relatively short range of dipolar recoupling techniques. As a solution to this problem, paramagnetic ions have been used to observe paramagnetic relaxation enhancements (PREs) that act as distance constraints for distances of up to ~20 Å (compared to a maximum of ~5-7 Å in the case of dipolar-based constraints).[104,218] In some cases, other techniques may also be able to provide complementary information that can assist in the determination of structures using SSNMR data. This idea is exemplified by the determination of the 3D structure of the Type III secretion system needle through the combined use of solid state NMR and electron microscopy (EM) by Loquet *et al.*[72,76]

SSNMR not only allows for the characterisation of structures of individual proteins, but also the interactions between them and with their immediate environment. Molecular interfaces can be explored through dipolar transfers, although isolating long-range intermolecular contacts from shorter-range intramolecular cross-peaks presents challenges. One method to overcome this is to use equimolar mixtures of ^{13}C- and ^{15}N-labelled proteins in combination with ^{15}N-^{13}C transfer schemes.[219] One of the more common NMR techniques in the context of protein-protein and protein-ligand interactions relies on the analysis of chemical shifts; for a given nucleus, proximity to the electrons of another molecule can lead to changes in the local magnetic field, modifying its chemical shift. By conducting experiments both before and after complex formation, the resulting chemical shift perturbations (CSPs) can be used to locate the interaction interface(s).[220,221] Finally, the topologies of protein-membrane systems may also be probed, for example by using oriented samples and exploiting the anisotropic nature of

interactions to establish the orientation of proteins within membranes.[222] In addition, surface-accessible residues may be identified via T_2-edited $^{1}H(^{1}H)^{13}C/^{15}N$ experiments, which exploit differences in dynamics to select magnetisation from protons in lipid or (frozen) water molecules prior to establishing dipolar contacts with the protein.[223-225] These approaches represent but a snapshot of the multitude of ingenious methods that have been used to elucidate the various features of a diverse array of biological systems.

3.5 Challenges and Progress

The field of biomolecular SSNMR continues to advance at a rapid pace as progress is made in hardware and experimental method development. However, that structure determination methods in solids are still relatively undeveloped compared with those in solution is illustrated by the fact that to date, a mere 34[xii] unique protein structures have been solved using MAS SSNMR, many of which had already been solved by solution NMR or x-ray diffraction. Poorer sensitivity and resolution, which lead to lengthy experimental time scales and overlapping peaks, remain primary challenges and can often prove to be major bottlenecks in the process of characterising proteins by SSNMR. As such, much effort is directed toward overcoming these issues, in hardware, sample preparation and SSNMR methods.

High magnetic fields are crucial for both sensitivity and resolution, and as a result is an area in which advances have always been pursued. At the time of writing, the highest field strength in use is 1 GHz, although such capability comes with astronomical cost (£millions). MAS technology has also incrementally advanced.[46,47,226,227] For many biological experiments, MAS frequencies of ~10-30 kHz, using 2.5-4 mm probes (where the measurement specified refers to the outer diameter of the associated MAS rotor), are routine, offering a good balance between sample volume and line-narrowing. In the last few years, spinning frequencies of >40 kHz have been made attainable, opening up new possibilities that come with more effective averaging of interactions. In particular, in combination with deuteration, proton detection is made viable (in particular for ^{15}N-^{1}H or methyl ^{13}C-^{1}H correlations), offering valuable gains in sensitivity that more than offset the loss in sample volume that accompanies smaller MAS rotors (*e.g.* 1.3 mm). Spinning at >50 kHz also brings significant benefits for dynamics studies (see Chapters 7-10). Even more recently, the introduction of probes that can spin samples up to 100-111 kHz

[xii] As of 19/05/2015, according to http://www.drorlist.com/nmr/SPNMR.html, which lists structures determined by SSNMR deposited in the Protein Data Bank (PDB).

(0.8-0.7 mm rotors) promises further advances in resolution enhancement, potentially in the application of proton-detected experiments on cheaper, fully protonated samples (explored in Chapter 9).[15,228]

With rapid development comes potential for applying SSNMR to increasingly complex systems, offering deeper understanding into the workings of biological mechanisms at the molecular level. Large proteins and complexes traditionally pose difficulties for solution-NMR studies, as a practical molecular size limit exists whereby the study of systems above a few tens of kDa becomes challenging due to increasingly slow overall molecular rotational diffusion and correspondingly fast nuclear relaxation and hence broadened lines.[229] For SSNMR, technical and practical considerations are the only obstacles in obtaining high resolution spectra of proteins above ~40 kDa.[230] This is a major area in which SSNMR can progress in the near future, although with increasing molecular size comes lower sensitivity as the number of molecules per sample is reduced, as well as increased spectral crowding as the number of resonances increases, especially in uniformly labelled samples. Other important systems such as membrane proteins similarly suffer from low experimental sensitivity as the lipids that they interact with account for much of the sample volume. This recurring problem is compounded by the fact that the amount of experimental time available on expensive high field instruments is often limited. In any case, greater signal averaging can only help to an extent as magnetic fields drift over time, leading to larger observed line widths for experiments run over a considerable period. Other samples may suffer from low expression yields and may therefore only be available in very small quantities. There is therefore a significant need for the development of new experimental methods to maximise the sensitivity of experiments, potentially by taking advantage of parallel developments in technology (*e.g.* MAS) or by streamlining existing methods,[231-235] allowing for shorter experimental times or alternatively a higher level of signal to noise within the same experimental time. The following three chapters are therefore primarily focussed on new and accelerated methods for obtaining resolved spectra in proteins, with a view that they may be applied to systems where sensitivity is (as ever) at a premium.

4

TIME-SHARED THIRD SPIN-ASSISTED RECOUPLING

Abstract

The often poor sensitivity of protein SSNMR experiments can lead to undesirably long experimental time scales. Here, a time-shared third spin assisted recoupling (TSTSAR) experiment is introduced that allows for simultaneous acquisition of homonuclear (^{13}C-^{13}C) and heteronuclear (^{15}N-^{13}C) long-distance contacts in biomolecular solids under magic angle spinning. TSTSAR leads to substantial time savings and increases the information content of 2D correlation spectra.

(Adapted from Lamley and Lewandowski, *Journal of Magnetic Resonance* **2012**, *218*, 30)

4.1 Introduction

A key limitation of solid-state NMR is its inherent lack of sensitivity when compared with other techniques. As a consequence, the signal averaging necessary for achieving acceptable signal to noise means that 2D and higher dimensionality correlation spectra of proteins often have an acquisition time scale on the order of days or even weeks. There is hence much interest in the development of faster, more time-efficient experiments, such that they may be completed in a reasonable time frame using hardware that already exists and is commonly available.

As discussed in Chapter 3, to solve the structures of proteins, intra- and inter-residue distance constraints are obtained from both homonuclear (*e.g.* ^{13}C-^{13}C) and heteronuclear (*e.g.* ^{13}C-^{15}N) correlation experiments, for which an entire plethora of pulse sequences have been developed, providing complementary information when used in conjunction with one another. The two closely related PAR[175,236,237] and PAIN-CP[176,199] methods, based on the more general TSAR mechanism, provide homonuclear and heteronuclear correlations respectively. The distance constraints obtained via these recoupling techniques have enabled the solution of various biomolecular structures and

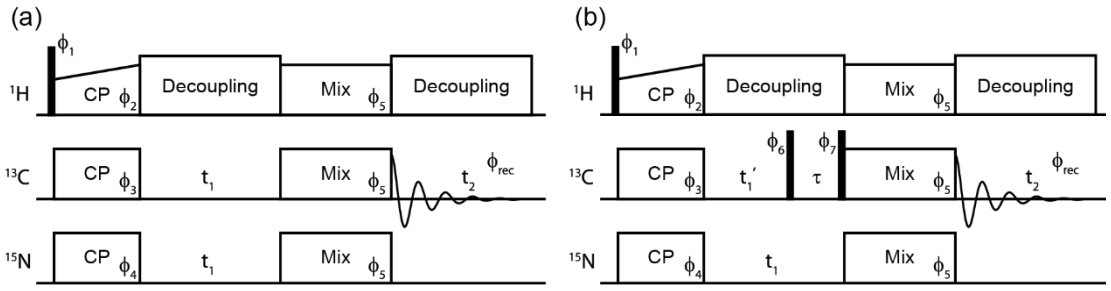

Figure 4.1. Time-shared TSAR pulse sequences for obtaining simultaneous 2D ^{13}C-^{13}C and ^{13}C-^{15}N correlation spectra. Solid black rectangles represent $\pi/2$ pulses. The TSAR mixing period consists of CW irradiation on the ^{1}H, ^{13}C and ^{15}N channels. Irradiation strengths are chosen to reintroduce second order cross terms (i) between ^{1}H-^{13}C dipolar couplings, and (ii) between ^{1}H-^{13}C and ^{1}H-^{15}N dipolar couplings to transfer polarisation (i) between ^{13}C nuclei and (ii) between ^{13}C and ^{15}N nuclei. (a) The simplest version of the sequence. (b) Variant of the sequence that allows for sampling a smaller spectral width in the ^{15}N dimension with a longer ^{15}N t_1 acquisition time. An equal number of t_1 points are recorded on ^{13}C and ^{15}N channels. $\tau = t_1 - t_1'$. Phase cycling: ϕ_1=(+y –y), ϕ_2= (+x), ϕ_3=(+x +x –x –x –y –y +y +y), ϕ_4=(-x -x +x +x y y -y -y), ϕ_5=(+x +x –x –x –y –y +y +y), ϕ_6=(+y +y –y –y +x +x –x –x), ϕ_7=(-y -y +y +y -x -x +x +x), ϕ_{rec}=(+x –x –x +x –y +y +y –y). ϕ_3 and ϕ_4 are incremented simultaneously for States or States-TPPI acquisition scheme.

lead to proposals of a range of structural models, including those of nanocrystalline proteins, (*e.g.* 17 kDa MMP-12[54]), fibrillar systems (*e.g.* HET-s[71], A-β[238], GNNQQNY[239,240]), precipitated oligomers of αB-crystalline[241], and the Type III secretion system needle[72]. In addition, these methods have been demonstrated to be effective at providing long range distance constraints in uniformly ^{13}C- and ^{15}N-labelled at spinning frequencies of $\omega_r/2\pi > 50$ kHz[242], and to be useful for assignment in sparsely labelled samples.[243] Unfortunately, the inherent sensitivity of the TSAR technique is relatively low compared to shorter-range methods (*e.g.* DARR), meaning that experiments can typically take hours or days to complete. As such, streamlining of TSAR-type experiments would undoubtedly prove useful for those wishing to solve solid-state protein structures.

Among various methods that have been presented to accelerate data acquisition,[244,245] so-called time-shared experiments in solution-state NMR have been shown to cut experimental times by effectively multiplying the amount of information gained per experiment.[246-249] Simultaneous evolution of coherences at multiple frequencies in the same time period, combined with appropriate phase cycling, allows for parallel acquisition of related experiments. Despite time-shared experiments becoming relatively commonplace in solution they are rarely undertaken in the solid state. Recently, ^{1}H-detected time-shared methods have been applied for assignment in deuterated

proteins (partially proton back-exchanged)[250]. Here, a new method is presented, time-shared Third Spin Assisted Recoupling (TSTSAR), which applies time-sharing principles to the ^{13}C-detected TSAR pulse sequence in solids to obtain both homonuclear and heteronuclear correlations simultaneously, without or with very small loss of intensity, with a view to gaining complementary distance constraints for biological systems.

4.2 Experimental Details

All experiments were performed on a Bruker Avance II+ spectrometer operating at 600 MHz ^{1}H Larmor frequency. A Bruker 2.5 mm triple resonance probe was used with an MAS frequency of 20 kHz to record [U-^{13}C,^{15}N]histidine spectra, while a Bruker 3.2 mm triple resonance probe was used with an MAS frequency of 16 kHz to record [U-^{13}C,^{15}N]-*N*-Acetyl-L-Val-L-Leu spectra. In each case, experiments using both a time-shared TSAR pulse sequence (Figure 4.1a) and an equivalent standard PAR sequence were carried out, where all equivalent pulse nutation frequencies were held constant to facilitate direct comparison.

Sequences were initialised with a $\pi/2$ r.f. pulse on the ^{1}H channel (100 kHz for histidine, 67 kHz for *N*-Acetyl-L-Val-L-Leu), followed by CP from ^{1}H to ^{13}C/^{15}N with constant ^{13}C/^{15}N irradiation of 50 kHz for 1 ms. ^{1}H CP irradiation was linearly ramped from 80-100%, with an average amplitude of [50 kHz + $\omega_r/2\pi$]. When conducting time-shared TSAR, the ^{15}N CP contact pulse was of opposite phase to that of the ^{13}C contact pulse, ultimately leading to negative ^{15}N-^{13}C cross-peaks relative to ^{13}C-^{13}C cross-peaks. Phase cycling can be found in the caption of Figure 4.1. Offsets on ^{13}C and ^{15}N channels were chosen to avoid overlap of the ^{13}C-^{13}C and ^{15}N-^{13}C cross-peaks: ^{15}N and ^{13}C carrier frequencies were 69.94 ppm and 99.01 ppm, respectively, for the experiment on histidine, and 100.65 ppm and 37.44 ppm for the experiment on N-Ac-VL (the carrier frequencies define the centres of the spectral windows in the indirect dimension for the appropriate nuclei). For TSAR polarisation transfer ^{1}H, ^{13}C and ^{15}N irradiation strengths (in units of spinning frequency) were p_H = 2.4 and $p_{C,N}$ = 2.7 (*i.e.* $\omega_{C,N}/2\pi$ = 43.2 kHz and 54 kHz at $\omega_r/2\pi$ = 16 and 20 kHz respectively) to promote both homonuclear and heteronuclear polarisation transfer with maximum efficiency. ^{13}C, ^{15}N, and ^{1}H r.f fields equal to ω_r and $2\omega_r$ were calibrated using rotary resonance. The r.f. field amplitudes required for TSTSAR, determined from numerical simulations, were calculated based on the calibrated spin-lock field. No further TSAR optimisations were performed, although additional optimisations may be beneficial to confirm the optimal settings and

compensate for any r.f. field miscalibrations. For the convenience of the reader, PAR and δp_0 PAIN-CP (where δp_n means $\delta p = p_N - p_C = n$, with n an integer) optimisation maps simulated with SPINEVOLUTION[251] for the regions used at $\omega_r/2\pi$=20 kHz are shown in Figure 4.2. Note that any combination of settings that corresponds to a red/orange-coloured region in Figure 4.2c, directly below the $n = 0$ Hartmann-Hahn condition, is appropriate for performing TSTSAR experiments. These conditions are not resonance conditions, but rather settings for which the dipolar coupling and CSA autocross terms (which are detrimental to TSAR polarisation transfer) are minimised (autocross terms appear as longitudinal terms in the subspace describing TSAR spin dynamics and thus lead to tilting of the TSAR recoupling axis and quenching of the TSAR polarisation transfer).[175,176] Suitable TSTSAR settings may be found when other PAIN-CP conditions (especially $\delta p_{\pm 1}$, see Ref. 176) are employed besides δp_0 PAIN-CP but they are not considered here since they do not necessarily provide any advantage over the regime proposed here. For experiments involving C' the optimisation maps in Figure 4.2 would need to be re-simulated because the larger CSA will lead to shifting of the optimal conditions. Changes in the resonance offset for ^{15}N have a slight effect on the optimal TSAR polarisation transfer settings, but at least at 600 MHz ^{1}H Larmor frequency and for resonance offsets < 50 ppm, the optimal settings may be chosen based on the on-resonance simulation.

70 kHz SPINAL-64[110] heteronuclear decoupling was applied during t_1 and t_2 acquisition periods, while quadrature detection was achieved through the States mode of acquisition[120] with phases indicated as ϕ_3 and ϕ_4 in Figure 4.1 incremented simultaneously. For each spectrum 8 transients were co-added, between each of which was a recycle delay of 2.5 s. All of the spectra displayed in the figures were acquired using the scheme presented in Figure 4.1a, using identical spectral widths and t_1 acquisition times for both ^{13}C and ^{15}N. For the experiments on *N*-Acetyl-L-Val-L-Leu, t_1 and t_2 acquisition times were 18 ms (180 x 100 μs, spectral width of 10 kHz, *i.e.* ~66 ppm for ^{13}C and ~165 ppm for ^{15}N) and 30 ms (2170 x 13.8 μs, spectral width of 36.2 kHz) respectively. Total experimental time per 2D experiment was ~2 h. For the experiments on [U-^{13}C,^{15}N]histidine, t_1 and t_2 acquisition times were 6 ms (150 x 40 μs, spectral width of 25 kHz, *i.e.* ~166 ppm for ^{13}C and ~412 ppm for ^{15}N) and 24 ms (1734 x 13.8 μs, spectral width of 36.2 kHz) respectively. Total experimental time was ~1.7 h per 2D experiment.

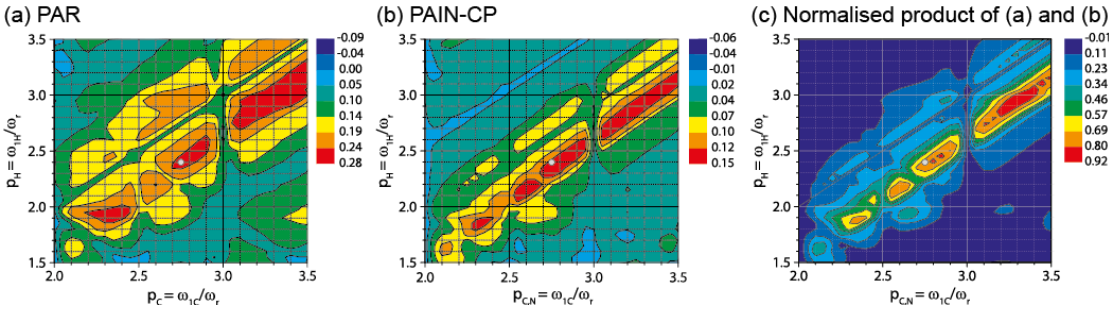

Figure 4.2. Numerical simulations of TSAR polarisation transfer after 3 ms in a $NC^{\alpha}H^{\alpha}C^{\beta}H^{\beta 1}H^{\beta 2}$ spin system as a function of ^{1}H, ^{13}C and ^{15}N r.f. field amplitudes (expressed as $p_X = \omega_{1X}/\omega_r$). Simulations were performed using SPINEVOLUTION[251] at 600 MHz ^{1}H Larmor frequency, 20 kHz MAS frequency using typical chemical shift values. (a) C^{α}-C^{β} PAR polarisation transfer efficiency. (b) N-C^{β} δp_0 PAIN-CP polarisation transfer efficiency (δp_0 means $\delta p = p_X - p_Y = 0$ where $p_X = \omega_{1X}/\omega_r$ and $p_Y = \omega_{1Y}/\omega_r$, see Ref. 176 for detailed description of different TSAR recoupling conditions and terminology). (c) Normalised product of data from maps (a) and (b), highlighting conditions mutually favourable for homonuclear and heteronuclear polarisation transfer. The grey dot indicates an example of favourable settings for performing TSTSAR experiment.

Spectra were processed in TopSpin 2.1 using zero filling and a QSINE window function (SSB=2). In general the optimal processing parameters may be different for ^{13}C-^{13}C and ^{15}N-^{13}C cross-peaks, and hence in some cases it may be beneficial to produce two sets of spectra: one with the processing optimal for ^{13}C-^{13}C cross-peaks and one with the processing optimal for ^{15}N-^{13}C cross-peaks. Chemical shifts were referenced externally with adamantane (downfield ^{13}C peak at 38.48 ppm as referenced with respect to neat TMS) and using IUPAC-recommended frequency ratios for ^{15}N (referenced to liquid NH_3 at -50°C).[252]

4.3 Results and Discussion

The pulse sequence for time-shared TSAR experiment is shown in Figure 4.1. In the simplest version of the experiment, magnetisation is prepared by simultaneous CP from protons to carbon and nitrogen. The CP contact time is chosen so as to provide the best compromise for the efficiency of ^{1}H-^{13}C and ^{1}H-^{15}N polarisation transfer (here ~1 ms). CP is followed by simultaneous t_1 evolution on ^{13}C and ^{15}N and then a TSAR mixing block, during which polarisation originating on carbon nuclei is transferred to other carbons via the PAR mechanism and polarisation originating on nitrogens is transferred to carbons via the PAIN-CP mechanism. The r.f. field amplitudes are chosen so as to provide a compromise between efficient PAR and PAIN-CP polarisation transfers. Such a compromise is relatively simple to achieve since the optimal irradiation settings for

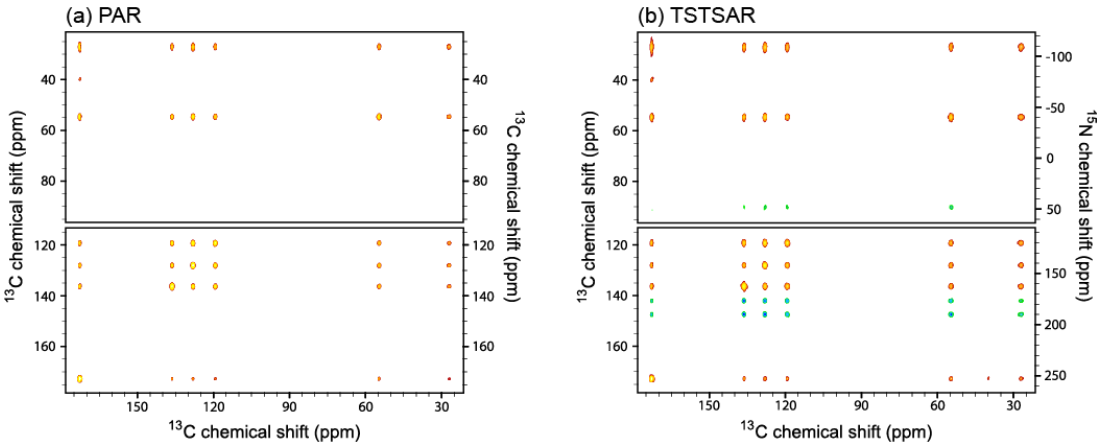

Figure 4.3. 2D spectra of [U-^{13}C,^{15}N]histidine using (a) proton-assisted recoupling (PAR) and (b) time-shared-TSAR (TSTSAR) pulse sequences at $\omega_H/2\pi$ = 600 MHz and $\omega_r/2\pi$ = 20 kHz, with mixing times of 6 ms. The PAR sequence gives a ^{13}C-^{13}C correlation spectrum only, while the TSTSAR sequence gives additional ^{13}C-^{15}N cross-peaks which appear with negative intensities (green-blue) compared to ^{13}C-^{13}C cross-peaks (red-yellow). For both sequences nutation frequencies (in units of spinning frequency) during the TSAR mixing period were p_H = 2.4 and $p_{C,N}$ = 2.7 where $p_X = \omega_{1X}/\omega_r$.

PAR and PAIN-CP are often very similar. The appropriate settings may be extracted from numerical simulations (see Figure 4.2). Often the coherence lifetimes of ^{15}N are longer than those of ^{13}C, while at the same time the spectral widths of ^{15}N spectra are usually much smaller than those of ^{13}C spectra. Presented in Figure 4.1b is a variant of the experiment which takes advantage of these facts. In this version of the experiment the number of t_1 points is the same between ^{13}C and ^{15}N, while the effectively longer t_1 increment on ^{15}N allows for longer t_1 acquisition time than on ^{13}C. In such an experiment the spectral width for ^{13}C is $1/\Delta t_1$', and for ^{15}N is $1/(\Delta t_1)=1/(\Delta t_1'+\Delta\tau)$, where Δ indicates an increment of the corresponding time period.

It is possible to set up TSAR-based methods in either a broadband or a band-selective manner, where the entire or a fraction of the ^{13}C spectral window is excited respectively.[175,176] A broadband-style time-shared TSAR sequence and an equivalent PAR sequence, with TSAR mixing times of 6 ms, were applied to [U-^{13}C,^{15}N]histidine. Figure 4.3 is a direct comparison of the resulting histidine spectra obtained via (a) PAR and (b) time-shared TSAR, each with identical base contour levels. Both show ^{13}C-^{13}C cross-peaks with positive intensity (red-yellow), while the time-shared spectrum exhibits additional, negative-intensity peaks corresponding to couplings of ^{13}C nuclei with HN,

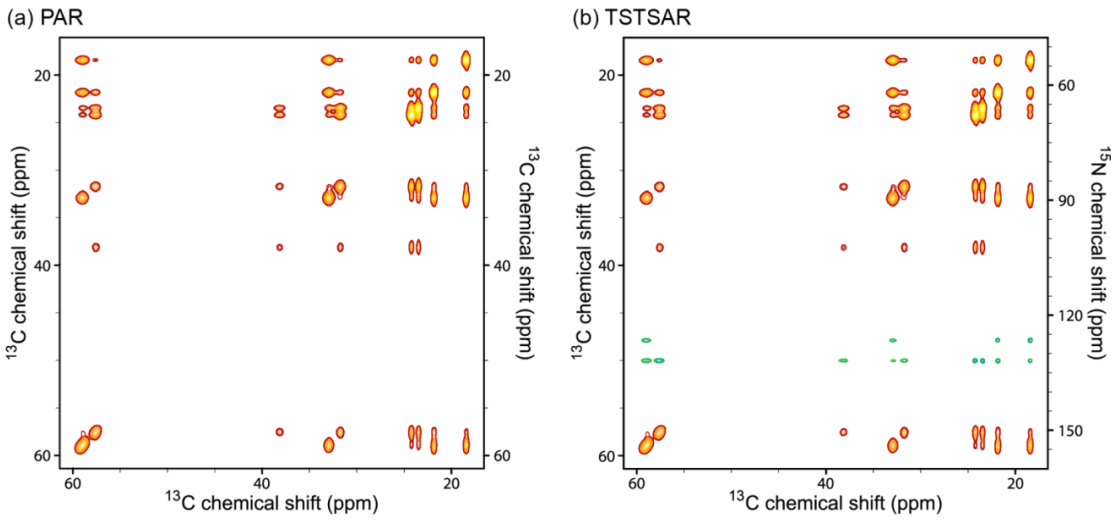

Figure 4.4. 2D spectra of [U-^{13}C,^{15}N]-*N*-Acetyl-L-Val-L-Leu using (a) proton-assisted recoupling (PAR) and (b) time-shared TSAR (TSTSAR) pulse sequences at $\omega_H/2\pi$ = 600 MHz and $\omega_r/2\pi$ = 16 kHz, with mixing times of 3 ms. The PAR sequence gives a ^{13}C-^{13}C correlation spectrum only, while the time-shared TSAR sequence gives additional ^{13}C-^{15}N cross-peaks which appear with negative intensities (green) compared to ^{13}C-^{13}C cross-peaks (red-yellow). For both sequences nutation frequencies (in units of spinning frequency) during the TSAR mixing period were p_H = 2.4 and $p_{C,N}$ = 2.7 where p_X = ω_{1X}/ω_r.

$HN_{\delta 1}$ and $HN_{\gamma 2}$, appearing in "empty" regions of the ^{13}C-^{13}C spectrum owing to the chosen ^{15}N carrier frequency. At a mixing time of 6 ms, correlations between all ^{13}C and ^{15}N are observed as all the sites are within 5 Å from each other in the crystal. In a broadband-style TSTSAR spectrum, the majority of ^{15}N-^{13}C cross-peaks may be folded either between aliphatic and aromatic or aromatic and carbonyl regions without the need for increasing the spectral width in the indirect dimension.

Figure 4.4 shows spectra of [U-^{13}C,^{15}N]-*N*-Acetyl-L-Val-L-Leu obtained using equivalent aliphatic PAR (a) and aliphatic time-shared TSAR (b) pulse sequences (*i.e.* band-selective), with mixing times of 3 ms and the same base contour levels. Again, the time-shared TSAR experiment gives not only the same ^{13}C-^{13}C cross-peaks as the PAR spectrum, but also ^{13}C-^{15}N cross-peaks, folded into the region between the $^{13}C^{\alpha}$ and $^{13}C^{\beta}$ resonances. As the initial magnetisation is transferred from protons it is important to consider the effect of the additional ^{1}H-^{15}N CP on the intensities of the ^{13}C-^{13}C cross-peaks. We compared the intensities of the ^{13}C-^{13}C cross-peaks in the equivalent PAR and TSTSAR spectra. For the more commonly-used aliphatic (band-selective) versions, the intensities of ^{13}C-^{13}C cross-peaks in the TSTSAR spectrum are generally, within noise, of equal intensity to those of the aliphatic PAR spectrum (ratios of intensity of 1 with standard deviation less than 1% for mixing times of 1-3 ms; see Figures 4.5a-c and B.1a-c

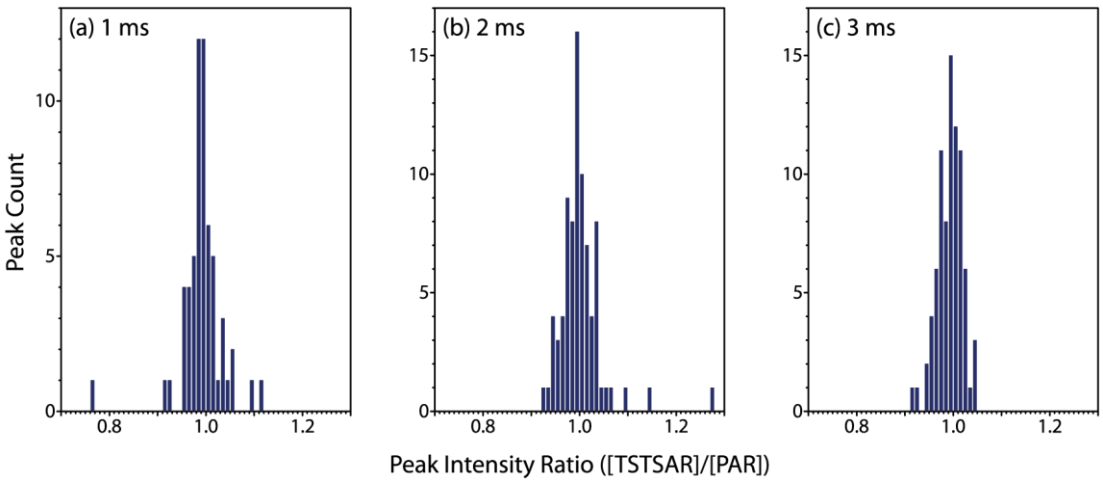

Figure 4.5. Distribution of ratios of time-shared TSAR vs. PAR ^{13}C-^{13}C cross peak intensities, measured from spectra of [U-^{13}C,^{15}N]-*N*-Acetyl-L-Leu-L-Val (Figure 4.4) with mixing times of (a) 1 ms, (b) 2 ms and (c) 3 ms. Spectra were recorded with $\omega_{0H}/2\pi =$ 600 MHz and $\omega_r/2\pi =$ 20 kHz. Peaks with signal to noise of less than 20 are excluded, as are those that are not isolated.

in Appendix B). This is understandable since in the TSTSAR case the source of magnetisation is different for ^{13}C and ^{15}N spins: the initial CP pools the magnetisation from aliphatic protons for ^{13}C and amide protons for ^{15}N. This situation is less favourable for ^{13}C sites without directly bonded protons in a broadband-style experiment: for the cross-peaks from C' to other carbons there is a decrease of cross-peak intensity due to the redirecting of a fraction of the amide proton magnetisation to ^{15}N. Note, however, that the equivalent aliphatic to C' cross-peaks are again less affected, and that the overall decrease of PAR cross-peak intensity is less than 30% in the broadband style spectrum. Consequently, even with ^{13}C-^{13}C cross-peaks of slightly reduced intensity, broadband TSTSAR results in significant time savings over running two separate PAR and PAIN-CP experiments. In general, running aliphatic TSTSAR is completely advantageous over running separate aliphatic PAR and PAIN-CP experiments. The TSTSAR experiment provides both ^{13}C-^{13}C and ^{15}N-^{13}C long distance contacts with the same efficiency as equivalent separate experiments but in a fraction of the overall experimental time. This time saving may be used to either shorten the required overall experimental time or to obtain data of higher quality in the available experimental time.

Graphs of polarisation build-up with TSTSAR mixing time, for representative (a) diagonal homonuclear cross-peaks, (b) one-, (c) two- and (d) three-bond ^{13}C-^{13}C transfers, and (e) ^{13}C-^{15}N cross-peaks, can be found in Appendix B (Figure B.2). As expected, polarisation builds up with mixing time, with transfer faster for shorter distances. Time-shared TSAR spectra taken at shorter mixing times may therefore aid

assignment, for which the additional ^{13}C-^{15}N cross-peaks give complementary contact information. The TSAR mechanism mitigates the dipolar truncation effects which inhibit long range transfers via first order mechanisms, and so long range geometrical constraints are accessible. A further advantage of the time-shared variant of the pulse sequence is that by simultaneously obtaining homonuclear and heteronuclear dipolar contacts, it is automatically ensured that resonances corresponding to a specific nuclear environment are aligned. Since chemical shifts are often somewhat sensitive to temperature changes it is often not trivial to account for chemical shift changes between spectra obtained under slightly different conditions. Because of this, chemical shift tolerances must often be introduced in order to match different spectra. The larger the required chemical shift tolerances, the higher the ambiguity of the assignments. Whilst for the samples discussed this may be insignificant, for larger (*e.g.* protein) molecules with many times more sites and crowded spectra this may become a real problem. For example, when probing intermolecular contacts in 50% ^{13}C and 50% ^{15}N-labelled protein mixtures, one of the main challenges for interpreting the resulting spectra is the often high assignment ambiguity of the intermolecular contacts. TSTSAR should alleviate such problems, as the presence of intra- and inter-residue ^{13}C-^{13}C contacts from the ^{13}C-labelled protein, in the same spectrum as the intermolecular ^{15}N-^{13}C cross-peaks, should allow for reduction of chemical shift tolerances otherwise necessary when comparing two separate spectra acquired with slightly different settings. For long-time scale experiments this approach also aids in accounting for the shifts due to magnetic field drift on systems without locking devices, thus avoiding problems with aligning ^{15}N-^{13}C and ^{13}C-^{13}C correlation spectra acquired separately. This should be of particular value for automated assignment and structure determination approaches.

4.4 Conclusions

We have introduced a new technique, which combines time-sharing and TSAR methodology in order to simultaneously obtain 2D homonuclear and heteronuclear correlation spectra in solids undergoing MAS, and hence shorten experimental time scales. The TSAR mechanism employed allows for long distance constraints to be obtained, and the increased information content of each spectrum may be helpful with reducing assignment ambiguity in more crowded spectra. Furthermore, effectively no intensity of homonuclear cross-peaks is seen to be lost compared with a standard aliphatic PAR sequence. The method should be of interest to those wishing to study the

structure and interactions of biological molecules, and for further time savings could be combined with other streamlining approaches such as non-uniform sampling methods.

5

SSNMR OF A PROTEIN IN A PRECIPITATED COMPLEX WITH A FULL-LENGTH ANTIBODY

Abstract

NMR is a key technique for characterising the structures and dynamics of biomolecular complexes but, for such systems, faces challenges of sensitivity and spectral resolution. Here, it is demonstrated that application of ^{1}H-detected experiments at >50 kHz magic angle spinning frequencies enables the recording, in a matter of minutes to hours, of SSNMR spectra suitable for quantitative analysis of protein complexes present in quantities as small as a few nanomoles (tens of micrograms for the observed component). This approach enables direct structure determination and quantitative dynamics measurements in domains of hundreds-of-kDa protein complexes. Protein-protein interaction interfaces can be mapped out by comparing the chemical shifts of proteins within solid-state complexes with those of the same constituent proteins free in solution. This methodology is exploited to characterize a >300 kDa complex of GB1 with full-length human immunoglobulin, where it is found that sample preparation by simple precipitation yields spectra of exceptional quality, a feature that is likely to be shared with some other precipitating complexes.

(Adapted from Lamley, J. M.; Iuga, D.; Öster, C.; Sass, H. J.; Rogowski, M.; Oss, A.; Past, J.; Reinhold, A.; Grzesiek, S.; Samoson, A.; Lewandowski, J. R. *Journal of the American Chemical Society* **2014**, *136*, 16800)

5.1 Introduction

Ultimately, a full understanding of biological processes at the molecular level requires the determination of structures and dynamics of not only isolated proteins, but biomolecular complexes of interacting proteins. Such studies are usually undertaken using either X-ray

crystallography[253-255] or solution NMR spectroscopy[256,257]. Unfortunately, solution NMR studies of commonly large biomolecular assemblies are limited by the broadening of lines that stems from slower tumbling (and consequently enhanced T_2 relaxation) at higher molecular weights. In contrast, the line widths of biomolecules in the solid state are, in principle, independent of the size of the molecule. Thus, provided that solid-state-specific line broadening and sensitivity challenges are addressed, solid-state NMR spectroscopy has the potential to become a viable alternative for obtaining atomic resolution structural and dynamic information on large protein complexes and supramolecular assemblies.[12,72,258]

Because of the small number of molecules per unit mass for large biomolecular complexes, it is extremely challenging to obtain the sensitivity required for detailed studies of their structure and dynamics. Most of the studied cases involve large multimeric assemblies of NMR-identical monomers that multiply the effective concentration of the observed domains (typically >70 nanomoles of monomer protein).[13,14,16,83] Adequate sensitivity is more difficult to obtain, though, for complexes lacking high levels of symmetry.[257] This challenge could be partially addressed with approaches such as DNP. For example, recently DNP enabled, in ~44 h, the recording of a 2D ^{13}C-^{13}C spectrum of 30 nanomoles of IF1 (8.2 kDa) in an 800 kDa complex with small ribosomal subunit (E30S).[259] Currently, however, biomolecular DNP performed at cryogenic temperatures faces the challenge of large inhomogeneous broadening that necessitates the use of specifically labelled samples. In addition, freezing of motions under these conditions impedes studies of functional dynamics.[260]

Under more conventional conditions, sensitivity may be maximised by detecting protons, which have the highest nuclear gyromagnetic ratio (barring tritium) and nearly 100% natural abundance. This has traditionally proved problematic owing to the dense networks of strong ^{1}H-^{1}H dipolar couplings present in proteins, which have an adverse effect on ^{1}H line widths and hence spectral resolution. However, thanks to developments in MAS technology and sample preparation (*e.g.* deuteration), which help to narrow ^{1}H line widths, proton-detected experiments on proteins are becoming more practicable.[163,261-264] In favourable cases, ν_r = 40-60 kHz and high magnetic fields are sufficient to obtain amide ^{1}H resolution for fully protonated proteins that is good enough for practical applications,[163,262,265] though still inferior to that for samples with partial deuteration under the same conditions.[163]

Another important contribution to inherent solid-state line widths comes from inhomogeneous broadening due to chemical shift disorder and differences in magnetic susceptibility in different parts of the sample. Broadening of this type is greatly influenced by sample preparation. Crystalline samples, for example, exhibit a high degree of order and thus can often give excellent resolution, but crystallisation of protein complexes is often extremely difficult or impossible. Sample sedimentation (or FROSTY)[13,14,266] holds much promise as a general alternative for the preparation of large proteins and complexes, and has already been successfully applied to 0.36-1.1 MDa soluble multimeric protein complexes.[13,16,83] Below we demonstrate that spectra with quality comparable to that for crystalline preparations may also, in some cases at least, be obtained for precipitated complexes, obviating the need for complicated preparation techniques and equipment.

To address the primary challenges of spectral resolution and sensitivity for the general case of a protein complex without a high level of symmetry, we have studied here a complex of a small protein with an antibody. Protein-antibody interactions are of great interest in molecular medicine and biology and underlie diverse applications ranging from therapeutic (antibodies are the fastest-growing class of protein therapeutics[267]) or diagnostic antibodies to immunoprecipitation. In the latter context, protein G (a cell-surface protein found in various *Streptococcal* bacteria) is widely used because it is able to specifically bind to a wide range of antibodies and the involved interactions are well-characterised. Protein G has been shown to bind strongly to the Fc fragment ($K_A = 2.7 \times 10^{10}$ M^{-1}) and more weakly to the Fab fragment ($K_A = 9.1 \times 10^6$ M^{-1}) of the human antibody immunoglobulin G (IgG).[268] While protein-protein interactions of various protein G domains with isolated fragments of IgG have been studied by both solution NMR spectroscopy and X-ray crystallography,[269-271] structures of protein G domains with full-length IgG are currently not available. However, as will be shown below, protein-protein interactions in the full-length complex can be characterised by solid-state NMR spectroscopy.

For the investigation, we prepared a complex of the B1 domain of protein G (GB1; ~6 kDa) and full-length human IgG (~150 kDa), which precipitates from solution in several seconds after combination of the components. Precipitation of samples often occurs as a result of non-specific interactions, resulting in NMR spectra of poor quality, with broad lines due to variation in molecular environments and thus chemical shifts. On the other hand, when precipitation is driven by specific interactions, leading to the

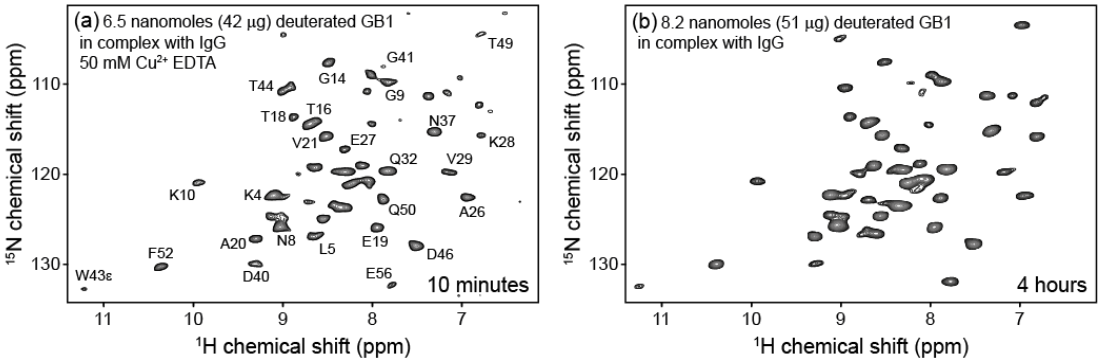

Figure 5.1. ^{15}N-^{1}H 2D correlation spectra of perdeuterated 100% back-exchanged labelled GB1 in a complex with full-length unlabelled immunoglobulin G (IgG). The samples in (a-b) contained ~6.5 nanomoles (~42 µg) and ~8.2 nanomoles (~51 µg) of GB1, respectively. Spectrum (a) was obtained in 10 minutes using fast recycling enabled by the addition of 50 mM Cu^{II}-EDTA. Spectrum (b) was obtained in 4 h without a paramagnetic dopant. Experiments were performed at MAS frequencies (ν_r) of (a) 55 kHz and (b) 60 kHz, at 850 MHz ^{1}H Larmor frequency and at a sample temperature of 27 ± 1 °C. Select assignments are indicated. Full assignments are shown in Figure 5.6.

formation of a homogeneous protein-protein complex, narrow and well-defined resonances can be expected. This is the case for the precipitated GB1-IgG complex, which yields spectra with a single set of narrow resonances (see Figure 5.1). Whilst it is not likely that precipitation will lead to high-quality spectra for every protein complex, the fact that it does for this system suggests that it is likely to also work for many others.

Herein, proton-detected[272] SSNMR spectroscopy of proteins under "ultrafast" (55-60 kHz) MAS conditions, in the absence and presence of paramagnetic doping to speed up the acquisition, is assessed as a general approach for quantitative structural and dynamics studies of large protein complexes in small quantities. For the results in this chapter, to obtain optimal resolution and sensitivity at the high MAS rates, a complex of deuterated ^{13}C- and ^{15}N-labelled GB1 (with 100% reprotonation at exchangeable sites) with natural-abundance IgG was used, which for convenience is referred to as the "deuterated GB1 complex". The Bruker 1.3 mm rotors used have an overall sample volume of 1.7 µL (with glued caps to prevent sample dehydration; this volume shrinks to ~1.0 µL when silicon spacers are used instead).

5.2 Results and Discussion

We begin our investigation by using a sample with 50 mM Cu^{II}-EDTA paramagnetic dopant to accelerate acquisition by reducing the recycle delay required, in this case from ~2 s to 0.4 s.[273] Spectral crowding is minimised by leaving the IgG unlabelled and observing only the ^{15}N-labelled GB1. Despite the nanomolar-range quantity of sample in

the 1.3 mm rotor, by combining the above approaches, good quality spectra for the deuterated GB1 complex can be obtained in a matter of minutes. Figure 5.1a shows a ^{1}H-detected ^{15}N-^{1}H 2D correlation spectrum obtained on ~1 mg of complex (containing ~6.5 nanomoles, ~42 μg, of GB1, which is roughly an order of magnitude less than the amounts of protein used in typical solid-state NMR studies of protein complexes in the literature) in ~10 minutes. The ^{1}H resonance line widths in this spectrum are in the 70-110 Hz (0.08-0.13 ppm) range and the average signal to noise ratio is 8 ± 3 (where 3 is the standard deviation of the peak intensities). Critically, this resulting level of sensitivity places within practical reach the majority of methods in the arsenal of solid-state NMR spectroscopy for characterising the structures and dynamics of proteins. For example, one can record ≥3D spectra for *de novo* assignment of domains in large complexes in cases where the usual "divide and conquer" approaches[257] fail to yield satisfactory results. It should be noted that the approaches presented here will be applicable to many other protein complexes whose precipitates yield well-resolved spectra, in addition to those that can be prepared by other means such as sedimentation or crystallisation.

To better understand the nature of the GB1-IgG interaction we performed spectral assignment of GB1 in the complex using a series of 3D experiments (the full sequence for GB1 can be found in §B.2 in Appendix B). Because of extensive changes in the local nuclear environments, the assignments could not have been obtained by simply adjusting GB1 chemical shifts from solution or crystal data (see Figure 5.2). Initial resonance assignments were obtained using a proton-detected H(H)NH 3D experiment, with 2.7 ms of RFDR ^{1}H-^{1}H mixing to establish inter-residue contacts between neighbouring H^{N} protons. In many cases, however, these assignments were ambiguous, especially because of the widespread presence of cross-peaks corresponding to magnetisation transfer across the β-sheet. Subsequent refinement was achieved by carrying out a "backbone walk" using a pair of complementary 3D spectra: a (H)C'(C^{α})NH to correlate ^{1}H and ^{15}N shifts with ^{13}C' of the same residue, and a (H)C'NH to correlate ^{1}H and ^{15}N shifts with ^{13}C' of the previous residue. Finally, a 3D (H)C^{α}NH experiment was used to obtain, for each ^{1}H/^{15}N shift, same-residue $^{13}C^{\alpha}$ chemical shifts. The large spread of the $^{13}C^{\alpha}$ chemical shifts proved especially useful for confirming the total numbers of resonances in crowded areas of the ^{15}N-^{1}H spectrum, for instance the areas around A23/Y33 (Figure 5.4b) and I6/N8 (Figure 5.4c). Each 3D spectrum was obtained in 1-3 days. Example strips, 2D planes and 1D slices from the 3D

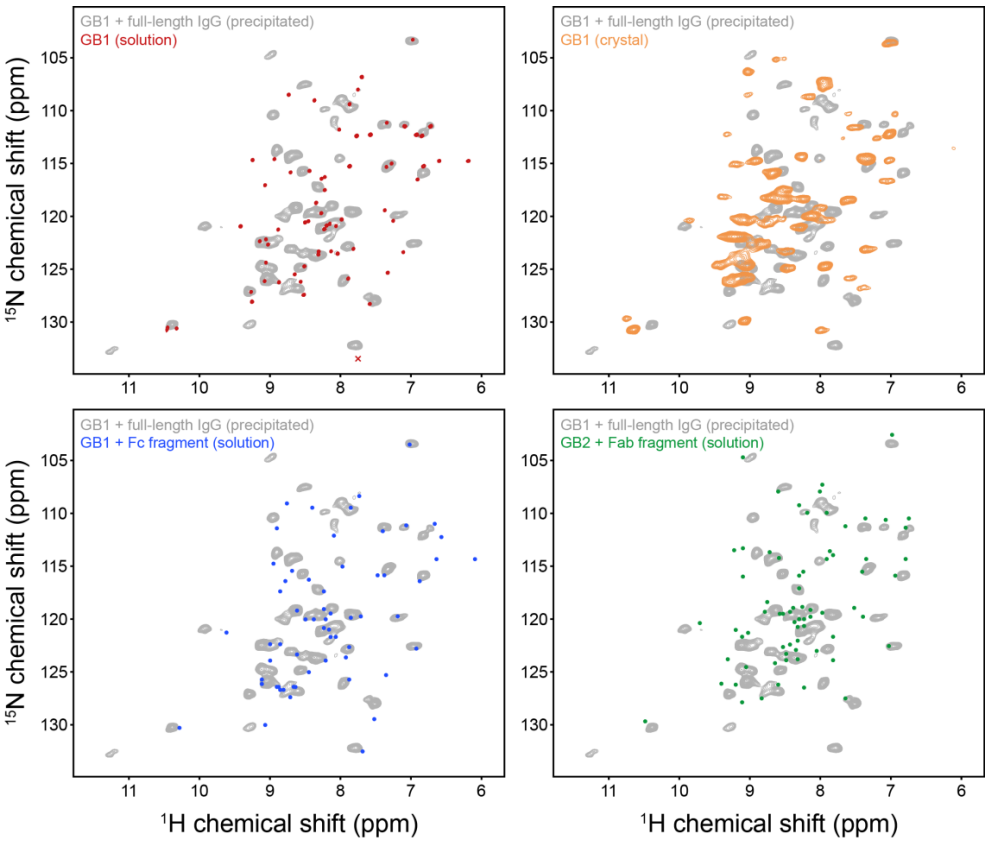

Figure 5.2. Overlays of 2D ^{15}N-^{1}H correlation spectra of GB1 in a precipitated complex with IgG (grey contours), with GB1 free in solution (red contours, top-left) and fully protonated crystalline GB1 at 1 GHz field[163] (orange contours, top-right). The bottom two panels show, over the same spectrum of precipitated GB1-IgG complex, the positions of peaks for GB1 in complex with the Fc fragment of IgG in solution[270] (blue points, bottom-left) and for GB2 in complex with the Fab fragment of IgG in solution[271] (green points, bottom-right). The conditions for the experiments are as follows: (GB1 in solution and in crystal) 27 °C, pH 5.5; (GB1-Fc) 35 °C, pH 5.8; (GB2-Fab) 25 °C, pH 6.5. The red cross in the top-left panel indicates the position of an aliased peak in the original solution spectrum (E56).

spectra are shown in Figures 5.3-5.5. The final assignments for the ^{15}N-^{1}H spectrum are shown in Figure 5.6.

In general, at the same temperature and pH the protein chemical shifts may be altered as a result of conformational changes or direct intermolecular interactions. Insights into the nature of GB1 interactions with the full-length IgG may hence be gained by comparison of the chemical shifts for GB1 in the complex with IgG with the chemical shifts of isolated GB1 in solution. Figure 5.7 shows the chemical shift perturbations (CSPs, calculated as $\sqrt{\frac{1}{2}\left(\delta_H{}^2 + (\delta_N/5)^2\right)}$, where δ_H and δ_N are changes in chemical shift for ^{1}H and ^{15}N, respectively) between isolated GB1 in solution (*i.e.* in the

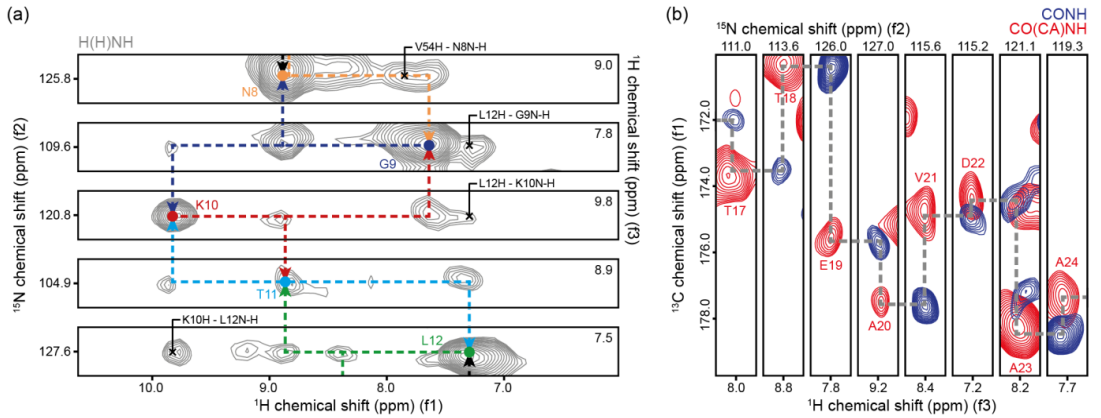

Figure 5.3. Representative strips from (a) H(H)NH and (b) CONH and CO(CA)NH 3D experiments on deuterated [U-^{13}C,^{15}N]GB1 in a precipitated complex with full-length human IgG. f3 is the dimension of direct detection. The H(H)NH experiment (a) used 2.7 ms of 100 kHz ^{1}H RFDR mixing to establish inter-residue contacts between neighbouring H^{N} protons. Coloured dashed lines show the assignment pathway; at each proton resonance in f3, cross-peaks are seen at the ^{15}N frequency of the same residue and ^{1}H frequency (f1) of neighbouring residues (and the same residue). Auto-peaks are labelled in colour. Peaks resulting from transfer across more than one residue are indicated with black crosses. Because the RFDR transfer is based on the dipolar mechanism (i.e. through-space), in many cases transfer can be seen along the helix or across the β-sheet (e.g. V54H-N8N-N8H) or loop regions (e.g. L12H-G9N-G9H). The CONH and CO(CA)NH experiments in (b) were used to carry out a "backbone walk"; the CO(CA)NH (red) correlates amide ^{1}H and ^{15}N shifts with the ^{13}C' of the same residue, while the CONH (blue) correlates amide ^{1}H and ^{15}N shifts with ^{13}C' of the previous residue. The grey dashed line shows the assignment pathway.

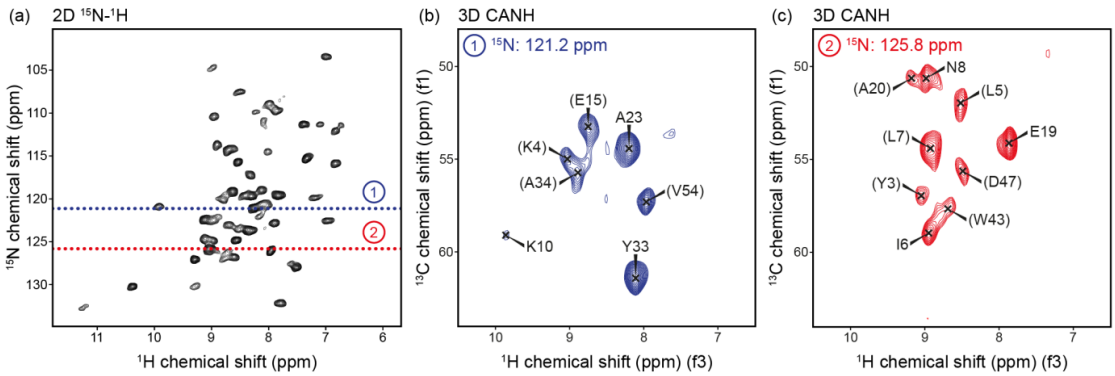

Figure 5.4. Representative planes from the CANH 3D experiment on deuterated [U-^{13}C,^{15}N]GB1 in a precipitated complex with full-length IgG. Examples (b) and (c) are ^{13}C-^{1}H planes of the 3D spectrum taken at the ^{15}N chemical shifts shown by the dotted lines in (a). Assignments are given in brackets for peaks whose centres do not lie at the exact given ^{15}N chemical shift (but are nearby, hence intensity is still seen).

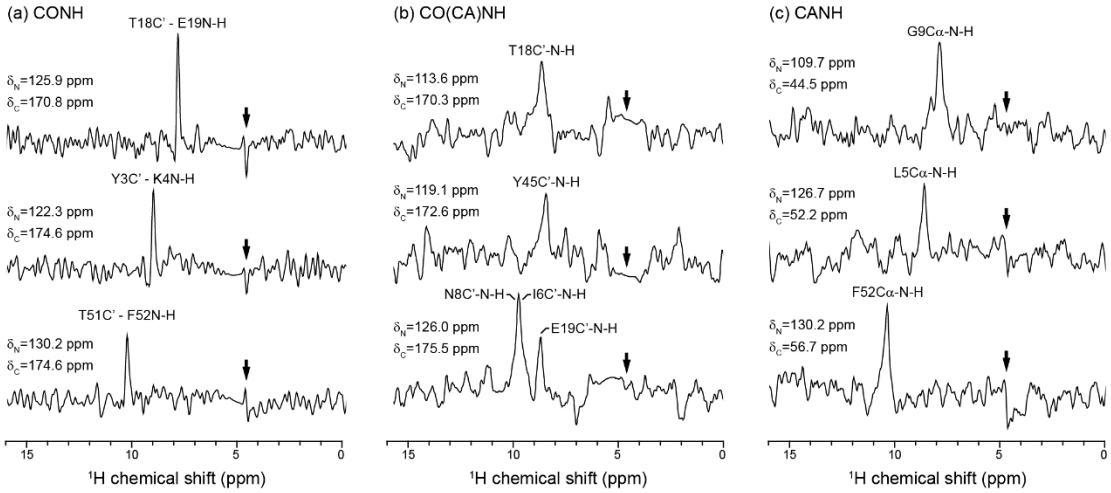

Figure 5.5. Representative 1D slices in the ^{1}H dimension from (a) CONH, (b) CO(CA)NH and (c) CANH proton-detected experiments on deuterated [U-^{13}C,^{15}N]GB1 in a precipitated complex with full-length IgG. Experiments took (a) ~23 h, (b) ~65 h and (c) ~13 h. The arrows indicate the chemical shift of the water signal, which was suppressed with 200 ms slpTPPM ^{1}H decoupling[114]. Line broadening of (a) 90-65-65 Hz, (b) 100-100-100 Hz and (c) 80-80-80 Hz was applied in the ^{1}H-^{15}N-^{13}C dimensions of the 3Ds respectively.

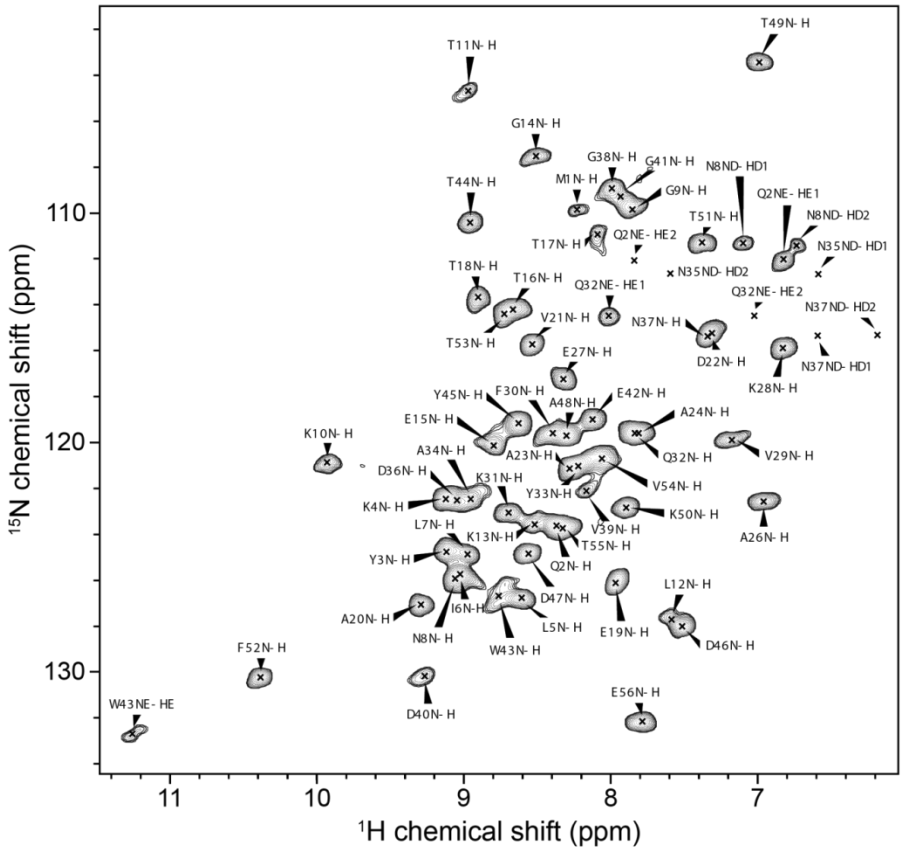

Figure 5.6. Spectral assignments for deuterated [U-^{13}C,^{15}N]GB1 in a complex with full length human IgG (natural abundance). The 2D ^{15}N-^{1}H correlation spectrum was obtained at ν_r = 60 kHz and ν_{0H} = 850 MHz with an effective sample temperature of 27±1 °C. Total experimental time was ~9.2 h. In this case, no paramagnetic dopant was used to accelerate the acquisition.

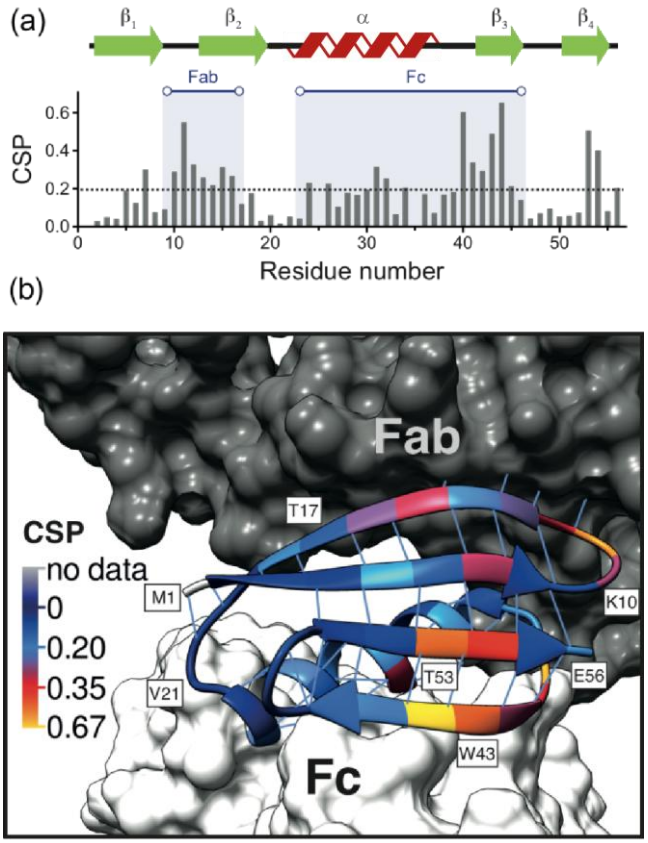

Figure 5.7. ^{15}N Chemical shift perturbations (CSPs) for GB1 in a precipitated complex with IgG and GB1 free in solution (a) as a function of residue number and (b) projected onto the structure of GB1 in a model of the complex. In (a), the binding interfaces to the Fab and Fc fragments of IgG are indicated above the graph. The two IgG molecules interacting with GB1 are coloured dark grey and light grey. The dotted line in (a) indicates the average value of the CSPs. There are no data for T25 or N35. All of the experiments were performed at 27-30° C and pH 5.5.

absence of intermolecular interactions with IgG; spectrum given in Figure B4, Appendix B) and GB1 in a precipitated complex with IgG. The largest CSPs are observed for residues L5, L7, K10-T16, A24-Y45 (except E27, Y33 and N37) and T53-V54.

To determine whether the observed CSPs are due directly to interactions with IgG or to conformational changes induced by these interactions, it is useful to compare our results to those from studies of protein G domains in complexes with IgG fragments, for which chemical shift changes were dominated by the effect of direct intermolecular interactions. The interactions of excised domains from protein G and fragments of (but not full-length) human and animal IgG have been investigated by both solution NMR spectroscopy and X-ray crystallography.[269-271,274,275] Mapping of CSPs upon complex formation was used to identify the interaction interface of GB1 with the isolated Fc fragment of IgG (62 kDa)[270] and of GB2 with the isolated Fab fragment of

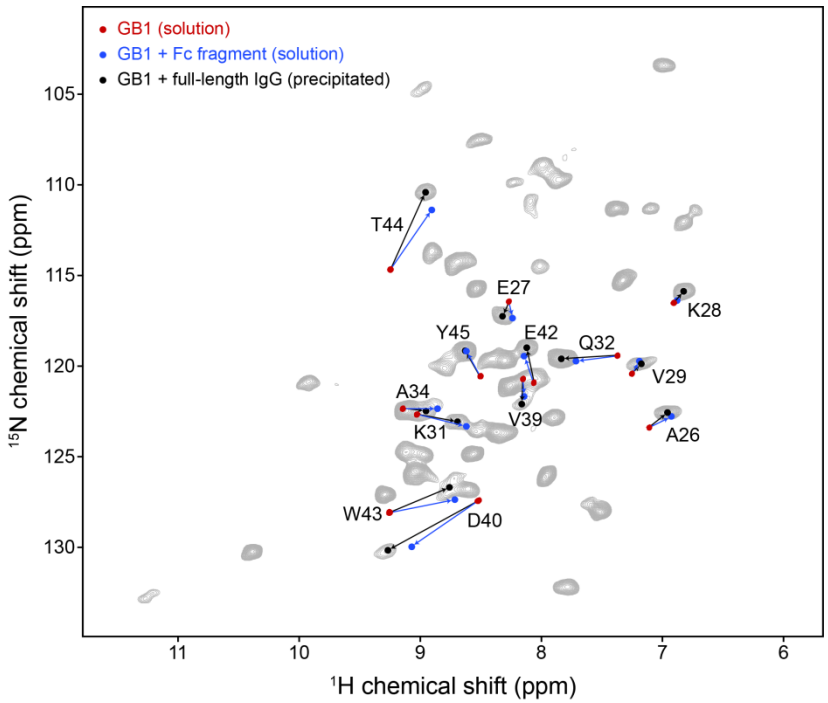

Figure 5.8. 2D ^{15}N-^{1}H correlation spectrum of deuterated [U-^{13}C,^{15}N]GB1 in a precipitated complex with IgG (grey contours). Overlaid, for interacting residues (generally high CSPs as indicated in Figure 5.7) in the Fc-binding region, are peaks for GB1 free in solution (red contours) and chemical shifts for GB1 in a complex with the Fc fragment of IgG in solution (blue circles)[270]. The chemical shifts for these residues in the full, precipitated complex are indicated with black circles. Residues for which assignment ambiguity is high (for GB1 in complex with Fc in solution) have been omitted. The figure illustrates that the cross peaks for the GB1 sites interacting with the Fc fragment of IgG appear at very similar chemical shifts for both GB1 in the complex with Fc fragment in solution and GB1 in the precipitated complex with full IgG.

IgG (54 kDa)[271]. According to the cited studies, the interactions of protein G domains involve: 1. primarily the helix, β_3 strand and the loop connecting them (corresponding to residues 23-46 in our GB1 construct; no significant CSPs were observed for residues 37-38 in the cited study) for the Fc fragment; and 2. the loop between the β_1 and β_2 strands as well as about two thirds of the β_2 strand (corresponding to residues 9-17 in our GB1 construct; notably, in the cited study CSPs were observed for some residues outside the direct interaction interface, including 7, 38 and 53) for the Fab fragment. A comparison to the CSPs in Figure 5.7 shows that these two binding interfaces correspond to the two longest stretches of residues with the largest CSPs observed for the complex of GB1 with full-length IgG. In addition, as shown in Figures 5.2 and 5.8-5.10, in spite of being recorded under relatively different conditions, the chemical shifts for the sites involved in binding to the Fc and Fab fragments are very similar for GB1 in the complex with IgG

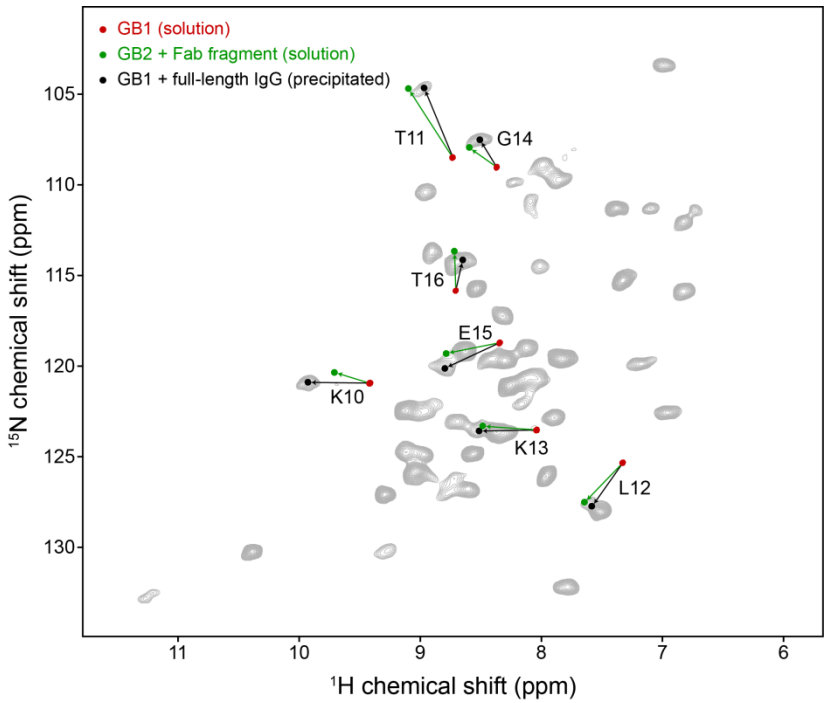

Figure 5.9. 2D ^{15}N-^{1}H correlation spectrum of deuterated [U-^{13}C,^{15}N]GB1 in a precipitated complex with IgG (grey contours). Overlaid, for interacting residues (generally high CSPs as indicated in Figure 5.7) in the Fab-binding region, are peaks for GB1 free in solution (red contours) and chemical shifts for GB2 in a complex with the Fab fragment of IgG in solution (green circles)[271]. The chemical shifts for these residues in the full, precipitated complex are indicated with black circles. Note that if directly comparing to the GB2 domain in Ref. 271, one needs to add 5 to the residue numbers given here.

and with its appropriate fragments. This remarkable similarity suggests that the changes in chemical shifts between isolated GB1 and GB1 in complex with IgG are primarily due to direct interactions of GB1 with Fc and Fab of IgG, analogous to those observed for the complexes with the fragments in solution. Notably, resonances from the Fab-binding interface are not shifted in the spectra of GB1 in complex with the Fc fragment (Figures 5.8 & 5.10), and resonances from the Fc-binding interface are not shifted in the spectra of GB2 in complex with Fab (Figures 5.9 & 5.10). On the other hand, both Fab-binding and Fc-binding sites are shifted in the GB1 complex with full-length IgG, suggesting that the observed changes are likely due to multiple-site binding rather than conformational changes at one interface induced by a direct interaction at another. Further evidence of the lack of substantial conformational change taking place upon formation of the GB1-IgG complex comes from the similarity of the C^{α} secondary chemical shifts between isolated GB1 and GB1 in the complex with IgG (Figure 5.11).

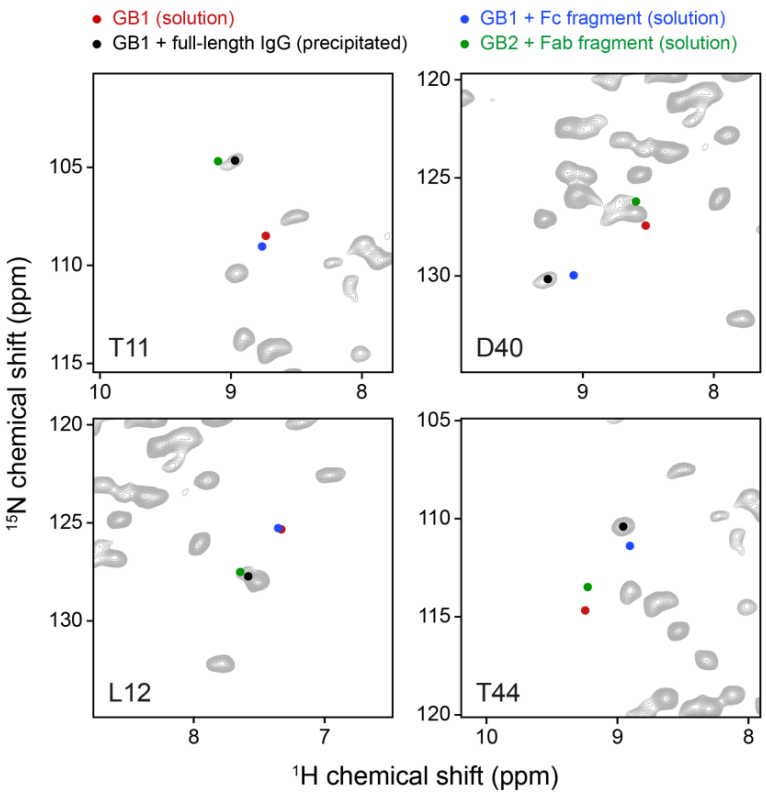

Figure 5.10. Example expansions of 2D ^{15}N-^{1}H correlation spectra of deuterated [U-^{13}C,^{15}N]GB1 in a precipitated complex with IgG, with the chemical shifts of four residues (T11, L12, D40 and T44) plotted for the following: GB1 free in solution (red), the precipitated complex of GB1 with IgG (black), GB1 in a complex with the Fc fragment of IgG in solution[270] (blue) and GB2 in a complex with the Fab fragment of IgG in solution[271] (green). Note that in the precipitated complex with full-length IgG, the shifts for T11 and L12 (in the Fab-binding region, left-hand panels) are similar to those in the complex of GB2 with Fab, whereas the shifts for the same residue in the complex with Fc are approximately unchanged from free in solution. The converse is true for residues D40 and T44 (in the Fc-binding region, right-hand panels): the shifts for the full precipitated complex and for GB1 with Fc in solution are remarkably similar when compared with the shifts of GB2 with Fab, which are much closer to the shifts of GB1 free in solution. In short, in the full, precipitated complex we see shifts consistent with binding of the GB1 to both the Fab and Fc fragments of the IgG antibody simultaneously. Large shift perturbations (from free in solution) are not seen for the Fab-binding region of GB1 when in complex with the Fc fragment only, and vice-versa. Note that if directly comparing to the GB2 domain in Ref. 271, one needs to add 5 to the residue numbers given here.

The cross-peaks for residues G9-T18, A26-T44 in the GB1-IgG complex are generally also significantly attenuated compared to peaks with the smallest CSPs (Figure 5.12), which is consistent with these residues being in direct contact with the fully protonated IgG, causing increased dipolar broadening. Moreover, the attenuation may indicate the presence of slow motions for the interacting residues, which are also suggested by the spinning frequency dependence of cross-peak intensities (see §6.4).

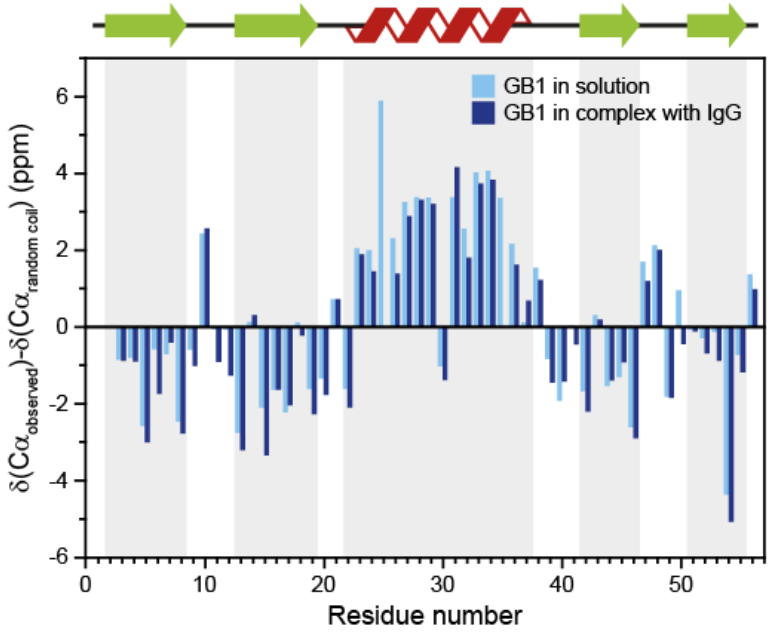

Figure 5.11. Comparison of the C^{α} secondary chemical shifts for free GB1 in solution and GB1 in a precipitated complex with IgG. The high level of similarity of the secondary chemical shifts indicates an absence of any large conformational change for GB1 in the complex compared to free GB1 in solution. There are no data for T25 or Y33 in the complex.

There is, however, some indication of the presence of small, localised conformational changes outside of the interaction interfaces. In particular, L5, L7, T53 and V54 are residues that are outside of the contiguous interaction interfaces but have large CSPs. Since similar CSPs are observed in the solution spectra of GB2 in complex with the Fab fragment,[271] we can identify this particular interaction as the cause for the slight conformational change. These large CSPs may be associated with modulation of the hydrogen bonds between strands β1 and β4 near the C-terminus, which occurs on a long time scale and is also present in crystalline GB1 (as indicated by elevated ^{15}N $R_{1\rho}$ measurements[276]). Such an interpretation is consistent with these residues being involved in the final steps of the GB1 folding pathway.[277]

The presence of a single set of relatively narrow resonances, with chemical shift changes for both GB1 binding interfaces, suggests that the most abundant species in the sample involves each molecule of GB1 interacting simultaneously through its Fc- and Fab-binding interfaces. In the case of one set of GB1 molecules binding to Fc and another set binding to Fab one would expect to observe, for each binding interface, two sets of resonances for GB1: one set for those resonances involved in a direct interaction with IgG and one set for those not involved. A similar principle was used, for example,

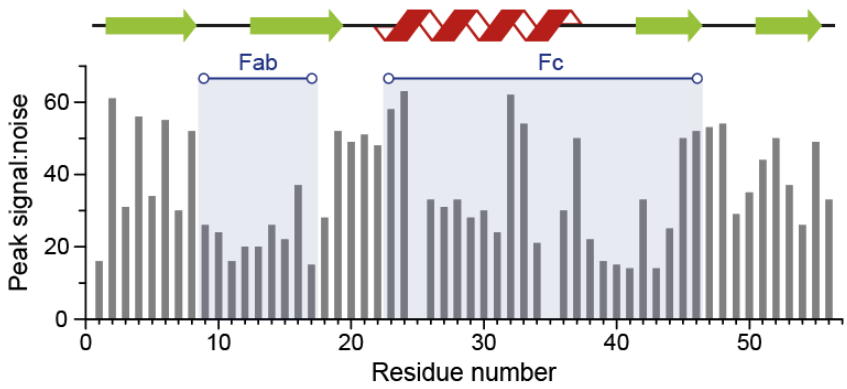

Figure 5.12. Signal to noise ratios as a function of residue number for cross peaks in Figure 5.6.

to identify supramolecular structures in amyloid fibrils.[70,240] Crude modelling using crystal structures of GB1-like molecules in complexes with IgG fragments, and the crystal structure of full-length IgG, suggests that it is sterically possible for GB1 to interact simultaneously with one molecule of IgG through the Fc interface and another molecule of IgG through the Fab interface (see Figure B.5 in Appendix B).[269,275,278] Alternatively, the Fab-binding interface could be involved in hydrogen bonding with another molecule of GB1 as in crystals of the C2-Fc complex,[275] though neither the absence of a E15-K13 cross-peak in the 3D H(H)NH spectrum, nor the similarity of CSPs for the GB2-Fab complex in solution[271] supports this. In either case, the resulting complex would be at least 300 kDa. The concentration of GB1 remaining in the supernatant after precipitation of the complex suggests that the complex is formed in a 1:1 or lower ratio of GB1 to IgG. In all calculations, a 1:1 ratio has been assumed.

The above findings suggest that changes of chemical shifts in complexes in the solid state, compared with those in constituent proteins free in solution, may be used to identify interacting protein-protein interfaces in analogy to chemical shift mapping during titration experiments in solution. This approach should be particularly valuable for mapping out interactions in complexes with low solubility.

The exceptionally reasonable durations of the experiments presented so far were largely possible because of the acceleration of acquisition by paramagnetic doping. While this strategy is suitable for structural applications (and some dynamics applications, *e.g.* measurements of dipolar order parameters[279]), paramagnetic relaxation, which is dependent primarily on the distance of a given site from the paramagnetic centre and on the electron relaxation, may mask the contributions of local motions to NMR relaxation. Experiments aiming to characterise protein dynamics using NMR relaxation therefore

often require measurements in the absence of paramagnetic dopants. Figure 5.1b illustrates that even without dopants, spectra with signal to noise suitable for quantitative measurements (average S/N = 30 ± 12) can be obtained in a few hours for the perdeuterated GB1 complex (4 h). This indicates that it is practically feasible to obtain a full series of spectra for quantification of protein dynamics by relaxation with experiment times on the order of a few days in the case of ^{15}N $R_{1\rho}$ measurements[276] or a few weeks in the case of ^{15}N R_1 measurements[280].

5.3 Conclusions

In summary, we have shown that ^{1}H detection at 50-60 kHz magic angle spinning frequencies, combined with sample deuteration (fully reprotonated at exchangeable sites) enables site-specific characterisation of domains in >300 kDa complexes in sample quantities as small as 6-8 nanomoles, with experimental time scales on the order of minutes to hours for 2D experiments. In the case of the GB1-IgG complex, the resolution of spectra of the precipitated complex rivals that of microcrystalline proteins. Sensitivity under these conditions is good enough for 3D experiments to be completed in a matter of hours-days, facilitating spectral assignment. Comparison of chemical shifts for constituent proteins in solution to the chemical shifts for the proteins in complexes in the solid state allows protein-protein interaction interfaces to be mapped out, in analogy to solution-state chemical shift mapping experiments. The presented approach enables quantitative structural and dynamics measurements to be performed on sample-size-limited systems such as proteins in large complexes or membrane proteins in lipid bilayers, which are often beyond the reach of other structural biology methods. It should be noted that similar approaches on fully protonated samples may be practical at higher spinning frequencies, although the smaller volumes of the rotors required may limit sensitivity – this issue is explored in the following chapter.[280]

5.4 Experimental Details

[^{13}C,^{15}N]-labelled GB1 (T2Q) was produced as described in Ref. 281. Deuterated [^{13}C,^{15}N]-labelled GB1 (T2Q) was expressed in *Escherichia coli* BL21(DE3) after one cycle of adaptation to D_2O in a 50 mL pre-culture. The production was carried out in a 3.6 L fermenter using 1 L of D_2O M9 minimal medium with 6 g of [^{2}H,^{13}C]-glucose and 1.5 g of $^{15}NH_4Cl$. The final yield after cell rupture by heating to 75 °C and HPLC purification (reversed-phase HPLC column, Jupiter 10 mm C_4 300 Å) was 152 mg. The level of

deuteration was approximately 87%, as estimated from solution-state 1D NMR spectra. After lyophilisation, the final buffer (10 mL) was adjusted by dialysis against 4 x 1 L 50 mM sodium phosphate (pH 5.5). Lyophilised IgG from human serum was purchased from Sigma-Aldrich. Complex samples were prepared for solid-state NMR experiments by mixing 0.3 mM GB1 and 0.15 mM IgG solutions (2:1 molar ratio), and centrifuging the resultant precipitate into NMR rotors.

All 2D solid-state NMR spectra shown, as well as the 3D H(H)NH spectrum, were recorded at 850 MHz ^{1}H Larmor frequency with a Bruker Avance III spectrometer, with a Bruker 1.3 mm triple-resonance probe. All other 3D experiments were performed on a Bruker Avance II+ spectrometer running at 600 MHz ^{1}H Larmor frequency, using a Bruker 1.3 mm triple-resonance probe. The 1.3 mm rotors were sealed either with silicone spacers (Bruker) or by gluing the rotor caps with a silicone-based sealant to eliminate water leakage. Bruker BCU-X cooling units were used to regulate the internal sample temperature to 27 ± 1 °C (measured from the chemical shift of water with respect to DSS[282]). These conditions were achieved by using a nitrogen gas flow of 670-800 L/h with a target temperature of -7 to -9 °C (at 600 MHz), or with a flow of 935-1470 L/h with a target temperature of -5 to -7 °C (at 850 MHz).

^{15}N-^{1}H 2D correlation spectra were recorded using a proton-detected heteronuclear correlation sequence (as in Figure 3.3d, with double-quantum CP contact times of 1 ms (^{1}H-^{15}N) and 0.4 ms (^{15}N-^{1}H). Total durations of these experiments were 10 minutes (Figure 5.1a; 60 t_1 increments, recycle delay of 0.4 s), ~4 h (Figure 5.1b; 74 t_1 increments, recycle delay of 2 s) and ~9.2 h (Figure 5.6; 54 t_1 increments, recycle delay of 0.4 s).

GB1 resonances were assigned on the basis of 3D H(H)NH, CONH, CO(CA)NH and CANH experiments recorded on the sample whose ^{15}N-^{1}H spectrum is shown in Figure 5.1a, at 60 kHz MAS. For each of these 3D experiments, CP contact times were 1.4-1.8 ms for initial ^{1}H-^{15}N/^{1}H-^{13}C transfers, and 700 μs for final ^{15}N-^{1}H transfers. In the H(H)NH experiment, 2.7 ms of 100 kHz RFDR[283] ^{1}H-^{1}H mixing was used to establish inter-residue contacts between neighbouring H^N protons via dipolar couplings. In the triple-channel experiments, transfers from ^{13}C'/$^{13}C^{\alpha}$ to ^{15}N were achieved by CP with 10 ms contact time. In the CO(CA)NH experiment, polarisation was transferred from ^{13}C' to $^{13}C^{\alpha}$ by dipolar couplings with a 10 ms DREAM step (30 kHz nutation frequency)[183]. For all 3D experiments, the recycle delay was set to 0.4 s,

leading to total experiment times of ~36 h (H(H)NH), ~23 h (CONH), ~65 h (CO(CA)NH) and ~13 h (CANH).

In all solid-state experiments, hard pulses were applied at nutation frequencies of 100 kHz (^{1}H and ^{13}C) or 83.3 kHz (^{15}N). 10 kHz WALTZ-16 heteronuclear decoupling was applied to ^{1}H during ^{15}N/^{13}C evolution, and to ^{15}N during direct ^{1}H acquisition, while quadrature detection was achieved using the States-TPPI method. Suppression of the water signal was achieved by saturation with 200 ms of slpTPPM ^{1}H decoupling[114] applied on resonance with water signal at an amplitude of ¼ of the MAS frequency. slpTPPM involves a sweep through a low power TPPM condition[284] with the lengths of the pulses changed from 120% to 80% of the reference π pulse, alternating the phases of the pulses between 0° and 41°.

A reference solution ^{15}N HSQC spectrum of [^{2}H,^{13}C,^{15}N]GB1 in 50 mM sodium phosphate buffer (pH 5.5) was recorded at 600 MHz ^{1}H Larmor frequency at a sample temperature of 30°C (see Appendix B).

All spectra were processed using TopSpin 3.2 or NMRPipe and subsequently assigned in Sparky.

6

^{1}H-Detected SSNMR Experiments at 80-100 kHz MAS

Abstract

Recent developments in magic angle spinning technology permit spinning frequencies of 100 kHz and over to be attained. Here, we examine the effects of spinning up to such rates upon proton line widths in the dipeptide β-Asp-Ala, and note that at fast (100 kHz) MAS and high (850 MHz) magnetic field, proton-proton dipolar couplings are averaged sufficiently for line widths approximately as narrow as those achievable by contemporary CRAMPS approaches to be reached, leading to a highly accessible and time-efficient approach for the study of natural abundance small organic molecules via proton detection. Furthermore, despite the small rotor volume, this kind of approach is found to be practical for samples of proteins and protein complexes, even when only 2-3 nanomoles are available.

6.1 Introduction

Proton NMR spectroscopy is widely used as a probe of the structure and dynamics of a vast range of molecules in solution, including large molecules such as proteins. For such studies, the proton (^{1}H) is an ideal nucleus since its high gyromagnetic ratio and natural abundance leads to high sensitivity. As has already been discussed, in solids, high-resolution proton studies are hampered by the significant line-broadening effects due to presence of strong ^{1}H-^{1}H couplings. Unfortunately, because the Hamiltonian for a dipolar network of like spins (*e.g.* a network of coupled protons) does not in general commute with itself at different points in time, the homogeneous broadening decreases relatively slowly with increasing spinning frequency (the homogeneous line broadening is inversely proportional to the product of magnetic field and MAS rate).[227,285] In most cases, MAS alone fails to completely remove the effects of homogeneous broadening,

even at rates of 60-70 kHz (as afforded by Bruker 1.3 mm probes), leading to poor spectral resolution.

Despite this drawback, ^{1}H NMR in the solid state has found numerous applications, including the study of small natural-abundance organic molecules and their crystal polymorphs that are pharmaceutically relevant.[286] To obtain spectral resolution, studies usually endeavour to either dilute the network of protons with deuterium atoms[156,157,287], or else employ so-called combined rotation and multiple pulse spectroscopy (CRAMPS) techniques to decouple the homonuclear dipolar couplings.[288,289] For proteins, the former of these approaches is most commonly used, where incorporation of deuterium is achieved by biosynthetic means,[261] enabling proton-detected ^{15}N-^{1}H correlation experiments to be performed at spinning frequencies of <40 kHz.[165,261] This approach is less suitable, however, for obtaining ^{13}C-^{1}H spectra because of the greater distances between the protons at exchangeable sites and the carbon sites. The cost of sample deuteration is also often very high, for proteins and especially for molecules that have to be synthesised by other chemical methods.

CRAMPS methods have developed rapidly in recent years and their application to small molecules has been greatly successful.[290-301] However, the high nutation frequencies and duty cycles that are often required for effective decoupling can generate a high degree of sample heating (in addition to potentially accelerated wear to probes that are pushed to their operational limits),[302] rendering them less attractive for studies of hydrated proteins. For example, a current state-of-the-art CRAMPS sequence such as eDUMBO-PLUS can achieve CH_2 proton line widths well below 300 Hz at fast (60 kHz) MAS and high (800 MHz) field strength, but requires r.f. amplitudes as high as 170 kHz for optimum performance.[298] Other potential drawbacks of CRAMPS stem from the complexity of experimental setup (which may require the optimisation of a host of experimental parameters[303,304]) and data analysis (owing to the introduction of chemical shift scaling factors[298,299] and sometimes unwanted spectral artefacts[292,296]).

In light of these obstacles, the ability in certain situations to achieve similar results through fast MAS alone is a desirable alternative. For proteins, there are numerous other potential advantages that render the ≥70 kHz spinning regime attractive, including improved suppression of spin diffusion effects,[114] improved coherence lifetimes,[163] and benefits for applications to paramagnetic systems.[305] Above all, ^{1}H detection in fully protonated systems should be aided by more effective removal of strong dipolar ^{1}H-^{1}H couplings under such conditions. Here, using state-of-the-art 0.8 mm MAS

instrumentation recently developed in the Samoson laboratory, we investigate the effects of MAS with frequencies of up to 100 kHz on proton line widths and the resulting spectral resolution, for both small molecules and protein samples.

6.2 Evaluation of Line Widths

Before assessing the suitability of such small rotors for protein samples (where sensitivity is limited), it is useful to evaluate the effects of increasing MAS averaging on proton line widths with a simple small molecule. To accomplish this, 1D experiments were conducted on the natural-abundance dipeptide *β*-Asp-Ala at spinning frequencies from 15 to 100 kHz at 850 ^{1}H Larmor frequency, with no homonuclear decoupling (Figure 6.1). At 15 kHz spinning frequency the proton spectrum is too broad for any features to be easily identified. As expected, more peaks become resolved as ω_r is increased, with the two Asp CH_2 proton resonances becoming resolvable at around 65 kHz. At this stage, these resonances have line widths of 418 ± 5 and 351 ±1 Hz (0.49 ppm and 0.41 ppm, Asp Hβ2 and Hβ3 respectively). As the MAS frequency is increased further, the Ala HN and Asp HN resonances finally become resolved and all other lines continue to narrow. Final proton line widths at 100 kHz are given in Table 1. The narrowest of these is that of Ala Hβ, at 0.25 ppm (211 ± 0.5 Hz). Also of particular note are the widths of the Asp Hβ2 and Hβ3 protons, at 0.34 ppm (292 ± 1 Hz) and 0.32 ppm (274 ± 2 Hz) respectively. These are comparable to the 0.36 ppm and 0.34 ppm corrected line widths that have been achieved using the state of the art eDUMBO-PLUS-1 homonuclear decoupling scheme at a similar field of 800 MHz.[298] CH_2 protons are usually the most difficult to decouple due to their proximity with one another and correspondingly strong ^{1}H-^{1}H couplings, as well as a lack of motional averaging typical of the CH_2 group. Averaging of the dipolar couplings by this simple "brute force" method does not introduce any undesired artefacts or chemical shift scaling factors.

Contributions to the proton line widths can be grouped into two categories: inhomogeneous broadening, which is primarily due to B_0 field and sample inhomogeneities, and homogeneous broadening, the majority of which originates from the incompletely averaged homonuclear dipolar couplings but which also contains contributions from J-coupling and incoherent relaxation. It is worth remarking that inhomogeneous broadening defines the limiting value for the measurable line width that cannot be eliminated by MAS (or decoupling) without removing chemical shift information altogether. As such it is useful to separate the two broadening components

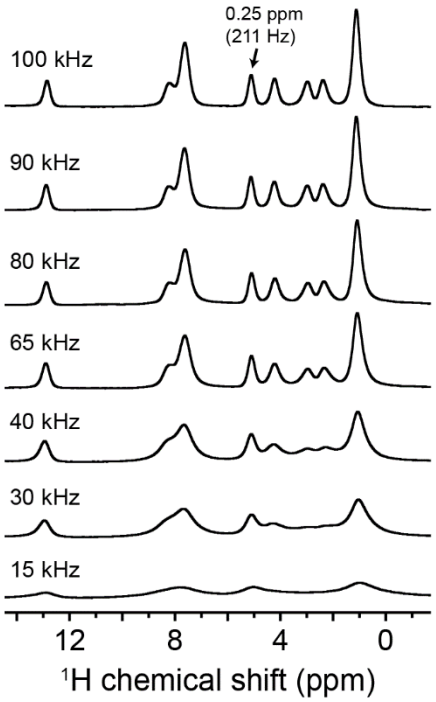

Figure 6.1. 1D ^{1}H spectrum of the dipeptide β-L-Asp-L-Ala as a function of MAS frequency at 850 MHz ^{1}H Larmor frequency. The proton background was suppressed with a spin echo (24 times the rotor period at each spinning frequency). The sample temperature was not controlled.

in our evaluation. Inhomogeneous contributions to the line widths are strongly sample-dependent; for proteins, effective sample preparation is key to producing samples that exhibit the local order necessary for narrow line widths.

To isolate the homogeneous part, T_2' values for each proton in the dipeptide, *i.e.* the transverse dephasing time during a spin-echo experiment, were measured at spinning frequencies from 30 to 100 kHz. Figure 6.2 shows the MAS frequency dependence of the total and spin-echo line widths (equal to $1/(\pi T_2')$) of the protons in β-Asp-Ala. As has been found in numerous other studies, the line width measurements diminish linearly with decreasing $1/\omega_r$ as the dipolar couplings are averaged more effectively.[162,227,285,306-309] The rate at which the line width is narrowed with increasing spinning frequency varies between proton sites, and is dependent on the both the local strength of the dipolar coupling and the geometry of the proton network.[285] The offset between the two sets of data for each proton represents the inhomogeneous contribution to the line width, which is refocused in a T_2' experiment. Although this contribution is approximately constant with varying ω_r, the offset is different for the different proton sites, indicating a different level of inhomogeneous broadening (but usually >125 Hz (>0.15 ppm)). The absolute

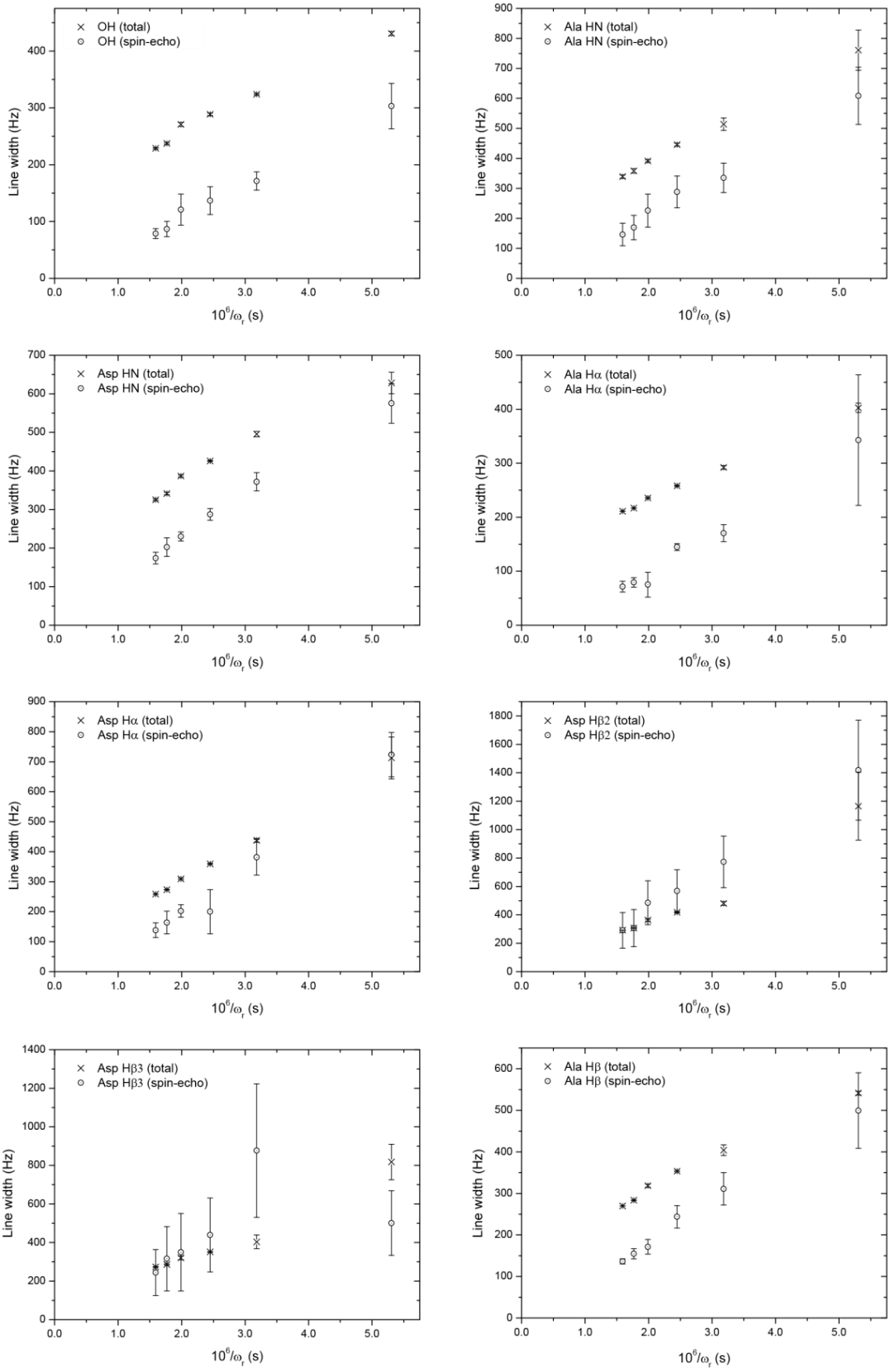

Figure 6.2. Total (crosses) and spin-echo (open circles) line widths for protons in β-Asp-Ala, as a function of inverse spinning rate at 850 MHz ^{1}H Larmor frequency. Spin echo line widths were calculated as $1/(\pi T_2')$, where T_2' is the magnetisation decay time constant measured in a spin-echo experiment.

spin-echo line widths should, however, be taken with some degree of care, as systematic errors can arise in cases where a single exponential fits the data T_2' data poorly (we observe such deviations in our data).[285] In these cases, the spin-echo line width can in fact appear larger even than the full line width of the proton resonance. The effects of this can be seen in the data for the largely unresolved Hβ2 and Hβ3 sites, where the spin echo line widths appear much higher than expected but with large associated error bars. For the other, more resolved protons, the lines of best fit for the spin-echo line width data show negative intercept values, as the ^{1}H-^{1}H dipolar couplings will be completely averaged at a finite spinning frequency (see below).

The spin-echo (homogeneous) line widths at 100 kHz MAS and 850 MHz ^{1}H Larmor frequency are detailed in Table 6.1. At this spinning frequency and field, for many sites the inhomogeneous contribution is at least as significant a proportion of the overall line width as the homogeneous contribution – in the absence of inhomogeneous broadening, spin-echo line widths at 100 kHz are as narrow as 71 Hz (for Ala Hβ, where the inhomogeneous contribution is twice as large). Because the inhomogeneous contribution constitutes a significant fraction of the observed line width, in going from 65 to 100 kHz MAS (for example), narrowing of the total line width is less than the ratio of the spinning frequencies (1.54), though it is still between a factor of 1.2 and 1.5 for all eight resonances (a reduction of over 120 Hz in some cases). There is clearly still much scope for further reductions in ^{1}H line widths with faster MAS (or new CRAMPS methods) – extrapolating the full, inhomogeneously-broadened line widths to an infinite spinning frequency yields minimum limiting inhomogeneous line widths of between 84±8 Hz (Asp Hβ) and 170±10 Hz (Ala NH), a theoretical improvement of ~2 times on average. Extrapolation of the homogeneous line width to a value of zero Hz suggests

Table 6.1. Total and homogeneous ^{1}H line widths in *β*-Asp-Ala, measured at 100 kHz spinning frequency and 850 MHz ^{1}H Larmor frequency.

Peak	OH	Ala HN	Asp HN	Ala Hβ	Asp Hβ	Asp Hβ2	Asp Hβ3	Ala Hβ
Line width (Hz)	229 ± 1	339 ± 5	325 ± 2	211 ± 0.5	259 ± 1	292 ± 0.5	274 ± 2	269 ± 0.5
Line width (ppm)	0.27	0.40	0.38	0.25	0.30	0.34	0.32	0.32
Spin-echo line width (Hz)	78 ± 9	146 ± 38	174 ± 15	71 ± 10	138 ± 25	290 ± 130	240 ± 120	136 ± 6

that (if the trend continues), for most protons directly bonded to carbons, around 240 kHz may be sufficient to completely average the homonuclear dipolar couplings. For the more mobile Ala Hβ (methyl), Ala HN, Ala OH, Asp HN and Asp OH, it appears that much higher spinning frequencies from around 430 to 1300 kHz will be required.

It is important to also consider the effects of molecular motions upon line narrowing, and the influence of MAS-induced heating upon this. To check that the narrowing observed at 100 kHz resulted primarily from averaging of the anisotropic interactions by MAS rather than by molecular motions, repeat measurements were performed in the presence of sample cooling. At 100 kHz with cooling applied, *β*-Asp-Ala line widths were different on average by less than 3 Hz (with some resonances wider and some narrower) compared to those in the unregulated experiments, indicating that the increase in temperature associated with spinning faster has, in this case, a negligible effect on the line widths compared to the averaging effect of the physical rotation itself.

6.3 Application to Small Molecules

The line narrowing afforded at 80-100 kHz MAS is sufficient to at least partially resolve all eight resonances in one dimension in the *β*-Asp-Ala dipeptide. For this and other similarly small organic molecules (*e.g.* pharmaceutical compounds) proton detection offers sufficient sensitivity for relatively rapid characterisation at natural abundance. In 1D, the signal to noise of more dilute, lower-γ spins such as ^{13}C can also be effectively improved by indirect detection of protons, with an enhancement factor inversely proportional to the square root of the proton line width.[272,310] Two dimensional heteronuclear correlation (*e.g.* ^{13}C-^{1}H) experiments can further resolve more crowded areas (*e.g.* NH and CH_2 regions in the dipeptide) by virtue of the large chemical shift spread of the ^{13}C nucleus,[311-314] and can reveal internuclear connectivities.[315-317] These experiments may be performed relatively straightforwardly at ultrafast MAS rates. Figure 6.3a shows the result of a 2D ^{13}C-^{1}H experiment on *β*-Asp-Ala at 80 kHz MAS, with no homonuclear decoupling during the direct ^{1}H acquisition. Here, double-quantum CP was used for polarisation transfer between those ^{1}H and ^{13}C nuclei close in space, although J-coupling-based methods may be used to give one-bond transfers only.[286] At this MAS frequency, all of the peaks are clearly resolved. Despite the fact that the internal volume of the rotor is only ~0.6 μL (~1 mg of dipeptide sample), the

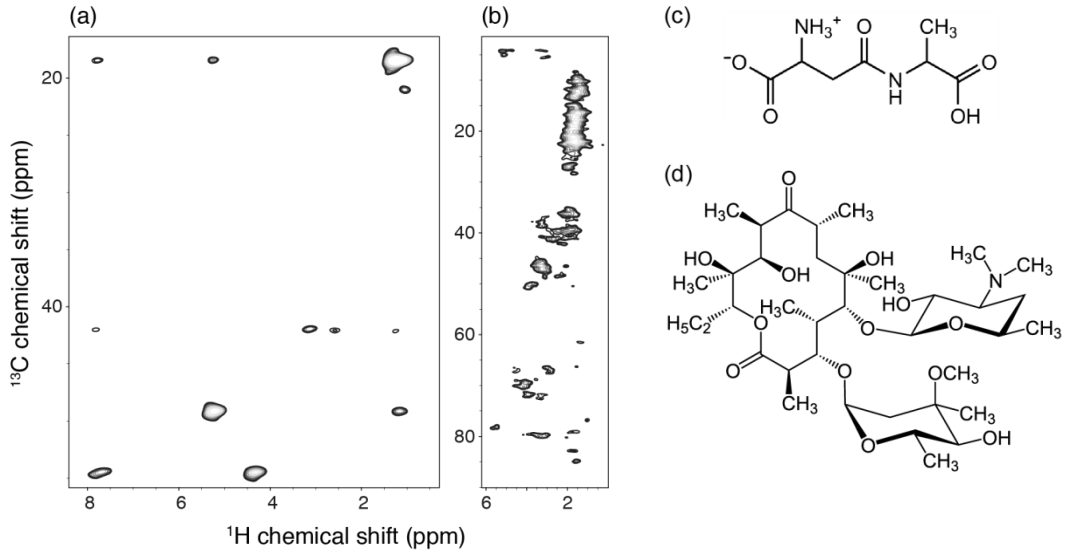

Figure 6.3. Heteronuclear ^{13}C-^{1}H 2D correlation spectra of (a) the dipeptide *β*-L-Asp-L-Ala and (b) erythromycin at 850 MHz ^{1}H Larmor frequency and spinning frequencies of (a) 80 kHz and (b) 95 kHz. The spectrum in (a) was acquired with 120 t_1 increments, 32 scans per increment and a 3 s recycle delay, resulting in an overall experimental time of ~3.3 h. The spectrum in (b) was acquired with 256 t_1 increments, 192 scans per increment and a 1.5 s recycle delay resulting in the overall experimental time of ~20.5 h. The structures of *β*-Asp-Ala and erythromycin are shown in (c) and (d), respectively.

spectrum was obtained in just 3.3 h. The S/N for the cross-peaks originating from one-bond transfers in this spectrum (when processed with broadening matched to the methyl line widths) is on average ~15 (with a maximum S/N of ~29 for the methyl sites).

A similar 20.5 h spectrum of the antibiotic erythromycin at 95 kHz MAS was also recorded, illustrating the applicability of the approach to samples with inferior sample homogeneity (Figure 6.3b).

6.4 Application to Proteins

As discussed, the potential benefits of conducting experiments on proteins at spinning frequencies of ~100 kHz are numerous. A key consideration for the practicality of experiments at such high MAS rates, however, is the quantity of sample that can be used. Because smaller-diameter rotors are required to achieve these higher spinning frequencies, the available sample volumes also tend to be smaller (*e.g.* 0.7 μL for a 0.8 mm rotor vs. 1.7 μL for a 1.3 mm rotor). However, sensitivity depends on factors other than just sample volume.[318] In particular, smaller receiver coils lead to better S/N per unit mass,[319] compensating somewhat for the overall loss in sample volume. The use of such small-volume rotors at higher spinning frequencies may therefore in fact be preferable

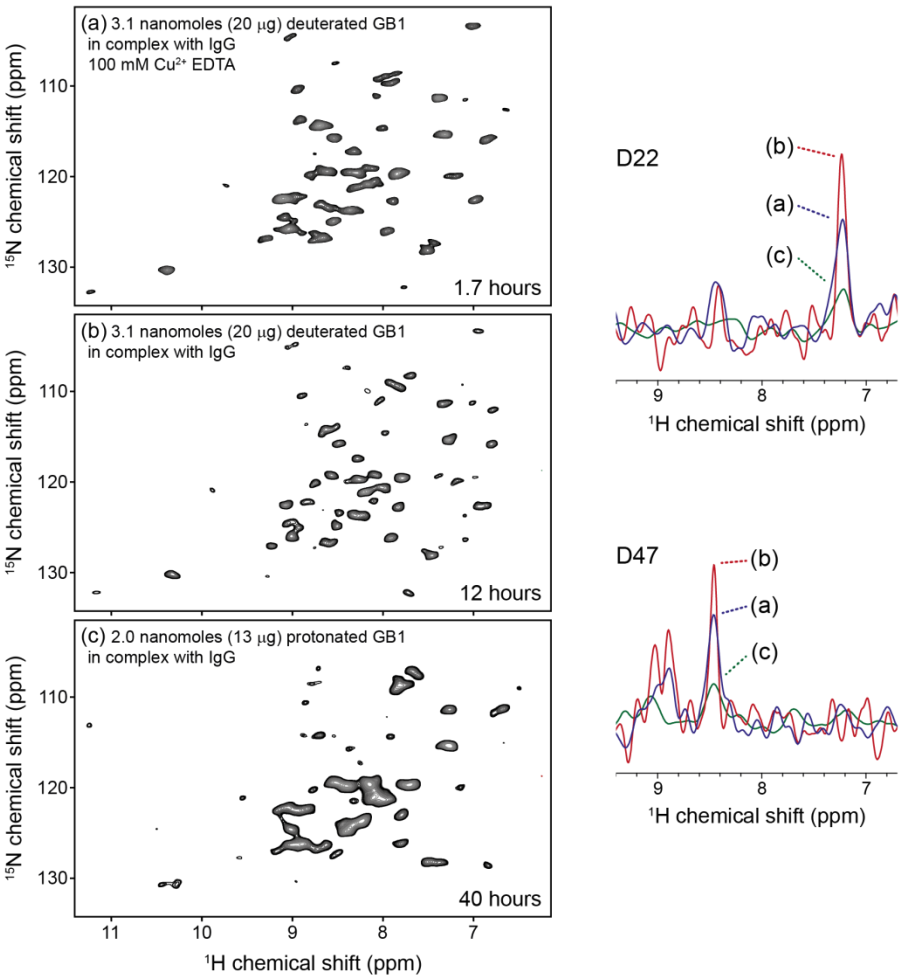

Figure 6.4. ^{15}N-^{1}H 2D correlation spectra of labelled (a, b) perdeuterated and (c) fully protonated GB1 in complexes with unlabelled full-length immunoglobulin (IgG) obtained using a 0.8 mm rotor. Conditions were: (a) ~3.1 nanomoles (20 μg) of GB1 at ν_r = 97.5 kHz, (b) ~3.1 nanomoles (20 μg) of GB1 at ν_r = 95 kHz and (c) ~2 nanomoles (13 μg) of GB1 at ν_r = 100 kHz. The sample in (a) also contained 100 mM Cu^{II}-EDTA to enable faster recycling. Total experimental times for (a-c) were respectively ~1.7 h, ~12 h and ~40 h. Representative 1D slices (peaks for residues D22 and D47) are shown on the right-hand side. All experiments were performed at a ^{1}H Larmor frequency of 850 MHz and a sample temperature of 27 ± 1 °C.

for applications where the sample size is limited (*e.g.* protein samples that are difficult or expensive to produce). Recently, it was shown by Agarwal *et al.* that for crystalline ubiquitin, the ability to use proton detection and the line narrowing afforded offset the limited sample size (sub-milligram) such that 3D structure determination techniques could be successfully applied relatively rapidly. To evaluate the practicality of using such small rotors for non-model samples, we conducted experiments at 90-100 kHz MAS on the 300 kDa GB1-IgG complex examined in Chapter 5, where sensitivity is at a significant premium compared to crystalline proteins. Even at full capacity, a 0.8 mm rotor can only contain a few nanomoles of such a sample.

Figure 6.4a shows a spectrum obtained at 97.5 kHz MAS on perdeuterated GB1 in complex with IgG, containing ~3.1 nanomoles (~20 μg) of GB1 and 100 mM Cu^{II}-EDTA. Figure 6.4b shows a spectrum of a similar sample without paramagnetic doping. The experimental durations for these spectra were (a) ~1.7 h and (b) ~12 h (with average cross-peak S/N ratio of 9 ± 3 and 13 ± 4 respectively), indicating that with a 0.8 mm rotor at 100 kHz MAS the same approach can be used as was presented in Chapter 5, where the larger 1.3 mm rotor was used. Interestingly, some of the cross-peaks for the residues at and near the interacting interfaces, *e.g.* K10 and T18, appear attenuated at 100 kHz MAS (10 μs rotor period) compared to with 60 kHz MAS (16.7 μs rotor period), suggesting the presence of slow, μs-regime motions that interfere more effectively with the averaging at faster MAS. On the other hand, the intensities of other cross-peaks, *e.g.* G41, are enhanced at 100 kHz compared with at 60 kHz.

Sample deuteration helps to narrow proton line widths and can lead to spectra with exceptional resolution and sensitivity. Ideally, however, because of simplicity and cost considerations, one would like to be able to perform measurements on fully protonated proteins. In addition, even for amide protons, greater sensitivity may be attained with fully protonated samples if the proton line widths can be narrowed to a sufficient degree (^{13}C-^{1}H experiments could benefit significantly from the use of fully protonated samples – this possibility is explored in Chapter 9). In light of the above, we attempted to record a ^{15}N-^{1}H 2D correlation spectrum of fully protonated GB1 complex with IgG, at 100 kHz MAS. The result, shown in Figure 6.4c, contains most of the cross-peaks present in the spectrum of the deuterated GB1 complex (Figure 6.4a) but with an additional 30-50 Hz broadening for the visible ^{1}H resonances. A few cross-peaks in the spectrum of fully protonated GB1 complex are broadened beyond detection. The observation of narrow ^{1}H resonances in crystalline GB1 under the same conditions (see §9.1, Figure 9.1) as well as in the perdeuterated complex (Figures 5.1a,b & 6.4a,b) suggests that this additional broadening may be homogeneous in nature and related to incoherent effects of molecular motions rather than coherent effects from incompletely averaged ^{1}H-^{1}H dipolar couplings. In a fully protonated sample and in the presence of sufficiently slow motions, even small-amplitude fluctuations of ^{1}H-^{1}H dipolar couplings between amide and aliphatic protons can result in a non-negligible contribution to ^{1}H T_2 and consequently a broader ^{1}H line width. In a deuterated sample, the main ^{1}H-^{1}H dipolar relaxation comes from the modulation of weaker amide-amide couplings, resulting in a significant attenuation of this effect. The presence of more prominent slow

motions in the complex compared with in our model crystalline sample of GB1 is corroborated by the ~6 times larger bulk ^{15}N $R_{1\rho}$ rates[276] measured, under the same conditions, in the complex compared with the crystal. Consequently, not only coherent averaging of ^{1}H-^{1}H dipolar couplings but also system dynamics are factors that should be taken into account when considering the feasibility of ^{1}H-detected experiments in proteins. Obviously, this factor will be strongly system-dependent.

6.5 Conclusions

In summary, it has been shown that under conditions of 80-100 kHz MAS and high magnetic field, high quality proton spectra can be obtained with ^{1}H line widths on the same order as those achievable with state of the art homonuclear decoupling schemes under optimal conditions. As a result of this, 2D ^{13}C-^{1}H heteronuclear correlation experiments can be performed on natural-abundance small organic molecules at high resolution, benefitting from the large sensitivity enhancement offered by proton detection. This leads to a relatively straightforward and time-efficient approach that is appropriate for the characterisation of small organic molecules at natural abundance (*i.e.* without any isotopic enrichment) in the solid state.

Further to this, ^{1}H detection at 90-100 kHz MAS frequencies enables the recording of 2D spectra of protein samples in quantities as small as 2 nanomoles in a matter of hours. This is particularly applicable to sample-size-limited systems, including (as shown) proteins in large complexes as well as membrane protein which may suffer from low expression yields, enabling quantitative studies of structures and dynamics (as presented in Chapter 9). Although deuteration still yields better ^{1}H resolution at 100 kHz MAS, spinning at such speeds facilitates studies on fully protonated protein samples, which are often far cheaper and easier to produce.

6.6 Experimental Details

All experiments were performed on a Bruker Avance III spectrometer at a proton Larmor frequency of 850 MHz, with a double resonance Samoson 0.8 mm probe.

6.6.1 *β*-L-Asp-L-Ala and Erythromycin Experiments

Powdered natural-abundance *β*-L-Asp-L-Ala dipeptide was purchased from Bachem and packed, without further recrystallisation, into a 0.8 mm rotor. 1D ^{1}H spectra of the dipeptide were obtained over a range of spinning frequencies ($\omega_r/2\pi$) between 15 and 100

kHz (±50 Hz). A spin-echo experiment was employed to improve the spectral base line, with a total echo length (2τ) of 24 times the rotor period. Spin-echo experiments were also run at each spinning frequency to measure, for each proton in the dipeptide, the transverse dephasing time in the absence of inhomogeneous broadening (T_2')[320]. These experiments were repeated in the presence of sample cooling to consider the effects of temperature on the line widths. A Bruker BCU-X cooling unit was used with the target temperature set to -80 °C and the input nitrogen gas pressure set to 0.2 bar at all spinning frequencies (leading to different internal sample temperatures at different spinning frequencies); while the exact sample temperature was not known, with cooling applied we estimate that the sample temperature was ~20-30 °C cooler than without.

2D ^{13}C-^{1}H spectra of β-Asp-Ala and erythromycin were acquired (without cooling) at $\omega_r/2\pi$ = 80 kHz and 95 kHz respectively, with a proton-detected heteronuclear correlation sequence (where the protons act as both the source and detection spins, as in Figure B.6 in Appendix B).[272] At 80 kHz MAS, CP from ^{1}H to ^{13}C (and vice versa) was achieved with 1.5 ms of 65 kHz and 15 kHz irradiation (80 kHz and 15 kHz at 95 kHz MAS) on ^{1}H and ^{13}C respectively, with a tangent shape on ^{1}H to adiabatically sweep[107] through the double-quantum Hartmann-Hahn condition.

For all experiments, the nutation frequencies for the hard 90° and 180° pulses were 100 kHz. Heteronuclear decoupling (slpTPPM[114]) was applied on the ^{13}C channel during ^{1}H acquisition (30 ms), at an amplitude of one quarter of the spinning frequency. The use of such a low-amplitude decoupling scheme at high spinning frequencies benefits both probe longevity and sample integrity when compared with the high-power decoupling used at lower spinning frequencies. 16 scans were collected for 1D experiments, with a recycle delay of 1.5 s. For the 2D experiments 10 kHz WALTZ-16 ^{1}H heteronuclear decoupling was applied during t_1 evolution ($t_{1,max}$=6 ms), which was sampled with a total of 120 increments (for β-Asp-Ala) or 256 increments (erythromycin) with 32 scans (β-Asp-Ala) or 192 scans (erythromycin) each. Recycle delays were 3 s (β-Asp-Ala) and 1.5 s (erythromycin). Quadrature detection was achieved using the States-TPPI method.[122]

Line widths were measured by fitting of the ^{1}H spectra in ACD/NMR Processor. Each line width presented corresponds to the mean result from five independent fits (for which the peak height, width, position and Lorentzian/Gaussian fraction were optimised) of the same spectrum, with varying starting fitting conditions. The standard deviations of the resulting width

measurements were used for the experimental errors. It should be noted that at lower spinning frequencies, these uncertainties were often large due to the unresolved nature of the spectrum (which meant that the same overall spectrum could be recreated with more than one different set of parameters for the eight peaks). T_2' values were found by fitting the decay curves of spin echo experiments (in Origin 8.5). For each curve, each point was obtained by measuring the intensity of the relevant resonance after deconvolution of the spectrum. The spin-echo line width (also known variously as the homogeneous line-width) was calculated as $1/(\pi T_2')$, with errors propagated from fit errors from the T_2' measurements.

6.6.2 Protein Experiments

[^{13}C,^{15}N]-labelled GB1 (T2Q) was produced as described previously.[281] Deuterated and protonated complex samples were produced as above (§5.4).[15] A Bruker BCU-X cooling unit was used to regulate the internal sample temperature to 27 ± 1 °C (measured from the chemical shift of water with respect to DSS[282]). These conditions were achieved by using a nitrogen gas flow of 670-1070 L/h, with the required flow ultimately dependent on the precise pressures required to spin the rotors, which varied slightly from sample to sample.

^{15}N-^{1}H and 2D correlation spectra were recorded using a proton-detected heteronuclear correlation sequence (Figure 3.3d). Double-quantum CP contact times were 1 ms (^{1}H-^{15}N) and 0.4 ms (^{15}N-^{1}H), and 1 ms (^{1}H-^{13}C) and 0.2 ms (^{13}C-^{1}H). Total durations of the ^{15}N-^{1}H experiments were ~1.7 h (Figure 6.4a; 72 t_1 increments, recycle delay of 0.5 s), ~12 h (Figure 6.4b; 60 t_1 increments, recycle delay of 1.5 s) and ~40 h (Figure 6.4c; 30 t_1 increments, recycle delay of 2 s).

In all experiments, hard pulses were applied at nutation frequencies of 100 kHz (^{1}H) or 83.3 kHz (^{15}N). 10 kHz WALTZ-16 heteronuclear decoupling was applied to ^{1}H during ^{15}N evolution, and to ^{15}N during direct ^{1}H acquisition, while quadrature detection was achieved using the States-TPPI method.[122] Suppression of the water signal was achieved by saturation with 200 ms of slpTPPM ^{1}H decoupling[114] applied on-resonance with the water signal at an amplitude of ¼ of the MAS frequency.

7

MAS-NMR Relaxation Methods for Characterising the Dynamics of Proteins

NMR is an ideal technique for characterising protein dynamics, offering a wealth of atomic-resolution information on almost the entire range of time scales that protein motions occur on. One of the most powerful methods for probing dynamics, in both solution and in the solid state, is nuclear relaxation. Below, in preparation for the final three results chapters, we review current relaxation methods for the characterisation of protein dynamics in the solid state, where the lack of overall molecular tumbling presents numerous experimental hurdles but ultimately brings about significant advantages in the range of motional time scales accessible.

7.1 Introduction

As discussed in §2.3, NMR relaxation experiments involve following the return of nuclear states back to equilibrium, the rate of which is directly related to the motions that they undergo through spectral densities. Much of the appeal of such experiments is based on the fact that *quantitative* amplitudes and time scales of motion can be obtained at the same time. Moreover, since the expressions for different relaxation rates (*e.g.* spin-lattice, spin-spin) involve different terms that include spectral densities evaluated at different frequencies, a variety of relaxation measurements can be used to probe motions across a huge range of time scales, from picoseconds all the way to microseconds and beyond. For these reasons, relaxation experiments are widely used in solution,[321] and such has been their success that, naturally, it has been desirable to develop and apply analogous methods in the solid state, especially in light of the great number of systems that are difficult to study in solution.

The lack of overall tumbling in the solid state presents many challenges for the measurement of relaxation rates. In particular, relaxation experiments in the solid state must be carefully designed to circumvent the effects of coherent processes, which arise

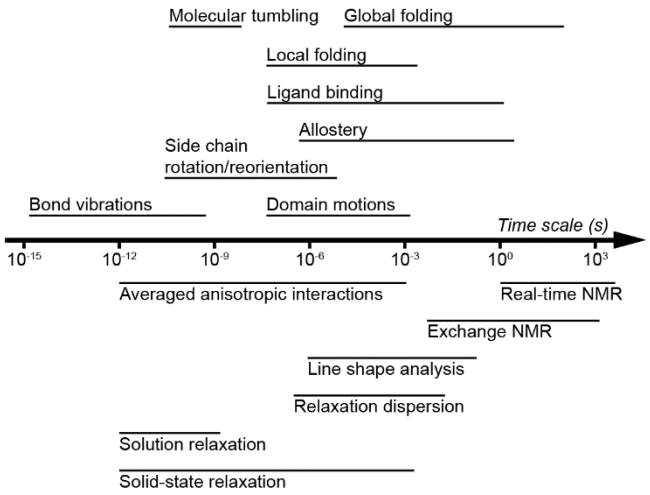

Figure 7.1. Examples of dynamic processes of proteins and the time scales they commonly occur on, along with NMR dynamic probes and the motional time scales they are sensitive to.

from anisotropic interactions that are not completely averaged by MAS. On the other hand, the same lack of tumbling brings its own advantages, namely that the entire time scale window of molecular dynamics is accessible (see Figure 7.1). This is in contrast to in solution, where the correlation time of the overall tumbling effectively represents an upper limit of what can be probed via standard relaxation experiments.[xiii] The reasons for this are explored in §7.6.

Before describing current SSNMR relaxation techniques, it is of course important to remark that relaxation methods are far from alone in offering information about dynamics. For example, a common strategy in solids is to identify motions based on their partial averaging effect upon anisotropic interactions. In particular, measured values of one-bond dipolar couplings (*e.g.* N-H) and ^{2}H quadrupolar couplings can directly yield quantitative motional amplitudes, albeit without specific time scales – such measurements report on motions occurring on all time scales up to the inverse of the strength of the interaction (in Hz). The amplitudes are expressed in the form of order parameters, S^2, equal to the ratio of the measured interaction strength to its calculated strength in the static limit, and running from 0 (unrestricted motion) to 1 (rigid limit). Slow conformational changes may be probed by "centreband-only detection of exchange" (CODEX) experiments,[323] in which dephasing caused by reorientations of CSA or dipolar tensors is monitored, while in some cases the presence of chemical

[xiii] Alternative methods for accessing these motions in solution do exist and are commonly used,[322] but they cannot give detailed information pertaining to both their amplitudes and time scales in the same manner.

exchange may also directly identified simply by observing the broadening of certain resonances. In general, dynamics occurring at rates comparable to the frequencies of MAS and/or decoupling interfere with these processes, causing broadening. Particularly mobile sites may also be highlighted in ^{1}H-^{15}N and ^{1}H-^{13}C "insensitive nuclei enhanced by polarisation transfer" (INEPT) experiments, where severe motional averaging extends coherence lifetimes and hence improves the efficiency of J-coupling-based INEPT transfer.[324]

By measuring a number of different parameters, a more complete dynamic picture can be deduced, with information about different time scales of motion inferred from the sensitivity of the various techniques to those time scales. For example, in an extensive study of the dynamics of reassembled thioredoxin, Yang *et al.* measured dipolar order parameters, ^{15}N CSA, ^{15}N T_1 relaxation rates in addition to signal intensities in temperature-dependent NCA experiments to identify motions occurring across a wide range of time scales.[325] However, compared to comprehensive relaxation studies (in which multiple relaxation parameters are measured and fitted), the depth of quantitative information available from the above techniques is limited. It is worth remarking, though, that in many cases the value of information gained from SSNMR relaxation studies may be maximised by combining it with findings from other SSNMR approaches (as well as from altogether different techniques such as solution NMR, neutron scattering and molecular dynamics (MD) simulations, amongst others[322,326-330]).[331] For instance, directly measured N-H order parameters can act as an important constraint of the overall order parameter during quantitative analysis of ^{15}N relaxation data.[332]

While reasonable questions do exist over whether the dynamics in solid samples truly reflect those that would be found in solution (the native environment for many proteins), mounting evidence suggests that, provided samples are hydrated properly, key dynamic features are preserved between the two states.[330,333-335] However, as explored in Chapter 8, the molecular environment of a protein (*e.g.* crystal packing, complex formation) can have dramatic effects on its motions,[336] and as such care may have to be taken when extrapolating to a biological context.

7.2 Relaxation Methods

The selection of relaxation experiments that can be conducted for dynamic studies of proteins is naturally defined by the types of nuclei that are present in, or can be introduced into, the samples being studied. In practice this means, with suitable sample

preparation[149], primarily ^{1}H, ^{2}H, ^{13}C and ^{15}N studies can be contemplated, and of these the latter three are regularly used to probe protein motions. For reasons that will be discussed, ^{1}H relaxation experiments remain largely problematic and procedures for site-specific measurements that can reliably yield motional amplitudes and time scales are yet to be developed. Deuterium (^{2}H) has been commonly used as a probe for studying local dynamics of selectively labelled proteins through the analysis of dipolar and quadrupolar couplings and the line narrowing that motions cause, as well as through the measurement of various relaxation parameters.[155,261] However, the requirement of MAS for achieving resolution in non-selectively labelled biological samples often renders ^{2}H experiments unattractive. Among other issues, MAS serves to enhance ^{2}H-^{2}H spin diffusion,[337] removing much of the site-specificity that constitutes one of the primary advantages of NMR-based dynamics approaches. The focus will therefore herein lie upon ^{15}N and ^{13}C relaxation approaches, which, thanks to recent developments in technology and methodology, can provide widespread dynamic information under the MAS conditions that dominate current studies.

7.3 Picosecond-Nanosecond Motions: Spin-Lattice Relaxation

Measurements of spin-lattice relaxation are particularly sensitive to motions occurring on time scales on the order of the inverse of the nuclear Larmor frequency (see figure 2.9c), *i.e.* hundreds of picoseconds to tens of nanoseconds. Assuming that sufficient resolution and sensitivity can be obtained, a primary obstacle for measuring T_1 relaxation in a site-specific manner in proteins is spin-diffusion[xiv], where magnetisation is transferred between nuclei via coherent mechanisms such as dipolar couplings.[193,338,339] If this transfer occurs sufficiently quickly compared with the relaxation times, then the measured R_1 relaxation rates will reflect an average over several different sites. In the most extreme cases this eliminates any site-specificity and renders the data useless for quantitative analysis.

Because spin diffusion in the solid state is driven by coherent processes, its effects may be reduced and eventually removed by suitable experimental design. The most efficient form of spin diffusion in proteins is proton-driven spin diffusion (PDSD), which is mediated by ^{1}H-^{15}N/^{1}H-^{13}C and ^{15}N-^{15}N/^{13}C-^{13}C dipolar couplings. These couplings can be reduced, and hence the effects of PDSD can be lessened, by (a)

[xiv] Note that in the solution state, the term spin diffusion is used to describe a distinctly different phenomenon whereby polarisation is transferred via incoherent cross-relaxation.

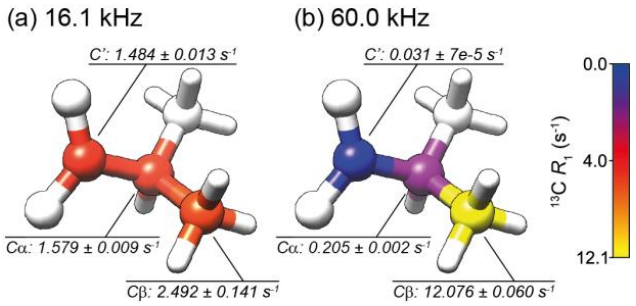

Figure 7.2. Measured ^{13}C longitudinal magnetisation decay rates (R_1) in [U-^{13}C,^{15}N]Ala at (a) 16.1 kHz and (b) 60.0 kHz MAS and at 900 MHz ^{1}H Larmor frequency. At the lower spinning frequency, measured decay rates are homogenised over the carbon sites due to spin diffusion, disguising the true ^{13}C R_1 values. Produced from data in Ref. 114.

increasing the MAS frequency, (b) exploiting isotopic labelling or sample deuteration or (c) by applying r.f. irradiation. The first two of these approaches are generally feasible, but averaging by r.f. is ordinarily unsuitable, as the nutation frequencies required are usually too high for equipment and sample integrity. Application of insufficiently high r.f. irradiation may in fact encourage spin diffusion, as is utilised in the case of the DARR recoupling technique.[197]

For amide nitrogen nuclei, PDSD is relatively slow and its effects can be overcome at fairly moderate spinning frequencies.[339] For this reason, in the solid state ^{15}N spin-lattice relaxation measurements were some of the first to be adopted for quantitative description of widespread site-specific dynamics.[340] Site-specific ^{15}N R_1 measurements can be successfully carried out in fully protonated proteins at spinning frequencies of ν_r >20 kHz, while in the 10-20 kHz MAS range the measured rates are still somewhat affected by PDSD unless deuteration is used.[338,339,341] In the case of ^{13}C, stronger ^{1}H-^{13}C and ^{13}C-^{13}C couplings (compared with ^{1}H-^{15}N and ^{15}N-^{15}N) make for much faster PDSD rates and so the averaging necessary to overcome its effects is much greater. Lewandowski *et al.* showed in 2010 that for fully protonated uniformly labelled proteins, site-specific ^{13}C' R_1 rates can be measured reliably under conditions of $\nu_r \geq 60$ kHz (see Figure 7.2),[114] although for side-chain measurements PDSD may still need to be taken into account for quantitative analyses.

As mentioned, PDSD rates are further reduced in extensively deuterated samples where the dense proton network is diluted,[341] although in the case of ^{13}C, fast MAS (>50 kHz) is still likely to be necessary to remove all its effects, as deuteration does not remove the main PDSD-mediating ^{13}C-^{13}C dipolar couplings. A somewhat more effective approach, explored in Chapter 9, could be to combine alternately labelled samples (*e.g.*

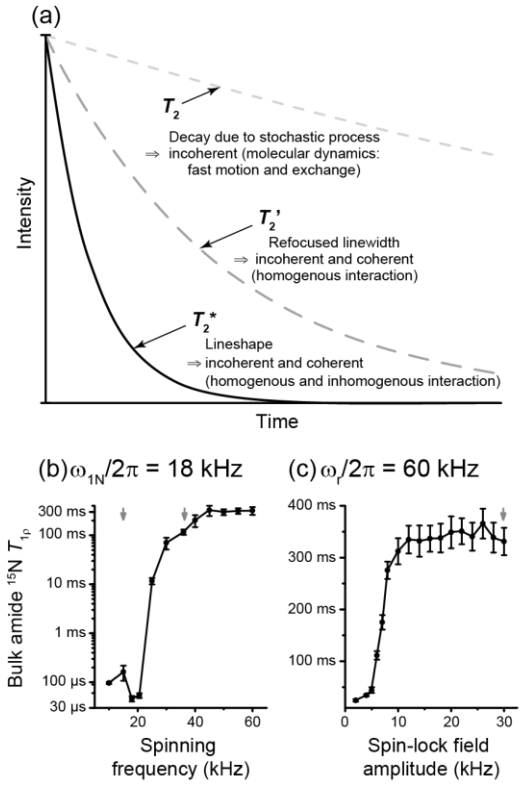

Figure 7.3. (a) Scheme illustrating different types of characteristic coherence decay times in solid samples (adapted from Ref. 94). Experiments must be carefully designed in order to access incoherent T_2 (=$1/R_2$) without contributions from coherent processes. (b,c) Measured bulk amide ^{15}N $T_{1\rho}$ rates in fully protonated [U-^{13}C,^{15}N]GB1 as a function of spinning frequency (b) and spin-lock nutation frequency (c) at 500 MHz field (reproduced from Ref. 276. Grey arrows indicate rotary resonance (left panels) and HORROR (right panels) conditions, where coherent interactions are to an extent reintroduced.

[1,3-^{13}C] and [2-^{13}C]) with fast MAS. Owing to the strength of ^{1}H-^{1}H dipolar couplings, ^{1}H R_1 rates cannot currently be obtained without severe spin diffusion effects.

7.4 Nanosecond-Millisecond Motions: Spin-Spin Relaxation and Spin-Lattice Relaxation in the Rotating Frame

In solution NMR, overall molecular tumbling makes it difficult to extract amplitudes and time scales of internal protein motions occurring on time scales equal to or longer than the correlation time for that tumbling. In solids, the absence of this limitation renders information about these motions accessible. While spin-lattice relaxation experiments are most sensitive to ps-ns motions, measurements of spin-spin relaxation (R_2) are sensitive to motions occurring on time scales of nanoseconds and longer, which coincide with the correlation times of such important processes as folding, ligand binding and enzymatic catalysis (see Figure 7.1). In practice, however, measuring R_2 relaxation rates in solid

proteins is problematic owing to the presence of coherent effects (from dipolar couplings), whose contributions dominate the rate of decay of transverse magnetisation in a traditional spin-echo experiment (R_2'). Measuring the incoherent R_2 decay must be therefore achieved by either designing the experiment such that the coherent contributions can be taken into account or ignored, or by attempting to directly average the coherent interactions that contribute to coherence decay.

The largest coherent contribution to the decay of transverse magnetisation is ^{1}H-^{1}H dipolar couplings, the effects of which may be somewhat reduced through extensive sample deuteration. Under currently available experimental conditions, however, contributions from coherent processes are still not negligible, and so R_2' rates measured in proteins may only be used as qualitative indicators of dynamics. For perspective, even at ν_r=60 kHz, in a solid perdeuterated protein coherent contributions may easily account for more than 75 % of the measured average R_2' rate.[276] Despite this fact, deuteration is still requisite for a number of other, quantitative methods by virtue of the long coherence lifetimes it affords. For example, Chevelkov *et al.* presented an approach whereby dynamic information is extracted from the difference between R_2' rates of the two components of the J_{NH} doublet.[334] Whereas the coherent contribution to each component is the same (to a good approximation), their overall rates of decay are different due to incoherent cross-correlated relaxation. Another approach was suggested by Tollinger *et al.* in which the difference between the decays of zero- and double-quantum coherences are measured.[342]

An alternative to measuring R_2 is measuring spin-lattice relaxation in the rotating frame, $R_{1\rho}$, *i.e.* the rate of transverse magnetisation decay under spin-lock irradiation.[343,344] $R_{1\rho}$ rates are sensitive to motions occurring on time scales of the inverse of the spin-lock nutation frequency (usually on the order of tens of kHz) through the $J(\omega_1)$ spectral density term in its expression (see §2.3.7; R_2 is sensitive to similarly slow motions through its $J(0)$ term). The spin-lock pulse also helps to decouple the coherent contribution to the decay, in addition to any exchange contributions. In fully protonated proteins in the solid state, MAS frequencies of >45 kHz and spin-lock nutation frequencies of >10 kHz can suppress the coherent contribution to ^{15}N $R_{1\rho}$ rates to a negligible level, allowing for the reliable extraction of amplitudes and time scales of motion. Since being demonstrated on microcrystalline GB1,[276] this approach has been applied to the microcrystalline enzyme superoxide dismutase (SOD)[55] and the transmembrane protein *Anabaena* Sensory Rhodopsin.[345] In Chapter 10 this methodology is extended to carbonyl ^{13}C sites. Again,

however, ^{1}H $R_{1\rho}$ rates measured under currently available experimental conditions are still strongly influenced by coherent effects and can at best only give qualitative information about amplitudes and time scales (although activation energies can still be extracted by conducting measurements at different temperatures[346,347]).

As in the case of R_1 experiments, perdeuteration can be used to reduce the coherent effects further, and hence in many cases the experimental requirements (MAS/r.f. frequencies) may be lowered.[348-350] However, a major advantage of the $R_{1\rho}$ method lies in its applicability to fully protonated samples,[276] which in general are easier and much less costly to produce. Figures 7.34b,c show how the measured ^{15}N $T_{1\rho}$ rates in fully protonated GB1 plateau with increasing MAS and spin-lock nutation frequencies, as the coherent contributions are averaged. It should be noted that $R_{1\rho}$ rates are in general ν_r-dependent[147] and above a certain MAS frequency (when the coherent contribution is completely suppressed) this behaviour could also be in part due to the presence of small-amplitude motions in the μs regime.[351]

7.5 Microsecond-Millisecond Exchange Processes: Relaxation Dispersion

In solution, relaxation dispersion experiments are used to characterise conformational exchange processes that occur on the μs-ms time scale. In the popular Carr-Purcell-Meiboom-Gill (CPMG) dispersion experiment, for example, the effective rate of single-quantum coherence decay, $R_{2,\text{eff}}$, is measured as a function of the repetition rate of refocusing 180° pulses, ν_{CPMG}, and the resulting dispersion profile provides information about interconversion rates and relative populations of excited states.[322] The pulse sequence is effectively a train of spin-echo elements, which act to decouple exchange contributions to the magnetisation decay by refocusing the chemical shift – the higher the repetition rate of the pulses, the more effective this decoupling. Sensitivity to a given time scale of motion is defined by the inverse of the effective r.f. field generated by the refocusing pulses, usually around 25-1000 Hz. Unsurprisingly, given our discussion about R_2, these measurements are more difficult in the solid state, since under normal circumstances the presence of coherent interactions all but precludes reliable measurement of incoherent transverse magnetisation decay. Nevertheless, Tollinger *et al.* recently showed that under conditions of extensive sample deuteration (protonation at only 20% of exchangeable sites) and fast MAS (≥45 kHz), the obtained (^{15}N) dispersion

profiles, while still influenced by coherent effects, are dominated by conformational exchange processes.[342]

Further to this, Ma *et al.* adapted ^{15}N $R_{1\rho}$ relaxation dispersion for use in solids, again by employing sample deuteration and MAS frequencies of ≥40 kHz.[350] These experiments are highly complementary to CPMG dispersion, as the higher effective fields lead to a sensitivity to faster exchange processes. Potentially, the dynamic ranges that the two experiments are sensitive to can overlap, although this is limited by the lowest nutation frequency that can reliably be used for the $R_{1\rho}$ experiments (*i.e.* where the coherent contributions are still suppressed sufficiently). This is highly dependent on the MAS frequency, and as such the faster spinning rates afforded by sub-mm diameter rotors[352] may in the near future prove vital (especially for fully protonated samples).

7.6 Quantitative Analysis of Relaxation Rates

If measured relaxation rates can be isolated from coherent contributions, then they may be analysed quantitatively through their relation to spectral densities (see §2.3). Spectral densities are related to random motions through amplitudes of motions and correlation times, although the exact relation depends on the model used. Currently, the models used to analyse solid-state data are derived from solution methods. In the latter field, a number of different models have been proposed, including Gaussian axial fluctuations (GAF)[353] and diffusion in a cone[280], but it is common to avoid choosing a "model" altogether and simply assume an exponentially decaying correlation function. This type of analysis, known as the "model-free" approach, was first proposed by Lipari and Szabo in 1982, and extraction of $S^2$and τ is achieved by fitting of the experimental data using the expressions for relaxation rates given in §§2.3.5-2.3.7 (*e.g.* by χ^2 minimisation – see Chapters 8 and 10).[33,34] The correlation function is parameterised by an amplitude (order parameter, S^2) and a time scale (τ):

$$C_{internal}(\tau) = S^2 + (1 - S^2)\mathrm{e}^{-t/\tau}\,. \tag{7.1}$$

In liquids, the correlation function of the overall tumbling must also be taken into account:

$$C_{overall}(\tau) = \mathrm{e}^{-t/\tau_R} \tag{7.2}$$

where the correlation time for the overall motion, τ_R, is related to the diffusion coefficient of the molecule. The total correlation time is the product of $C_{internal}$ and $C_{overall}$, which gives rise to a Lorentzian spectral density of the form:

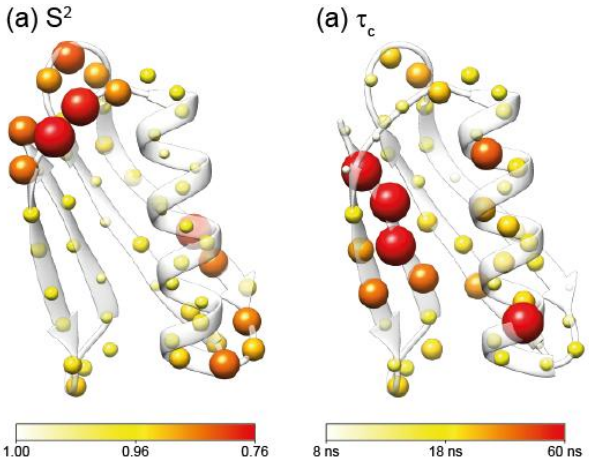

Figure 7.4. Site-specific (a) order parameters, S^2, and (b) time scales, τ, for motions of amide ^{15}N in hydrated crystalline GB1 projected onto the crystal structure of the molecule, calculated using a simple model-free (SMF) analysis of ^{15}N R_1 and $R_{1\rho}$ relaxation rates at 600 and 850 MHz field. High amplitude motions can be seen particularly in the loop regions, while the β4 strand is characterised by especially slow motions. It should be noted that the internal protein motions would likely be better described by a two- (or more) time scale analysis (see Chapter 10).

$$J(\omega) = (1 - S^2)\frac{\tau'}{1 + \omega^2\tau'^2} + S^2\frac{\tau_R}{1 + \omega^2\tau_R{}^2} \tag{7.3}$$

where $\frac{1}{\tau'} = \frac{1}{\tau} + \frac{1}{\tau_R}$. This type of analysis works well if the correlation time of the internal motion is much smaller than that of the overall tumbling, but if they are similar or $\tau_R < \tau$ then $J(\omega)$ becomes dominated by contributions from the overall tumbling and the internal motions are effectively masked. Solution-state relaxation studies of this type therefore cannot access motions slower than a few ns in proteins.

In solids, this tumbling does not occur and the spectral density is therefore simply

$$J(\omega) = (1 - S^2)\frac{\tau}{1 + \omega^2\tau^2} \tag{7.4}$$

with no scaling from overall rotation of the molecule and hence no "blind spot" in the dynamic range of protein motions. For site-specific measurements, a quantitative analysis can be performed for individual nuclei within a molecule and the resulting dynamic parameters mapped onto its structure (*e.g.* see Figure 7.4), potentially revealing correlations with secondary structure elements or active sites (for example). The more independent measurements that can be conducted (*e.g.* R_1 and $R_{1\rho}$ at different fields), the more frequencies the spectral density can be sampled at and hence the more reliably the

dynamic parameters can be determined. Note that in actuality, relaxation in the solid state is generally non-exponential owing to the dependence of relaxation rates on crystallite orientation with respect to the magnetic field.[354] This behaviour can be explicitly taken into account in the analysis,[280] although often in practice (in the cases considered so far) the deviations from monoexponential behaviour are small and hence only negligible errors are incurred in the calculation of order parameters and time scales if it is neglected.[355,356]

In general, protein motions can occur on multiple time scales, and in many cases a single time scale model is insufficient for effectively describing the potentially multiple-time scale backbone motions of proteins.[329,332,351,356,357] To better take into account the more complex modes of motion that occur in proteins, the model-free analysis can be modified for the inclusion of two or more time scales, giving rise to the so-called extended model-free (EMF) analysis.[358,359] With motions occurring on two distinct time scales, the solid-state EMF spectral density modifies to:[332]

$$J(\omega) = \left(1 - S_f^2\right)\frac{\tau_f}{1 + \left(\omega\tau_f\right)^2} + S_f^2(1 - S_s^2)\frac{\tau_s}{1 + (\omega\tau_s)^2} \tag{7.5}$$

where τ_i is the correlation time and S_i^2 order parameters for the motion with indices *i*=*f* and *i*=*s* indicating fast and slow motion, respectively. For clarity, in all that follows the single-time scale model-free analysis is referred to as the "simple model-free" (SMF) analysis. In principal there is no limit on the number of time scales that can be invoked; similar extensions to 3 or more component models have also been considered and applied to necessarily sizeable data sets.[351] However, whilst it is conceptually straightforward to simply add more time scales into the analysis, in practice the addition of more parameters demands the collection of an ever greater number of independent data sets to constrain the model.

Measurements of relaxation at different temperatures can also be used to find activation energies for motions. For example, the formidable ability of SSNMR relaxation experiments to piece together a complete, wide-ranging and coherent picture of the entire hierarchy of protein dynamics was exemplified in a recent study by Lewandowski *et al.*, in which temperature-dependent relaxation measurements were used to identify the various modes of motion occurring in GB1 and their activation energies.[260] Activation energies may further be added into model-free (or other) fitting procedures.[351]

Among the most comprehensive SSNMR protein dynamics studies to date are those of microcrystalline ubiquitin by Schanda *et al.* (where up to six relaxation rates in addition to dipolar couplings were measured for each backbone ^{15}N site)[356,360] and of microcrystalline SH3 domain of alpha-spectrin by Zinkevich *et al.* (where dipolar couplings and up to eleven relaxation rates – including rates measured at different temperatures – were measured per ^{15}N nucleus).[351] Chapter 10 of this work culminates in a quantitative analysis of the dynamics of microcrystalline GB1 that utilises up to eight ^{13}C' and ^{15}N relaxation parameters and ^{15}N-^{1}H dipolar couplings per peptide plane.[357]

As it becomes clearer that many-parameter models/analyses are a requirement for an effective description of protein dynamics, the development of experiments that can provide further independent data sets remains one of the primary challenges facing SSNMR dynamics studies of proteins. However, considering the unique potential of such studies to so comprehensively characterise protein motions across essentially the entire dynamic range, it is clearly one that is worth addressing. In light of this, Chapters 8, 9 and 10 are dedicated to the exploring new probes of protein dynamics to be used as further independent measurements for quantitative analyses.

8

SLOW PROTEIN DYNAMICS IN DIFFERENT MOLECULAR ENVIRONMENTS: >300 KDA COMPLEX VERSUS CRYSTAL

Abstract

Understanding the dynamics of interacting proteins is a crucial step towards comprehensively describing many biophysical processes. Here, we show that solid-state NMR enables the study of the backbone dynamics in typically intractable protein complexes of hundreds of kDa. Site-specific ^{15}N $R_{1\rho}$ relaxation rate measurements in a precipitated >300 kDa complex of GB1 with full-length human immunoglobulin are presented. These are compared to ^{15}N $R_{1\rho}$ and ^{15}N $R_{1\rho}$ relaxation dispersion measurements in crystalline GB1, revealing that, while many of the dynamic features of the protein are conserved between the two environments, there is an overall greater prevalence of slow (ns-ms) motions in the complex.

(Adapted from Lamley, J. M.; Öster, C.; Stevens, R. A.; Lewandowski, J. R. *Angewandte Chemie International Edition* **2015**, *54*, 15374)

8.1 Introduction

Protein dynamics are fundamental to a wide range of biophysical processes. Often, the functional mechanisms that underlie these processes rely on the interactions of proteins with other molecules. As such, characterization of the dynamics of complexed proteins is required to fully understand them. In general, the local molecular environment of a protein potentially has significant effects upon motions that may be relevant to its function.[361] NMR can offer access to atomic-resolution details about these dynamics,[325,362] but in solution, proteins and protein complexes above a few tens of kDa represent a severe challenge owing to acute line broadening due to slow molecular tumbling. Because this size-dependent broadening does not occur in solids, SSNMR offers a chance to study the motions of biomolecules of several hundred kDa and beyond, provided

intrinsic challenges of sensitivity and resolution can be successfully addressed.[14,16,83,84,88,259,363,364]

In Chapter 5, it was demonstrated that high quality spectra could be obtained on precipitated large protein complexes, by using an approach based on a combination of high field, fast (60-100 kHz) MAS and optional sample deuteration.[15] Notably, this methodology is applicable to a general case of systems with little or no overall symmetry, and samples containing only a few nanomoles of protein can yield spectra with the sensitivity and resolution suitable for performing quantitative measurements of structure and dynamics. In the following, we capitalise on this capability in order to, for the first time, use SSNMR to conduct widespread site-specific relaxation measurements in a large (>300 kDa) protein-antibody complex. Comparison of the relaxation rates measured under identical experimental conditions, and determination of residues undergoing chemical exchange on the μs-time scale, for the same protein in a complex and a crystal enables us to shed light on the relationship between protein dynamics and intermolecular interactions.

We consider the same complex of the B1 domain of protein G (GB1, ~6 kDa) with full-length human immunoglobulin (IgG, ~150 kDa). Aside from forming this >300 kDa precipitated complex, GB1 on its own also forms crystals that, owing to their high level of structural order, yield well-resolved SSNMR spectra, a property that has been exploited in numerous method development studies.[51,104,114,236,276,365-367] By measuring the same parameters for GB1 crystals and GB1 in a complex, we are in a unique position to compare motions of the same protein in these two different molecular environments. Since comparison of C^{α} chemical shifts indicates that the backbone conformation of GB1 is very similar in both types of assemblies,[15] we can gain insights into the influence of different intermolecular interactions and packing on the overall protein dynamics.

In contrast to in solution, in the solid state the absence of overall tumbling enables access to motions in the full range from ps to ms (or at least μs) through NMR relaxation measurements. Motions on ns-μs time scale potentially include whole domain motions and large-scale conformational changes, and as such are particularly pertinent in the context of functional protein-protein interactions. As discussed, spin-lattice relaxation in the rotating frame, $R_{1\rho}$, is a sensitive probe of these slow motions.[276,348]

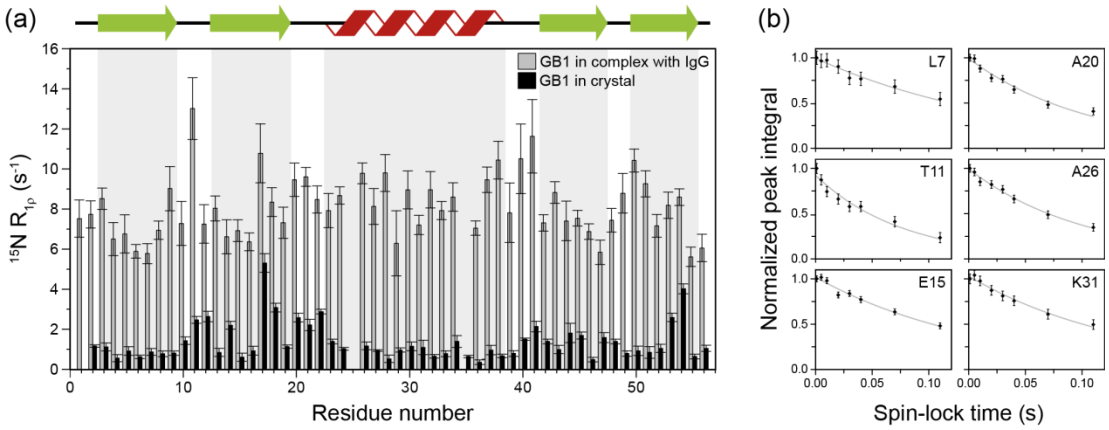

Figure 8.1. (a) ^{15}N $R_{1\rho}$ measurements for deuterated (100% proton back-exchanged [U-^{13}C,^{15}N]) GB1 in complex with IgG (grey) and crystal (black) plotted against residue number. Experiments were performed at 850 MHz spectrometer, 60 kHz MAS and with a 17 kHz spin-lock field. Sample temperature was 27 °C as calculated from the chemical shift of water protons.[282] (b) Example ^{15}N $R_{1\rho}$ relaxation curves for the GB1 in complex with IgG. Each spectrum in the relaxation series on the complex took ~10 h to record.

8.2 Results and Discussion

We first measured backbone ^{15}N $R_{1\rho}$ rates at 60 kHz MAS for 100% back-exchanged deuterated [U-^{13}C,^{15}N]GB1 in crystal and in complex with full-length IgG. Both samples were prepared in 50 mM phosphate buffer at pH 5.5 and the relaxation rates were measured under the same external conditions, including sample temperature (27 °C), magnetic field (850 MHz) and spin-lock nutation frequency (17 kHz). All samples were fully hydrated with bulk solvent being present in the rotors. Assigned ^{15}N-^{1}H spectra of the two samples can be found in Figures C.1 (Appendix C) and 5.6.

Figure 8.1a shows the measured ^{15}N $R_{1\rho}$ rates for GB1 in both environments as a function of the residue number (complex rates in grey, crystal rates in black). Six example $R_{1\rho}$ decay curves for GB1 in the complex are shown in Figure 8.1b. What is immediately striking is that the rates in the complex are, on average, ~6 times higher than those in the crystal (mean $R_{1\rho}$ values of 8.1 s^{-1} and 1.4 s^{-1} respectively), indicating generally more prominent slow motions throughout the complex. The bulk ^{15}N R_1 measured in the complex (under the same conditions), however, is ~0.03 s^{-1}, which is approximately two times smaller than in the crystal. This implies that motions in the complexed GB1 are not simply "amplified" across all time scales compared to in crystalline GB1, as this scenario would result in similarly increased R_1 rates. We can therefore deduce that the motions dominating the ^{15}N $R_{1\rho}$ rates in the complex must be generally slower, rather than simply

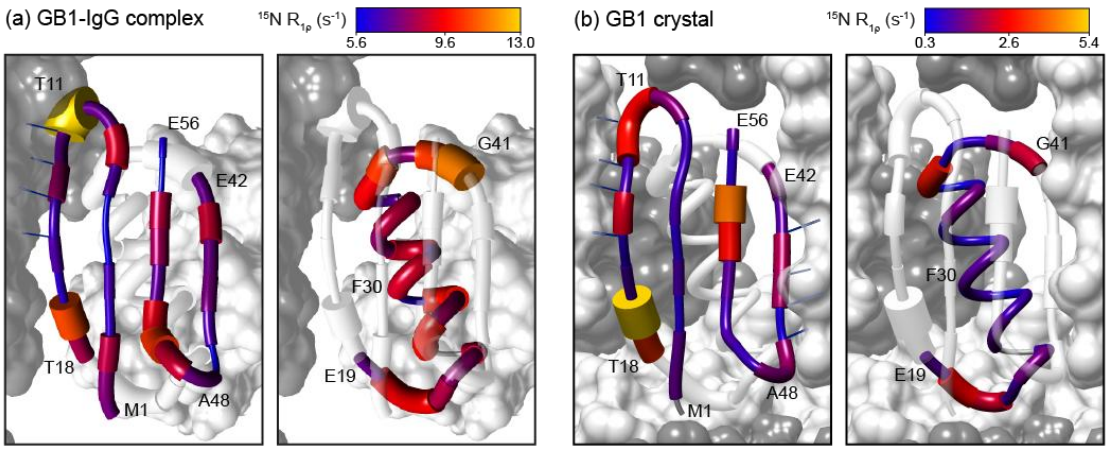

Figure 8.2. Measured ^{15}N $R_{1\varrho}$ rates for (a) GB1 in complex with IgG and (b) crystalline GB1, projected onto the structure of the protein. Left-hand panels show the β-sheet and loops 1 and 4, while the right-hand panels show the helix and loops 2 and 3. The radii and colouring of the tubes reflect the magnitude of the measured relaxation rates. Rates not shown due to missing or unassigned resonances are shown in grey (T25 and N35 in the complex, M1 in the crystal). Intermolecular hydrogen bonds at the edges of the β-sheet are shown as dark blue lines extending to the neighbouring molecule.

of larger amplitude, as $R_{1\rho}$ measurements are far more sensitive to slow motions than R_1 (see Figure 2.9c).

Aside from the overall offset between the rates in the complex and in the crystal, the two sets of data are in many ways similar. In both molecular environments, elevated rates are observed in flexible loops, while generally lower rates can be found towards the centres of the β-strands. In fact, the general relative pattern of relaxation rates along the backbone seems to be largely conserved in the complex in many areas, implying that generally similar modes of motion within the domain are taking place in either molecular environment. Further interpretation is aided by projecting the data onto the backbone structure of GB1 as in Figure 8.2, where the measured relaxation rates are expressed through both the radius and the colour of the tube for each residue. To facilitate direct comparison between the two different molecular environments, the radii and colours are scaled such that the minimum and maximum radii (coloured blue and yellow respectively) correspond approximately to the minimum and maximum relaxation rates in either case.

When the data are viewed this way more similarities are made clear, including higher rates around residues T17-T18 and T53-V54, and lower rates at various points in the β-sheet. Scaling in this manner also highlights a number of interesting differences: in the complex, the ^{15}N $R_{1\rho}$ rates for residues Y3 and especially T49-T51 appear noticeably enhanced relative to rest of the structure. On the other hand, the measured relaxation

rate for L12 appears much lower than might be expected, though this is most likely due to peak overlap with D46, which has a much slower rate of decay. Most notably, whereas in the crystal the ^{15}N $R_{1\rho}$ relaxation rates for the helical residues are generally lower than in much of the rest of the protein, in the complex these rates appear somewhat elevated relative to those across the β-sheet. There are at least two possible explanations for this. The first is that when GB1 is in complex with IgG, the helix undergoes motions of greater amplitude and/or with slower correlation times (relative to the rest of the protein) than in crystal (although larger-amplitude helix motions are unlikely considering, as mentioned, the much smaller measured bulk ^{15}N R_1 rates). Assuming the 2:1 IgG:GB1 model proposed in Chapter 5 (Ref. 15), whereby GB1 is bound to the Fc fragment of one IgG molecule and simultaneously to the Fab fragment of another, it is easy to imagine a situation where the two different binding parts of the IgG molecules exhibit different dynamics, directly influencing the motions of the separate regions of GB1 they are each bound to.

Alternatively, the apparent relative increase of the rates in the helix compared to the rest of the residues may in fact be caused by an anisotropic overall motion of the helix or the entire molecule.[365,368] The primary source of relaxation in the case of amide nitrogen sites is N-H dipolar vector fluctuations. Rotations occurring about an axis parallel to that vector are less effective in inducing ^{15}N relaxation compared to motions perpendicular to it. In this way the measured relaxation rates are affected to a different degree by the motions in different directions.[368,369] In GB1, the helix is oriented such that the N-H vectors within it (which are all approximately aligned with the axis of the helix) lie at a significant angle (~60° or more) to those in the β-sheet (which all point, roughly, across the sheet). A whole-body "rocking" motion about a given axis would hence generate ^{15}N relaxation preferentially in either the β-sheet or the helix (whereas a completely isotropic whole-body motion would enhance the relaxation equally for all residues). Figure C.2 in Appendix C illustrates this idea by showing the simulated effect upon the ^{15}N $R_{1\rho}$ rates in GB1 of an overall anisotropic rocking motion of the molecule about three orthogonal axes.

Of course, the true origin of the differences is likely to be a combination of a number of factors, including, for example, separate anisotropic collective motions (ACMs) of the rigid β-sheet and helix parts of GB1, modified by their intermolecular interactions.[365] A definitive answer to this question cannot be obtained without further measurements, but even using this single set of data it is clear that the molecular

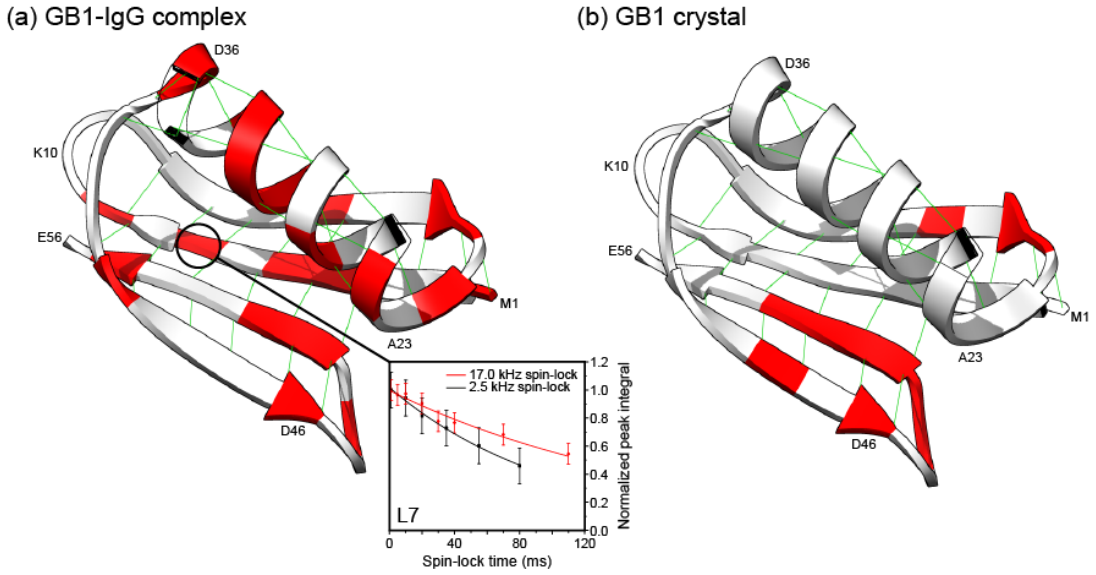

Figure 8.3. Residues clearly exhibiting chemical exchange on the µs time scale (in red) in (a) GB1 in complex with IgG and (b) crystalline GB1 (see Figures C.3 & C.4 in Appendix C for selection criteria). Example decay curves from measurements on the complex are shown in the inset of panel (a). Residues for which no data is available are shown as transparent.

environment and binding of a protein have measurable effects on its slow dynamics.

Conformational exchange processes occurring on a µs-time scale can be further probed, in the solid-state, by conducting $R_{1\rho}$ relaxation dispersion experiments at high MAS frequencies.[350] We first measured relaxation dispersion for 100% back-exchanged deuterated crystalline GB1 (at 50-60 kHz MAS apparently no further dilution of the proton network is required, with coherent contributions being around just 1 s^{-1} at lower spin-lock fields). Clear dispersion is observed for only a handful of residues in crystalline GB1 (see Figure C.3 in Appendix C) suggesting that only these residues undergo µs-range motions. In general, residues undergoing µs-range motions cluster in two regions: parts of β_1, β_2 and the loop connecting them (residues 44, 46, 48-53), and the C-terminal end of β_3 and loop 3 (residues 17, 19-20). To qualitatively search for the presence of chemical exchange in the complex, we repeated our measurements with a spin-lock field of 2.5 kHz and compared them to the measurements obtained using a 17 kHz ^{15}N spin-lock field. Under these conditions, considerably elevated rates were found for many of the GB1 residues, indicative of an exchange contribution to the measured rates (at 17 kHz these exchange contributions are decoupled). Although generally the regions displaying conformational exchange on the µs-time scale in the crystal show similar behaviour in the complex, there are many more such residues in the latter. Interestingly, the residues for which this effect is observed most severely appear to be mostly grouped

at the C-terminal end of the helix and along the β_1 strand (see Figure 8.3) even though these residues are generally "silent" on the same time scale in the crystal. These results confirm that overall slower motions are observed in the complex, particularly in the helix, compared to in the crystal.

8.3 Conclusions

In summary, the results of site-specific ^{15}N $R_{1\rho}$ measurements in a >300 kDa protein complex of deuterated GB1 with full-length human IgG have been presented, which were made possible through the application of proton-detected experiments at high magnetic fields and fast MAS frequencies. This capability has allowed a comparison of the slow (ns-μs range) motions of the protein GB1 in a complex with those of the same molecule in a crystal, where differences in dynamics are attributed to differences in local molecular environment. An overall greater prominence of slow motions, with majority of them being in the μs range, was detected in the complex, where particularly enhanced relaxation rates in the helix also hinted at either an overall anisotropic rocking motion or differential dynamics of the secondary structural elements of the GB1. ^{15}N $R_{1\rho}$ relaxation dispersion on crystalline GB1 showed clear evidence of μs-range motions for only a few residues, suggesting that the dynamics for most sites can be well explained by ps-ns motions (though nothing is known about ms-range motions). In contrast, μs-range conformational exchange processes are evident for many of the residues of GB1 in the complex. The results presented pave the way for the characterization of dynamics in biologically important but sensitivity-limited protein samples, and also show the value of directly probing the dynamics of proteins within functional complexes, where significant dynamic changes may occur compared to the isolated proteins. On the other hand, the fact that many dynamic features were found to be shared between the two different environments suggests that examination of dynamics in "isolated" proteins will remain a key part of overall strategies for characterising biological processes.

8.4 Experimental Details

The deuterated GB1-IgG complex sample was the same as that used in Chapter 5. For the crystalline sample, GB1 was crystallised from a 10 mg/mL solution with the aid of a precipitant of 2:1 2-methylpentane-2,4-diol:propan-2-ol.[281] The resulting nanocrystals were then centrifuged into a Bruker 1.3 mm rotor.

All solid-state NMR spectra shown, except for ^{15}N $R_{1\rho}$ relaxation dispersion on crystalline GB1, were recorded at 850 MHz ^{1}H Larmor frequency with a Bruker Avance III spectrometer, with a Bruker 1.3 mm triple resonance probe operating at an MAS frequency of 60 kHz. ^{15}N $R_{1\rho}$ relaxation dispersion experiments on crystalline GB1 were recorded at 600 MHz ^{1}H Larmor frequency with a Bruker Avance II+ spectrometer, with a Bruker 1.3 mm triple resonance probe operating at an MAS frequency of 50 kHz. The rotor caps were sealed with a silicone-based glue to eliminate water leakage, while a Bruker BCU-X cooling unit was used to regulate the internal sample temperature to 27 ± 1 °C (measured from the chemical shift of water with respect to DSS[282]). ^{15}N $R_{1\rho}$ rates in the complex were measured by recording a series of ^{15}N -^{1}H correlation spectra a proton-detected pulse sequence similar to that shown in Figure 3.3d, but with a ^{15}N spin-lock pulse situated immediately after the initial ^{1}H-^{15}N CP, whose length, τ, was incremented between full experiments. For measurements on the complex, double-quantum CP contact times were 1 ms (^{1}H-^{15}N) and 0.4 ms (^{15}N-^{1}H), with nutation frequencies of 10 kHz and ~50 kHz for ^{15}N and ^{1}H respectively. Relaxation series were collected with spin-lock nutation frequencies of both 17 kHz and 2.5 kHz. For each experiment within the 17 kHz series, 224 scans of 74 t_1 increments were taken, while for the 2.5 kHz series 96 scans of 64 t_1 increments were taken per experiment. Recycle delays were 2 s. For ^{15}N $R_{1\rho}$ relaxation dispersion on crystalline GB1, a series of interleaved ^{15}N $R_{1\rho}$ measurements were performed at spin-lock frequencies 1.95, 2.44, 3, 4, 5, 6 and 8 kHz. Each $R_{1\rho}$ curve was sampled using 10-12 points with spin-lock pulse lengths up to 0.5 s. 4 scans of 70 t_1 increments were collected, with a recycle delay of 2 s. ^{1}H-^{15}N and ^{15}N-^{1}H CP contact times were 1.5 and 1.0 ms, respectively, with nutation frequencies of 10 kHz (^{15}N) and ~40 kHz (^{1}H). For all experiments, 10 kHz WALTZ-16 heteronuclear decoupling was applied to ^{1}H during ^{15}N evolution, and to ^{15}N during direct ^{1}H acquisition, while suppression of the ^{1}H signal of water was achieved by saturation with 200 ms (for the complex) or 50 ms (for the crystals) of slpTPPM ^{1}H decoupling[114] applied at an amplitude of ¼ of the MAS frequency. In all experiments, hard pulses were applied at nutation frequencies of 100 kHz (^{1}H and ^{13}C) or 83.3 kHz (^{15}N). Quadrature detection was achieved using the States-TPPI method. Each of the spin-lock frequencies were determined using nutation experiments.

TopSpin 3.2 and CcpNmr Analysis 2.2.2 were used to process spectra and analyze the relaxation data, which was subsequently fitted using Origin 9.1. Figures 8.2-8.3 were produced using the UCSF Chimera package.[370]

9

^{1}H-DETECTED SSNMR MEASUREMENTS OF $^{13}C^{\alpha}$ RELAXATION IN FULLY PROTONATED PROTEINS

Abstract

SSNMR relaxation measurements at MAS frequencies >50 kHz are powerful tools for the characterisation of the dynamics of backbone ^{13}C and ^{15}N sites in proteins, but equivalent measurements for aliphatic sites are often hampered by spin diffusion effects. Here, we examine these effects and find that, whilst prominent at 60 kHz MAS in uniformly ^{13}C-labelled samples, they are essentially removed in alternately labelled samples where only every other carbon is ^{13}C-labelled, allowing for the reliable measurement of aliphatic R_1 and $R_{1\rho}$ relaxation rates, even in fully protonated samples. Spinning at MAS rates of >80 kHz with 0.8 mm MAS instrumentation also allows for resolved $^{13}C^{\alpha}$-$^{1}H^{\alpha}$ correlations, providing a framework for $^{13}C^{\alpha}$ relaxation measurements which are subsequently conducted in fully protonated crystalline [1,3-^{13}C,^{15}N]GB1. These results are analysed quantitatively with a model-free treatment, but it is noted that a greater number of independent parameters are required for a reliable analysis involving multiple time scales.

9.1 Introduction

Of all the SSNMR methods for characterising the dynamics of proteins, relaxation measurements rank among the most powerful. By measuring an array of relaxation parameters, increasingly complex models with large numbers of independent parameters can now be implemented. Over the last few years, the suite of relaxation experiments that can be implemented for this purpose has grown to include backbone ^{15}N R_1, ^{15}N $R_{1\rho}$, ^{13}C' R_1 and now (see Chapter 7) ^{13}C' $R_{1\rho}$, with the possibility of measuring these parameters at multiple fields. Clearly, conducting a larger number of unique measurements will lead to a more complete dynamic picture of a protein.

Notably absent from the above list of observables are the relaxation rates of $^{13}C^{\alpha}$ sites. Measurements of aliphatic ^{13}C relaxation rates in fully protonated proteins have until very recently remained impeded by the presence of coherent processes arising from anisotropic interactions. These are much more difficult to eliminate for aliphatic nuclei thanks to the high concentration of surrounding protons and correspondingly dense network of strong dipolar couplings. The effects of PDSD upon $^{13}C^{\alpha}$ R_1 rates, for example, are still distinctly non-negligible in fully protonated samples even at 60 kHz MAS. Recently, Asami *et al.* showed that a combination of fast MAS (>40 kHz), extensive deuteration and alternate ^{13}C labelling alleviated this problem, suppressing spin diffusion through truncation of the ^{1}H-^{13}C/^{13}C-^{13}C and ^{13}C-^{13}C/^{13}C-^{13}C dipolar cross-terms that it stems from, and hence enabling the measurement of entirely site-specific aliphatic ^{13}C ($^{13}C^{\alpha}$ and side-chain ^{13}C) R_1 rates.[146]

In Chapter 10 we prove that direct coherent contributions to ^{13}C rotating frame relaxation ($R_{1\rho}$) rates (including $^{13}C^{\alpha}$) are effectively removed in fully protonated samples by a combination of fast MAS (>50 kHz) and moderate spin-lock irradiation (>8kHz).[357] However, similarly to $^{13}C^{\alpha}$ R_1 rates, $^{13}C^{\alpha}$ $R_{1\rho}$ rates are under these conditions affected by spin diffusion between neighbouring carbon sites, which is promoted by the spin-lock irradiation (see below). Here, we investigate whether site-specific $^{13}C^{\alpha}$ R_1 and $R_{1\rho}$ relaxation rates can be reliably measured in fully protonated samples by exploiting "ultrafast" MAS rates (≥60 kHz) to average the dipolar couplings responsible for the coherent effects upon measured relaxation rates. The use of fully protonated samples, rather than deuterated samples, is desirable for a number of reasons. Besides being easier and much less costly to produce in the yields necessary for NMR, the use of fully protonated samples is beneficial for overall sensitivity, as the higher concentration of protons maximises the efficiency of the initial CP polarisation step. This is especially true in the case of $^{13}C^{\alpha}$, for which the nearest ^{1}H is the amide proton (>2 Å away, compared to ~1 Å for directly-bonded methyl C-H or amide N-H). We combine the fast MAS rates with alternate carbon labelling ([1,3-^{13}C]) to remove the one-bond ^{13}C-^{13}C dipolar couplings that are implicit in spin diffusion. According to LeMaster *et al.*, [1,3-^{13}C]-labelled proteins should exhibit the enrichment pattern shown in Figure 3.1.[151] It should be expected that the use of this labelling scheme will have a greater impact upon the rates of spin diffusion than deuteration alone, as the latter leaves the ^{13}C-^{13}C/^{13}C-^{13}C dipolar cross terms completely intact.

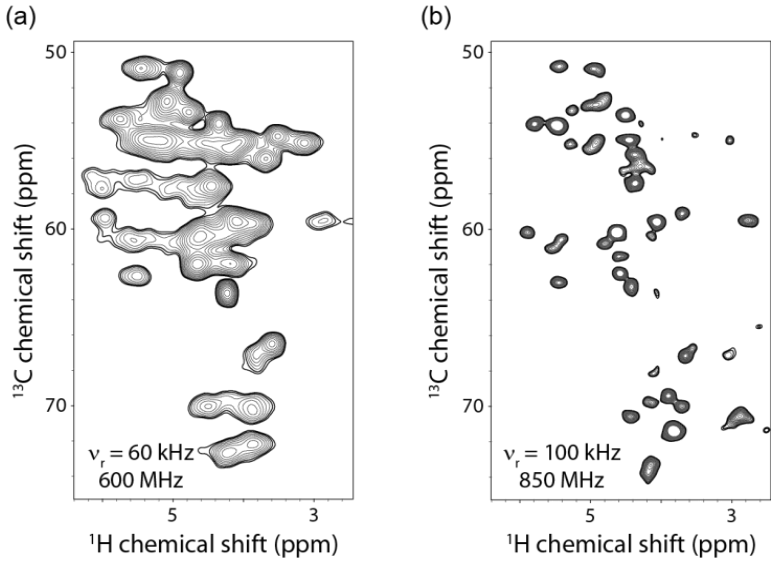

Figure 9.1. Expansions from ^{13}C-^{1}H 2D correlation spectra obtained on (a) fully protonated [U-^{13}C,^{15}N]GB1 at ν_r = 60 kHz with a 600 MHz spectrometer and (b) [1,3-^{13}C,^{15}N]GB1 at ν_r = 100 kHz with an 850 MHz spectrometer. The spectrum in (b) was obtained in 2.6 h on ~0.3 mg (~46 nanomoles) of crystalline material. The ^{1}H line widths in (b) are ≥95 Hz (0.11 ppm). Assignments are given in Figure C.5 in Appendix C.

The recently-developed MAS instrumentation utilised in Chapter 6 (up to 100 kHz), in addition to potentially eliminating the effects of spin diffusion, also facilitates proton detection in fully protonated protein samples (see Figure 6.4), especially when combined with a high magnetic field. The improvement in resolution for fully protonated samples is especially striking in the case of the $^{13}C^{\alpha}$-^{1}H spectrum, which is usually subject to far more broadening than an equivalent ^{15}N-^{1}H spectrum thanks to the higher concentration of protons nearby. Figure 9.1 demonstrates this through a comparison of expansions of spectra of (a) [U-^{13}C,^{15}N]GB1 at ν_r = 60 kHz on a 600 MHz spectrometer and (b) [1,3-^{13}C,^{15}N]GB1 at ν_r = 100 kHz on a 850 MHz spectrometer. A clear improvement in resolution at the higher field and spinning frequency can be seen. The alternate carbon labelling scheme further aids resolution by eliminating one-bond J-couplings (30-50 Hz). The average aliphatic ^{1}H line width for the improved spectrum in Figure 9.1b is 155 ± 42 Hz (0.18 ± 0.05 ppm) (the peak overlap in Figure 9.1a prohibits reliable measurement of the average ^{1}H line width). This is itself a not insignificant result, as it proves the utility of such an approach for the exploitation of ^{13}C-^{1}H correlations (*e.g.* as part of a 3D experiment) in proteins. Currently, such correlations can be viable in deuterated samples for methyl protons (if a directly-bonded proton is present)[161,263] but sensitivity is otherwise considerably diminished owing to significantly reduced CP efficiency. In the context of this investigation, this approach provides an ideal basis for

$^{13}C^{\alpha}$ relaxation experiments in fully protonated samples, with the sensitivity enhancement provided by proton detection allowing for more rapid measurements than would be available through carbon- or nitrogen-detection with the same amount of sample. The experimental time scale for the spectrum in Figure 9.1b of only 2.6 hours confirms that relaxation experiments based on this method will be possible to complete within a matter of hours or days. This short "baseline" experimental time is especially relevant in the case of R_1 measurements, which are usually extremely time-consuming owing to the long T_1 times present (*e.g.* up to tens of seconds, compared with $T_{1\rho}$ values of up to hundreds of milliseconds). In the absence of full 3D assignment spectra, the assignments used (see Figure C.5 in Appendix C) were inferred from those of a different crystal form,[262] with minor shifts due to intermolecular interactions.[xv]

9.2 Evaluation of Spin Diffusion Effects

To assess the extent to which PDSD is suppressed with alternately labelled samples, experiments were conducted at 60 kHz MAS (using a Bruker 1.3 mm probe) on both uniformly and alternately labelled samples of fully protonated GB1 at 600 MHz field. For each sample, aliphatic carbon-detected 2D experiments were run with a "mixing" period (see experimental details) consisting of a typical R_1 relaxation delay. Any cross-peaks observed in such experiments would be evidence of magnetisation transfer between ^{13}C sites by PDSD. Figure 9.2 shows the spectra resulting from these experiments, with mixing times of 1 s and 3 s. As the bulk T_1 for the $^{13}C^{\alpha}$ sites in fully protonated GB1 (measured first in 1D) is ~8 s (some individual resonances will be shorter), these times should easily allow sufficient time for any potential polarisation transfer via PDSD, whilst at the same time ensuring that cross-peaks are not unobservable simply because they have decayed beyond detection.

Even at 60 kHz MAS, the difference between the uniformly and alternately labelled samples is stark: after 1 s, numerous cross-peaks are observed for the uniformly labelled sample across the entire aliphatic region (Figure 9.2a). In this case, the total integrated intensity of all aliphatic cross peaks is 47% of that of the diagonal. After 3 s many cross peaks are still seen, with the ratio of cross-peak integrals to diagonal peak integrals even larger at 77%, although most of the peaks originating from CH_2 and CH_3 sites are missing due to their shorter T_1 times. For the [1,3-^{13}C,^{15}N]-labelled sample,

[xv] While the majority of assignments can be taken as correct with a high degree of certainty, the assignments for I6, T11, T16, T44, T49, T53 and T55 should be taken as markedly less reliable (and therefore used for proof-of-concept purposes only).

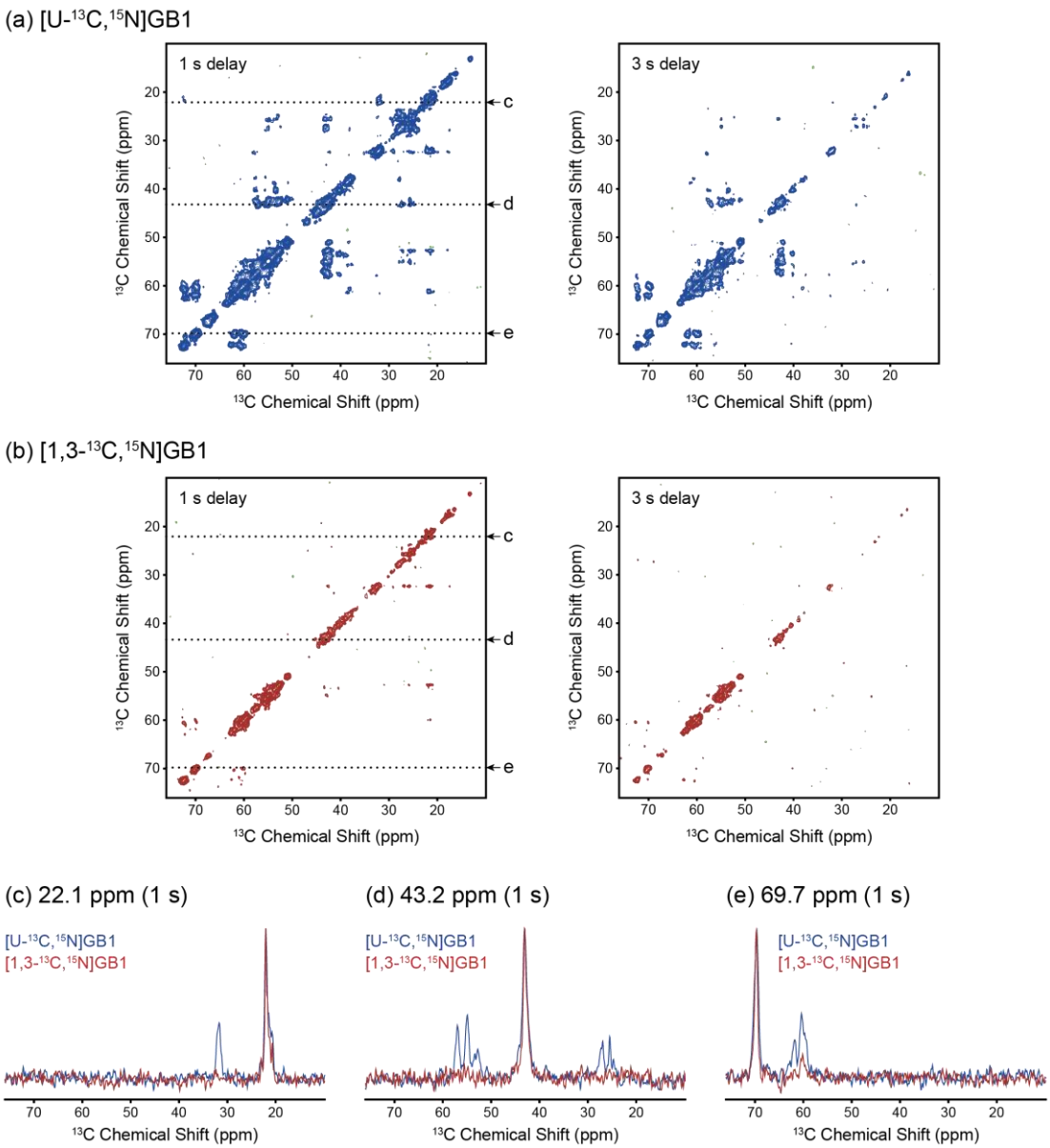

Figure 9.2. 2D ^{13}C-^{13}C correlation spectra obtained from experiments at 600 MHz field and 60 kHz MAS using a pulse sequence in which the mixing period consisted of a typical R_1 delay of 1 s (left) and 3 s (right), for (a) fully protonated [U-^{13}C,^{15}N]GB1 (blue) and (b) fully protonated [1,3-^{13}C,^{15}N]GB1 (red). Comparisons of example slices (taken at the chemical shifts shown with dotted lines in (a) and (b)) are shown in (c-e). In each case, the slices are scaled such that the intensities of the autopeaks of the red and blue spectra are matched.

almost no cross-peaks are observed at either mixing time (Figure 9.2b). At 1 s (3 s), the total integral of all cross-peak intensity is just 9% (11%) of the total auto-peak integral, representing an 81% (86%) reduction in relative peak integral. These are likely to be reduced even further at the higher MAS frequencies available with the 0.8 mm probe. Figures 9.2c-e show comparative slices of the spectra in Figures 9.2a and 9.2b (at the chemical shifts indicated with dotted lines). The most significant cross-peaks that remain

in the spectrum of the alternately labelled sample appear between ~59 ppm and ~75 ppm in either dimension,[xvi] which correspond to dipolar transfer between the $^{13}C^{\alpha}$ and $^{13}C^{\beta}$ sites of threonine residues. According to the labelling pattern given by LeMaster *et al.* (illustrated in Figure 3.1), only the C^{α} sites should be ^{13}C-enriched, although the presence of both $^{13}C^{\alpha}$-^{1}H peaks (<67 ppm in the ^{13}C dimension) and $^{13}C^{\beta}$-^{1}H peaks (>67 ppm in the ^{13} dimension) for threonine residues in Figure 9.1 attests otherwise. In this respect, the labelling pattern is, then, more alike to that given by Castellani *et al.*[49], where both the C^{α} and C^{β} sites in threonine are fractionally ^{13}C-labelled. This would explain the presence of $^{13}C^{\alpha}$-$^{13}C^{\beta}$ cross peaks in Figure 9.2b – whilst suppressed to an extent, a certain fraction of the threonine residues in the protein will be enriched at both sites, leading to efficient PDSD. This is likely to be exacerbated in threonine residues where the chemical shift differences between $^{13}C^{\alpha}$ and $^{13}C^{\beta}$ sites are relatively small. Note, however, that neither suggested labelling pattern predicts the presence of alanine ^{13}C resonances as are observed (albeit relatively weakly) in Figure 9.1 (and Figure C.5).

Similar experiments were conducted to test for the occurrence of r.f.-driven spin diffusion in aliphatic ^{13}C $R_{1\rho}$ experiments. These again consisted of 2D ^{13}C-detected experiments, but with a ^{13}C spin-lock pulse of typical nutation frequency (17 kHz) during each "mixing" period. Spin-lock times of 10 ms and 100 ms were chosen based on the measured bulk $^{13}C^{\alpha}$ relaxation time of ~100 ms. The results of these experiments are shown in Figure 9.3, for both the uniformly labelled sample (Figure 9.3a) and the [1,3-^{13}C,^{15}N]-labelled sample (Figure 9.3b). Example slices are given in Figures 9.3c-e. Once again, even at 60 kHz, the use of alternate carbon labelling significantly suppresses polarisation transfer, with the spectra in Figure 9.3b virtually devoid of cross-peaks. The ratios of total cross-peak integrated intensities to the total diagonal integrated intensities are 14% and 30% for the uniformly labelled sample at 10 ms and 100 ms (respectively), which drop to just 3% and 2% for the alternately labelled sample. Interestingly, cross peaks appear predominantly within a distinctive band running perpendicular to the diagonal and centred at the r.f. frequency. Because of this, the threonine $^{13}C^{\alpha}$-$^{13}C^{\beta}$ cross peaks that were relatively intense in the R_1-like experiments above (Figure 9.2) are much weaker here. With alternate labelling, it is instead cross-peaks nearer the centre of the spectrum that apparently are of more concern, namely between ~25 ppm and ~37 ppm in either dimension. The cause of these is likely again to be fractional labelling of carbon

[xvi] Note that for both samples at 1 s, the horizontal rows of weak cross-peaks that appear at 32.2 ppm and 52.6 ppm in the F_1 dimension – a separation of 10.2 ppm either side of the resonance offset – are most likely artefacts from improper phase cycling.

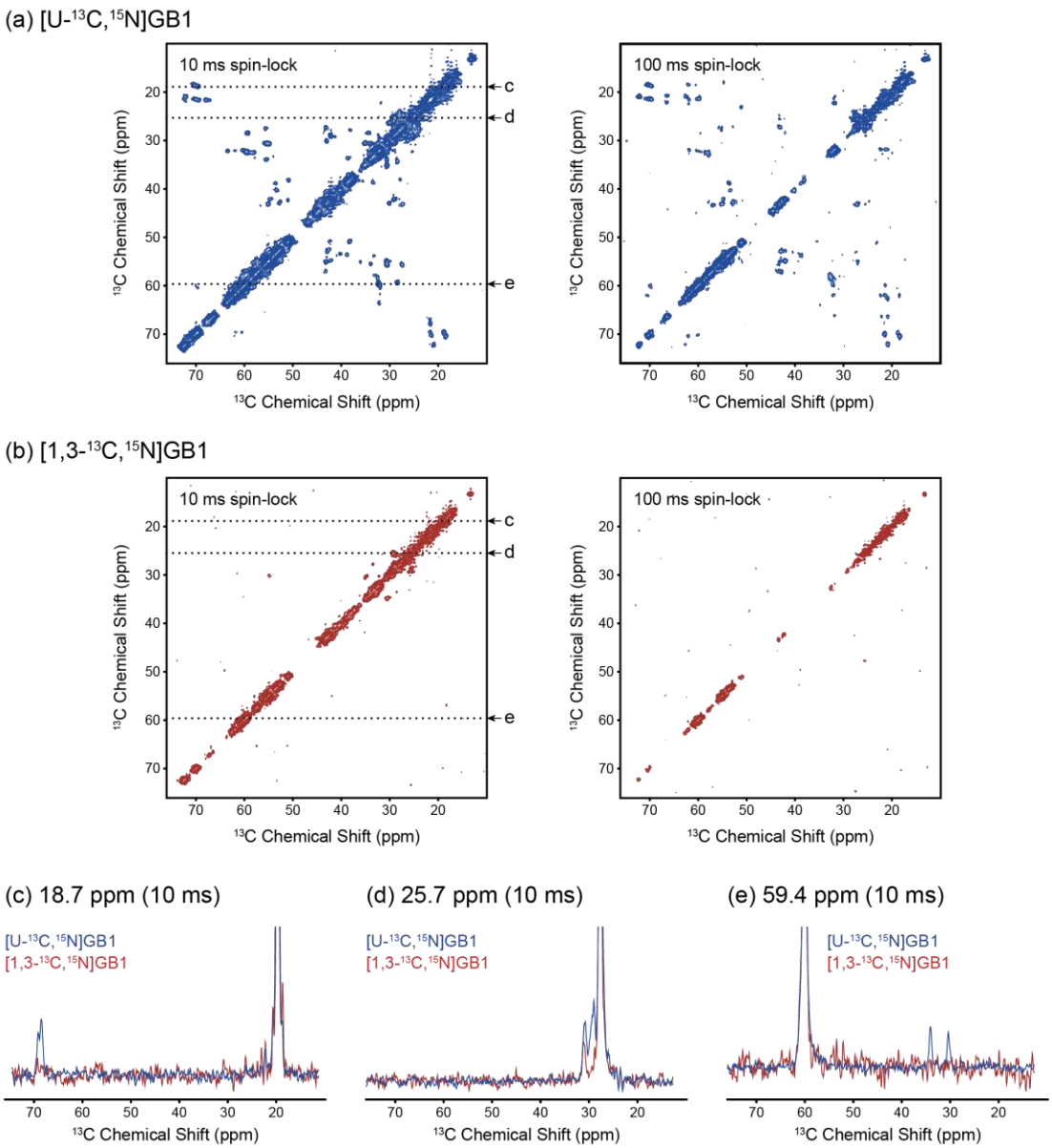

Figure 9.3. 2D ^{13}C-^{13}C correlation spectra obtained from experiments at 600 MHz field and 60 kHz MAS using a pulse sequence in which the mixing period consisted of a typical $R_{1\varrho}$ spin-lock pulses of 10 ms (left) and 100 ms (right), for (a) fully protonated [U-^{13}C,^{15}N]GB1 (blue) and (b) fully protonated [1,3-^{13}C,^{15}N]GB1 (red). Comparisons of example slices (taken at the chemical shifts shown with dotted lines in (a) and (b)) are shown in (c-e). In each case, the slices are scaled such that the intensities of the autopeaks of the red and blue spectra are matched.

sites (of for example lysine residues) that are neighbouring and/or are close in chemical shift. There are no cross peaks for $^{13}C^{\alpha}$ sites at all.

It can therefore be concluded that, under ≥60 kHz (and potentially slower) spinning conditions, spin diffusion for C^{α} sites (as well as the majority of other aliphatic sites) is sufficiently inhibited in alternately labelled proteins for both R_1 and $R_{1\rho}$ experiments to be conducted reliably, with the caveat that for certain residues it can only

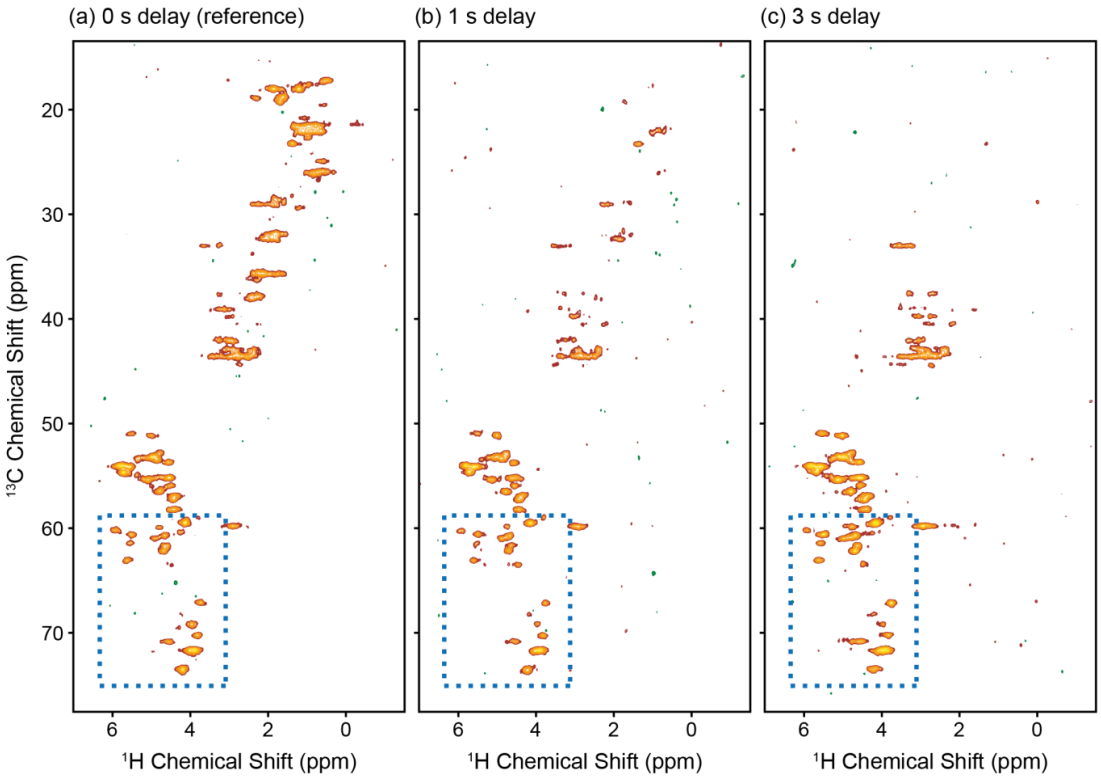

Figure 9.4. 2D ^{13}C-^{1}H spectra of crystalline fully protonated [1,3-^{13}C,^{15}N]GB1 obtained at 850 MHz field and 86 kHz MAS using a proton-detected heteronuclear correlation pulse sequence with an "R_1-like" delay after ^{13}C evolution of (a) 0 s, (b) 1 s and (c) 3 s. The presence of additional cross-peaks at longer delay times would be an indication of spin-diffusion effects. The region outlined by the blue dashed line indicates that in which threonine $^{13}C^{\alpha}$-$^{1}H^{\beta}$ and/or $^{13}C^{\beta}$-$^{1}H^{\alpha}$ cross-peaks arising from spin diffusion would appear.

be significantly reduced rather than eliminated entirely unless more sparsely enriched samples can be used. Spinning the sample even faster will reduce these effects still further for an even smaller contribution to measured relaxation decay rates. This is confirmed for the R_1 case (no $^{13}C^{\alpha}$ cross peaks were seen for the $R_{1\rho}$ case even at 60 kHz) by the spectra shown in Figures 9.4b,c, which are the results of aliphatic ^{1}H-detected ^{13}C-^{1}H experiments at 86 kHz MAS, which, as above, were performed with typical R_1 delay periods of 1 s and 3 s. Within the pulse sequence, these elements were inserted after the ^{13}C evolution period. Magnetisation transfer from carbon "A" to carbon "B" would thus be observed as a cross peak with an identical ^{13}C chemical shift to carbon A, and with the same ^{1}H chemical shift as carbon B's directly-bonded protons. In the context of PDSD between threonine C^{α} and C^{β} sites, these would appear within the box (blue dashed line) indicated in the figures. Comparing Figures 9.4b,c to a reference ^{1}H spectrum (with no extra delay or spin-lock pulse, and therefore no spin diffusion; Figure 9.4a), it appears

that no cross-peaks of this sort are present above the level of the noise. Peaks are seen only to disappear (compared to the reference spectrum) due to relaxation effects.

9.3 Measurement of $^{13}C^{\alpha}$ R_1 and $R_{1\rho}$ Relaxation Rates

Taking advantage of the ability to conduct sensitive proton-detected carbon measurements, we measured site-specific $^{13}C^{\alpha}$ R_1 and $R_{1\rho}$ relaxation rates in [1,3-^{13}C,^{15}N]GB1 using proton-detected ^{13}C-^{1}H experiments at an MAS frequency of 86 kHz and a ^{1}H Larmor frequency of 850 MHz. The sample temperature was maintained at 27 °C, as measured from the chemical shift of water protons with respect to DSS.[282] At 86 kHz (or even 100 kHz) in the fully protonated sample, many of the methyl and methylene ^{1}H resonances are still rather broad (see Figure 9.4), resulting in a lack of resolution that defeats site-specific relaxation experiments, although such measurements would be possible via ^{13}C-^{13}C correlations as in Figures 9.2 and 9.3. For the proton detection of methyl sites, deuteration would therefore usually be essential.

Figures 9.5a,b show the measured $^{13}C^{\alpha}$ relaxation rates as a function of residue number. Considerable variation is observed throughout the protein in both sets of data, further supporting our assertion that spin diffusion is successfully suppressed. While elevated rates are observed in loop 1, interestingly, correlation of rates with secondary structure appears considerably less strong than in the cases of ^{15}N and ^{13}C' rates (also see §10.3).[114,276] This may be linked with the fact that the $^{13}C^{\alpha}$ sites do not lie within rigid peptide planes, but rather act as the "pivots" between them. This type of trend (or lack thereof) was similarly observed by Asami *et al.* in deuterated SH3.[146] The rates for a number of residues were not measured owing to a lack of peak intensity for the relevant cross peaks, a consequence of using an alternately labelled sample. Full dynamic characterisation would therefore be best achieved with a combination of experiments on both [1,3-^{13}C]-labelled samples and [2-^{13}C]-labelled samples, which exhibit the opposite labelling pattern.

A key advantage of relaxation measurements is that they can give access to information about both the time scales and amplitudes of motions, by fitting the measured rates to quantitative analyses. Figures 9.5c,d show the result of an SMF analysis of the data (with dipolar C^{α}-H^{α} as the only interaction present), with order parameter and correlation time fit parameters plotted against residue number. Although an analysis involving only a single time scale can be extremely useful in highlighting general dynamic features, it must be stressed that the absolute values of order parameters and correlation

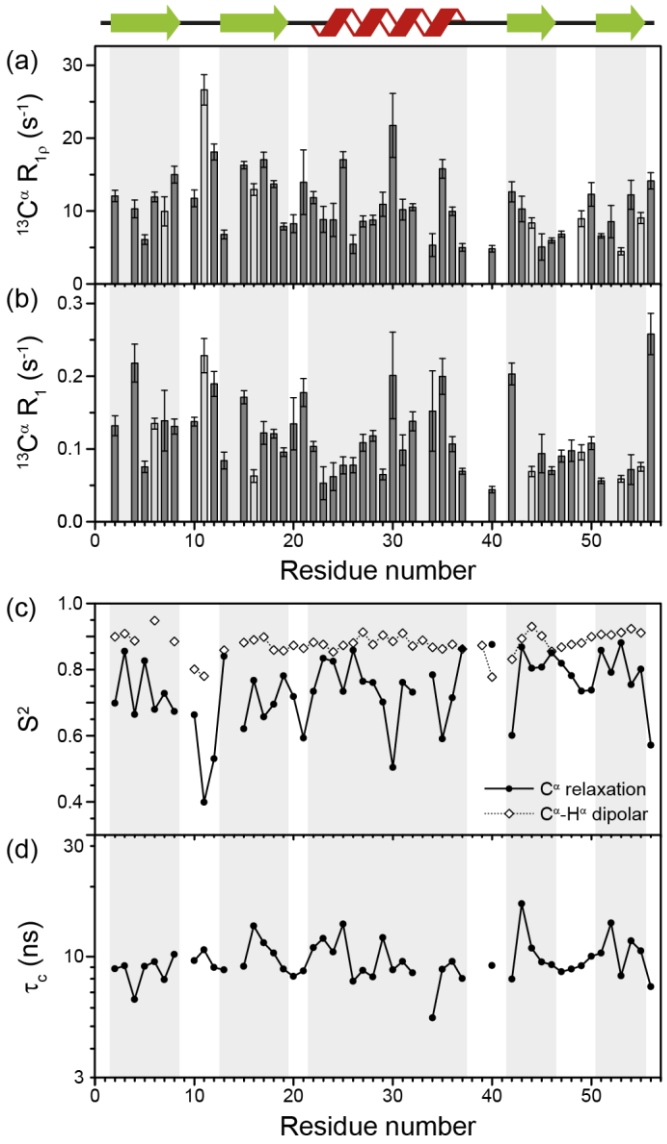

Figure 9.5. Measured $^{13}C^{\alpha}$ $R_{1\rho}$ (a) and R_1 (b) relaxation rates for fully protonated crystalline [1,3-^{13}C,^{15}N]GB1 as a function of residue number. The absence of a number of relaxation rates is a result of low peaks intensities for specific residue types due to the alternate labelling scheme of the protein. Rates shown in light grey correspond to sites for which assignments are ambiguous. The measured rates were analysed using SMF formalism, yielding (c) order parameters and (d) correlation times (black lines). White circles in (c) show dipolar C^{α}-H^{α} order parameters measured by Wylie *et al.*[366]

times should be interpreted with a great deal of caution – as is found in §§10.4-10.6, if multiple time scales of motion are present in a protein (as is generally the case), analysis of these with a single time scale model in the solid state will in general yield unsatisfactory results. This is clearly the case here, as the SMF order parameters appear far lower than the directly measured order parameters for the $^{13}C^{\alpha}$-$^{1}H^{\alpha}$ dipolar interaction[366] (which is the primary contribution to the relaxation). Nevertheless, the SMF analysis reveals certain features, such as high amplitude motions around loops and

the C-terminus, that are also seen in the order parameters derived from ^{15}N and ^{13}C' relaxation measurements in the same protein at 60 kHz (see §§10.4 & 10.6), as well as those found in solution studies.[371,372] In addition, however, certain residues of the helix (which are usually seen to be fairly rigid) display surprisingly low order parameters. Some of the differences may be accounted for by the sensitivity of $^{13}C^{\alpha}$ relaxation to an inherently different set of directions than either ^{13}C' or amide ^{15}N relaxation, but beyond this proof-of-concept analysis, obtaining a more realistic view of the dynamics of the C^{α} sites would require additional measurements at different fields in order to enable the consideration of multiple time scales (as discussed in depth in Chapter 10).

One of the main challenges facing dynamics studies in the solid state is the relatively small set of independent measurable parameters, which hence limits the maximum number of variables in the models used for analysis. In general, the measurement of a greater number of different types of dynamic parameters will ensure the capture of motions occurring across a wider range of time scales and in different directions, even if not they are not subsequently analysed in a completely quantitative manner. The ability to measure $^{13}C^{\alpha}$ relaxation rates is therefore a highly valuable one, and comprehensive studies can seek to combine these measurements with others such as ^{15}N and ^{13}C' R_1 and $R_{1\rho}$ under different conditions (*e.g.* different fields) and dipolar couplings for a much more detailed description of a protein's dynamics. Whilst the measurements presented here may not be combined with others for a peptide plane analysis as presented in Chapter 10 (because the C^{α} site does not sit within that rigid element), this does not exclude the possibility of using them together for analyses of collective motions of, for example, secondary structure elements.[365]

9.4 Conclusions

In summary, the use of alternately labelled samples at ultrafast MAS frequencies (*e.g.* ≥60 kHz) enables the reliable measurement of site-specific side-chain $^{13}C^{\alpha}$ R_1 and $R_{1\rho}$ relaxation rates in solid-state fully protonated proteins with negligible averaging effects from spin diffusion. At spinning frequencies of ~80 kHz and above, proton detection of $^{1}H^{\alpha}$ sites is rendered practical, with resolution of cross-peaks in $^{13}C^{\alpha}$-$^{1}H^{\alpha}$ correlation spectra facilitating the extraction of site-specific information with small amounts of sample. Using the presented measurements, an atomic-level quantitative description of protein dynamics can be extracted, providing both amplitudes and timescales of motions, with potential extension to more complex models (*e.g.* multiple time scales) possible

through combination with other measured dynamic parameters or more measurements at different fields. Although at 100 kHz proton detection is still not viable for resolution of the majority of side-chain carbon sites, their relaxation rates can still be measured reliably (*i.e.* free from spin-diffusion effects) by using alternately labelled samples even at 60 kHz as evidenced by the lack of cross-peaks in the ^{13}C-^{13}C spectra of Figures 9.2 and 9.3. This could prove especially useful as side-chain motions play a crucial role in protein-protein interactions. This information should be highly complementary to ^{15}N side chain measurements that are limited to a few specific residue types such as glutamine and asparagine (which have been used to probe intermolecular interfaces in fibrils[240]).

9.5 Experimental Details

Hydrated [1,3-^{13}C,^{15}N]GB1 and [U-^{13}C,^{15}N]GB1 crystals were prepared in the same manner as the crystalline sample in Chapter 8. 1.3 mm rotors were packed by centrifugation, whereupon they were sealed using a silicone-based glue. [1,3-^{13}C,^{15}N]GB1 crystals were packed into a 0.8 mm rotor manually using micro-spatulas under a magnifying glass.

The NMR experiments at 60 kHz MAS were performed with a Bruker 1.3 mm triple-resonance probe, on a Bruker Avance II+ spectrometer operating a 600 MHz ^{1}H Larmor frequency. The proton-detected experiments at 86 kHz MAS were performed using a Samoson 0.8 mm double-resonance probe and on a Bruker Avance III spectrometer at 850 MHz ^{1}H Larmor frequency. Note that at least at present, the maximum spinning frequency attainable using the 0.8 mm probe is highly dependent on the condition of each individual rotor; the condition of the rotor used in these experiments was such that 86 kHz was the maximum spinning frequency available. All experiments were performed at a sample temperature of 27 ± 0.5 °C, as measured by the ^{1}H chemical shift of water with respect to DSS,[282] with sample cooling provided by a Bruker BCU-X cooling unit.

To evaluate spin diffusion effects at 60 kHz MAS, 2D ^{13}C-^{13}C experiments were run using a pulse sequence of the form shown in Figure 2.7c, with the mixing step consisting of representative R_1 delays or $R_{1\rho}$ spin-lock pulses (17 kHz). For these experiments, t_2 and maximum t_1 times were 24 ms and 8 ms, respectively. 24 scans were collected for each experiment.

The $^{13}C^{\alpha}$ R_1 and $R_{1\rho}$ relaxation rates measured at 86 kHz were obtained from ^{13}C-^{1}H 2D correlation spectra recorded using a proton-detected heteronuclear correlation

sequence (see Figure B.6 in Appendix B) with an additional delay period (for R_1) or spin-lock pulse (for $R_{1\rho}$) directly after the ^{1}H-^{13}C CP. Their lengths, τ, were incremented between full experiments to map out the relaxation behaviour of the $^{13}C^{\alpha}$ nuclei (τ ranged between 5 ms and 10 s for R_1 and 5 and 110 ms for $R_{1\rho}$). ^{13}C nuclei were polarised via 1 ms adiabatic double-quantum CP from protons. The maximum times for subsequent t_1 evolution were 12 ms. The spectra in Figure 9.4 were obtained with a similar pulse sequence, but with the τ delay after t_1 evolution (maximum t_1 of 10 ms). The water signal was suppressed by saturation with 100 ms of 21.5 kHz slpTPPM ^{1}H decoupling (with 100 kHz π/2 ^{13}C pulses were applied either side of this). The contact times for CP from ^{13}C back to ^{1}H (prior to detection) were just 0.2 ms to ensure one-bond transfers only.

For all experiments, hard pulses were administered at nutation frequencies of 100 kHz (^{1}H and ^{13}C). The nutation frequencies for CP were $\omega_{1H}/2\pi \approx 10$ and $\omega_{1C}/2\pi = (\nu_r - 10)$ kHz. slpTPPM decoupling was applied during t_1 evolution periods at a field strength of ($\nu_r/4$) kHz. Detection of protons (t_2) was achieved using the States-TPPI method and lasted for 30 ms in all cases, during which 10 kHz WALTZ-16 decoupling was applied to ^{13}C. Recycle delays were all 2 s.

For the relaxation experiments, 32 scans of 96 t_1 increments were collected, resulting in total experimental durations of $R_{1\rho}$ experiments of between 1.8 and 2 hours each, and of R_1 experiments of ~1.8 h (5 ms delay), ~2.7 h (500 ms delay), ~3.5 h (1 s delay), ~7 h (3 s delay), ~ 12 h (6 s delay) and ~19 h (10 s delay).

Spectra were processed and analysed using TopSpin 3.2, and the final relaxation curve fitting was completed on Origin 9.1.

Fitting of the relaxation data to SMF equations was performed in MATLAB, with minimisation was performed using code based on the *fminsearch* function. The best-fit amplitude (S^2) and time scale (τ_c) parameters were determined by minimizing the χ^2 target function:

$$\chi^2 = \sum_i \frac{\left(X_{i,calc} - X_{i,exp}\right)^2}{{\sigma_{i,exp}}^2} \tag{9.1}$$

where X_i are relaxation rates and σ_i are the corresponding experimental errors. The rigid limit C^{α}-H^{α} distance was assumed to be 1.12 Å.

10

PROTEIN BACKBONE MOTIONS FROM COMBINED ^{13}C' AND ^{15}N SSNMR RELAXATION MEASUREMENTS

Abstract

Protein dynamics typically involve a complex hierarchy of motions occurring on different time scales between conformations separated by a range of different energy barriers. NMR relaxation experiments can in principle provide a site-specific picture of both the time scales and amplitudes of these motions, but independent relaxation rates sensitive to fluctuations on different time scale ranges are required to obtain a faithful representation of the underlying dynamic complexity. Below, ^{13}C spin-lattice relaxation in the rotating frame ($R_{1\rho}$) is introduced as a probe of backbone nanosecond-microsecond motions in proteins in the solid state. Measurements of ^{13}C' $R_{1\rho}$ rates in fully protonated crystalline protein GB1 at 600 and 850 MHz ^{1}H Larmor frequencies are presented and compared to ^{13}C' R_1, ^{15}N R_1 and $R_{1\rho}$ measured under the same conditions. The addition of carbon relaxation data to the model-free analysis of nitrogen relaxation data leads to greatly improved characterisation of the time scales of protein backbone motions, minimising the occurrence of fitting artefacts that may be present when ^{15}N data is used alone. We also discuss how internal motions characterised by different time scales contribute to ^{15}N and ^{13}C relaxation rates in the solid state and solution state, leading to fundamental differences between them, as well as phenomena such as underestimation of picosecond-range motions in the solid state and nanosecond-range motions in solution.

(Adapted from Lamley, J. M.; Lougher, M. J.; Sass, H. J.; Rogowski, M.; Grzesiek, S.; Lewandowski, J. R. *Physical Chemistry Physical Chemistry* **2015***, 17*, 21997)

10.1 Introduction

Slow motions occurring on the ns-ms time scale are often fundamental to protein function.[3] Solid-state NMR relaxation measurements provide an attractive method for extracting quantitative information about such motions.[276,332,342,348,356,373,374] Specifically, the correlation times and amplitudes of ns-ms internal motions are theoretically accessible through the measurement of site-specific spin-spin (R_2) relaxation rates obtained in the solid state, which could thus provide a powerful tool to complement dynamical information available from solution studies, where the time scale of motions accessible with relaxation is limited by the correlation time of overall molecular tumbling. In practice, however, the measurement of R_2 rates in solids is difficult, as typically the measured decay rate of the transverse magnetization in a spin echo experiment ($R_2'=1/T_2'$) is dominated by coherent contributions (*e.g.* dipolar dephasing[375]), even in perdeuterated samples where the dense proton networks are diluted with deuterium spins.[276] In order to gain insights into dynamic transformations of biomolecules it is the incoherent R_2 (here referred to simply as the transverse relaxation rate) that is required, which is purely due to the stochastic modulation of local fields by molecular motion.

In solution, in the presence of chemical exchange, on-resonance $R_{1\rho}$ is a sum of pure R_2 relaxation and a scaled exchange contribution. As described in §7.4, in the solid state, it has been demonstrated for amide ^{15}N that a spin-lock field of greater strength, in combination with a MAS frequency of more 45 kHz, may be used to decouple both the exchange contribution and any contributions from coherent processes, and hence an $R_{1\rho}$ measurement can provide a reliable estimate of incoherent R_2.[276] It is straightforward to carry this out in a site-specific manner even in fully protonated protein samples without additional heteronuclear decoupling.[276]

Analysis of site-specific values of ^{15}N $R_{1\rho}$ measured in [U-^{13}C, ^{15}N]GB1 at a single spin-lock field strength yielded order parameters and correlation times for backbone N-H vector motions, although the overall order parameters found were systematically higher than those measured using relaxation times in the solution state if a single time scale was assumed for each amide nitrogen.[276,360] Recently, a comparison of molecular dynamics (MD) simulations and ^{15}N relaxation measurements in GB1 showed that the order parameters are often dominated by slow motions and that ^{15}N R_1 (spin-lattice relaxation rates) and $R_{1\rho}$ may not be sufficient to effectively constrain the complex models required for a realistic description of protein dynamics in the solid state.[376] In general, consideration of ^{15}N relaxation alone may lead to an underestimation of the

extent of backbone protein dynamics.[360] Additional relaxation parameters from ^{13}C nuclei may thus provide further valuable constraints for motional models. In particular, ^{13}C' rates are sensitive to backbone motions with fluctuations (rotations) occurring about an axis parallel to N-H dipolar vectors, which are not detected by ^{15}N relaxation measurements.

^{13}C' R_1 relaxation rates have been shown to allow quantification of protein motions in fully protonated proteins.[114] However, even though the dipolar ^{13}C-^{13}C contribution to ^{13}C R_1 rates in [U-^{13}C]-labelled proteins is sensitive to slower (ns-μs) motions (as the expression for ^{13}C R_1 involves the $J(\omega_{C1} - \omega_{C2}) \approx J(0)$ spectral density[377]) other independent ^{13}C relaxation probes are desirable for achieving more reliable quantification of slow dynamics.

In the following, we demonstrate the feasibility of measuring site-specific ^{13}C' $R_{1\rho}$ relaxation rates as a method to probe backbone motions on ps-μs time scales in proteins in the solid state, and show how in combination with ^{13}C' R_1 and ^{15}N R_1 and $R_{1\rho}$ measurements they may be used to quantitatively characterise those motions. The methodology presented should aid in constraining models for slow motions in proteins, and also potentially pave the way for considering the directionality of motions.[345,365] The results that follow are organised into 5 subsections: in §10.2, the validity of our method is investigated by evaluating the extent to which the coherent contributions to the measured ^{13}C $R_{1\rho}$ rates are averaged under typical experimental conditions. In §10.3, a comprehensive range of ^{13}C' and ^{15}N relaxation rate measurements in crystalline [U-^{13}C,^{15}N]GB1 at 600 and 850 MHz ^{1}H Larmor frequencies are presented. These rates are quantified in §10.4 and §10.6 using models of increasing complexity. The intriguing results of the simplest model-free analysis in section §10.4 lead to a discussion in §10.5 on how motions with different time scales contribute to relaxation rates in the solid and solution states, highlighting fundamental differences in how dynamics influence measurements in the two phases. This exploration provides some understanding on such phenomena as observation of very high order parameters when analysing relaxation rates in the solid state and underestimation of nanosecond motions in solution.

10.2 Evaluation of Coherent Contributions to ^{13}C' $R_{1\rho}$

Measured $R_{1\rho}$ relaxation rates potentially reflect not only the effect of incoherent motions, but also contributions from anisotropic NMR interactions (*e.g.* dipolar couplings) that might not be completely removed by the magic angle spinning. We first

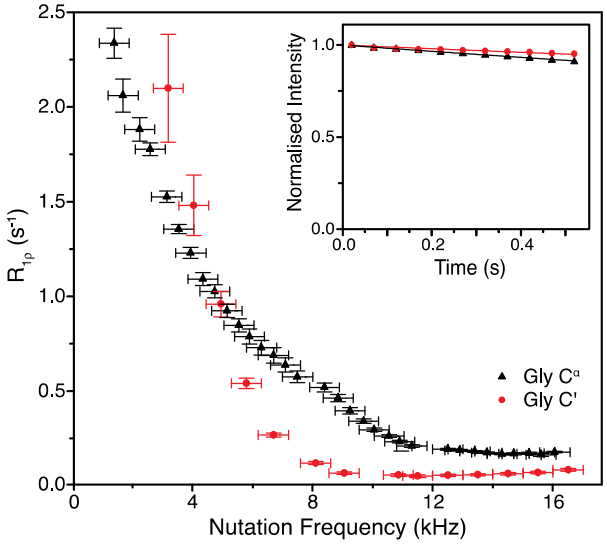

Figure 10.1. $R_{1\varrho}$ dispersion for ^{13}C' (red circle) and $^{13}C^{\alpha}$ (black triangle) in [U-^{13}C,^{15}N]glycine at $\omega_{0H}/2\pi$= 600 MHz, $\omega_r/2\pi$ = 60 kHz, and (inset) example $R_{1\rho}$ decay curves for with $\omega_1/2\pi$ = 17 kHz.

consider the magnitudes of contributions to measured $R_{1\rho}$ rates that originate from such coherent mechanisms, and the degree to which they might hamper extraction of the parameters needed for characterization of molecular motions.

Since for the ^{13}C' nucleus the interactions contributing to the coherent residual are different from those in the previously considered case of ^{15}N,[276] it is important to assess the extent to which they are averaged under typical experimental conditions. The coherent contribution depends on the geometry of the molecular system and the extent of the MAS and r.f. averaging (*e.g.* faster MAS frequencies lead to better averaging of the coherent residuals). For the same experimental set-up and similar sample geometries, the coherent contribution to ^{13}C $R_{1\rho}$ should be similar and therefore an estimate of an upper limit for this contribution under fast MAS should be obtainable from non-hydrated crystalline amino acids. Crystalline amino acid samples have similar internuclear geometries to proteins but the backbone motions and thus the relaxation rates are minimised.

To obtain such an estimate, on-resonance ^{13}C $R_{1\rho}$ rates in [U-^{13}C]glycine were measured at $\omega_r/2\pi$ = 60 kHz and $\omega_{0H}/2\pi$ = 600 MHz. Example decay curves for ^{13}C' and $^{13}C^{\alpha}$ (with a spin-lock pulse nutation frequency of $\omega_1/2\pi$ = 17 kHz) are shown in Figure 10.1 (inset). Note that in both cases the magnetization decays very little in 0.5 s, the length of the longest employed spin-lock pulse (data points were not sampled at longer spin-lock lengths due to hardware limitations). The main panel of Figure 10.1 shows the

dependence of the measured $R_{1\rho}$ rates upon the nutation frequency of the spin-lock pulse, again for both ^{13}C' and $^{13}C^{\alpha}$. Among the different types of carbon sites in proteins, a CH_2 group would be expected to have the largest coherent contribution to ^{13}C transverse magnetization decay because of the strong proton-proton couplings present and the lack of efficient motional averaging (this is also reflected in methylene carbons being the most difficult type of carbon site geometry to decouple from protons). Even so, $R_{1\rho}$ rates for $C^{\alpha}H_2$ in glycine plateau at a value of just 0.18 ± 0.01 s^{-1} ($T_{1\rho}$ = 5.68 ± 0.01 s) for ^{13}C nutation frequencies above ~12 kHz. In the case of ^{13}C', where there are no directly bonded protons, the measured $R_{1\rho}$ becomes 0.06 ± 0.01 s^{-1} at nutation frequencies above ~9 kHz, corresponding to an exceptionally long $T_{1\rho}$ of 16.7 ± 2.8 s. This means that even in the "worst case" of the CH_2 group, if the decay of transverse magnetization was purely the result of coherent processes then the coherent residual for protonated ^{13}C would have an upper limit of only ~0.18 s^{-1} at 600 MHz. Similarly, for ^{13}C', the residual of 0.06 s^{-1} is virtually negligible (*e.g.* < 1% of the measured ^{13}C' average $R_{1\rho}$ in [U-^{13}C,^{15}N]GB1, see below). This suggests that much greater decay rates measured in proteins (see below) are primarily determined by contributions induced by stochastic motions. Note that the increasing $R_{1\rho}$ values for nutation frequencies < 8 kHz are most likely in large part due to inadequately decoupled coherent contributions. Nevertheless, the rates at a nutation frequency of 2 kHz do not exceed 2.5 s^{-1}, which means that for cases where the exchange contributions to the rates are much larger than this value, relaxation dispersion may provide at least qualitative information about exchange processes.

Obviously, the observed $R_{1\rho}$ rates in amino acids such as glycine are not entirely due to coherent processes. In crystalline amino acids the dominant motional contribution to ^{13}C' relaxation originates from the rotations of CH_3 and NH_3 groups that modulate ^{1}H-^{13}C' dipolar couplings.[378] As the minimal ^{1}H-^{13}C' distance for both CH_3 and NH_3 groups is ~2.4 Å in glycine and alanine (and indeed the sum of all the dipolar couplings from protons < 5 Å from ^{13}C' is almost the same), the correlation time (τ_c) of the motions should be the main differentiating factor between the relaxation behaviours of ^{13}C' in these amino acids.[378] The correlation time of NH_3 rotation in crystalline glycine at room temperature is shorter (~0.9 ns) than the correlation times of the rotations of both CH_3 and NH_3 groups in crystalline alanine: τ_c for CH_3 is ~1.6 ns, while for NH_3 τ_c is orders of magnitude greater.[378] The slower motions of the CH_3 and NH_3 groups in alanine are expected to cause faster ^{13}C' transverse relaxation than the more rapid

rotation of the NH_3 group in glycine. Comparison of the $R_{1\rho}$ values measured for $^{13}C'$ in these two amino acids therefore allows further assessment of the coherent and relaxation contributions to the decay of transverse $^{13}C'$ magnetization under fast MAS conditions.

As expected from the slower correlation times for rotation of CH_3 and NH_3 groups, the measured $R_{1\rho}$'s are larger for alanine than for glycine under the same conditions, further confirming that the measured rates are almost exclusively due to relaxation induced by molecular motions. At $\omega_{0H}/2\pi$ = 600 MHz, $\omega_r/2\pi$ = 60 kHz and $\omega_1/2\pi$ = 16 kHz, the on-resonance $^{13}C'$ $R_{1\rho}$ rate for [1-^{13}C]alanine was measured at 0.83 ± 0.07 s^{-1} ($T_{1\rho}$ =1.2 ± 0.1 s), which is 14 times larger than the value for glycine $^{13}C'$. Note that since the $R_{1\rho}$ rates observed in glycine can be quite well accounted for by the relaxation induced by the incoherent motion of NH_3 (for example, for a correlation time of 0.9 ns and an order parameter of 0.65, $^{13}C'$ and $^{13}C^{\alpha}$ $R_{1\rho}$ calculated using an SMF approach are 0.18 and 0.06 s^{-1} respectively, *i.e.* the same as the measured rates), the coherent residuals are in reality even smaller than the values quoted above.

It should be noted that at rotary resonance and HORROR conditions, the coherent residual will be much larger (leading to a faster decay) due to the reintroduction of CSA and/or dipolar couplings. The experimental settings that match these conditions should either be avoided, if one is interested in the pure relaxation contribution,[147,344,365,379] or the effect should be taken directly into account.[350] As shown for the ^{15}N nucleus, larger $R_{1\rho}$ values are also observed at lower spinning frequencies due to less effective MAS averaging of the coherent residual in protonated samples (Figure C.6 in Appendix C).

In summary, in order to minimise the coherent contribution and obtain a reliable estimate of the incoherent R_2 for ^{13}C (including carbons with directly bonded protons) from $R_{1\rho}$ measurements in fully protonated samples, experiments should be performed at spinning frequencies above 45 kHz and employing spin-lock fields of >10 kHz with a reasonable offset from the rotary resonance and HORROR conditions. Additional experimental considerations of "mis-setting" the magic angle (small effect on the measured rate), sample heating (small effect) and polarisation transfer during r.f. irradiation (no significant polarisation transfer due to r.f. driven spin diffusion is observed) are addressed in Appendix C (§§C.4.1-C.4.3).

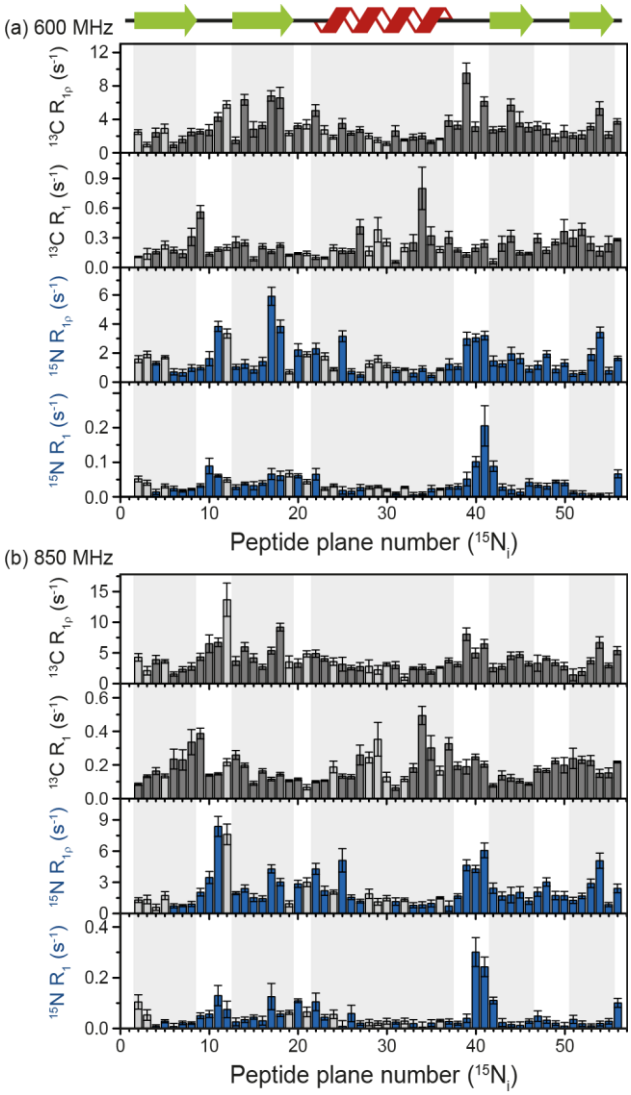

Figure 10.2. ^{13}C' and ^{15}N R_1 and $R_{1\rho}$ relaxation rates measured on [U-^{13}C,^{15}N]GB1 as a function of peptide plane (numbering following residue number for ^{15}N). The measurements were performed at $\omega_{0H}/2\pi$ = 850 MHz and $\omega_r/2\pi$ = 60 kHz. The spin-lock nutation frequency was $\omega_1/2\pi$ = 17 kHz for both ^{13}C' and ^{15}N $R_{1\rho}$ measurements. Sample temperature was 27 °C for all experiments as determined by the chemical shift of water.[282] Rates that were extracted from peaks with partial overlap are shown in light grey.

10.3 Measurement of ^{13}C' and ^{15}N R_1 and $R_{1\rho}$ Relaxation Rates

The above discussion suggests that in hydrated proteins in the solid state, $R_{1\rho}$ rates for each individual ^{13}C' atom in the backbone may be measured in order to build up a dynamic picture of the molecule that should be highly complementary to that emerging from ^{15}N measurements. In this spirit, we measured site-specific ^{13}C' $R_{1\rho}$ for fully protonated, hydrated microcrystalline [U-^{13}C, ^{15}N]GB1 at $\omega_{0H}/2\pi$ = 850 MHz and 600 MHz, with $\omega_r/2\pi$ = 60 kHz, $\omega_1/2\pi$ = 17 kHz, and a sample temperature of 27 °C. In order to enhance spectral resolution the effect of one-bond C'-C$^\alpha$ scalar couplings was

eliminated in these experiments by including an S^3E block in the pulse sequence.[380,381] The measured rates are shown in Figure 10.2, along with $^{13}C'$ R_1 and amide ^{15}N R_1 and $R_{1\rho}$ measured at both fields under the same experimental conditions. All of the rates are plotted against the number of the peptide plane containing the particular ^{13}C or ^{15}N nucleus (which by convention follows the number of the ^{15}N nucleus, *e.g.* peptide plane 2 refers to ^{15}N in residue 2 and $^{13}C'$ in residue 1). Rates flagged in light grey were extracted from resonances with partial overlap (see spectrum in Figure C.7 in Appendix C for assignments) and thus are likely to be less accurate than those derived from fully resolved peaks. Tabulated values for the fit parameters for $^{13}C'$ and ^{15}N $R_{1\rho}$ and R_1 relaxation curves for all resonances can be found in Ref. 357 (the average rates for 850 and 600 MHz are, respectively, $^{13}C'$ R_1 0.1 & 0.2 s^{-1}, $^{13}C'$ $R_{1\rho}$ 4.2 & 3.2 s^{-1}, ^{15}N R_1 0.05 & 0.04 s^{-1}, ^{15}N $R_{1\rho}$ 2.3 & 1.6 s^{-1}).

Upon inspection of Figure 10.2 it is immediately obvious that, at both fields, the measured $^{13}C'$ $R_{1\rho}$ rates and the differences between them across different residues are one to two orders of magnitude greater than the upper limit of the coherent contribution as given by the measurement on glycine at 600 MHz (0.06 ± 0.01 s^{-1}). The rates measured in the protein are evidently almost exclusively due to relaxation induced by molecular motions. It is also clear that there is a strong correlation between rates at different fields, and generally the same features are present in both sets of data. For example, elevated rates are seen in the flexible loop and terminal regions (*e.g.* T11C' with $R_{1\rho} = 14.6 \pm 2.9$ s^{-1} at $\omega_{0H}/2\pi = 850$ MHz), while generally lower rates are observed in the α-helix and the central residues in β-strands with a minimum of 1.6 ± 0.4 s^{-1} for L5C' at $\omega_{0H}/2\pi = 850$ MHz. Our generous estimate for the upper bound of the coherent residual at $\omega_{0H}/2\pi = 600$ MHz is in fact more than 11-14 times smaller than the mean experimental error in $^{13}C'$ $R_{1\rho}$ (0.68 s^{-1} at $\omega_{0H}/2\pi = 850$ MHz and 0.84 s^{-1} at $\omega_{0H}/2\pi = 600$ MHz).

While $R_{1\rho}$ and R_1 rates for both ^{15}N and ^{13}C vary significantly between residues, many features along the backbone are common between them (in particular for the ^{15}N and ^{13}C located in the same peptide planes, *i.e.* $^{15}N_i$ and $^{13}C'_{i-1}$, which is expected due to the rigid planar nature of the peptide bond). On the other hand, some features are apparent in the R_1 rates that are not present in the $R_{1\rho}$ rates (*e.g.* a marked increase in ^{13}C R_1 at Y33C'). This is likely due to the different dependence of these relaxation rates on the time scales of the motions causing the relaxation. Further analysis of these phenomena is carried out in the following sections via quantitative modelling.

10.4 Quantification of ^{13}C' and ^{15}N Relaxation Rates using the Simple Model-Free Approach

To explore the influence of backbone dynamics on ^{15}N and ^{13}C' relaxation data in greater depth, in the following we fit our data using SMF and EMF approaches (see below). Nuclear relaxation originates from fluctuations of local magnetic fields, caused by modulation of interactions (*e.g.* dipolar couplings or CSA) by incoherent molecular motions. Quantitative modelling of ^{13}C' relaxation is potentially more complex than that of ^{15}N owing to a larger number of interactions that must be included in the modelling. ^{15}N relaxation is dominated by a dipolar contribution, but with a substantial contribution from the CSA mechanism at higher fields:

$$R_{1,N} = R_{1,NH} + R_{1,NCSA} \tag{10.1}$$

$$R_{1\rho,N} = R_{1\rho,NH} + R_{1\rho,NCSA} \tag{10.2}$$

where each of the terms can be expressed in terms of spectral densities as outlined in §2.3. ^{13}C' relaxation, even though dominated by the CSA, may require consideration of several other contributions. For example, multiple dipolar contributions including those from C$^{\alpha}$, N and nearby protons may need to be included depending on the desired precision of modelling:

$$R_{1,C'} = R_{1,C'CSA} + R_{1,C'C\alpha} + R_{1,C'N} + R_{1,C'H} \tag{10.3}$$

$$R_{1\rho,C'} = R_{1\rho,C'CSA} + R_{1\rho,C'C\alpha} + R_{1\rho,C'N} + R_{1\rho,C'H} \tag{10.4}$$

Slow fluctuations of the dipolar C'-C$^{\alpha}$ vector may contribute significantly to spin-lattice relaxation, as this depends on the spectral density sampled near zero frequency, which increases monotonically with the increasing correlation time of the motions. For the analyses below, site-specific ^{15}N CSAs, parameterised using ^{15}N isotropic chemical shifts,[366] and site-specific ^{13}C' CSA, parameterised using ^{13}C' isotropic chemical shifts,[382] were used (see Table C.1 in Appendix C). Under the conditions employed in this study, the ratios between the spin-lock field strengths and frequency offsets were such that the tilt angle did not exceed 4° even at 850 MHz. The rates are therefore analysed here as on-resonance $R_{1\rho}$ (though the effect could be included – see §2.3.7).

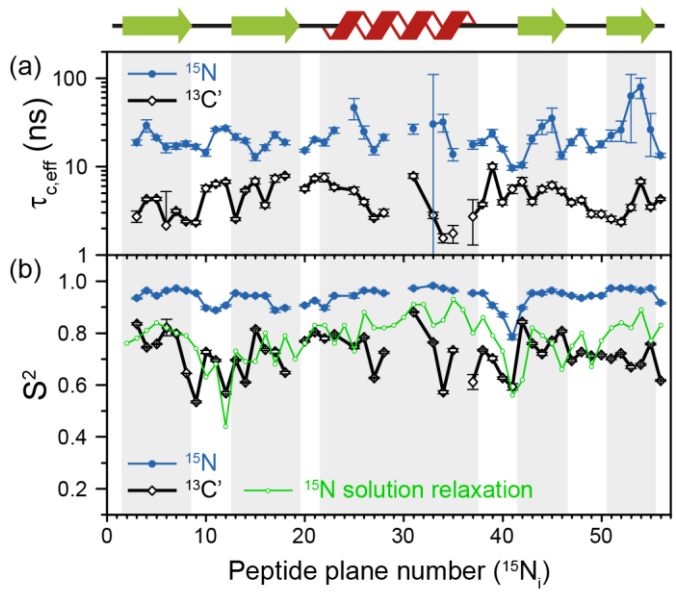

Figure 10.3. Comparison of results from a simple model-free (SMF) analysis of backbone motions in GB1 based on measured ^{15}N and ^{13}C' $R_{1\rho}$ and R_1 rates (see Figure 10.2): (a) correlation time ($\tau_{c,eff}$) and (b) order parameter for ^{15}N (S^2_{NH}, blue circles) and ^{13}C' ($S^2_{C'}$, black diamonds) as a function of peptide plane number (numbering according to the residue number for ^{15}N). The green line in (b) depicts S^2_{NH} obtained from GB1 relaxation in solution.[371,372] The data for which severe peak overlap hindered accurate measurement of relaxation rates have been excluded.

A specific form of the spectral density *J(ω)* (*i.e.* the Fourier transform of the correlation function describing the time dependence of local magnetic field fluctuations) needs to be assumed to compute relaxation rates. In the first instance, neglecting any orientational dependence of the relaxation rates, we assume the simplest case of isotropic motion occurring on a single time scale. Accordingly, to model the relaxation rates we use the simple model-free (SMF)[33,359] formalism with spectral densities expressed as in equation 7.4. Although this over-simplified model will not describe the motions occurring on multiple time scales, and may have shortcomings in modelling correlation functions in the solid state, which generally are non-exponential in nature,[354] it still proves to be an informative and useful approximation. In particular, in several cases considered to date, the order parameters obtained by analysing the relaxation data either by the SMF approach (which does not take orientational dependence of relaxation rates into account) or diffusion-in-a-cone with EAS (which does take into account orientational dependence of relaxation rates) are almost the same.[55,147]

The results of the analysis of our relaxation rates using the SMF form of the spectral density, when ^{15}N and ^{13}C' R_1 and $R_{1\rho}$ relaxation rates are considered separately, are presented in Figure 10.3. The S^2 values determined from ^{13}C' and ^{15}N data follow

similar trends but the $S^2_{C'}$ values are on average lower than S^2_{NH} by >0.2 (Figure 10.3b). The largest deviations from the overall trend are generally observed for the residues in the loops or edges of the secondary structure elements, *e.g.* peptide planes 35 to 40.

In Figure 10.3b the SMF order parameters from the solid-state relaxation are also compared to the overall solution-state S^2_{NH} derived from relaxation measurements (and thus reporting generally on <4 ns motions; light green).[371] It is clear that the S^2_{NH} values determined in the solid state are unusually high, if they are to be treated as the overall order parameters (*i.e.* order parameters for motions in the ps-μs range affecting the solid state relaxation rates).[276,360,376] The $S^2_{C'}$ values, however, are similar to the overall S^2_{NH} values determined in solution except for parts of the helix and the β_4 strand where the $S^2_{C'}$ values are systematically lower. The effective SMF correlation times obtained from ^{13}C' solid-state data (average ~5 ns) are also systematically different from the effective correlation times obtained from ^{15}N solid-state data (average ~23 ns) (see Figure 10.3a).

10.5 Differences Between Results of SMF Analyses of ^{13}C' and ^{15}N Relaxation Rates

In the light of typically high level of correlation of S^2_{NH} and $S^2_{C'}$ observed in solution NMR studies for the same peptide plane,[383] the large offset observed between such values in the solid state may appear initially perplexing. Even in the presence of anisotropic motions[372] one would expect the order parameters and the time scales to be more similar than what we observe here. As we will see in the following, the observation of the very high solid state SMF S^2_{NH} order parameters, as well as the overall offsets between S^2_{NH} and $S^2_{C'}$ and between the correlation times, may be understood by considering how motions occurring on different time scales contribute to the spectral densities used to calculate the relaxation rates. Such an inspection provides valuable insights into the fundamental nature of relaxation in the solid state, especially when contrasted against relaxation in the solution state.

As mentioned, the exact form of the spectral densities is model-dependent; in §10.4 we used a single time scale SMF analysis, but in general protein motions can occur on multiple time scales. Such a situation can generally be better accounted for by using an extended model-free (EMF) analysis, which includes two (or more) different time scales and associated order parameters (equation 7.5).[358,359] According to a solution NMR study by Idiyatullin *et al.*, all of the residues in GB1 are characterised by both picosecond-range

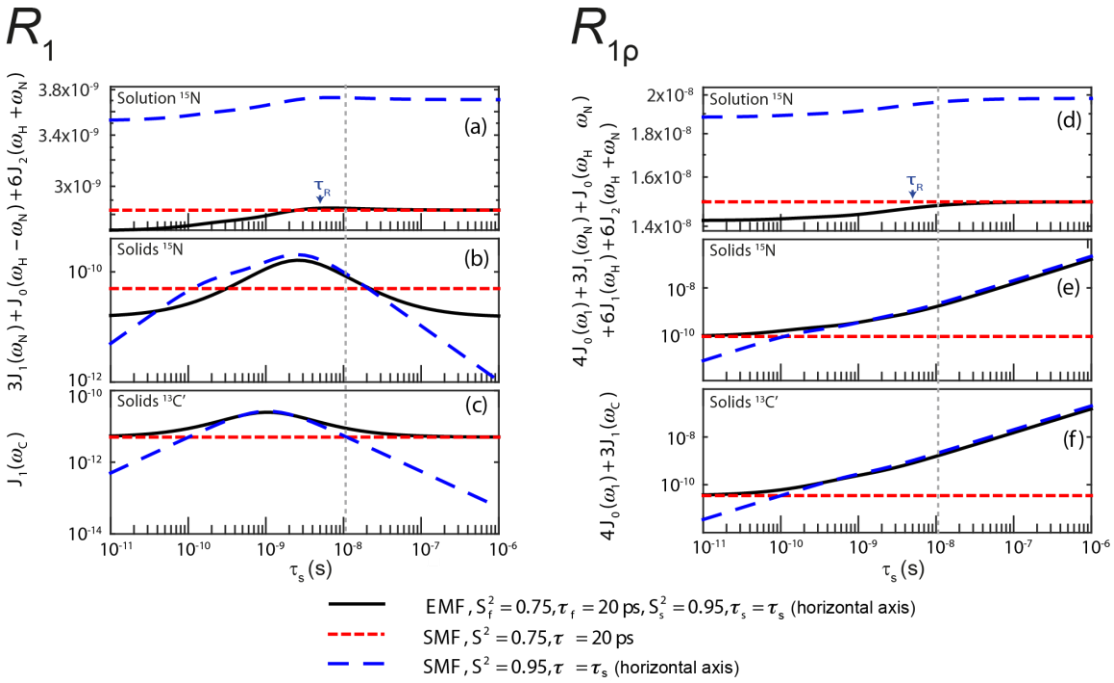

Figure 10.4. Simulations of contributions of a typical fast picosecond motion and a low-amplitude slow nanosecond motion to the main contributing spectral densities to R_1 (a-c) and $R_{1\varrho}$ (d-f) rates in solution and solids. (a,d) Spectral densities for ^{15}N dipolar relaxation in solution. (b,e) Spectral densities for ^{15}N dipolar relaxation in solids. (c,f) Spectral densities for ^{13}C' CSA relaxation in solids. Red short-dashed lines represent spectral densities calculated using the SMF for a fast motion with S^2=0.75, τ_f= 20 ps. Blue long-dashed lines represent spectral densities calculated using the SMF for a slow motion with S_s^2=0.95 and τ_s as indicated on the horizontal axis. All simulations were performed with $\omega_{0H}/2\pi$ = 600 MHz. The overall rotational diffusion correlation time for the solution simulation was assumed to be 4 ns. The expressions and other parameters used for the simulations are given in § 7.6 and §§ C.2&C.3 in Appendix C.

and nanosecond-range motions.[384] An EMF analysis yielded an average fast motion order parameter, S_f^2, of approximately 0.75, a fast motion correlation time, τ_f, on the order of tens of picoseconds, a slow motion order parameter, S_s^2, greater than 0.9 and a slow motion correlation time, τ_s, on the order of a few nanoseconds.

To assess the different contributions of these typical fast and slow motions to relaxation rates calculated by model-free analyses, we simulated the spectral density terms for a fast motion (τ_f= 20 ps, S_f^2 = 0.75) and for a smaller amplitude slow motion (10^{-11} < τ_f < 10^{-6} s, S_s^2 = 0.95), using the solution- and solid-state SMF formalisms (Equations 7.3 and 7.4). We also conducted simulations for the same motions occurring simultaneously using the solution- and solid-state EMF formalisms (Equation C.1 in Appendix C and Equation 7.5). The results of these simulations are shown in Figure 10.4, for ^{15}N in both solution and solids and for ^{13}C in solids, as a function of the correlation time of the slow

motion. This figure shows the behaviour of R_1 and $R_{1\rho}$ relaxation rates calculated by an SMF treatment of pure slow motion (dashed blue line) or pure fast motion (dashed red line), as well as by an EMF treatment of both fast and slow motions simultaneously (solid black line).

Assuming the motions in GB1 occur on both ps and ns time scales,[384] the spectral densities calculated by the EMF will be more "correct", *i.e.* the calculated relaxation rates will be closer to those that would be measured experimentally given motion on those two time scales. By analysing the same two motions separately with the SMF, we can observe how the spectral densities calculated compare to those calculated using the EMF. We can then use these observations to extrapolate to a case where the SMF is used to model a two-component motion.

Figure 10.4 illustrates that the same fast and slow motions contribute differently to the spectral densities (and hence calculated relaxation rates) in the solution state and in the solid state. For EMF in the solution state, the presence of overall rotational diffusion modifies the effective correlation times for the fast and slow motions, with the result that the spectral densities (for both R_1 and $R_{1\rho}$) calculated by the EMF are similar to those calculated by the SMF including *only the fast motion* (see Figures 10.4a,d – the black lines closely follow the dashed red lines). Conversely, in the solid state, the absence of overall tumbling means that the fast and slow motion contributions to EMF spectral densities are purely dependent on the order parameters and time scales of those motions. Compared to the solution case, this results in a greater relative contribution of slow motions to the spectral densities. For example, in the case of both ^{15}N and ^{13}C $R_{1\rho}$, the fast motion contribution to the spectral densities can be smaller than 1% of the slow motion contribution, even if S_f^2 is much lower than S_s^2. The result of this is that the $R_{1\rho}$ relaxation rates calculated by the EMF are very similar to those calculated for correlation times of >0.1 ns by the SMF using *only the slow motion* (see Figures 10.4e,f – the black lines closely follow the dashed blue lines).

A similar situation arises for R_1 in solids: for a wide range of τ_s the contributions of the small amplitude slow motions to spectral densities are much larger than the contributions of larger amplitude fast motions. Above a certain time scale, however, the fast motion contribution begins to dominate (see Figures 10.4b,c – the black line veers toward the dashed red line above ~10^{-8} s). Crucially, the time scale at which this occurs is shorter for ^{13}C than it is for ^{15}N. As a guide, the vertical dashed grey line indicates the slow motion time scale at which the fast motion SMF spectral densities begin to

dominate over the slow motion SMF spectral densities for ^{13}C' R_1. At this time scale (and for a range of slower time scales) the slow motion still dominates for ^{15}N. As a result, a situation can occur where the calculated ^{15}N R_1 is dominated by the *slow motion* component while the calculated ^{13}C' R_1 is dominated by the *fast motion* component.

Consequently, in the solid state, if the SMF approach is used to analyse ^{15}N relaxation rates induced by both a fast motion and a slow motion (of *e.g.* 15 ns), the data often may be almost entirely accounted for by the slow motion only, even if the amplitude of the slow motion is small compared to that of the fast motion (an observation also made in Ref. 360). In such a case, for ^{15}N a good SMF fit will be obtained with an order parameter, S^2_{SMF}, closer to the slow motion order parameter, S^2_s, rather than the overall order parameter, $S^2_{overall} = S^2_f \cdot S^2_s$, and with an effective correlation time faster than the actual correlation time for the slow motion, τ_s (see also Figure C.8 in Appendix C). This explains why solid-state SMF analyses of ^{15}N relaxation rates in relatively rigid proteins such as GB1 and ubiquitin yield very high order parameters.[276,360] In contrast, the same nanosecond/picosecond motions would result in a much larger contribution from the fast motion to ^{13}C', with the determined order parameter, S^2_{SMF}, being closer to the order parameter for fast motion, S^2_f, and the effective correlation time much smaller than the correlation time for the slow motion, τ_s. This is exactly what we observe when fitting solid-state relaxation in GB1 using the SMF formalism (see also Figure C.8). Thus, the offset between SMF order parameters for ^{15}N and ^{13}C' confirms that *all residues in GB1 undergo motions on at least two distinct time scales* – picosecond-range and nanosecond range or even slower.

The dominant contribution of fast picosecond motions to spectral densities in solution leads to the opposite effect to that observed in solids. Based on the analysis of synthetic data, even in the presence of small amplitude nanosecond motions, a good SMF fit can be obtained with motional parameters close to the amplitude and time scale of the fast picosecond motion (*i.e.* a single-time scale fast motion model can explain the two-time scale motion well when the slow motion has a small amplitude, because the spectral densities calculated by the EMF and SMF are similar). If the amplitude of the slow motion is much smaller than that of the fast motion then the use of an EMF analysis may not be statistically justifiable. It is likely that such a phenomenon is partially behind the fact that the EMF seems to be required primarily only for modelling residues in loop regions of proteins, where the amplitudes of slow motions are sufficiently large to lead to a statistically valid improvement of an EMF fit over an SMF fit. Another

consequence of this behaviour is that, in solution, a large number of independent data points (*e.g.* data at several different magnetic fields) may be necessary to identify motions that are slow (but still faster than the correlation time for the overall rotational diffusion) but of relatively small amplitude. In line with these observations, recent relaxometry experiments show that nanosecond motions are likely to be significantly underestimated by the traditional EMF analysis based on solution relaxation data obtained at one or two magnetic field strengths.[385]

The above considerations of the spectral densities in the solid state have profound consequences for the interpretation of the solid-state relaxation data. Firstly, even in relatively rigid systems such as GB1, SH3 or ubiquitin, solid-state relaxation data need to be interpreted by models including multiple time scales.[332,356,386] This is also consistent with the hierarchy of protein motions established by variable temperature relaxation measurements in the solid state, where for every residue at least two motional modes with distinct activation energies were identified for backbone motions.[260] Secondly, relaxation rates alone are not sufficient to obtain a good estimate of the overall order parameter. Notably, addition of ^{13}C' R_1 and $R_{1\rho}$ to the analysis of ^{15}N R_1 and $R_{1\rho}$ does not assist in obtaining a good estimate of the overall order parameter (only one parameter out of four, ^{13}C' R_1, is dominated by the fast motion; when weights of the data points in the fitting procedure are related to the experimental errors no special weight is given to ^{13}C' R_1, resulting in slow motion domination). Lack of sensitivity to fast motions may in fact be beneficial in certain situations, for example when modelling concerted anisotropic motions of a protein fragment.[345,365] In such a case, neglecting fast picosecond motions in the fitting routine should not incur large errors for estimating the amplitudes of slow overall motions. Currently, the only way to obtain an estimate of $S^2_{overall}$ and S^2_f is to constrain the overall amplitudes of motion by independent measurements of dipolar couplings or CSA.[332,356,360] In the absence of an overall constraint on the order parameter, even though the relaxation rates originate from motions on multiple time scales, employing an EMF fit is unlikely to yield realistic values for S^2_f.[360,376] A caveat of this approach is that a relatively small error in the determination of the dipolar order parameter may lead to quite a significant error in the subsequent estimate of S^2_f.[376]

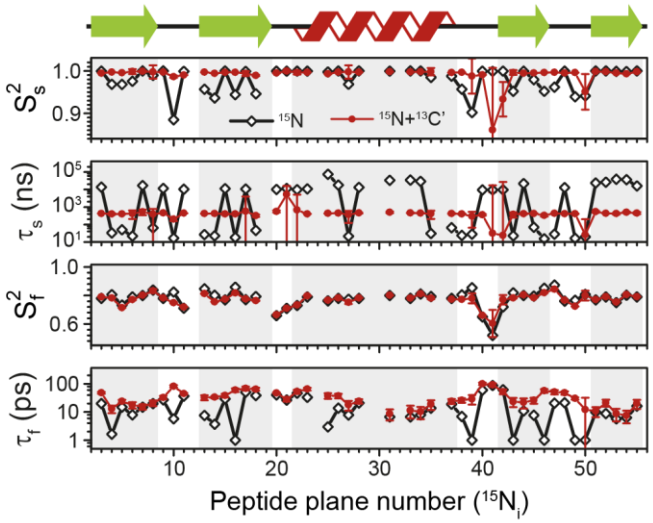

Figure 10.5. Comparison of an extended model-free (EMF) analysis of backbone dynamics based on ^{15}N R_1 and $R_{1\rho}$ relaxation (black line) and combined ^{15}N R_1 and $R_{1\rho}$ and ^{13}C' R_1 and $R_{1\rho}$ relaxation for the sites in the same peptide planes (red line). S_s^2, τ_s, S_f^2 and τ_f are, respectively: order parameter for the slow motion, correlation time for the slow motion, order parameter for the fast motion and correlation time for the fast motion. Measurements performed both at 600 and 850 MHz spectrometers were used in both cases. The overall amplitude of motion was constrained by measurements of N-H dipolar couplings, which are averaged by motions faster than the inverse of its rigid limit value. The data for which N-H dipolar couplings were not available or for which severe peak overlap hindered accurate measurement of relaxation rates were excluded.

10.6 Extended Model-Free Analysis of Peptide Plane Motions

The above discussion indicates that to adequately describe dynamics in crystalline GB1 using relaxation, models involving motions occurring on at least two timescales need to be considered. Based on the case of crystalline SH3, Zinkevich *et al.* have argued that in some cases three time scales may be required.[386] In §8.2, we found using ^{15}N $R_{1\rho}$ relaxation dispersion that only a handful of residues in crystalline GB1 exhibit μs-range motions (clear dispersion is observed only for residues 17, 19, 20, 44, 46, 49-53), suggesting that for the majority of residues the dynamics can be well described by motions in the ps-ns range (though nothing is known at present about ms-range motions). Because this range of time scales is shorter than the inverse of the N-H dipolar coupling strengths (in Hz), measurements of dipolar couplings may be used to constrain the overall amplitudes of the motions (the μs-range motions highlighted by the dispersion measurements, on the other hand, are likely too slow to effectively influence the directly measured dipolar order parameter). In addition, the expressions for $R_{1\rho}$ presented in §§2.3.5-2.3.7 can be used without including the influence of spinning

frequency[147], which should generally be taken account of if motions in the μs-ms regime are present.

First, to establish our baseline, we performed a fit using only ^{15}N R_1 and $R_{1\rho}$ data measured at 600 MHz and 850 MHz magnetic fields, with dipolar NH order parameters[366,376] used to constrain the overall amplitude of motions. This scheme represents roughly the current state of the art in the literature.[280,332,356,360,386] To model ^{15}N relaxation, we included dipolar contributions from the directly bonded proton, C^{α} and C', site-specific ^{15}N CSA, and dipolar contributions from other protons implemented as an additional effective N-H coupling[387] (see Table C.1 in Appendix C). The results of the fits are presented in Figure 10.5 (black diamonds and lines). The emerging picture of the dynamics in crystalline GB1 is consistent with similar analyses on other model crystalline systems such as SH3 and ubiquitin: all residues seem to be characterised by larger amplitude picosecond motions and smaller amplitude (order parameters close to 1) slow motions with a correlation time in the ns-μs range. Only a few residues in loops exhibit larger-than-average slow motions. Notably, the order parameters for the fast picosecond motions are on average similar to the overall order parameters for GB1/GB3 in solution,[371,384,388] providing another example that indicates the overall high level of similarity of fast picosecond dynamics for globular proteins in solution and hydrated crystals.[335,359]

In spite of this reassuringly familiar view of GB1 dynamics, there are a few points of concern: for a number of residues the fast correlation times are in the low-picosecond regime (or at the 1 ps bound imposed in the fitting procedure; several such points were also found in a recent EMF analysis of ^{15}N relaxation in ubiquitin[360]) and for the majority of the residues slow correlation times are in the microsecond regime. Both of these features are likely to be fitting artefacts, with the data not providing sufficient basis for an accurate description of the dynamics. Motions with correlation times of a few picoseconds have a negligible effect on the measured relaxation rates and as such these kinds of motions are unlikely to be accurately determined from relaxation measurements. On the other hand, the omnipresence of microsecond motions is inconsistent with the lack of microsecond exchange as demonstrated by ^{15}N $R_{1\rho}$ relaxation dispersion in crystalline GB1 (similarly, in ubiquitin a few residues, *e.g.* 10, 44, 63, were found where microsecond motions were detected through an EMF analysis of ^{15}N relaxation rates but not confirmed in ^{15}N relaxation dispersion[350,360]). An examination of the determined parameters reveals that, for many residues, the parameters for the fast

motion are such that they have negligible contributions to $R_{1\rho}$ and the parameters for the slow motions have negligible contributions to R_1. These results suggest that even though the considered data set is sufficient to obtain fairly reasonable estimates of the amplitudes of motion, it is not sufficient to facilitate accurate determination of time scales of motions.

This situation may improve as data measured at a larger number of magnetic fields, or at least much more different magnetic fields, is available to provide better sampling of the spectral density at different frequencies. Indeed, if we include ^{15}N R_1 and $R_{1\rho}$ previously measured at a magnetic field of 1000 MHz,[276] the "artefactual" microsecond slow motions and 1 ps fast motions are eliminated for several residues (see Appendix C, Figure C.9.). For many others, however, microsecond motions are still detected, in direct disagreement with the relaxation dispersion data. The situation is not greatly improved by using expressions for $R_{1\rho}$ that explicitly include spinning frequency effects (see Appendix C, Figure C.9.).[147]

A potential solution to this problem could be to supplement the data with ^{13}C' data, which, at the same magnetic fields, enable sampling of spectral densities at very different frequencies. Typically, in solution, order parameters for ^{15}N and ^{13}C' in the same peptide planes are highly correlated, with only a slight offset between them.[383] This is expected because due to the rigid planarity of the peptide bond, ^{15}N and ^{13}C' are likely to undergo similar motions. Even though such motions are expected to be anisotropic in nature,[372,383] to the first approximation data can be treated reasonably well by assuming isotropic fluctuations of the peptide planes.[383]

Following the assumption of isotropic peptide plane motions we refitted the data, adding ^{13}C' R_1 and $R_{1\rho}$ data at 600 MHz and 850 MHz magnetic fields to the EMF analysis. To model ^{13}C' relaxation we included site-specific ^{13}C' CSA, dipolar contributions from the couplings to C^{α}, N and H^N, and dipolar contributions from other protons implemented as an additional effective ^{13}C'-^{1}H coupling[387] (see Table C.1 in Appendix C). The results of the combined ^{13}C' and ^{15}N fits are depicted in Figure 10.5 (red circles and lines), where they are overlaid with the results of analysis based on ^{15}N data only. For most residues, the changes in order parameters upon inclusion of ^{13}C' relaxation rates in the analysis are relatively small. However, there is a pronounced effect on the determined time scales. In particular, the slow correlation times are less than 1 μs for most residues (average ~500 ns), in line with the results of ^{15}N relaxation dispersion. The overall fairly consistent time scale for slow motions in the secondary structure

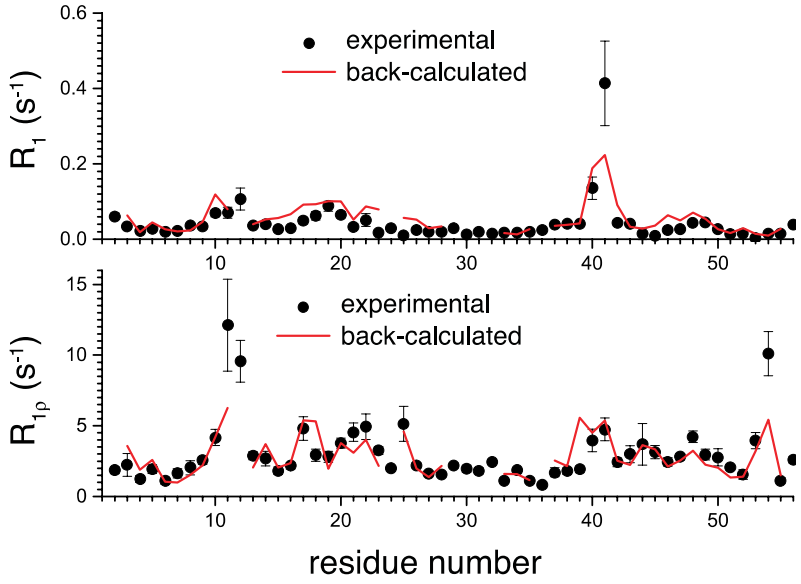

Figure 10.6. Comparison of ^{15}N relaxation rates measured in crystalline GB1 at 1 GHz ^{1}H Larmor frequency (black points) and those back-calculated from an EMF analysis based on ^{15}N and ^{13}C' R_1 and $R_{1\varrho}$ measurements performed at 600 and 850 MHz ^{1}H Larmor frequency with ^{15}N dipolar coupling measurements used for constraining the overall amplitude of motions (red line).

elements (very different time scales only appear in the loops) may be suggestive of an overall small amplitude motion.[365] A few resonances for which clear relaxation dispersion is observable may require a model that includes motions occurring on three time scales but it is not entirely obvious how one could constrain their amplitude (the dipolar order parameter only reflects motions faster than the inverse of the coupling's strength, *i.e.* in the µs-regime). In addition, the artefactual low picosecond motions are removed and the overall trend of time scales along the protein backbone varies more "smoothly" from residue to residue. Interestingly, the determined fast correlation times become overall similar to the fast correlation times determined in GB1 under similar conditions in solution, which, together with similar S_f^2,[371] again further highlights the similarity of fast protein dynamics in solution and hydrated crystals.

To further validate the obtained picture of GB1 dynamics, we back-calculated ^{15}N R_1 and $R_{1\rho}$ rates for 1000 MHz ^{1}H Larmor frequency based on the EMF analysis of 600 and 850 MHz data and compared them to previously-measured experimental values.[276] In spite of the fact that the measurements at 1000 MHz were not conducted at the exact same temperature as those at 600/850 MHz (25 °C vs. 27 °C), the back-calculated values agree remarkably well with the experimental values (Figure 10.6).

10.7 Conclusions

In summary, ^{13}C $R_{1\rho}$ measurements under conditions of >50 kHz MAS and >8 kHz spin-lock fields is a robust, quantitative probe of slow protein motions in the solid state that is highly complementary to ^{15}N relaxation measurements. It was shown that solid-state $R_{1\rho}$ rates are exceedingly sensitive to even very small-amplitude slow conformational changes. A comparison of simple model-free analyses of ^{15}N and $^{13}C'$ R_1 and $R_{1\rho}$ data illustrated that relaxation in GB1 in solid state is in general induced by motions occurring on multiple time scales, but usually dominated by the slower nanosecond-range motions. Analysing the differences between solution- and solid-state spectral densities, we could explain why very high order parameters are obtained from simple model-free analyses of ^{15}N relaxation in the solid state, and why nanosecond motions are likely to be underestimated in a standard relaxation analysis of solution NMR. It was also shown that by combining ^{15}N and $^{13}C'$ relaxation data it is possible to obtain a more physically meaningful dynamical description of proteins that is highly complementary to the picture provided by other techniques.

10.8 Experimental Details

NMR experiments were conducted on a Bruker Avance III spectrometer operating at $\omega_{0H}/2\pi$ = 850 MHz and a Bruker Avance II+ spectrometer operating at $\omega_{0H}/2\pi$ = 600 MHz, using a Bruker 1.3 mm triple-resonance probe at each field. Unless otherwise stated, experiments were performed at 60 kHz MAS frequency, at a sample temperature of 27.0 ± 0.5 °C as measured by the ^{1}H chemical shift of water with respect to DSS.[282] The pulse sequence used to collect $^{13}C'$ $R_{1\rho}$ rates (Figure C.10a in Appendix C) was based on a standard NCO DCP[186] sequence followed by a spin-lock pulse on the carbon channel whose length was incremented across each series of experiments. An S^3E block[380] was added to enhance resolution in the direct dimension by removing the effect of one-bond C'-C^{α} scalar couplings. A similar sequence (but with the spin-lock pulse instead on the ^{15}N channel, before the indirect acquisition (t_1) period) was used to measure site-specific backbone amide ^{15}N $R_{1\rho}$ rates (see Fig. S10). For all $^{13}C'$ and ^{15}N $R_{1\rho}$ experiments (unless otherwise stated), the spin-lock nutation frequency was set to 17 kHz, calibrated using nutation spectra.

^{13}C and ^{15}N R_1 rates were measured using sequences based on a standard NCO, but with a delay period (directly before t_1 acquisition for ^{15}N R_1, directly after ^{15}N-^{13}C CP for $^{13}C'$ R_1) that was incremented between experiments. $\pi/2$ pulses were applied either

side of this delay (100 kHz on ^{13}C for $^{13}C'$ R_1, 83.3 kHz on ^{15}N for ^{15}N R_1). All sequences are given in Appendix C (Figure C.10).

All sequences were initialised with a 100 kHz $\pi/2$ ^{1}H pulse, followed by adiabatic double-quantum CP[107] from ^{1}H to ^{15}N (1.5 ms, $\omega_{1H}/2\pi \approx 50$ kHz, $\omega_{1N}/2\pi = 10$ kHz). After t_1 evolution, magnetization was transferred to ^{13}C by a second adiabatic CP (9 ms, $\omega_{1N}/2\pi \approx 50$ kHz, $\omega_{1C}/2\pi = 10$ kHz). During t_1 ($t_{1,max}$ =10 ms) and t_2 (40 ms at 850 MHz, 25 ms at 600 MHz) acquisition, slpTPPM decoupling[114] was applied at a field strength of ~15 kHz.

Spectra were processed with TopSpin 2.1, and the relaxation series were subsequently analysed using CcpNmr Analysis 2.2.2. Final relaxation curve fitting was completed in Origin 8.5.

Fitting of the relaxation data to SMF and EMF equations was performed in Matlab. The magnitudes of each of the interactions included are detailed in Appendix C (Table C.1). The minimisation was performed using code based on the *fminsearch* function with several random starting points to ensure a global minimum was found. The best-fit amplitude and time scale parameters for all the models were determined by minimizing the χ^2 target function:

$$\chi^2 = \sum_i \frac{\left(X_{i,calc} - X_{i,exp}\right)^2}{{\sigma_{i,exp}}^2} \tag{10.5}$$

where X_i are relaxation rates and dipolar coupling measurements, σ_i appropriate experimental errors. The rigid limit NH distance was assumed to be 1.02 Å. Errors for the EMF amplitudes and time scales were estimated using Monte Carlo error analysis. Briefly, relaxation rates were back-calculated from the best fit parameters, random noise within the bounds of experimental error was added to the rates and the resulting rates fitted to the model. This procedure was iterated 1000 times and the error set at a two times the standard deviation of the results from all the runs.

11

SUMMARY AND OUTLOOK

SSNMR is a valuable technique for the characterisation of the structures and dynamics of biomolecules. Key to its success is that the structural and dynamical information available is both quantitative and can be obtained at atomic resolution, providing a practical route for the elucidation of the complex relationships between molecular structure, dynamics and function. Furthermore, solid-state NMR is extremely versatile and currently stands as the only available approach for determining the structures and dynamics of systems such as large protein complexes, membrane proteins and amyloid fibrils, many of which perform vital roles in life processes or in the progression of diseases. The continuing success of SSNMR in this role is only made possible by the extraordinarily rapid advances that are continually made in methodology and technology. In the preceding chapters of this work, several methodological tools were presented for the application of determining the structures of proteins and the dynamics that they undergo.

Chapters 4-6 focussed on exploiting existing and new technologies to conceive advanced methods for obtaining information about proteins, in particular spectra that can be used for the extraction of structural (or dynamical) information. To be able to tackle some of the more challenging systems that SSNMR is be uniquely applicable to, the enduring issues of spectral resolution and in particular sensitivity must be addressed, especially in light of often intensifying competition for experimental time on the highest-field instruments available. In the first of these chapters, a streamlined method was introduced that maximised the amount of information available in TSAR experiments, which are currently some of the most valuable techniques for obtaining long-range distance constraints in proteins thanks to their ability to circumvent the problem of dipolar truncation. The method presented here, dubbed time-shared TSAR, allows for the simultaneous recording of homonuclear (^{13}C-^{13}C) and heteronuclear (^{15}N-^{13}C) correlations without any discernible loss in sensitivity in the case of aliphatic carbon sites, or a small but expected loss in the case of ^{13}C sites with no directly bonded protons (*e.g.* ^{13}C'). In either situation, significant time savings (or equivalently greater signal to noise in

the same experimental time) are achieved with little in the way of extra experimental optimisations.

Among the most important frontiers within biophysical science is the shift from the study of single proteins to the assessment and characterisation of their roles within complex and dynamic supramolecular systems. Studies of large complexes by SSNMR have thus far been predominantly focused on samples that contain multiple repeats of identical subunits, alleviating somewhat the extreme sensitivity issues that arise from such large molecular sizes. In Chapter 5, a practical approach for studying "general case" large protein complexes was demonstrated, based on a combination of fast MAS (*e.g.* ≥60 kHz), high magnetic field, proton detection, sample deuteration and optional paramagnetic doping. With the sensitivity and resolution afforded with just a few nanomoles of sample, full assignment of the protein GB1 in complex with full-length IgG using 3D experiments was possible, leading to characterisation of the binding interfaces. Moreover, without further information it was possible to deduce a lower bound for the complex's size of ~300 kDa. While this method would be equally effective for sedimented or crystallised samples, simple precipitation was found to be a suitable preparation method for this complex, which by extension is likely to be similarly successful for others. This approach also therefore represents a potential option for the study of systems, large or small, that naturally precipitate upon mixing of the component molecules and which therefore solution NMR is precluded from studying.

Cutting-edge 0.75-0.8 mm MAS technology has recently made reaching spinning frequencies of up to 100 kHz or more possible, with potentially valuable gains in line-narrowing for proton-rich molecular environments. Chapter 6 was devoted to investigating the applicability of this new capability to small organic molecules and proteins, in particular for the direct detection of protons. In exploring the effect of increasing spinning frequency with a 0.8 mm probe upon the proton line widths in the dipeptide *β*-Asp-Ala (at natural abundance), it was found that proton line widths continued to decrease linearly with decreasing rotor period, as has been observed by others at lower MAS rates. Extrapolation of these trends showed that complete averaging of the ^{1}H-^{1}H dipolar couplings is not likely to be possible by MAS alone until MAS frequencies of ~300 kHz are within reach. Even at 100 kHz, however, proton line widths are narrow enough to yield well-resolved proton-detected ^{13}C-^{1}H spectra, leading to a potentially useful approach for the study of small organic molecules at natural abundance. It was recently shown by others that, despite the relatively tiny sample

volume available, by conducting multidimensional proton-detected experiments under such conditions the 3D structures of deuterated microcrystalline proteins could be determined.[48] Here we assessed whether the drop in volume is a hindrance to the study of more sensitivity-challenged systems such as large proteins and complexes by applying the method to the >300 kDa complex introduced in Chapter 5, and showed that such an approach is still eminently practical. In addition, the technology unlocks the potential for proton-detected experiments in fully protonated samples, though still not with the resolution provided by deuteration.

The most unique capability of SSNMR is perhaps not its ability to determine the structures of proteins with atomic resolution, but to further characterise the manner in which these structures evolve through time across the entire range of time scales relevant to protein function. The second collection of results presented in this thesis was dedicated to the development of methods for extracting and evaluating dynamical information. In Chapter 5, it was shown that proton detection and deuteration offer enough sensitivity for the extraction of quantitative information in large protein complexes. We explored this idea further in Chapter 8 by measuring relaxation parameters sensitive to slow (ns-μs) dynamics in the same GB1-IgG complex, and we were subsequently able to, for the first time, compare these findings with results of identical experiments on the same protein in a crystalline form. Significant differences were observed in the slow dynamics of the two sample types, in particular a higher level of widespread slower motions in the complex, which were attributed to the dissimilar molecular environments of GB1 in each. The similarities and differences observed showed that while considering the motions of individual proteins will clearly still remain an important element of dynamics studies of biological systems, a complete picture of the functional dynamics of a protein may be better found by conducting measurements on the molecule when it is undergoing relevant interactions with others (*i.e.* when it is in complex).

The comprehensive characterisation of protein dynamics with NMR relies on the measurement of a multitude of independent parameters sensitive to different motional time scales, of which a greater number is always desirable. There is thus a high demand for new independent probes of dynamics. Currently, for the backbone, these observables can take the form of $^{13}C'$ or ^{15}N relaxation rates. In Chapter 9, the utility of ultrafast (≥60 kHz) MAS rates in combination with alternate ^{13}C labelling for the measurement of the relaxation rates of $^{13}C^{\alpha}$ sites, which under more usual conditions are adversely affected by

spin diffusion effects, was investigated for fully protonated proteins. It was successfully shown that, for almost all aliphatic sites, such labelling severely truncates the effects of spin diffusion for both R_1 and $R_{1\rho}$ sequences at 60 kHz MAS, with still further suppression guaranteed with higher MAS frequencies. This allows for the reliable measurement of aliphatic carbon relaxation rates for characterising protein side chain dynamics, which are often implicated in intermolecular interactions. Further to this, we found that by using 0.8 mm MAS instrumentation and spinning the sample at >80 kHz, excellent resolution could be obtained in proton-detected ^{13}C-^{1}H correlation experiments in fully protonated experiments (an experiment that suffers from reduced sensitivity in deuterated samples), paving the way for the widespread use of such correlations within 3D and higher dimensional experiments for assignment and structure determination purposes, as well as providing an effective foundation for sensitive $^{13}C^{\alpha}$ relaxation experiments. Combining these findings, we proceeded to demonstrate the application of proton-detected $^{13}C^{\alpha}$ relaxation measurements in fully protonated microcrystalline GB1 in order for quantitative information to be extracted.

In Chapter 10, the measurement of another previously inaccessible relaxation parameter, carbonyl $R_{1\rho}$, was shown to be possible in fully protonated, uniformly labelled protein samples at spinning frequencies of >50 kHz and with spin-lock nutation frequencies of more than around 8 kHz. Under these conditions, it was shown using amino acid samples that coherent contributions to the measured rates amount to less than 0.06 s^1, an essentially negligible figure when compared to the likely experimental error when performing such an experiment on a protein. This proof-of-concept allowed us to measure a full set of site-specific carbon and nitrogen relaxation parameters – ^{15}N and ^{13}C R_1 and $R_{1\rho}$ – for each peptide plane within microcrystalline GB1.

One of the primary advantages of relaxation measurements is that they can be analysed in a quantitative manner through fitting to motional models, or alternatively "model-free" analyses that assume singly-exponential correlation functions. While SSNMR can give unobstructed access to fast and slow protein motions, there are many challenges regarding the formation of an accurate and consistent description of dynamics over such a vast range of time scales. For example, when analysing the data compiled for GB1 with a single time scale, appreciable offsets were found between the resultant order parameters and correlation times for ^{13}C and ^{15}N data. By examining the nature of the spectral densities, we discovered that the origin of these discrepancies was the presence of multiple modes of motion on separate time scales. Nitrogen measurements in

particular appear dominated by the slower motions even if they are of far smaller amplitude, resulting in a relatively poor estimate of the fast order parameter. A corollary of this is that in some cases it may be possible to analyse these measurements with only a single time scale if only the slow motions are of interest. In general, however, these findings strongly support the notion that if an accurate picture of protein dynamics is required, solid-state relaxation data should be analysed using at least two time scales, if not more. Despite the greater sensitivity of carbon measurements to faster motions, it appears that accurate determination of the fast order parameter still requires the inclusion of directly measured motionally averaged interactions (*e.g.* dipolar order parameters) in quantitative analyses. However, the inclusion of $^{13}C'$ data in addition to ^{15}N data in a two-time scale (EMF) analysis, assuming rigid peptide planes, clearly improved the quality of fitting thanks to sampling of the spectral densities at different frequencies. As ^{13}C relaxation experiments are in principle no more difficult to carry out than ^{15}N analogues, this approach should therefore be of great use in future quantitative studies of protein dynamics in the solid state.

To conclude, to fully realise the potential of SSNMR for studying biological macromolecules, improvements and innovations in methodology (as well as in technology) are a necessity. The last few decades has already witnessed enormous growth in the field. The progressing abilities of SSNMR are often compared to benchmarks set by the field of solution NMR, which, thanks to the presence of molecular tumbling and associated benefits, has proved to be a hugely successful technique. However, thanks to recent advances in methodology shown here and by many others, SSNMR is beginning to demonstrate that its unique attributes and capabilities should allow it to rapidly surpass solution NMR in a number of critically important areas, notably in the study of large proteins and complexes and in the study of functional protein dynamics. In the latter case, dynamics measurements in the solid state are likely to become highly complementary to those performed in solution, and in some circumstances it may even prove to be beneficial to use samples prepared as solids for this purpose even if they are soluble (though in these cases care should clearly be taken regarding interpretation in terms of their native biological environments). Given this huge potential, with further development it is inevitable that SSNMR spectroscopy will continue to become an increasingly formidable and essential technique for the study of proteins.

APPENDIX A

Expressions for Quantum Mechanics

A.1 Spin Operators and Matrices

Spin matrices (for a spin-½ nucleus, I):

$$I_x = \frac{1}{2}\begin{pmatrix} 0 & 1 \\ 1 & 0 \end{pmatrix} \qquad I_y = \frac{1}{2i}\begin{pmatrix} 0 & 1 \\ -1 & 0 \end{pmatrix} \qquad I_z = \frac{1}{2}\begin{pmatrix} 1 & 0 \\ 0 & -1 \end{pmatrix}$$

Ladder operators:

$$\hat{I}_+ = \hat{I}_x + i\hat{I}_y \qquad \hat{I}_- = \hat{I}_x - i\hat{I}_y$$

$$\hat{I}_x = \frac{1}{2}(\hat{I}_+ + \hat{I}_-) \qquad \hat{I}_y = \frac{1}{2i}(\hat{I}_+ - \hat{I}_-)$$

Commutators:

$$[\hat{I}^2, \hat{I}_z] = 0$$

$$[\hat{I}_x, \hat{I}_y] = i\hat{I}_z \qquad [\hat{I}_y, \hat{I}_z] = i\hat{I}_x \qquad [\hat{I}_z, \hat{I}_x] = i\hat{I}_y$$

A.2 Tensors and Rotations

General correspondence between Cartesian and spherical tensor components:

$$A_{00} = -\frac{1}{\sqrt{3}}(A_{xx} + A_{yy} + A_{zz}) = -\frac{1}{\sqrt{3}}\mathrm{Tr}(A)$$

$$A_{10} = \frac{i}{\sqrt{2}}(A_{xy} - A_{yx}) \qquad A_{1\pm1} = \frac{1}{2}[A_{zx} - A_{xz} \pm i(A_{zy} - A_{yz})]$$

$$A_{20} = \frac{1}{\sqrt{6}}[3A_{zz} - (A_{xx} + A_{yy} + A_{zz})]$$

$$A_{2\pm1} = \mp\frac{1}{2}[A_{xz} + A_{zx} \pm i(A_{yz} + A_{zy})] \qquad A_{2\pm2} = \frac{1}{2}[A_{xx} - A_{yy} \pm i(A_{xy} + A_{yx})]$$

Reduced Wigner rotation matrix elements, $d^{j}_{mm'}(\beta)$:

$$d^0_{00}(\beta) = 1$$
$$d^1_{00}(\beta) = \cos\beta$$
$$d^1_{01}(\beta) = d^1_{-10}(\beta) = -d^1_{0-1}(\beta) = -d^1_{10}(\beta) = \frac{1}{\sqrt{2}}\sin\beta$$
$$d^1_{1-1}(\beta) = d^1_{-11}(\beta) = \sin^2\left(\frac{\beta}{2}\right) = \frac{1}{2}(1-\cos\beta)$$
$$d^1_{11}(\beta) = d^1_{-1-1}(\beta) = \cos^2\left(\frac{\beta}{2}\right) = \frac{1}{2}(1+\cos\beta)$$
$$d^2_{00}(\beta) = \frac{1}{2}(3\cos^2\beta - 1)$$
$$d^2_{10}(\beta) = d^1_{0-1}(\beta) = -d^1_{01}(\beta) = -d^1_{-10}(\beta) = -\sqrt{\frac{3}{2}}\sin\beta\cos\beta$$
$$d^2_{1-1}(\beta) = d^1_{-11}(\beta) = \frac{1}{2}(2\cos\beta + 1)(1-\cos\beta)$$
$$d^2_{11}(\beta) = d^1_{-1-1}(\beta) = \frac{1}{2}(2\cos\beta - 1)(1+\cos\beta)$$
$$d^2_{20}(\beta) = d^2_{02}(\beta) = d^2_{-20}(\beta) = d^2_{0-2}(\beta) = \sqrt{\frac{3}{8}}(3\sin^2\beta)$$
$$d^2_{21}(\beta) = -d^2_{12}(\beta) = -d^2_{-2-1}(\beta) = -d^2_{-1-2}(\beta) = -\frac{1}{2}\sin\beta\,(\cos\beta + 1)$$
$$d^2_{2-1}(\beta) = d^2_{1-2}(\beta) = -d^2_{-21}(\beta) = -d^2_{-12}(\beta) = \frac{1}{2}\sin\beta\,(\cos\beta - 1)$$
$$d^2_{22}(\beta) = d^2_{-2-2}(\beta) = \cos^4\left(\frac{\beta}{2}\right)$$
$$d^2_{2-2}(\beta) = d^2_{-22}(\beta) = \sin^4\left(\frac{\beta}{2}\right)$$

A.3 Chemical Shift

Spin operators, $\hat{T}_{jm}$, for the chemical shift of a spin I induced by a magnetic field $\boldsymbol{B}$:[89]

$$\hat{T}_{00} = -\frac{1}{\sqrt{3}}\left(\hat{I}_z B_z + \hat{I}_z B_z + \hat{I}_z B_z\right)$$

$$\hat{T}_{10} = i\frac{1}{\sqrt{2}}\left(\hat{I}_x\hat{B}_y - \hat{I}_y\hat{B}_x\right) \qquad \hat{T}_{1\pm1} = -\frac{1}{2}\left(\hat{I}_z\hat{B}_x - \hat{I}_x\hat{B}_z \pm i\left(\hat{I}_z\hat{B}_y - \hat{I}_y\hat{B}_z\right)\right)$$

$$\hat{T}_{20} = \frac{1}{\sqrt{6}}\left(2\hat{I}_z\hat{S}_z - \hat{I}_x\hat{B}_x - \hat{I}_y\hat{B}_y\right)$$

$$\hat{T}_{2\pm1} = \mp\frac{1}{2}\left(\hat{I}_x\hat{B}_z + \hat{I}_z\hat{B}_x \pm i\left(\hat{I}_y\hat{B}_z + \hat{I}_z\hat{B}_y\right)\right) \qquad \hat{T}_{2\pm2} = \frac{1}{2}\left(\hat{I}_x\hat{B}_x + \hat{I}_y\hat{B}_y \pm i\left(\hat{I}_x\hat{B}_y + \hat{I}_y\hat{B}_x\right)\right)$$

For a field aligned with the z-direction, $\boldsymbol{B} = (0,0,B_z)$ and the above expressions simplify accordingly.

Irreducible tensor components, Λ, for the chemical shift tensor, $\tilde{\sigma}$, in its principal axis system (PAS):

$$\Lambda_{00} = -\frac{1}{\sqrt{3}}\gamma\left(\sigma_{xx}^{P} + \sigma_{yy}^{P} + \sigma_{zz}^{P}\right)$$

$$\Lambda_{10} = \Lambda_{1\pm1} = 0$$

$$\Lambda_{20} = \frac{1}{\sqrt{6}}\gamma\left(2\sigma_{zz}^{P} - \sigma_{yy}^{P} - \sigma_{xx}^{P}\right)$$

$$\Lambda_{2\pm1} = 0$$

$$\Lambda_{2\pm2} = \frac{1}{\sqrt{6}}\gamma\left(\sigma_{xx}^{P} - \sigma_{yy}^{P}\right)$$

In the PAS, the expression for the chemical shift Hamiltonian is therefore:

$$\widehat{\mathcal{H}}_{CS} = \Lambda_{00}\hat{T}_{00} + \Lambda_{20}\hat{T}_{20} + \Lambda_{22}\hat{T}_{22} + \Lambda_{2-2}\hat{T}_{2-2}$$

A.4 Dipolar Coupling

Spin operators, $\hat{T}_{j,m}$, for dipolar coupling between spins I and S:

$$\hat{T}_{00} = -\frac{2}{\sqrt{3}}\left(\hat{I}_z\hat{S}_z + \frac{1}{2}\left(\hat{I}_+\hat{S}_- - \hat{I}_-\hat{S}_+\right)\right)$$

$$\hat{T}_{10} = -\frac{1}{\sqrt{2}}\left(\hat{I}_+\hat{S}_- - \hat{I}_-\hat{S}_+\right) \qquad \hat{T}_{1\pm1} = \left(\hat{I}_z\hat{S}_\pm - \hat{I}_\pm\hat{S}_z\right)$$

$$\hat{T}_{20} = \frac{1}{\sqrt{6}}\left(3\hat{I}_z\hat{S}_z - \hat{\boldsymbol{I}}\cdot\hat{\boldsymbol{S}}\right) \qquad \hat{T}_{2\pm1} = \mp\frac{1}{2}\left(\hat{I}_z\hat{S}_\pm + \hat{I}_\pm\hat{S}_z\right) \qquad \hat{T}_{2\pm2} = \frac{1}{2}\hat{I}_\pm\hat{S}_\pm$$

Irreducible tensor components, Λ for the dipolar coupling tensor, $\widetilde{D}$, in its PAS:

$$\Lambda_{00} = 0$$

$$\Lambda_{10} = \Lambda_{1\pm1} = 0$$

$$\Lambda_{20} = -\sqrt{6}\widetilde{D}_{zz}^{P} = \sqrt{6}d_{IS}$$

$$\Lambda_{2\pm1} = 0$$

$$\Lambda_{2\pm2} = 0$$

d_{IS} is defined as in §2.1.5. In the PAS, the expression for the dipolar coupling Hamiltonian is therefore:

$$\widehat{\mathcal{H}}_{CS} = \Lambda_{20}\hat{T}_{20}$$

APPENDIX B

SUPPLEMENTARY INFORMATION FOR STRUCTURAL SSNMR STUDIES

B.1 Supplementary Figures for Chapter 4

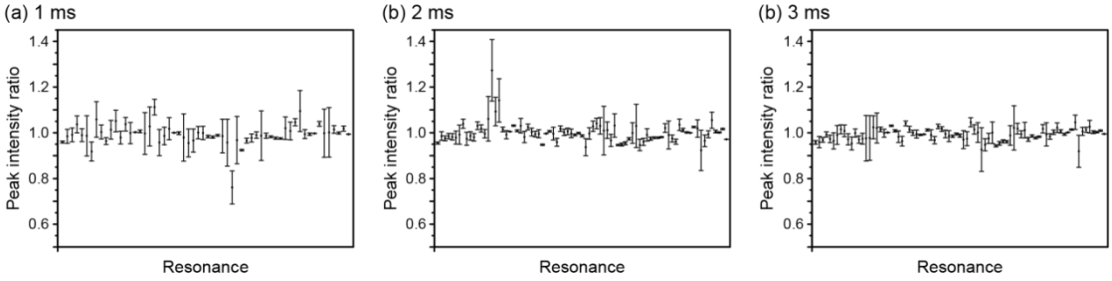

Figure B.1. Ratios of time-shared TSAR vs. PAR ^{13}C-^{13}C cross peak intensities, measured from spectra of [U-^{13}C,^{15}N]-*N*-Acetyl-L-Leu-L-Val (Figure 4.4) with 3 ms mixing time, $\omega_{0\mathrm{H}}/2\pi$ = 600 MHz and $\omega_r/2\pi$ = 20 kHz. Errors are derived from two times the spectral noise.

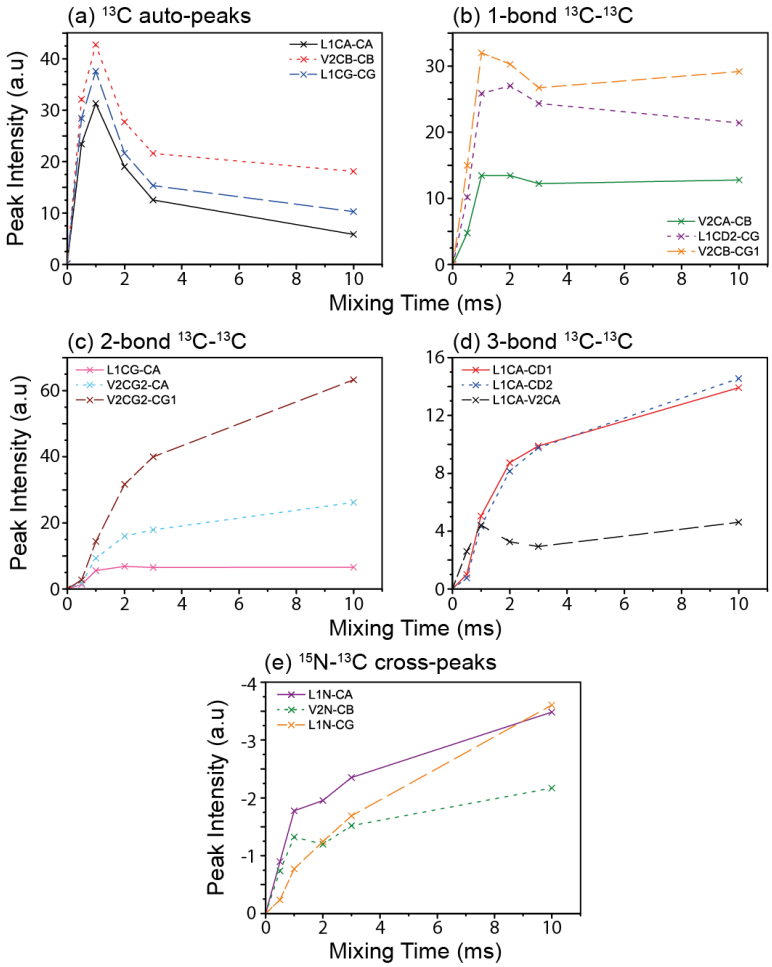

Figure B.2. Representative experimental time-shared TSAR magnetisation build-up curves, obtained from measured peak intensities of [U-^{13}C,^{15}N]-*N*-Acetyl-L-Leu-L-Val spectra at $\omega_{0H}/2\pi$ = 600 MHz and $\omega_r/2\pi$ = 20 kHz. (a) ^{13}C-^{13}C diagonal peaks; (b) one-bond ^{13}C-^{13}C polarisation transfer; (c) two-bond ^{13}C-^{13}C transfer; (d) three-bond ^{13}C-^{13}C transfer; (e) ^{13}C-^{15}N cross peaks. Errors given by twice the spectral noise appear too small to display.

B.2 Amino acid sequence and structure of the B1 domain of Protein G (GB1 – 56 residues)

M Q Y K L I L N G K T L K G E T T T E A V D A A T A E K V F K Q Y A N D N
G V D G E W T Y D D A T K T F T V T E

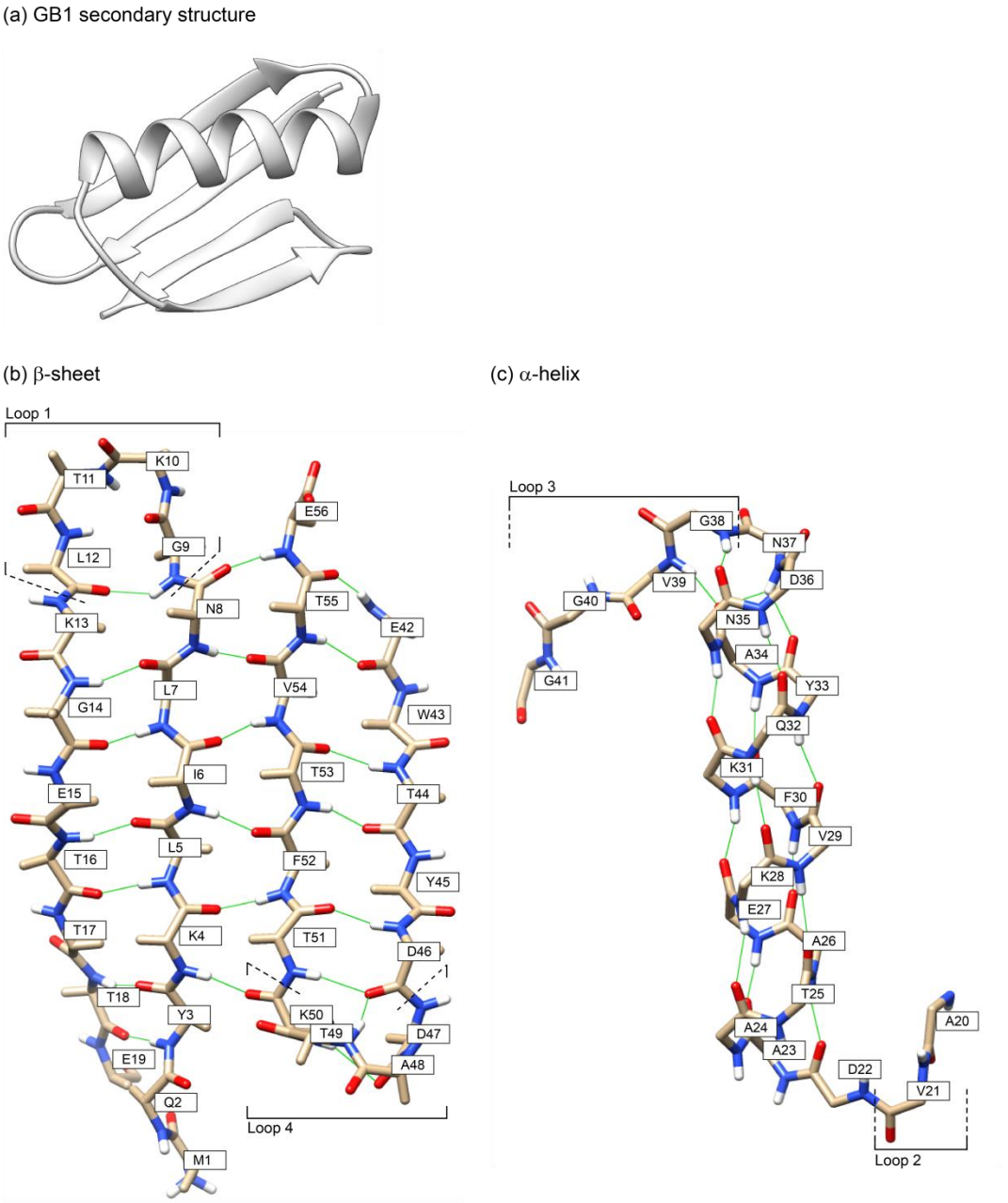

Figure B.3. (a) Ribbon diagram illustrating the secondary structure of the protein GB1. Below, the location of each residue is shown for (a) the β-sheet, which contains four strands, and for (c) the α-helix (no side chains shown).

B.3 Supplementary Figures for Chapter 5

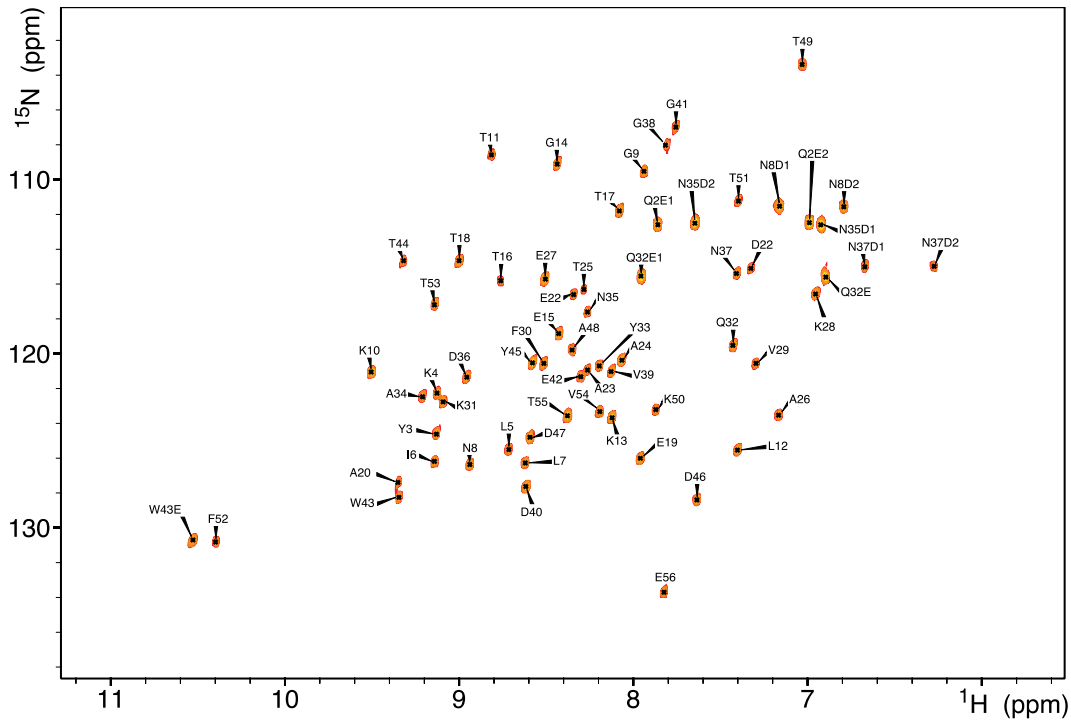

Figure B.4. Reference solution 2D ^{15}N HSQC spectrum of GB1 (50 mM phosphate buffer, pH 5.5, 30°C) obtained at $\omega_{0H}/2\pi$ = 600 MHz.

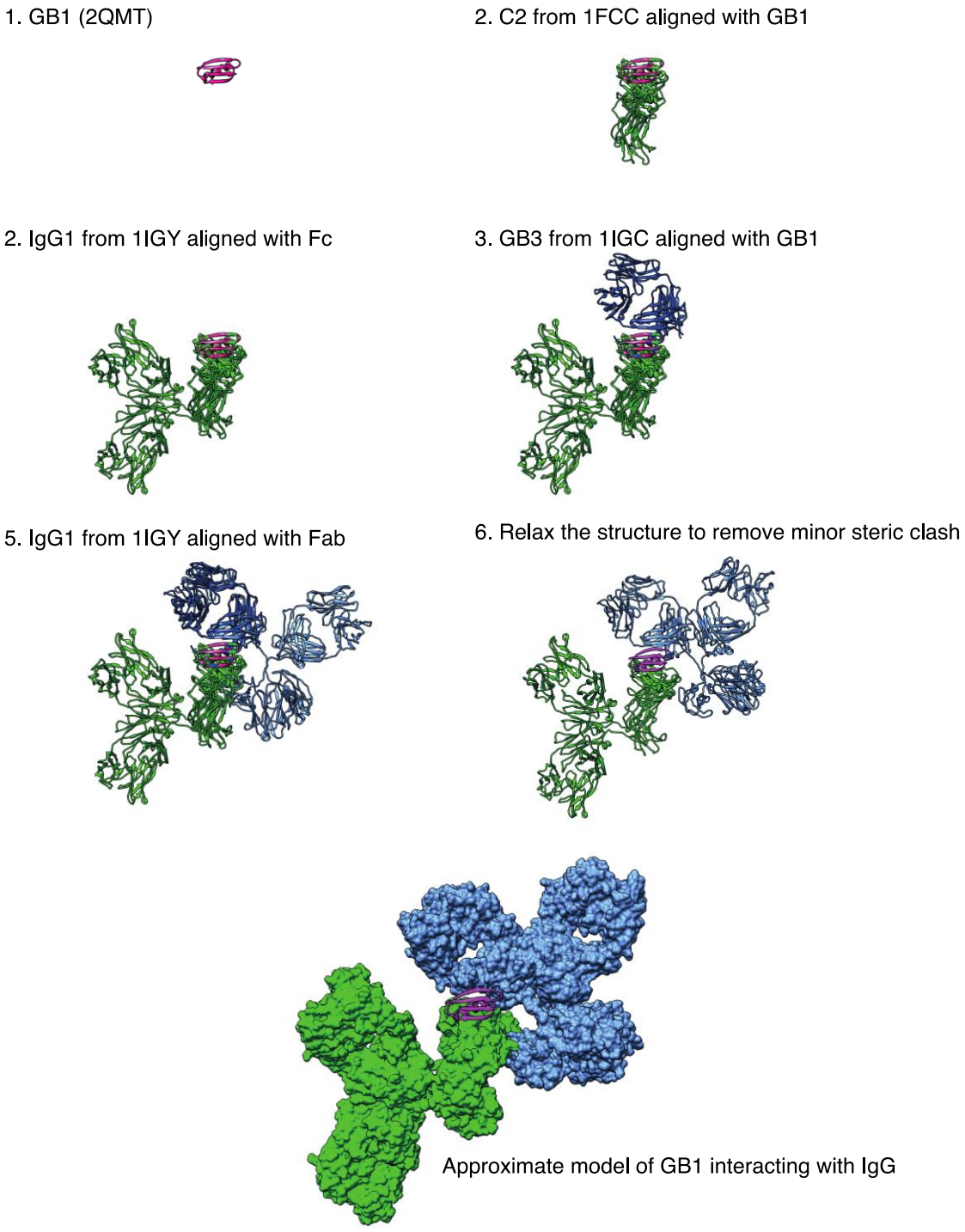

Figure B.5. A crude model for the GB1 interaction with full length IgG can be built by aligning protein G domains from crystal structures of their complexes with Fc and Fab fragments of IgG (1FCC[275] and 1IGC[389] respectively), with the crystal structure of GB1 (2QMT[390]). This is followed by alignment of the Fc and Fab domains with the crystal structure of immunoglobulin (1IGY[278]). This simple alignment procedure results in a particle with only minor steric clashes that can be removed by slight relaxation of the structure. This model explains the observed narrow GB1 resonances observed in a precipitated complex: the local environment of GB1 is almost entirely defined by interaction with IgG, with packing heterogeneity affecting only some of the IgG sites that are not observed in the spectra due to lack of isotopic labelling.

B.4 Supplementary Figures for Chapter 6

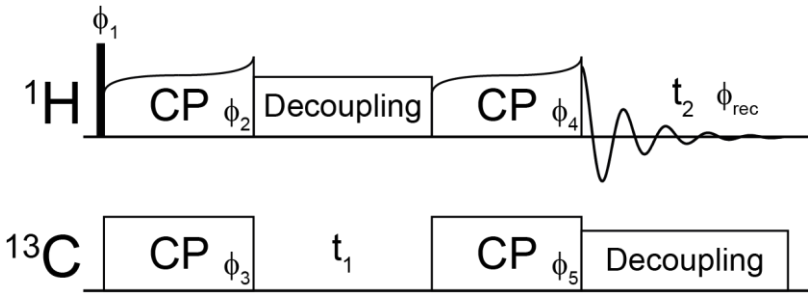

Figure B.6. Pulse sequence for obtaining proton-detected heteronuclear (^{13}C-^{1}H) correlation spectrum. The sequence is initialised with a hard ^{1}H $\pi/2$ pulse (black rectangle). At fast MAS frequencies, double-quantum CP ($\omega_{1H} + \omega_{1C} = \omega_r$) and low power decoupling (*e.g.* slpTPPM[114] or XiX[115]) are preferable so as to minimise probe wear and sample heating. Phase cycling: $\phi_1 = \phi_3 = (+y)$, $\phi_2 = (+x)$, $\phi_4 = (+y\ -y\ +y\ -y)$, $\phi_5 = (+y\ +y\ -y\ -y)$, $\phi_{rec} = (+y\ -y\ -y\ +y)$.

APPENDIX C

SUPPLEMENTARY INFORMATION FOR SSNMR DYNAMICS STUDIES

C.1 Supplementary Figures for Chapter 8

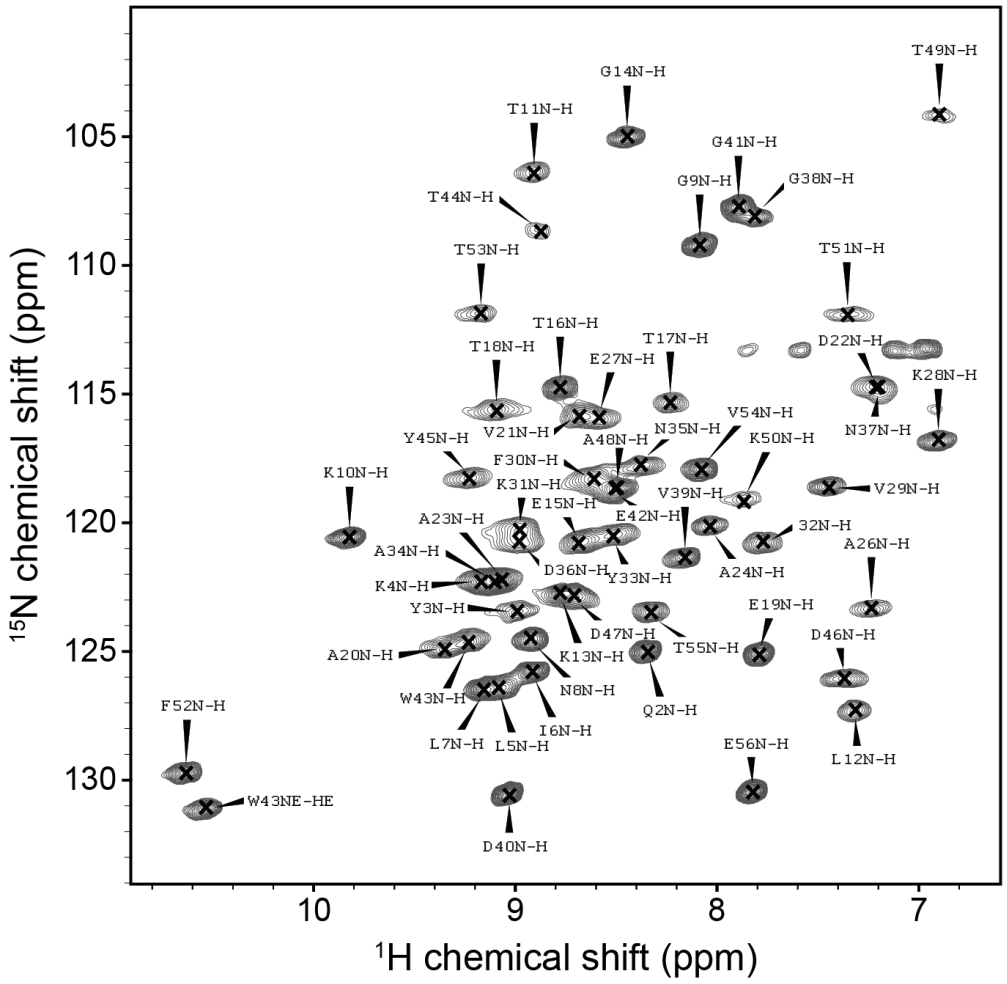

Figure C.1. Assigned 2D ^{15}N-^{1}H spectrum of deuterated (full-protonated at exchangeable sites) crystalline [U-^{13}C,^{15}N]GB1, recorded at a ^{1}H Larmor frequency of 850 MHz and at an MAS frequency of 60 kHz. Assignments were made on the basis of 3D (H)C'NH and (H)C'(C$^{\alpha}$)NH experiments performed at 600 MHz ^{1}H Larmor frequency.

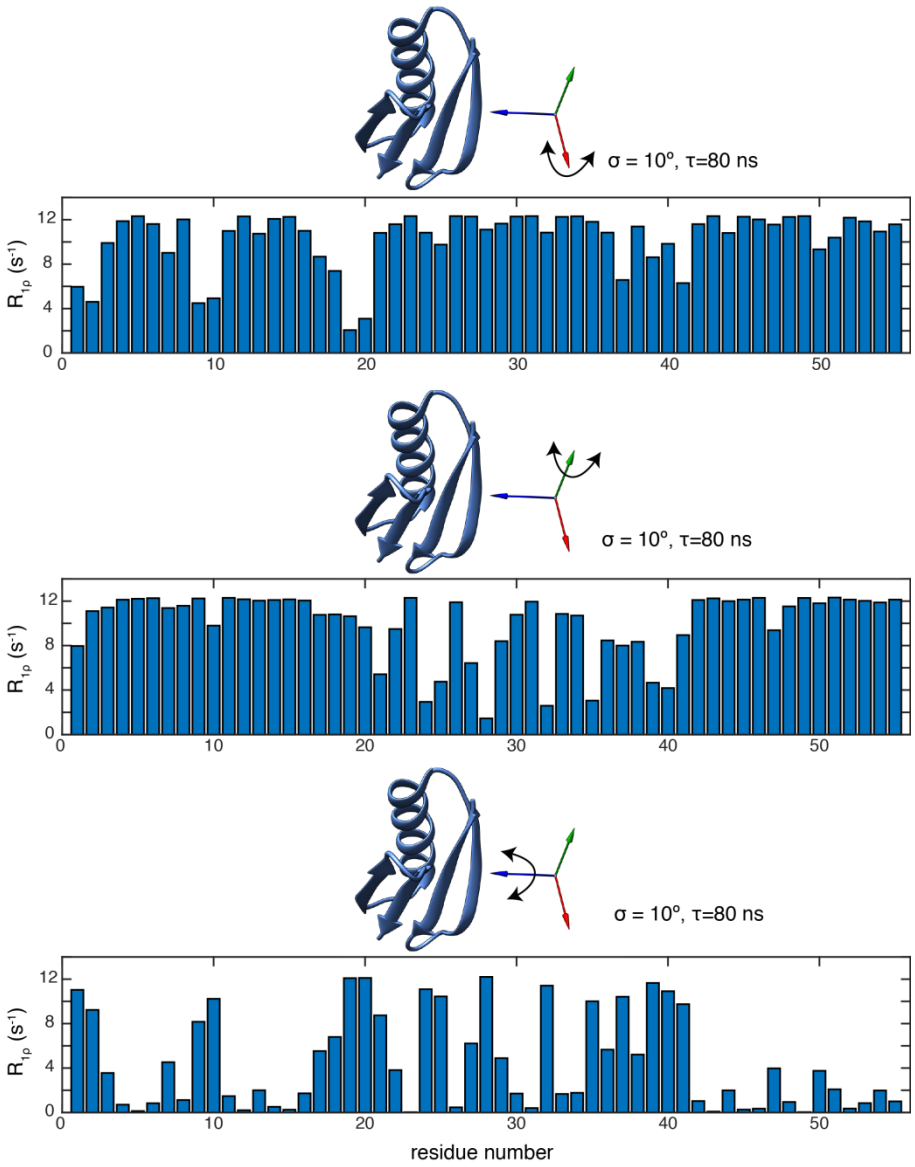

Figure C.2. Simulated ^{15}N $R_{1\rho}$ rates for overall anisotropic motion of GB1 about three different motional axes (inertia axes for GB1 structure, PDB ID: 2qmt). The rates were simulated using a 3D GAF[369] analysis for a 10 degree fluctuation against the indicated axes, with a correlation time of 80 ns at 850 ^{1}H Larmor frequency. Both ^{15}N-^{1}H dipolar and ^{15}N CSA contributions were considered. For ^{15}N CSA, the following parameters were assumed: σ_{11}=231.4 ppm, σ_{22} = 80.6 ppm and σ_{33}=54.0 ppm.

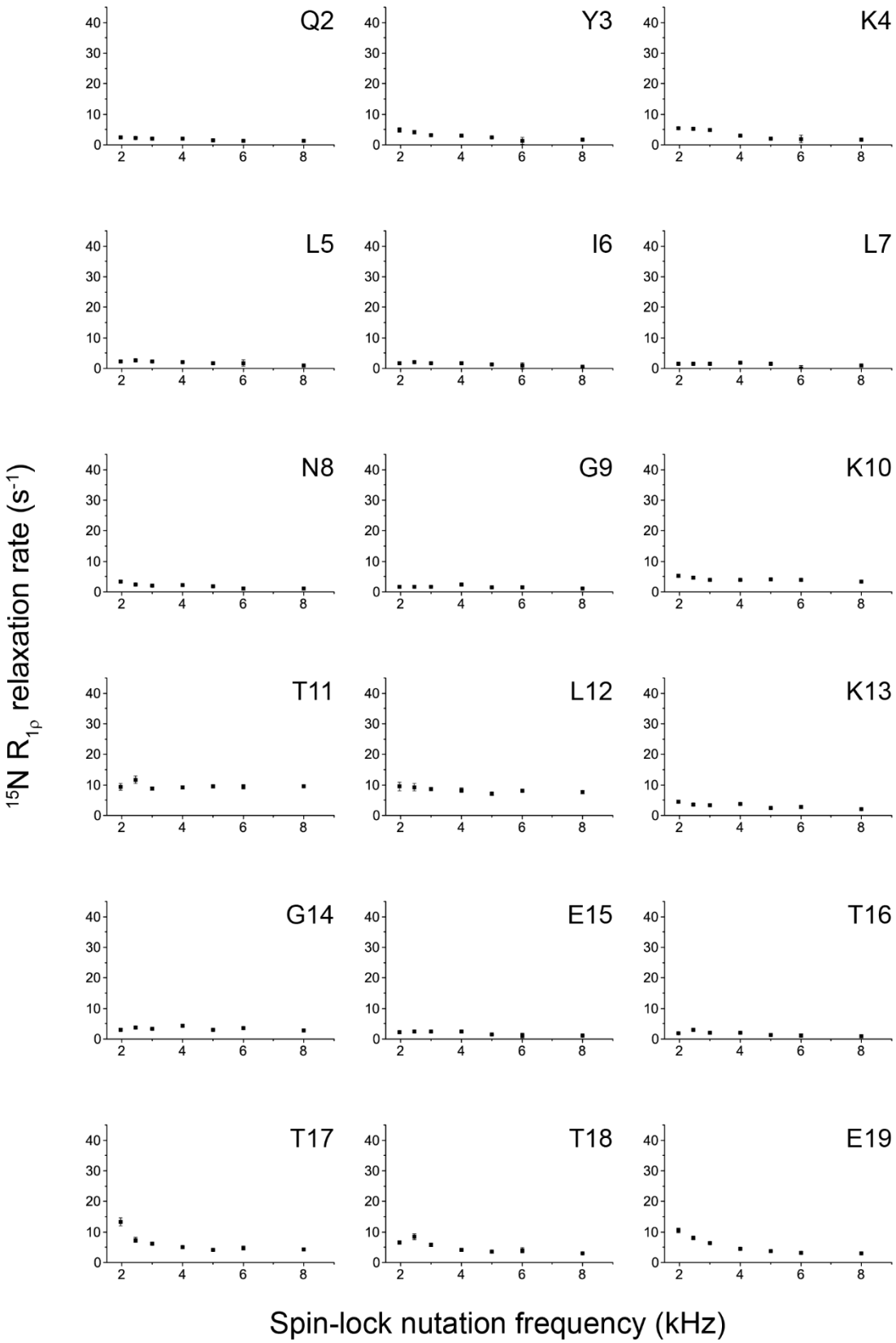
Q2
Y3
K4
L5
I6
L7
N8
G9
K10
T11
L12
K13
G14
E15
T16
T17
T18
E19
^{15}N $R_{1\rho}$ relaxation rate (s^{-1})
Spin-lock nutation frequency (kHz)

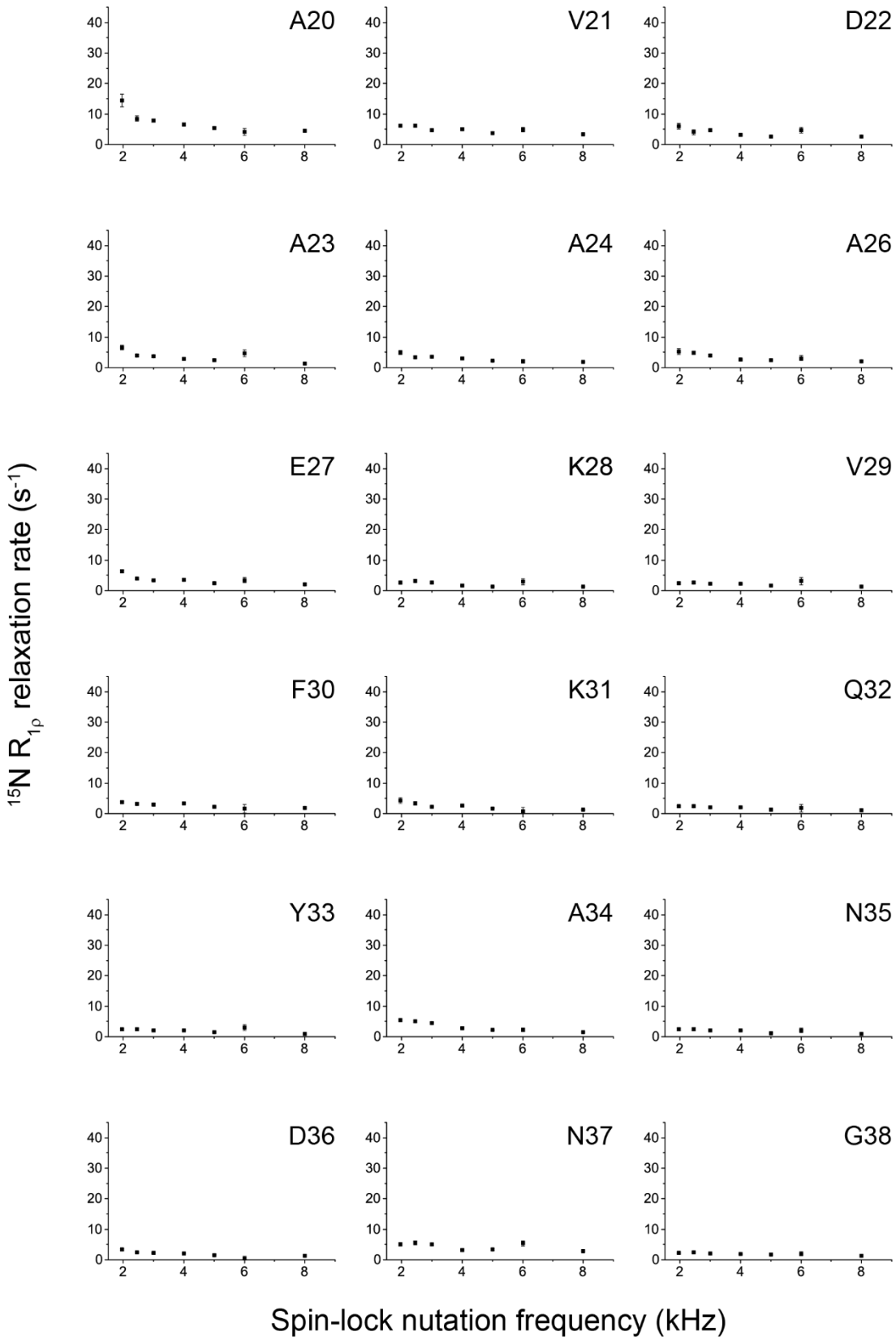
A20
V21
D22
A23
A24
A26
E27
K28
V29
F30
K31
Q32
Y33
A34
N35
D36
N37
G38
^{15}N $R_{1\rho}$ relaxation rate (s^{-1})
Spin-lock nutation frequency (kHz)

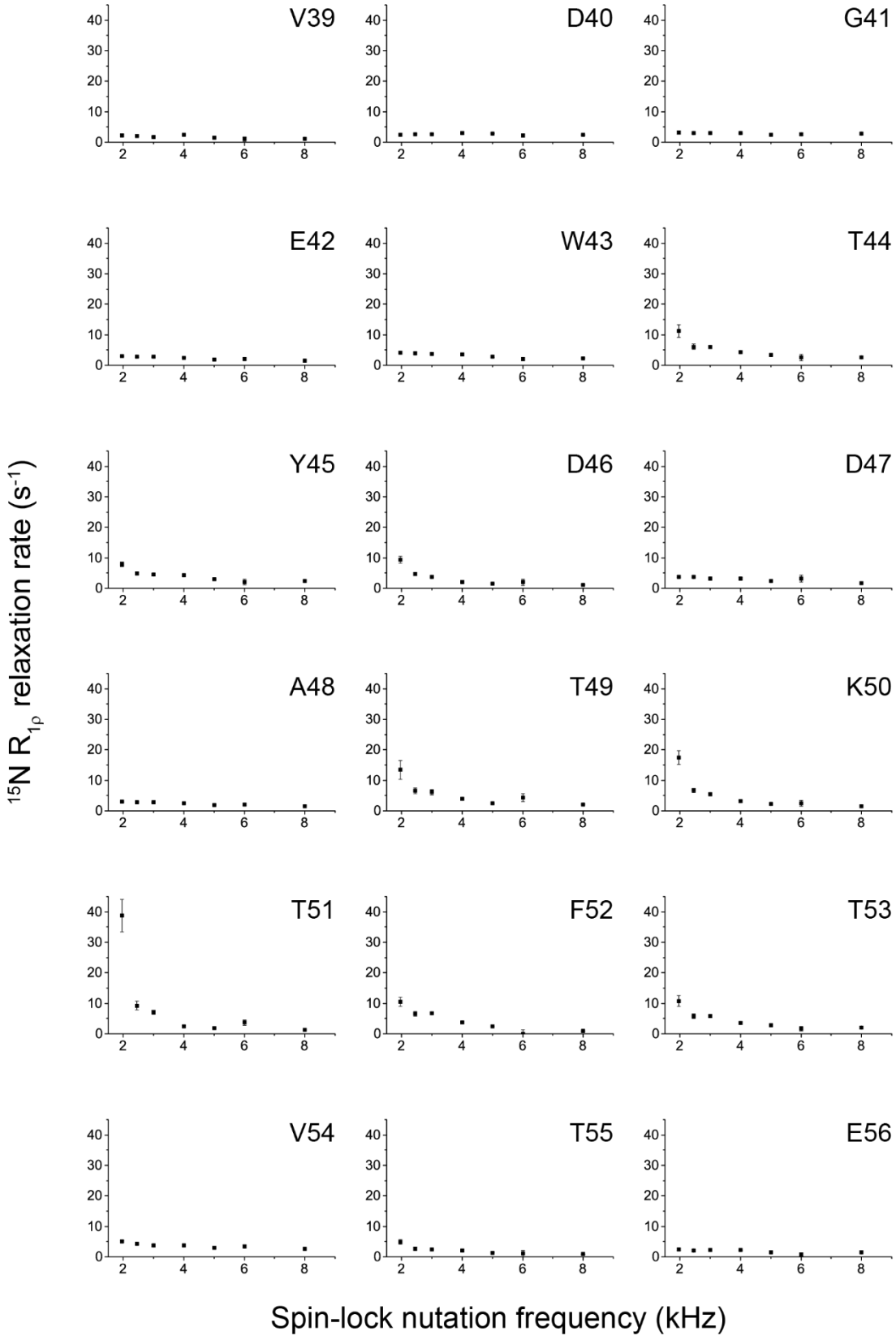

Figure C.3. ^{15}N $R_{1\rho}$ relaxation dispersion curves measured on crystalline 100% back-exchanged [U-^{2}H,^{13}C,^{15}N]GB1 at a ^{1}H Larmor frequency of 600 MHz, 50 kHz MAS and at a sample temperature of 27 °C. Spin-lock frequencies were determined by recording nutation experiments. While the majority of residues display little in the way of *(Cont'd)*

dispersion (*i.e.* most are flat), residues 17, 19, 20, 44, 46, 49, 50, 51, 52 and 53 show clear dispersion (displayed in Figure 8.3b). For those that are "flat", the $R_{1\rho}$ rate at a spin-lock field of 1.95 kHz is actually on average 1.7 s^{-1} higher than the plateau value at 8 kHz spin-lock, an increase we attribute to the presence of coherent contributions to the measured rates at the lower spin-lock field.

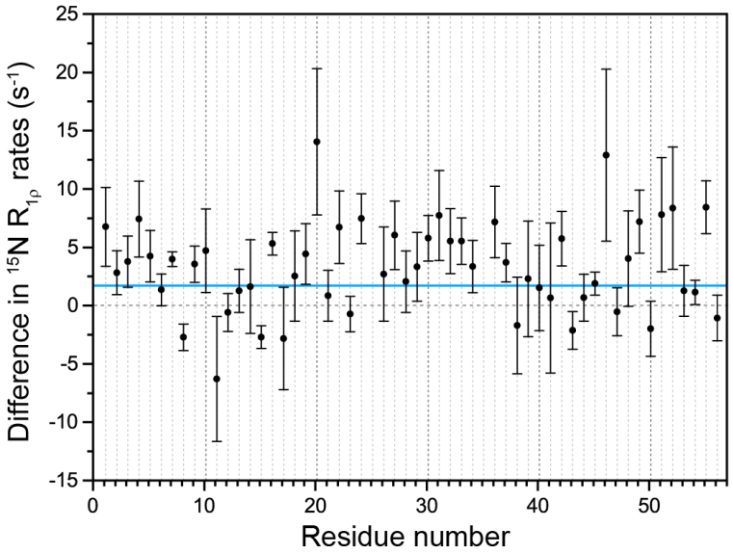

Figure C.4. Differences between the ^{15}N $R_{1\rho}$ relaxation rates measured at 2.5 kHz and 17 kHz spin-lock fields (*i.e.* $R_{1\rho}$[2.5 kHz] - $R_{1\rho}$[17 kHz]) in 100% back-exchanged deuterated GB1 in complex with IgG, at a sample temperature of 27 °C. Exchange contributions are decoupled at 17 kHz, but at 2.5 kHz have observable effects on the decay rates. The horizontal blue line at 1.7 s^{-1} represents the average coherent contribution to measured rates as found in crystalline deuterated GB1 at 50 kHz MAS and a spin-lock field amplitude of 1.95 kHz. While the latter conditions differ slightly from those used here (60 kHz MAS and 2.5 kHz spin-lock), this fact only ensures that 1.7 s^{-1} is a safe overestimate of the coherent contribution in this case. All residues for which $R_{1\rho}$[2.5 kHz] - $R_{1\rho}$[17 kHz] is greater than this threshold by at least one clear error bar (calculated from fit errors) were taken to be undergoing exchange processes on the µs-time scale (displayed in Figure 8.3a). These are residues 1, 4, 5, 7, 9, 16, 19, 20, 22, 24, 27, 30, 31, 32, 33, 36, 37, 42, 46, 49, 51, 52 and 55.

C.2 Supplementary Figures for Chapter 9

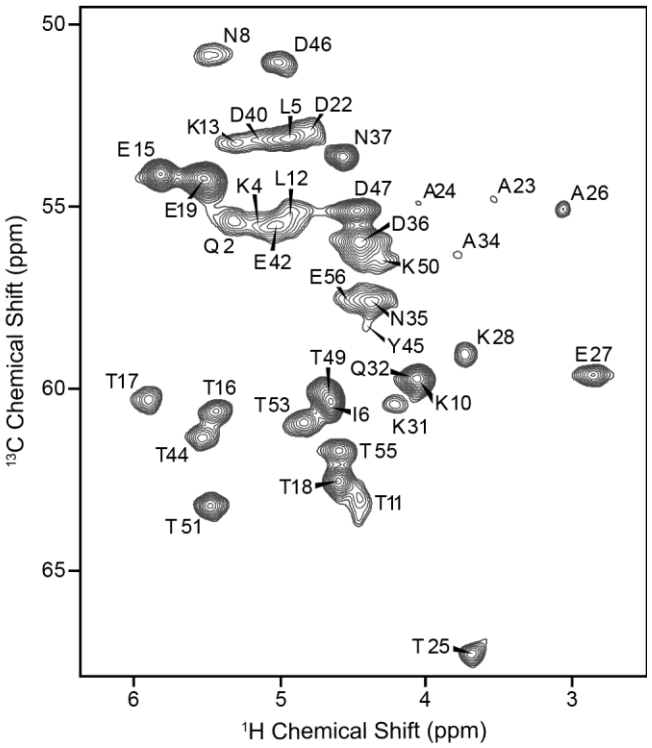

Figure C.5. Assignments for the $^{13}C^{\alpha}$-$^{1}H^{\alpha}$ region of an aliphatic ^{13}C-^{1}H spectrum of fully protonated crystalline [1,3-^{13}C,^{15}N]GB1. The assignments are derived from those given by Zhou *et al.* in Ref. 262.

C.3 Supplementary Figures for Chapter 10

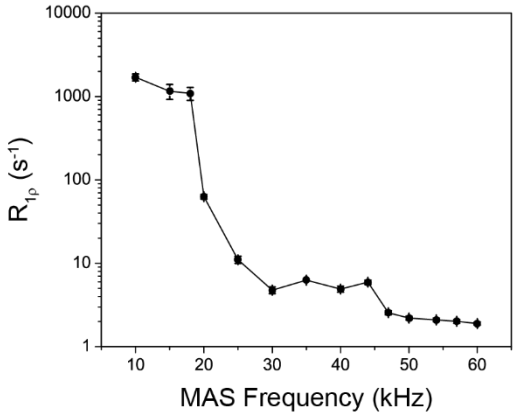

Figure C.6. Bulk carbonyl ^{13}C $R_{1\rho}$ in [U-^{13}C, ^{15}N]GB1, measured as a function of MAS frequency, with a constant spin-lock amplitude of 17 kHz and at a field of 14.1 T (600 MHz ^{1}H Larmor frequency). The sample temperature was 27 °C for all experiments, as determined by the chemical shift of water with respect to DSS.[282] Rates were found in 1D by measuring total carbonyl peak integrals at incrementally longer spin-lock pulses. ^{13}C $R_{1\rho}$ rates clearly plateau at spinning frequencies greater than ~45 kHz.

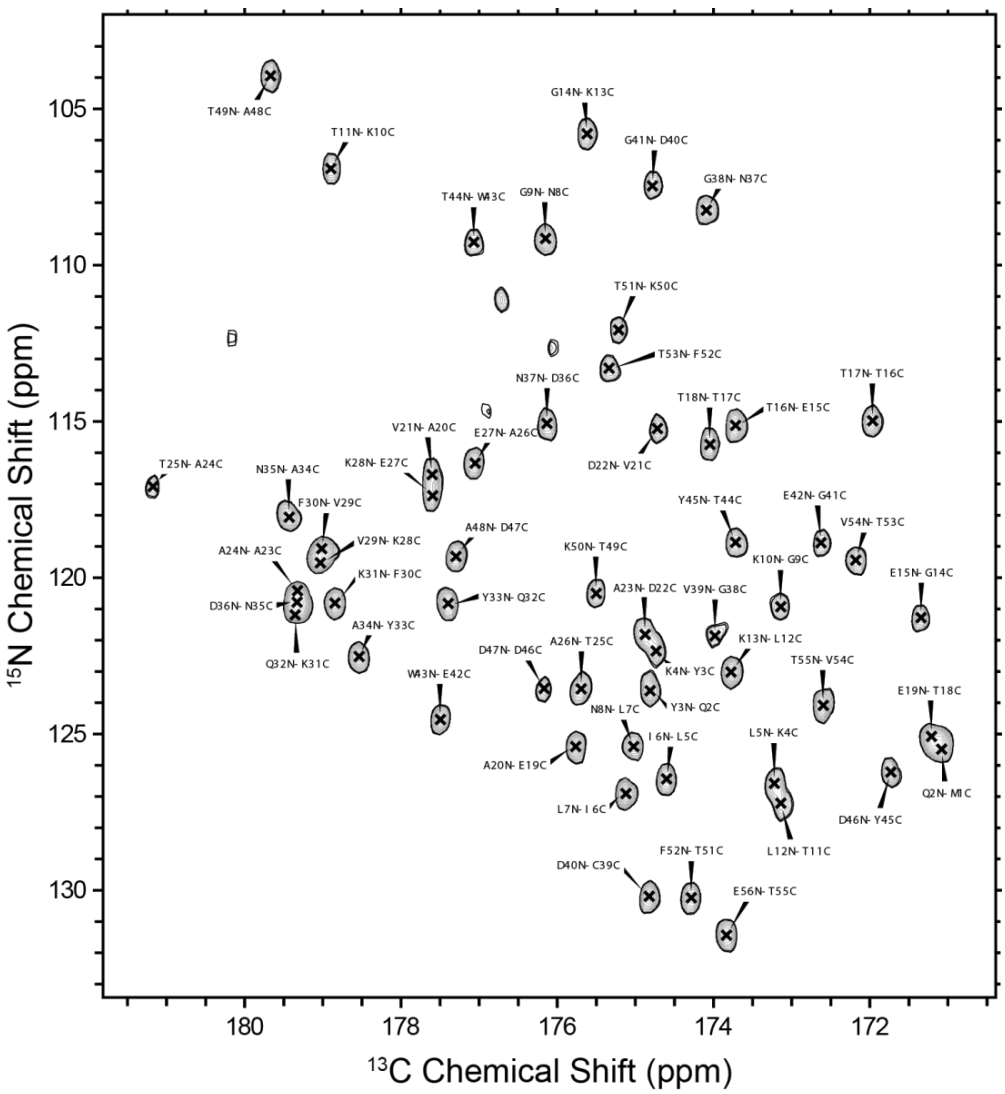

Figure C.7. NCO S^3E DCP spectrum measured at $\omega_{0H}/2\pi$ = 850 MHz showing resonance assignments. Note that a number of peaks partially overlap and as such the rates extracted from them may be distorted. Assignments are not shown for side-chain cross peaks.

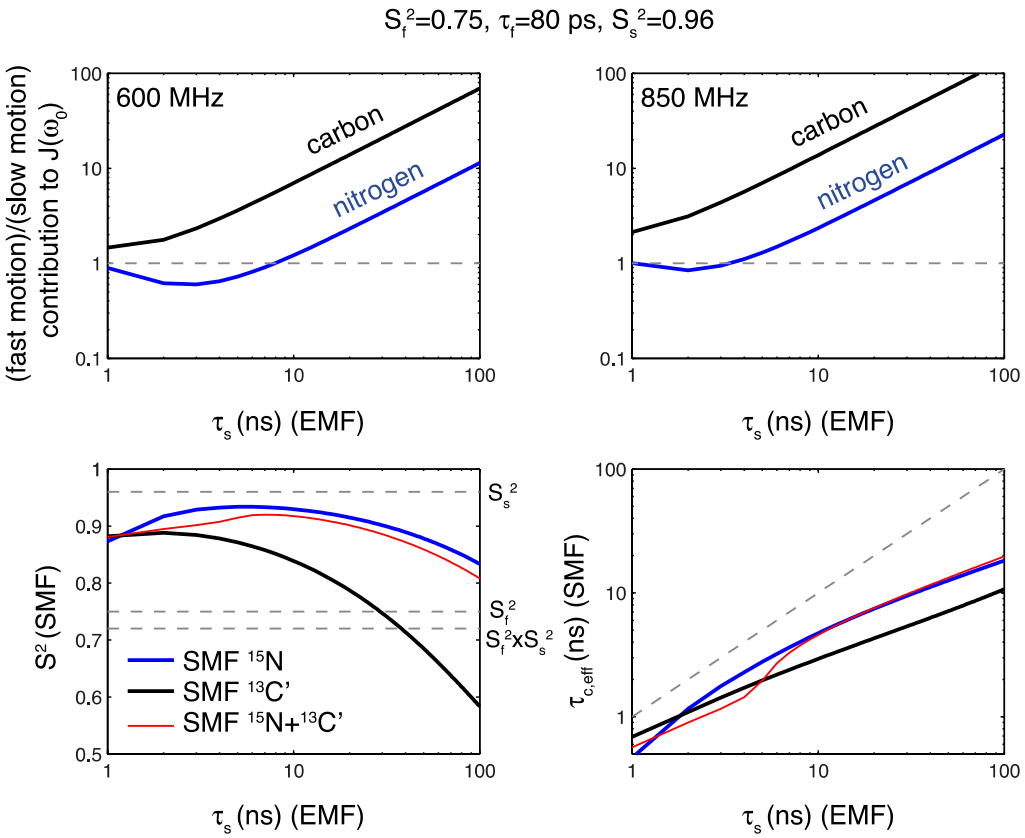

Figure C.8. *Top panels*: Ratios of the fast motion contribution to $J_1(\omega_0)$ (with τ_f = 80 ps, S_f^2 = 0.75) to that of a slow motion (S_s^2 = 0.94, τ_s indicated on the horizontal axis), calculated using a simple model-free (SMF) analysis at $\omega_{0H}/2\pi$ = 600 and 850 MHz. *Bottom panels*: The results (order parameters, S^2, and correlation times, $\tau_{c,eff}$) of fitting rates simulated using two-timescale motion (using EMF) to a single timescale motion (using SMF), with the settings as in the top panels (S_f^2, S_s^2 and $S_f^2 \cdot S_s^2$ are indicated by dashed grey lines). We assumed 10% error for the simulated rates in the SMF fit. Note the offset between the order parameter for ^{15}N and ^{13}C' when SMF is used for modelling the data resulting from the two-timescale motion.

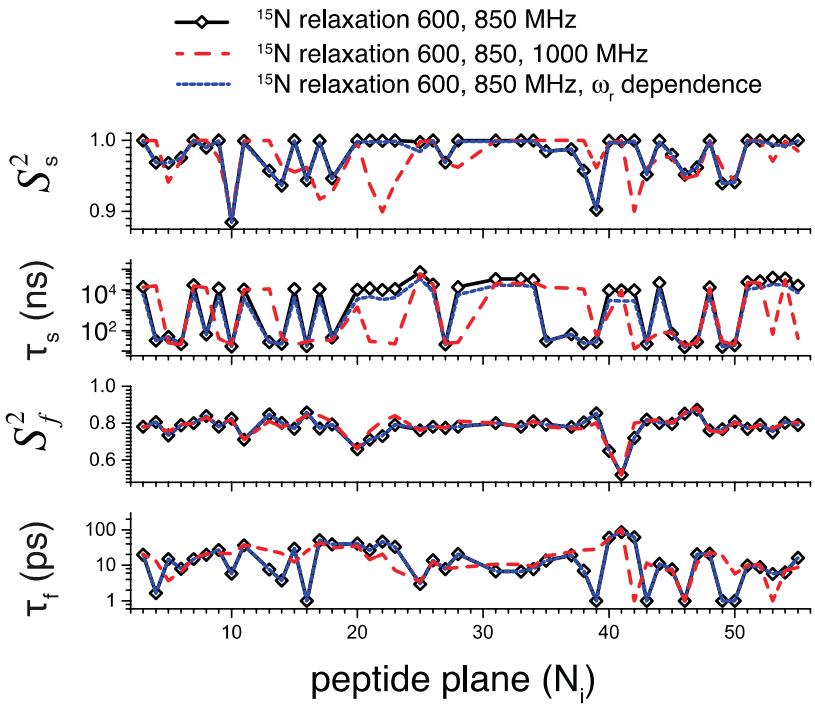

Figure C.9. EMF analysis of backbone dynamics in crystalline GB1 based on ^{15}N R_1 and $R_{1\rho}$ measurements performed at 600 and 850 MHz ^{1}H Larmor frequency and ^{15}N dipolar coupling measurements (diamond black line), compared to an analogous analysis with the addition of ^{15}N R_1 and $R_{1\rho}$ measured at 1 GHz ^{1}H Larmor frequency (red dashed line) and an analysis where the generalized expressions for $R_{1\rho}$ including the effect of spinning frequency were used (blue dotted line). Neither of these approaches leads to complete elimination of fitting artefacts.

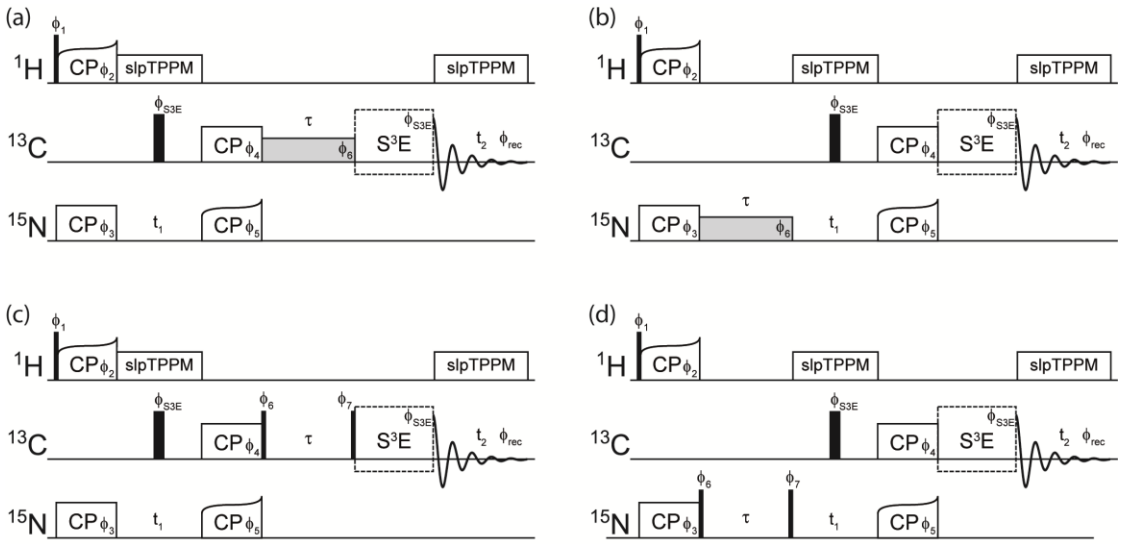

Figure C.10. Pulse sequences for the site-specific measurement of (a) carbonyl ^{13}C $R_{1\rho}$, (b) amide ^{15}N $R_{1\rho}$, (c) carbonyl ^{13}C R_1 and (d) amide ^{15}N R_1. ^{13}C and ^{15}N frequency offsets are set to the centres of the carbonyl and amide regions respectively. Pulses with a flip angle of $\pi/2$ are indicated with a narrow black rectangle, while π pulses are denoted by a thicker black rectangle. Spin-lock pulses (for (a) and (b)) are indicated in light grey. Indirect and direct acquisition periods are labelled as "t_1" and "t_2" respectively, while phases are shown as "ϕ". For all sequences, slpTPPM[114] decoupling is applied on the proton channel during acquisition periods at a ^1H amplitude of one quarter of the sample spinning frequency. Site-specific relaxation rates are obtained from curves obtained by monitoring the intensity of cross peaks in 2D experiments as a function of relaxation time, τ (length of spin-lock pulse for $R_{1\rho}$ measurements, delay length for R_1 measurements). No ^1H decoupling is applied during relaxation periods. In each sequence, the rectangle with a dashed outline represents an S^3E block, which may be optionally included to improve resolution in the direct dimension by minimizing the effect of one-bond C'-C^α J-couplings.[380] Experiments containing "A" and "B" blocks (which differ in the positioning of the band-selective pulses – see Ref. 380) are run in an interleaved fashion, to be split and recombined when processing. The two different phase cycles associated with these are differentiated by use of square brackets below. The phases of all S^3E pulses (including the π pulse on ^{13}C during t_1 evolution) are identical, labelled as ϕ_{S3E}. Phase cycling (with S^3E):

(a) ϕ_1 = (+y –y), $\phi_2 = \phi_3 = \phi_5 = \phi_{S3E}$ = (+x), $\phi_4 = \phi_6$ = (+x +x –x –x [A] / –y –y +y +y [B]), ϕ_{rec} = (+x –x +x –x).

(b) ϕ_1 = (+y –y), $\phi_2 = \phi_3 = \phi_5 = \phi_6 = \phi_{S3E}$ = (+x), ϕ_4 = (+x +x –x –x [A] / –y –y +y +y [B]), ϕ_{rec} = (+x –x +x –x).

(c) ϕ_1 = (+y –y), $\phi_2 = \phi_3 = \phi_5 = \phi_{S3E}$ = (+x), ϕ_4 = (+x +x –x –x [A] / –y –y +y +y [B]), $\phi_6 = -\phi_7$ = (+y –y [A] / +x –x [B]) ϕ_{rec} = (+x –x +x –x).

(d) ϕ_1 = (+y –y), $\phi_2 = \phi_3 = \phi_5 = \phi_{S3E}$ = (+x), ϕ_4 = (+x +x –x –x [A] / –y –y +y +y [B]), $\phi_6 = -\phi_7$ = (+y –y) ϕ_{rec} = (+x –x +x –x).

C.4 Evaluation of Robustness of ^{13}C' $R_{1\rho}$ Experiments

C.4.1 Magic Angle Mis-Adjustment

As magic angle spinning plays a crucial role in averaging the interactions contributing to the coherent mechanisms for the magnetization decay, it is important to consider the influence of "mis-setting" the magic angle upon the efficiency of averaging by MAS. We examine the effect of mis-setting the angle of rotation on the measured coherence lifetimes in [1-^{13}C]Ala in Figure C.11, where the measured $R_{1\rho}$ rates for ^{13}C' are plotted as a function of the ^{13}C' line width measured in a CP experiment. At the magic angle (~54.736°) the ^{13}C' line width was ~21 Hz, and from here the angle was systematically mis-adjusted up to a setting that yielded a ^{13}C' line width of 54 Hz. In the explored range we found that the measured $R_{1\rho}$ changed by less than 2%, suggesting that the $R_{1\rho}$ measurement is relatively forgiving to a slight mis-adjustment of the magic angle.

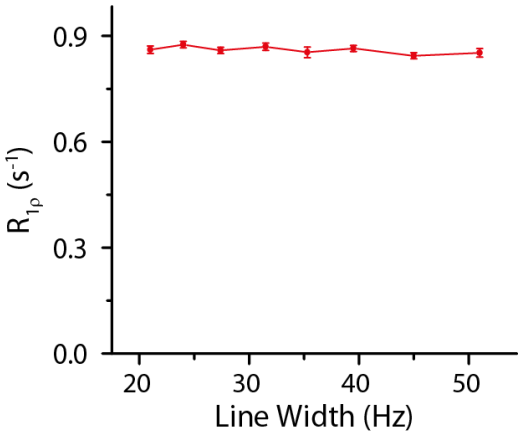

Figure C.11. ^{13}C' $R_{1\rho}$ in [1-^{13}C]alanine as a function of deviation of the rotor axis from the magic angle. The horizontal axis depicts ^{13}C' line width, itself a function of the rotor angle setting; 21 Hz corresponds to a "well-set" magic angle, while a larger line width indicates a larger deviation from the magic angle. Measurements were performed at $\omega_{0H}/2\pi$ = 600 MHz, $\omega_r/2\pi$ = 60 kHz and $\omega_1/2\pi$ = 17 kHz.

C.4.2 Temperature Effects

The ^{13}C' $R_{1\rho}$ experiment is relatively robust with respect to sample temperature changes (from r.f.-induced heating) during the spin-lock pulse. We measured the temperature change of the GB1 sample (50 mM salt, pH 5.5) at $\omega_{0H}/2\pi$ = 600 MHz and $\omega_r/2\pi$ = 60 kHz (using a Bruker 1.3 mm rotor) upon application of a ^{13}C spin-lock pulse prior to acquisition. The temperature was measured based on the chemical shift of water protons.[282] For reference, the sample temperature without any ^{13}C irradiation was 26.9 ±

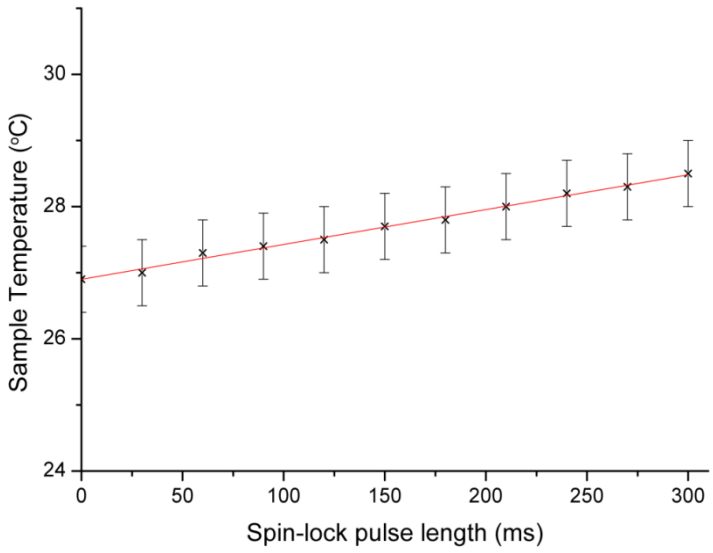

Figure C.12. Sample temperature as a function of spin-lock pulse length, as measured by the chemical shift of water protons with respect to internal DSS in a sample of [U-^{13}C,^{15}N]GB1 (50 mM salt concentration, pH 5.5).[282] Experiments were measured at 14.1 T at 60 kHz MAS frequency, with a spin-lock nutation frequency of 17 kHz (corresponding to 2.49 W) and the initial (*i.e.* in the absence of spin-lock) sample temperature of 26.9 ± 0.5 °C.

0.5 °C. A total of 50 experiments with 0.3 s of 17 kHz spin-lock irradiation were performed (32 scans per experiment with a recycle delay of 2 s, resulting in a total time for each experiment of ~74 s) back to back, for a total of ~62 minutes. The measured sample temperature had increased by 1.5 ± 0.5 °C after a single experiment, but then remained at a constant 28.4 ± 0.5 °C for the remainder of the 62 minute run, showing that equilibrium is reached quickly (a few transients) without the long stabilization time observed for larger rotors at slower spinning frequencies and under the application of high power heteronuclear decoupling. As 0.3 s is at the limit of what must typically be sampled experimentally (we sampled to 0.2 s at 17 kHz for ^{13}C, plus a combined 50 ms of 15 kHz slpTPPM decoupling during t_1 and t_2 acquisition periods), internal sample temperatures should not be expected to exceed a temperature 1.5 °C higher than equilibrium at any point during an $R_{1\rho}$ experiment.

To examine the relationship between temperature increase and spin-lock pulse length under typical experimental conditions (60 kHz MAS, 17 kHz spin-lock field strength), further test experiments were conducted with spin-lock pulses ranging from 10 ms to 300.01 ms (see Figure C.12). Naturally, the sample was observed to increase in temperature with increased pulse length, but at a rate of just ~0.005 K ms^{-1} (assuming a linear relationship). The difference in sample temperature between different spin-lock

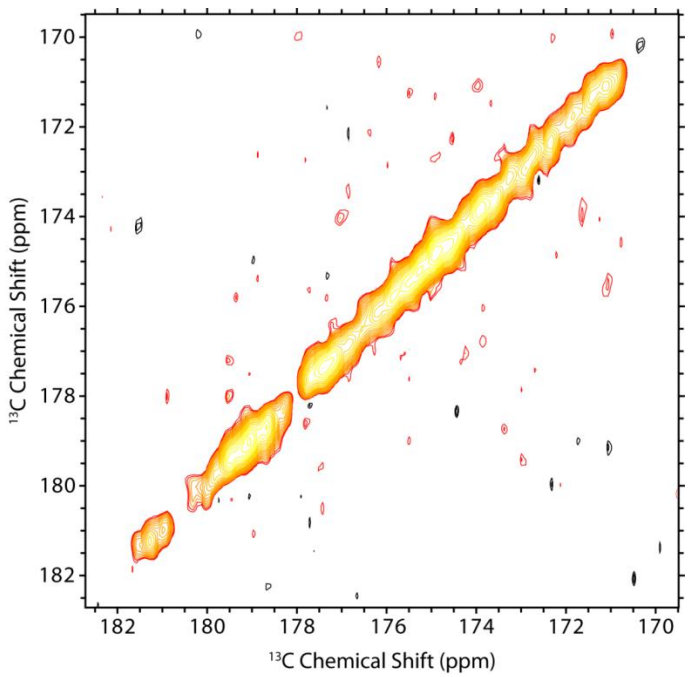

Figure C.13. Spectrum resulting from an experiment to test for the occurrence of polarisation transfer during a spin-lock pulse typical of that employed in a ^{13}C' $R_{1\rho}$ experiment. After a 150 ms "mixing" block of 17 kHz ^{13}C' irradiation, no ^{13}C'-^{13}C' cross-peaks are seen above the level of noise (negative contours in black, positive in red-yellow), implying little or no polarisation transfer occurs.

lengths sampled is clearly very small (maximum of 1.5 °C difference between shortest and longest spin-lock pulses employed in an experiment) and for most purposes may be considered negligible.

These results also illustrate that the technology employed here provides a practical and safe approach for measuring relaxation dispersion for spin-lock frequencies in the range from ~1 kHz to a few tens of kHz (or more if the length of spin-lock is limited to a few tens of milliseconds), which significantly expands the range of time scales accessible with such methodology to a few microseconds, and complementing CPMG in perdeuterated proteins.[342] Relaxation dispersion in the solid state could potentially be highly complementary to similar measurements in solution, where currently even with cryo-cooled NMR probe heads the current limit for safe spin-lock field strengths is ~6.4 kHz (corresponding to a minimum detectable time scale of $1/(2\pi*6.4\text{ kHz}) \approx 25$ ms).[391]

C.4.3 Polarisation Transfer

Another potential complication associated with carbonyl $R_{1\rho}$ experiments is that of polarisation transfer between different sites during the spin-lock pulse, namely via isotropic mixing or r.f.-driven spin diffusion mechanisms. In the solution state it has

been noted that evolution under homonuclear three-bond scalar couplings can lead to magnetization transfer during spin-locking ("isotropic mixing") between carbonyls of neighbouring residues whose resonances are close in chemical shift, leading to inaccurate $R_{1\rho}$ measurements.[392] To check that neither this nor r.f.-driven spin diffusion would compromise our solid-state experiments, we ran a 2D ^{13}C-^{13}C experiment (on-resonance with ^{13}C') with a "mixing" block (between t_1 and t_2 acquisition) consisting of a 150 ms, 17 kHz spin-lock pulse. After a total of 56 scans (~14.5 hours) no off-diagonal cross-peaks were observed above the noise level (spectrum in Figure C.13) between carbonyls (or between ^{13}C' and $^{13}C_\alpha$), suggesting that neither mechanism is efficient for polarisation transfer under the employed conditions. Note, however, that r.f.-driven spin diffusion may become more of a concern for aliphatic carbons.

C.5. Details of Quantitative Analysis of Relaxation Data

Table C.1. Relaxation-active interactions in the peptide plane frame, used for quantitative analysis of motions of GB1. ^{15}N-^{1}H^{other} and ^{13}C'-^{1}H^{other} dipolar contributions represent overall, effective contributions from non-directly-bonded protons. The ^{15}N and ^{13}C' CSA components were parameterised using linear fits of the CSA components versus isotropic chemical shift for solid-state NMR CSA measurements on crystalline GB1.[366,382]

Relaxation active interaction	Geometrical/CSA parameters
^{15}N-^{1}H^{N}	1.02 Å
^{15}N-^{1}H^{other}	r_{eff} = 1.80 Å[393]
^{15}N CSA	σ_{xx}= 1.1283σ_{iso} + 93.77 (ppm)[366] σ_{yy}= 1.0086σ_{iso} – 42.475 (ppm)[366] σ_{zz}= 0.8631σ_{iso} – 51.295 (ppm)[366]
^{15}N-^{13}C'	1.33 Å
^{15}N-^{13}C$^{\alpha}$	1.46 Å
^{13}C'-^{13}C$^{\alpha}$	1.525 Å
^{13}C'-^{1}H^{N}	2.04 Å
^{13}C' CSA	σ_{11}= 0.24σ_{iso} + 200 (ppm)[382] σ_{22}= 2.82σ_{iso} – 305 (ppm)[382] σ_{33}= 96.5 (ppm)[382]
^{13}C'-^{1}H^{other}	r_{eff} = 1.82 Å[393]

Contributions to the various relaxation rates were assumed as presented in §10.4. The magnitudes of the interactions included are given in Table C.1. ^{15}N CSA components were parameterised using nitrogen isotropic chemical shifts, based on linear fits of the CSA components versus isotropic chemical shift for solid-state NMR CSA measurements on crystalline GB1.[366] A similar method was used for ^{13}C' CSA parameterisation.[382] $J(\omega_{C'} - \omega_{C\alpha})$ was evaluated at a frequency equivalent to 120 ppm for ^{13}C.

C.6. Solution-State Extended Model-Free Analysis

A two-time scale EMF analysis in the solution state uses the following expressions for spectral densities:[358]

$$J(\omega) = S_f^2 S_f^2 \frac{\tau_R}{1 + (\tau_R \omega)^2} + \left(1 - S_f^2\right) \frac{\tau_f{}'}{1 + \left(\omega \tau_f{}'\right)^2} + S_f^2 (1 - S_s^2) \frac{\tau_s{}'}{1 + (\omega \tau_s{}')^2} \qquad \text{(C.1)}$$

with $\frac{1}{\tau_f{}'} = \frac{1}{\tau_f} + \frac{1}{\tau_R}$ and $\frac{1}{\tau_s{}'} = \frac{1}{\tau_s} + \frac{1}{\tau_R}$. S^2 is the order parameter and τ is the motional correlation time, and associated subscripts R, f and s denote overall rotational diffusion and fast and slow internal motions, respectively.

BIBLIOGRAPHY

(1) Purcell, E. M.; Torrey, H. C.; Pound, R. V. *Physical Review* **1946**, *69*, 37.
(2) McCammon, J. A.; Karplus, M. *Accounts of Chemical Research* **1983**, *16*, 187.
(3) Henzler-Wildman, K.; Kern, D. *Nature* **2007**, *450*, 964.
(4) Dill, K. A.; MacCallum, J. L. *Science* **2012**, *338*, 1042.
(5) Kühlbrandt, W. *Science* **2014**, *343*, 1443.
(6) Williamson, M. P.; Havel, T. F.; Wüthrich, K. *Journal of Molecular Biology* **1985**, *182*, 295.
(7) Krogh, A.; Larsson, B.; Von Heijne, G.; Sonnhammer, E. L. *Journal of Molecular Biology* **2001**, *305*, 567.
(8) Overington, J. P.; Al-Lazikani, B.; Hopkins, A. L. *Nature Reviews Drug Discovery* **2006**, *5*, 993.
(9) McDermott, A. *Annual Review of Biophysics* **2009**, *38*, 385.
(10) Pulawski, W.; Ghoshdastider, U.; Andrisano, V.; Filipek, S. *Applied Biochemistry and Biotechnology* **2012**, *166*, 1626.
(11) Tycko, R. *Annual Review of Physical Chemistry* **2011**, *62*, 279.
(12) Han, Y.; Ahn, J.; Concel, J.; Byeon, I.-J. L.; Gronenborn, A. M.; Yang, J.; Polenova, T. *Journal of the American Chemical Society* **2010**, *132*, 1976.
(13) Bertini, I.; Luchinat, C.; Parigi, G.; Ravera, E.; Reif, B.; Turano, P. *Proceedings of the National Academy of Sciences* **2011**, *108*, 10396.
(14) Mainz, A.; Bardiaux, B.; Kuppler, F.; Multhaup, G.; Felli, I. C.; Pierattelli, R.; Reif, B. *Journal of Biological Chemistry* **2012**, *287*, 1128.
(15) Lamley, J. M.; Iuga, D.; Öster, C.; Sass, H. J.; Rogowski, M.; Oss, A.; Past, J.; Reinhold, A.; Grzesiek, S.; Samoson, A. *Journal of the American Chemical Society* **2014**, *136*, 16800.
(16) Gardiennet, C.; Schütz, A. K.; Hunkeler, A.; Kunert, B.; Terradot, L.; Böckmann, A.; Meier, B. H. *Angewandte Chemie International Edition* **2012**, *51*, 7855.
(17) Bloch, F.; Hansen, W. W.; Packard, M. *Physical Review* **1946**, *70*, 474.
(18) Proctor, W.; Yu, F. *Physical Review* **1950**, *77*, 717.
(19) Dickinson, W. *Physical Review* **1950**, *77*, 736.
(20) Ramsey, N. F. *Physical Review* **1950**, *78*, 699.
(21) Pake, G. *The Journal of Chemical Physics* **1948**, *16*, 327.
(22) Bloch, F. *Physical Review* **1946**, *70*, 460.
(23) Bloembergen, N.; Purcell, E.; Pound, R. *Nature* **1947**, *160*, 475.
(24) Torrey, H. C. *Physical Review* **1953**, *92*, 962.
(25) Nelson, F.; Weaver, H. *Science* **1964**, *146*, 223.
(26) Ernst, R. R.; Anderson, W. *Review of Scientific Instruments* **1966**, *37*, 93.
(27) Saunders, M.; Wishnia, A.; Kirkwood, J. G. *Journal of the American Chemical Society* **1957**, *79*, 3289.
(28) Aue, W.; Bartholdi, E.; Ernst, R. R. *The Journal of Chemical Physics* **1976**, *64*, 2229.
(29) Nagayama, K.; Kumar, A.; Wüthrich, K.; Ernst, R. *Journal of Magnetic Resonance (1969)* **1980**, *40*, 321.
(30) Jeener, J.; Meier, B.; Bachmann, P.; Ernst, R. *The Journal of Chemical Physics* **1979**, *71*, 4546.
(31) Kumar, A.; Ernst, R.; Wüthrich, K. *Biochemical and Biophysical Research Communications* **1980**, *95*, 1.
(32) Kay, L. E.; Torchia, D. A.; Bax, A. *Biochemistry* **1989**, *28*, 8972.
(33) Lipari, G.; Szabo, A. *Journal of the American Chemical Society* **1982**, *104*, 4546.

(34) Lipari, G.; Szabo, A. *Journal of the American Chemical Society* **1982**, *104*, 4559.
(35) Andrew, E.; Bradbury, A.; Eades, R. **1958**.
(36) Lowe, I. *Physical Review Letters* **1959**, *2*, 285.
(37) Sarles, L. R.; Cotts, R. *Physical Review* **1958**, *111*, 853.
(38) Waugh, J.; Wang, C.; Huber, L.; Vold, R. *The Journal of Chemical Physics* **1968**, *48*, 662.
(39) Waugh, J.; Huber, L.; Haeberlen, U. *Physical Review Letters* **1968**, *20*, 180.
(40) Haeberlen, U.; Waugh, J. *Physical Review* **1968**, *175*, 453.
(41) Mehring, M.; Pines, A.; Rhim, W. K.; Waugh, J. *The Journal of Chemical Physics* **1971**, *54*, 3239.
(42) Hartmann, S.; Hahn, E. *Physical Review* **1962**, *128*, 2042.
(43) Pines, A.; Gibby, M.; Waugh, J. *The Journal of Chemical Physics* **1973**, *59*, 569.
(44) Schaefer, J.; Stejskal, E. *Journal of the American Chemical Society* **1976**, *98*, 1031.
(45) Bhattacharya, A. *Nature News* **2010**, *463*, 605.
(46) Samoson, A.; Tuherm, T.; Past, J.; Reinhold, A.; Anupõld, T.; Heinmaa, I. In *New Techniques in Solid-State NMR*; Springer: 2005, p 15.
(47) Kobayashi, T.; Mao, K.; Paluch, P.; Nowak-Król, A.; Sniechowska, J.; Nishiyama, Y.; Gryko, D. T.; Potrzebowski, M. J.; Pruski, M. *Angewandte Chemie* **2013**.
(48) Agarwal, V.; Penzel, S.; Szekely, K.; Cadalbert, R.; Testori, E.; Oss, A.; Past, J.; Samoson, A.; Ernst, M.; Böckmann, A. *Angewandte Chemie International Edition* **2014**, *53*, 12253.
(49) Castellani, F.; van Rossum, B.; Diehl, A.; Schubert, M.; Rehbein, K.; Oschkinat, H. *Nature* **2002**, *420*, 98.
(50) Lange, A.; Becker, S.; Seidel, K.; Giller, K.; Pongs, O.; Baldus, M. *Angewandte Chemie International Edition* **2005**, *44*, 2089.
(51) Zhou, D. H.; Shea, J. J.; Nieuwkoop, A. J.; Franks, W. T.; Wylie, B. J.; Mullen, C.; Sandoz, D.; Rienstra, C. M. *Angewandte Chemie International Edition* **2007**, *46*, 8380.
(52) Loquet, A.; Bardiaux, B.; Gardiennet, C.; Blanchet, C.; Baldus, M.; Nilges, M.; Malliavin, T.; Böckmann, A. *Journal of the American Chemical Society* **2008**, *130*, 3579.
(53) Manolikas, T.; Herrmann, T.; Meier, B. H. *Journal of the American Chemical Society* **2008**, *130*, 3959.
(54) Bertini, I.; Bhaumik, A.; De Paepe, G.; Griffin, R. G.; Lelli, M.; Lewandowski, J. R.; Luchinat, C. *Journal of the American Chemical Society* **2010**, *132*, 1032.
(55) Knight, M. J.; Pell, A. J.; Bertini, I.; Felli, I. C.; Gonnelli, L.; Pierattelli, R.; Herrmann, T.; Emsley, L.; Pintacuda, G. *Proceedings of the National Academy of Sciences* **2012**, *109*, 11095.
(56) Yan, S.; Hou, G.; Schwieters, C. D.; Ahmed, S.; Williams, J. C.; Polenova, T. *Journal of Molecular Biology* **2013**, *425*, 4249.
(57) Mani, R.; Tang, M.; Wu, X.; Buffy, J.; Waring, A.; Sherman, M.; Hong, M. *Biochemistry* **2006**, *45*, 8341.
(58) Cady, S. D.; Mishanina, T. V.; Hong, M. *Journal of Molecular Biology* **2009**, *385*, 1127.
(59) Traaseth, N. J.; Shi, L.; Verardi, R.; Mullen, D. G.; Barany, G.; Veglia, G. *Proceedings of the National Academy of Sciences* **2009**, *106*, 10165.
(60) Tang, M.; Sperling, L. J.; Berthold, D. A.; Schwieters, C. D.; Nesbitt, A. E.; Nieuwkoop, A. J.; Gennis, R. B.; Rienstra, C. M. *Journal of Biomolecular NMR* **2011**, *51*, 227.
(61) Das, B. B.; Nothnagel, H. J.; Lu, G. J.; Son, W. S.; Tian, Y.; Marassi, F. M.; Opella, S. J. *Journal of the American Chemical Society* **2012**, *134*, 2047.
(62) Park, S. H.; Das, B. B.; Casagrande, F.; Tian, Y.; Nothnagel, H. J.; Chu, M.; Kiefer, H.; Maier, K.; De Angelis, A. A.; Marassi, F. M. *Nature* **2012**, *491*, 779.

(63) Shahid, S. A.; Bardiaux, B.; Franks, W. T.; Krabben, L.; Habeck, M.; van Rossum, B.-J.; Linke, D. *Nature Methods* **2012**, *9*, 1212.
(64) Wang, S.; Munro, R. A.; Shi, L.; Kawamura, I.; Okitsu, T.; Wada, A.; Kim, S.-Y.; Jung, K.-H.; Brown, L. S.; Ladizhansky, V. *Nature Methods* **2013**, *10*, 1007.
(65) Tang, M.; Nesbitt, A. E.; Sperling, L. J.; Berthold, D. A.; Schwieters, C. D.; Gennis, R. B.; Rienstra, C. M. *Journal of Molecular Biology* **2013**, *425*, 1670.
(66) Iwata, K.; Fujiwara, T.; Matsuki, Y.; Akutsu, H.; Takahashi, S.; Naiki, H.; Goto, Y. *Proceedings of the National Academy of Sciences* **2006**, *103*, 18119.
(67) Ferguson, N.; Becker, J.; Tidow, H.; Tremmel, S.; Sharpe, T. D.; Krause, G.; Flinders, J.; Petrovich, M.; Berriman, J.; Oschkinat, H. *Proceedings of the National Academy of Sciences* **2006**, *103*, 16248.
(68) Petkova, A. T.; Yau, W.-M.; Tycko, R. *Biochemistry* **2006**, *45*, 498.
(69) Paravastu, A. K.; Leapman, R. D.; Yau, W.-M.; Tycko, R. *Proceedings of the National Academy of Sciences* **2008**, *105*, 18349.
(70) Nielsen, J. T.; Bjerring, M.; Jeppesen, M. D.; Pedersen, R. O.; Pedersen, J. M.; Hein, K. L.; Vosegaard, T.; Skrydstrup, T.; Otzen, D. E.; Nielsen, N. C. *Angewandte Chemie International Edition* **2009**, *48*, 2118.
(71) Van Melckebeke, H.; Wasmer, C.; Lange, A.; Eiso, A. B.; Loquet, A.; Bockmann, A.; Meier, B. H. *Journal of the American Chemical Society* **2010**, *132*, 13765.
(72) Loquet, A.; Sgourakis, N. G.; Gupta, R.; Giller, K.; Riedel, D.; Goosmann, C.; Griesinger, C.; Kolbe, M.; Baker, D.; Becker, S. *Nature* **2012**, *486*, 276.
(73) Lu, J.-X.; Qiang, W.; Yau, W.-M.; Schwieters, C. D.; Meredith, S. C.; Tycko, R. *Cell* **2013**, *154*, 1257.
(74) Fitzpatrick, A. W.; Debelouchina, G. T.; Bayro, M. J.; Clare, D. K.; Caporini, M. A.; Bajaj, V. S.; Jaroniec, C. P.; Wang, L.; Ladizhansky, V.; Müller, S. A. *Proceedings of the National Academy of Sciences* **2013**, *110*, 5468.
(75) Loquet, A.; Habenstein, B.; Chevelkov, V.; Vasa, S. K.; Giller, K.; Becker, S.; Lange, A. *Journal of the American Chemical Society* **2013**, *135*, 19135.
(76) Demers, J.-P.; Habenstein, B.; Loquet, A.; Vasa, S. K.; Giller, K.; Becker, S.; Baker, D.; Lange, A.; Sgourakis, N. G. *Nature Communications* **2014**, *5*.
(77) Schütz, A. K.; Vagt, T.; Huber, M.; Ovchinnikova, O. Y.; Cadalbert, R.; Wall, J.; Güntert, P.; Böckmann, A.; Glockshuber, R.; Meier, B. H. *Angewandte Chemie International Edition* **2015**, *54*, 331.
(78) Morag, O.; Sgourakis, N. G.; Baker, D.; Goldbourt, A. *Proceedings of the National Academy of Sciences* **2015**, *112*, 971.
(79) Fiaux, J.; Bertelsen, E. B.; Horwich, A. L.; Wüthrich, K. *Nature* **2002**, *418*, 207.
(80) Gelis, I.; Bonvin, A. M.; Keramisanou, D.; Koukaki, M.; Gouridis, G.; Karamanou, S.; Economou, A.; Kalodimos, C. G. *Cell* **2007**, *131*, 756.
(81) Sprangers, R.; Gribun, A.; Hwang, P. M.; Houry, W. A.; Kay, L. E. *Proceedings of the National Academy of Sciences of the United States of America* **2005**, *102*, 16678.
(82) Sprangers, R.; Kay, L. E. *Nature* **2007**, *445*, 618.
(83) Mainz, A.; Religa, T. L.; Sprangers, R.; Linser, R.; Kay, L. E.; Reif, B. *Angewandte Chemie International Edition* **2013**, *52*, 8746.
(84) Barbet-Massin, E.; Huang, C. T.; Daebel, V.; Hsu, S. T. D.; Reif, B. *Angewandte Chemie International Edition* **2015**, *54*, 4367.
(85) Reif, B. *Journal of Magnetic Resonance* **2012**, *216*, 1.
(86) Maly, T.; Debelouchina, G. T.; Bajaj, V. S.; Hu, K.-N.; Joo, C.-G.; Mak–Jurkauskas, M. L.; Sirigiri, J. R.; van der Wel, P. C.; Herzfeld, J.; Temkin, R. J. *The Journal of Chemical Physics* **2008**, *128*, 052211.
(87) Hyberts, S. G.; Arthanari, H.; Robson, S. A.; Wagner, G. *Journal of Magnetic Resonance* **2014**, *241*, 60.

(88) Mainz, A.; Jehle, S.; van Rossum, B. J.; Oschkinat, H.; Reif, B. *Journal of the American Chemical Society* **2009**, *131*, 15968.
(89) Duer, M. J. *Introduction to Solid-State NMR Spectroscopy*; Wiley-Blackwell, 2005.
(90) Luginbühl, P.; Wüthrich, K. *Progress in Nuclear Magnetic Resonance Spectroscopy* **2002**, *40*, 199.
(91) Keeler, J. *Understanding NMR Spectroscopy*; John Wiley & Sons, 2011.
(92) Hore, P. J.; Jones, J. A.; Wimperis, S.; Hore, P. *NMR: The Toolkit*; Oxford University Press Oxford, 2000; Vol. 92.
(93) Levitt, M. H. *Spin Dynamics: Basics of Nuclear Magnetic Resonance*; John Wiley & Sons, 2001.
(94) McDermott, A. E.; Polenova, T. *Solid State NMR Studies of Biopolymers*; John Wiley & Sons, 2012.
(95) Abragam, A. *The Principles of Nuclear Magnetic Resonance*; Clarendon, Oxford, 1961.
(96) Munowitz, M.; Munowitz, M. *Coherence and NMR*; Wiley New York, 1988.
(97) Morcombe, C. R.; Zilm, K. W. *Journal of Magnetic Resonance* **2003**, *162*, 479.
(98) Harris, R. K.; Becker, E. D.; De Menezes, S. M. C.; Granger, P.; Hoffman, R. E.; Zilm, K. W. *Solid State Nuclear Magnetic Resonance* **2008**, *33*, 41.
(99) Apperley, D. C.; Harris, R. K.; Hodgkinson, P. *Solid State NMR: Basic Principles & Practice*; Momentum, 2012.
(100) Bryce, D. L.; Wasylishen, R. E. *Journal of Biomolecular NMR* **2003**, *25*, 73.
(101) Friebolin, H.; Becconsall, J. K. *Basic One-and Two-Dimensional NMR Spectroscopy*; VCH Weinheim, 1993.
(102) Torchia, D. A. *Annual Review of Biophysics and Bioengineering* **1984**, *13*, 125.
(103) Otting, G. *Annual Review of Biophysics* **2010**, *39*, 387.
(104) Sengupta, I.; Nadaud, P. S.; Jaroniec, C. P. *Accounts of Chemical Research* **2013**, *46*, 2117.
(105) Jaroniec, C. P. *Journal of Magnetic Resonance* **2015**, *253*, 50.
(106) Metz, G.; Wu, X.; Smith, S. *Journal of Magnetic Resonance, Series A* **1994**, *110*, 219.
(107) Hediger, S.; Meier, B.; Ernst, R. *Chemical Physics Letters* **1995**, *240*, 449.
(108) Bloom, A. L.; Shoolery, J. N. *Physical Review* **1955**, *97*, 1261.
(109) Bennett, A. E.; Rienstra, C. M.; Auger, M.; Lakshmi, K.; Griffin, R. G. *The Journal of Chemical Physics* **1995**, *103*, 6951.
(110) Fung, B.; Khitrin, A.; Ermolaev, K. *Journal of Magnetic Resonance* **2000**, *142*, 97.
(111) Tekely, P.; Palmas, P.; Canet, D. *Journal of Magnetic Resonance, Series A* **1994**, *107*, 129.
(112) Detken, A.; Hardy, E. H.; Ernst, M.; Meier, B. H. *Chemical Physics Letters* **2002**, *356*, 298.
(113) Shaka, A.; Keeler, J.; Frenkiel, T.; Freeman, R. *Journal of Magnetic Resonance (1969)* **1983**, *52*, 335.
(114) Lewandowski, J. R.; Sein, J.; Sass, H. J. r.; Grzesiek, S.; Blackledge, M.; Emsley, L. *Journal of the American Chemical Society* **2010**, *132*, 8252.
(115) Ernst, M.; Samoson, A.; Meier, B. H. *Chemical Physics Letters* **2001**, *348*, 293.
(116) Ernst, R. R.; Bodenhausen, G.; Wokaun, A. *Principles of Nuclear Magnetic Resonance in One and Two Dimensions*; Clarendon Press Oxford, 1987; Vol. 14.
(117) Frydman, L.; Harwood, J. S. *Journal of the American Chemical Society* **1995**, *117*, 5367.
(118) Medek, A.; Harwood, J. S.; Frydman, L. *Journal of the American Chemical Society* **1995**, *117*, 12779.
(119) Brown, S. P.; Wimperis, S. *Journal of Magnetic Resonance* **1997**, *128*, 42.
(120) States, D. J.; Haberkorn, R. A.; Ruben, D. J. *Journal of Magnetic Resonance* **1982**, *48*, 286.

(121) Marion, D.; Wüthrich, K. *Biochemical and Biophysical Research Communications* **1983**, *124*, 774.
(122) Marion, D.; Ikura, M.; Tschudin, R.; Bax, A. *Journal of Magnetic Resonance (1969)* **1989**, *85*, 393.
(123) Griesinger, C.; Sorensen, O.; Ernst, R. *Journal of Magnetic Resonance (1969)* **1989**, *84*, 14.
(124) Kay, L. E.; Ikura, M.; Tschudin, R.; Bax, A. *Journal of Magnetic Resonance (1969)* **1990**, *89*, 496.
(125) Sattler, M.; Schleucher, J.; Griesinger, C. *Progress in Nuclear Magnetic Resonance Spectroscopy* **1999**, *34*, 93.
(126) Ikura, M.; Kay, L. E.; Bax, A. *Biochemistry* **1990**, *29*, 4659.
(127) Schuetz, A.; Wasmer, C.; Habenstein, B.; Verel, R.; Greenwald, J.; Riek, R.; Böckmann, A.; Meier, B. H. *ChemBioChem* **2010**, *11*, 1543.
(128) Clore, G. M.; Gronenborn, A. M. *Progress in Nuclear Magnetic Resonance Spectroscopy* **1991**, *23*, 43.
(129) Huber, M.; Hiller, S.; Schanda, P.; Ernst, M.; Böckmann, A.; Verel, R.; Meier, B. H. *ChemPhysChem* **2011**, *12*, 915.
(130) Huber, M.; Böckmann, A.; Hiller, S.; Meier, B. H. *Physical Chemistry Chemical Physics* **2012**, *14*, 5239.
(131) Xiang, S.; Chevelkov, V.; Becker, S.; Lange, A. *Journal of Biomolecular NMR* **2014**, *60*, 85.
(132) Bloembergen, N.; Purcell, E. M.; Pound, R. V. *Physical Review* **1948**, *73*, 679.
(133) Solomon, I. *Physical Review* **1955**, *99*, 559.
(134) Overhauser, A. W. *Physical Review* **1953**, *92*, 411.
(135) Anderson, W.; Freeman, R. *The Journal of Chemical Physics* **1962**, *37*, 85.
(136) Carver, T. R.; Slichter, C. P. *Physical Review* **1956**, *102*, 975.
(137) Anet, F.; Bourn, A. *Journal of the American Chemical Society* **1965**, *87*, 5250.
(138) Herrmann, T.; Güntert, P.; Wüthrich, K. *Journal of Biomolecular NMR* **2002**, *24*, 171.
(139) Hahn, E. L. *Physical Review* **1950**, *80*, 580.
(140) Wangsness, R. K.; Bloch, F. *Physical Review* **1953**, *89*, 728.
(141) Redfield, A. G. *IBM Journal of Research and Development* **1957**, *1*, 19.
(142) del Amo, J. M. L.; Agarwal, V.; Sarkar, R.; Porter, J.; Asami, S.; Rübbelke, M.; Fink, U.; Xue, Y.; Lange, O. F.; Reif, B. *Journal of Biomolecular NMR* **2014**, *59*, 241.
(143) Goldman, M. *Journal of Magnetic Resonance (1969)* **1984**, *60*, 437.
(144) Kumar, A.; Christy Rani Grace, R.; Madhu, P. *Progress in Nuclear Magnetic Resonance Spectroscopy* **2000**, *37*, 191.
(145) Sein, J.; Giraud, N.; Blackledge, M.; Emsley, L. *Journal of Magnetic Resonance* **2007**, *186*, 26.
(146) Asami, S.; Porter, J.; Lange, O. F.; Reif, B. *Journal of the American Chemical Society* **2015**.
(147) Kurbanov, R.; Zinkevich, T.; Krushelnitsky, A. *The Journal of Chemical Physics* **2011**, *135*, 184104.
(148) Baneyx, F. *Current Opinion in Biotechnology* **1999**, *10*, 411.
(149) Lian, L.-Y.; Middleton, D. A. *Progress in Nuclear Magnetic Resonance Spectroscopy* **2001**, *39*, 171.
(150) McIntosh, L. P.; Dahlquist, F. W. *Quarterly Reviews of Biophysics* **1990**, *23*, 1.
(151) LeMaster, D. M.; Kushlan, D. M. *Journal of the American Chemical Society* **1996**, *118*, 9255.
(152) Loquet, A.; Lv, G.; Giller, K.; Becker, S.; Lange, A. *Journal of the American Chemical Society* **2011**, *133*, 4722.

(153) LeMaster, D. M. *Methods in Enzymology* **1989**, *177*, 23.
(154) Alam, T. M.; Drobny, G. P. *Chemical Reviews* **1991**, *91*, 1545.
(155) Hoatson, G.; Vold, R. In *Solid-State NMR III Organic Matter*; Springer: 1994, p 1.
(156) McDermott, A.; Creuzet, F.; Kolbert, A.; Griffin, R. *Journal of Magnetic Resonance (1969)* **1992**, *98*, 408.
(157) Reif, B.; Jaroniec, C.; Rienstra, C.; Hohwy, M.; Griffin, R. *Journal of Magnetic Resonance* **2001**, *151*, 320.
(158) Chevelkov, V.; van Rossum, B. J.; Castellani, F.; Rehbein, K.; Diehl, A.; Hohwy, M.; Steuernagel, S.; Engelke, F.; Oschkinat, H.; Reif, B. *Journal of the American Chemical Society* **2003**, *125*, 7788.
(159) Paulson, E. K.; Morcombe, C. R.; Gaponenko, V.; Dancheck, B.; Byrd, R. A.; Zilm, K. W. *Journal of the American Chemical Society* **2003**, *125*, 15831.
(160) Linser, R.; Dasari, M.; Hiller, M.; Higman, V.; Fink, U.; Lopez del Amo, J. M.; Markovic, S.; Handel, L.; Kessler, B.; Schmieder, P. *Angewandte Chemie International Edition* **2011**, *50*, 4508.
(161) Agarwal, V.; Reif, B. *Journal of Magnetic Resonance* **2008**, *194*, 16.
(162) Reif, B.; Griffin, R. *Journal of Magnetic Resonance* **2003**, *160*, 78.
(163) Lewandowski, J. R.; Dumez, J.-N.; Akbey, U.; Lange, S.; Emsley, L.; Oschkinat, H. *J Phys Chem Lett* **2011**, *2*, 2205.
(164) Chevelkov, V.; Rehbein, K.; Diehl, A.; Reif, B. *Angewandte Chemie International Edition* **2006**, *45*, 3878.
(165) Akbey, Ü.; Lange, S.; Franks, W. T.; Linser, R.; Rehbein, K.; Diehl, A.; van Rossum, B.-J.; Reif, B.; Oschkinat, H. *Journal of Biomolecular NMR* **2010**, *46*, 67.
(166) Martin, R. W.; Zilm, K. W. *Journal of Magnetic Resonance* **2003**, *165*, 162.
(167) Zech, S. G.; Wand, A. J.; McDermott, A. E. *Journal of the American Chemical Society* **2005**, *127*, 8618.
(168) Bertini, I.; Luchinat, C.; Parigi, G.; Ravera, E. *Accounts of Chemical Research* **2013**, *46*, 2059.
(169) Bertini, I.; Engelke, F.; Luchinat, C.; Parigi, G.; Ravera, E.; Rosa, C.; Turano, P. *Physical Chemistry Chemical Physics* **2012**, *14*, 439.
(170) Bertini, I.; Engelke, F.; Gonnelli, L.; Knott, B.; Luchinat, C.; Osen, D.; Ravera, E. *Journal of Biomolecular NMR* **2012**, *54*, 123.
(171) Piotto, M.; Saudek, V.; Sklenář, V. *Journal of Biomolecular NMR* **1992**, *2*, 661.
(172) Hoult, D. I. *Journal of Magnetic Resonance (1969)* **1976**, *21*, 337.
(173) Bodenhausen, G.; Ruben, D. J. *Chemical Physics Letters* **1980**, *69*, 185.
(174) De Paëpe, G. *Annual Review of Physical Chemistry* **2012**, *63*, 661.
(175) De Paëpe, G.; Lewandowski, J. R.; Loquet, A.; Böckmann, A.; Griffin, R. G. *The Journal of Chemical Physics* **2008**, *129*, 245101.
(176) De Paëpe, G.; Lewandowski, J. R.; Loquet, A.; Eddy, M.; Megy, S.; Böckmann, A.; Griffin, R. G. *The Journal of Chemical Physics* **2011**, *134*, 095101.
(177) Andrew, E. R.; Clough, S.; Farnell, L.; Gledhill, T. D.; Roberts, I. *Physics Letters* **1966**, *21*, 505.
(178) Raleigh, D. P.; Levitt, M. H.; Griffin, R. G. *Chemical Physics Letters* **1988**, *146*, 71.
(179) Creuzet, F.; McDermott, A.; Gebhard, R.; Van der Hoef, K.; Spijker-Assink, M.; Herzfeld, J.; Lugtenburg, J.; Levitt, M.; Griffin, R. *Science* **1991**, *251*, 783.
(180) Raleigh, D.; Levitt, M.; Griffin, R. *Chemical Physics Letters* **1988**, *146*, 71.
(181) Oas, T. G.; Griffin, R. G.; Levitt, M. H. *The Journal of Chemical Physics* **1988**, *89*, 692.
(182) Nielsen, N. C.; Bildso, H.; Jakobsen, H. J.; Levitt, M. H. *The Journal of Chemical Physics* **1994**, *101*, 1805.

(183) Verel, R.; Baldus, M.; Ernst, M.; Meier, B. H. *Chemical Physics Letters* **1998**, *287*, 421.
(184) Verel, R.; Ernst, M.; Meier, B. H. *Journal of Magnetic Resonance* **2001**, *150*, 81.
(185) Westfeld, T.; Verel, R.; Ernst, M.; Böckmann, A.; Meier, B. H. *Journal of Biomolecular NMR* **2012**, *53*, 103.
(186) Schaefer, J.; McKay, R. A.; Stejskal, E. O. *Journal of Magnetic Resonance (1969)* **1979**, *34*, 443.
(187) Bennett, A. E.; Griffin, R. G.; Ok, J. H.; Vega, S. *The Journal of Chemical Physics* **1992**, *96*, 8624.
(188) Gullion, T.; Schaefer, J. *Journal of Magnetic Resonance* **1989**, *81*, 196.
(189) Gullion, T. *Concepts in Magnetic Resonance* **1998**, *10*, 277.
(190) Lee, Y. K.; Kurur, N. D.; Helmle, M.; Johannessen, O. G.; Nielsen, N. C.; Levitt, M. H. *Chemical Physics Letters* **1995**, *242*, 304.
(191) Carravetta, M.; Eden, M.; Zhao, X.; Brinkmann, A.; Levitt, M. H. *Chemical Physics Letters* **2000**, *321*, 205.
(192) Levitt, M. H. *The Journal of Chemical Physics* **2008**, *128*, 052205.
(193) Bloembergen, N. *Physica* **1949**, *15*, 386.
(194) Szeverenyi, N. M.; Sullivan, M. J.; Maciel, G. E. *Journal of Magnetic Resonance (1969)* **1982**, *47*, 462.
(195) Heise, H.; Seidel, K.; Etzkorn, M.; Becker, S.; Baldus, M. *Journal of Magnetic Resonance* **2005**, *173*, 64.
(196) Lange, A.; Seidel, K.; Verdier, L.; Luca, S.; Baldus, M. *Journal of the American Chemical Society* **2003**, *125*, 12640.
(197) Takegoshi, K.; Nakamura, S.; Terao, T. *Chemical Physics Letters* **2001**, *344*, 631.
(198) Morcombe, C. R.; Gaponenko, V.; Byrd, R. A.; Zilm, K. W. *Journal of the American Chemical Society* **2004**, *126*, 7196.
(199) Lewandowski, J. R.; De Paëpe, G.; Griffin, R. G. *Journal of the American Chemical Society* **2007**, *129*, 728.
(200) Fossi, M.; Castellani, F.; Nilges, M.; Oschkinat, H.; van Rossum, B. J. *Angewandte Chemie* **2005**, *117*, 6307.
(201) Moseley, H. N.; Sperling, L. J.; Rienstra, C. M. *Journal of Biomolecular NMR* **2010**, *48*, 123.
(202) Tycko, R.; Hu, K.-N. *Journal of Magnetic Resonance* **2010**, *205*, 304.
(203) Guerry, P.; Herrmann, T. *Quarterly Reviews of Biophysics* **2011**, *44*, 257.
(204) Schmidt, E.; Gath, J.; Habenstein, B.; Ravotti, F.; Székely, K.; Huber, M.; Buchner, L.; Böckmann, A.; Meier, B. H.; Güntert, P. *Journal of Biomolecular NMR* **2013**, *56*, 243.
(205) Linser, R.; Fink, U.; Reif, B. *Journal of Magnetic Resonance* **2008**, *193*, 89.
(206) Vijayan, V.; Demers, J. P.; Biernat, J.; Mandelkow, E.; Becker, S.; Lange, A. *ChemPhysChem* **2009**, *10*, 2205.
(207) Barbet-Massin, E.; Pell, A. J.; Jaudzems, K.; Franks, W. T.; Retel, J. S.; Kotelovica, S.; Akopjana, I.; Tars, K.; Emsley, L.; Oschkinat, H. *Journal of Biomolecular NMR* **2013**, *56*, 379.
(208) Barbet-Massin, E.; Pell, A. J.; Knight, M. J.; Webber, A. L.; Felli, I. C.; Pierattelli, R.; Emsley, L.; Lesage, A.; Pintacuda, G. *ChemPhysChem* **2013**, *14*, 3131.
(209) Chevelkov, V.; Habenstein, B.; Loquet, A.; Giller, K.; Becker, S.; Lange, A. *Journal of Magnetic Resonance* **2014**, *242*, 180.
(210) Barbet-Massin, E.; Pell, A. J.; Retel, J. S.; Andreas, L. B.; Jaudzems, K.; Franks, W. T.; Nieuwkoop, A. J.; Hiller, M.; Higman, V.; Guerry, P.; Bertarello, A.; Knight, M. J.; Felletti, M.; Le Marchand, T.; Kotelovica, S.; Akopjana, I.; Tars, K.; Stoppini, M.; Bellotti, V.; Bolognesi, M.; Ricagno, S.; Chou, J.; Griffin, R. G.;

Oschkinat, H.; Lesage, A.; Emsley, L.; Herrmann, T.; Pintacuda, G. *Journal of the American Chemical Society* **2014**, *136*, 12489.
(211) Bertini, I.; McGreevy, K. S.; Parigi, G. *NMR of Biomolecules: Towards Mechanistic Systems Biology*; John Wiley & Sons, 2012.
(212) Wishart, D. S.; Sykes, B. D. *Journal of Biomolecular NMR* **1994**, *4*, 171.
(213) Bower, P. V.; Oyler, N.; Mehta, M. A.; Long, J. R.; Stayton, P. S.; Drobny, G. P. *Journal of the American Chemical Society* **1999**, *121*, 8373.
(214) Rienstra, C. M.; Hohwy, M.; Mueller, L. J.; Jaroniec, C. P.; Reif, B.; Griffin, R. G. *Journal of the American Chemical Society* **2002**, *124*, 11908.
(215) Hong, M. In *Modern Magnetic Resonance*; Springer: 2006, p 727.
(216) Cornilescu, G.; Delaglio, F.; Bax, A. *Journal of Biomolecular NMR* **1999**, *13*, 289.
(217) Brünger, A. T.; Adams, P. D.; Clore, G. M.; DeLano, W. L.; Gros, P.; Grosse-Kunstleve, R. W.; Jiang, J.-S.; Kuszewski, J.; Nilges, M.; Pannu, N. S. *Acta Crystallographica Section D: Biological Crystallography* **1998**, *54*, 905.
(218) Sengupta, I.; Nadaud, P. S.; Helmus, J. J.; Schwieters, C. D.; Jaroniec, C. P. *Nature Chemistry* **2012**, *4*, 410.
(219) Etzkorn, M.; Böckmann, A.; Lange, A.; Baldus, M. *Journal of the American Chemical Society* **2004**, *126*, 14746.
(220) Williamson, M. P. *Progress in Nuclear Magnetic Resonance Spectroscopy* **2013**, *73*, 1.
(221) Lange, A.; Giller, K.; Hornig, S.; Martin-Eauclaire, M.-F.; Pongs, O.; Becker, S.; Baldus, M. *Nature* **2006**, *440*, 959.
(222) De Angelis, A. A.; Jones, D. H.; Grant, C. V.; Park, S. H.; Mesleh, M. F.; Opella, S. J. *Methods in Enzymology* **2005**, *394*, 350.
(223) Huster, D.; Yao, X.; Hong, M. *Journal of the American Chemical Society* **2002**, *124*, 874.
(224) Ader, C.; Schneider, R.; Seidel, K.; Etzkorn, M.; Becker, S.; Baldus, M. *Journal of the American Chemical Society* **2008**, *131*, 170.
(225) Wang, T.; Cady, S. D.; Hong, M. *Biophysical Journal* **2012**, *102*, 787.
(226) Hafner, S.; Spiess, H. W. *Concepts in Magnetic Resonance* **1998**, *10*, 99.
(227) Samoson, A.; Tuherm, T.; Gan, Z. *Solid State Nuclear Magnetic Resonance* **2001**, *20*, 130.
(228) Böckmann, A.; Ernst, M.; Meier, B. H. *Journal of Magnetic Resonance* **2015**, *253*, 71.
(229) Gardner, K. H.; Zhang, X.; Gehring, K.; Kay, L. E. *Journal of the American Chemical Society* **1998**, *120*, 11738.
(230) Franks, W. T.; Kloepper, K. D.; Wylie, B. J.; Rienstra, C. M. *Journal of Biomolecular NMR* **2007**, *39*, 107.
(231) Gopinath, T.; Veglia, G. *Journal of Magnetic Resonance* **2012**, *220*, 79.
(232) Lamley, J. M.; Lewandowski, J. R. *Journal of Magnetic Resonance* **2012**, *218*, 30.
(233) Nielsen, A. B.; Székely, K.; Gath, J.; Ernst, M.; Nielsen, N. C.; Meier, B. H. *Journal of Biomolecular NMR* **2012**, *52*, 283.
(234) Martineau, C.; Decker, F.; Engelke, F.; Taulelle, F. *Solid State Nuclear Magnetic Resonance* **2013**, *55*, 48.
(235) Linser, R.; Bardiaux, B.; Andreas, L. B.; Hyberts, S. G.; Morris, V. K.; Pintacuda, G.; Sunde, M.; Kwan, A. H.; Wagner, G. *Journal of the American Chemical Society* **2014**, *136*, 11002.
(236) Lewandowski, J. R.; De Paëpe, G.; Eddy, M. T.; Griffin, R. G. *Journal of the American Chemical Society* **2009**, *131*, 5769.
(237) Lewandowski, J. R.; De Paëpe, G.; Eddy, M. T.; Struppe, J.; Maas, W. E.; Griffin, R. G. *Journal of Physical Chemistry B* **2009**, *113*, 9062.
(238) Bertini, I.; Gonnelli, L.; Luchinat, C.; Mao, J.; Nesi, A. *Journal of the American Chemical Society* **2011**, *133*, 16013.

(239) van der Wel, P. C. A.; Lewandowski, J. R.; Griffin, R. G. *Biochemistry* **2010**, *49*, 9457.
(240) Lewandowski, J. R.; van der Wel, P. C. A.; Rigney, M.; Grigorieff, N.; Griffin, R. G. *J. Am. Chem. Soc.* **2011**, *133*, 14686.
(241) Jehle, S.; Rajagopal, P.; Bardiaux, B.; Markovic, S.; Kuhne, R.; Stout, J. R.; Higman, V. A.; Klevit, R. E.; van Rossum, B. J.; Oschkinat, H. *Nature structural & molecular biology* **2010**, *17*, 1037.
(242) Lewandowski, J. R.; De Paepe, G.; Eddy, M. T.; Struppe, J.; Maas, W.; Griffin, R. G. *Journal of Physical Chemistry B* **2009**, *113*, 9062.
(243) Loquet, A.; Lv, G.; Giller, K.; Becker, S.; Lange, A. *Journal of the American Chemical Society* **2011**, *133*, 4722.
(244) Freeman, R.; Kupce, E. *Journal of Biomolecular NMR* **2003**, *27*, 101.
(245) Atreya, H. S.; Szyperski, T. *Method Enzymol* **2005**, *394*, 78.
(246) Boelens, R.; Burgering, M.; Fogh, R. H.; Kaptein, R. *Journal of Biomolecular NMR* **1994**, *4*, 201.
(247) Frueh, D. P.; Arthanari, H.; Wagner, G. *Journal of Biomolecular NMR* **2005**, *33*, 187.
(248) Parella, T.; Nolis, P. *Concept Magn Reson A* **2010**, *36A*, 1.
(249) Kodama, Y.; Reese, M. L.; Shimba, N.; Ono, K.; Kanamori, E.; Dotsch, V.; Noguchi, S.; Fukunishi, Y.; Suzuki, E.; Shimada, I.; Takahashi, H. *J Struct Biol* **2011**, *174*, 434.
(250) Linser, R.; Bardiaux, B.; Higman, V.; Fink, U.; Reif, B. *Journal of the American Chemical Society* **2011**, *133*, 5905.
(251) Veshtort, M.; Griffin, R. G. *Journal of Magnetic Resonance* **2006**, *178*, 248.
(252) Harris, R. K.; Becker, E. D.; De Menezes, S. M. C.; Granger, P.; Hoffman, R. E.; Zilm, K. W. *Pure Appl Chem* **2008**, *80*, 59.
(253) Ban, N.; Nissen, P.; Hansen, J.; Moore, P. B.; Steitz, T. A. *Science* **2000**, *289*, 905.
(254) Leibundgut, M.; Maier, T.; Jenni, S.; Ban, N. *Current Opinion in Structural Biology* **2008**, *18*, 714.
(255) Garman, E. F. *Science* **2014**, *343*, 1102.
(256) Zuiderweg, E. R. P. *Biochemistry* **2002**, *41*, 1.
(257) Frueh, D. P.; Goodrich, A. C.; Mishra, S. H.; Nichols, S. R. *Current Opinion in Structural Biology* **2013**, *23*, 734.
(258) Fricke, P.; Chevelkov, V.; Shi, C.; Lange, A. *Journal of Magnetic Resonance* **2015**, *253*, 2.
(259) Gelis, I.; Vitzthum, V.; Dhimole, N.; Caporini, M. A.; Schedlbauer, A.; Carnevale, D.; Connell, S. R.; Fucini, P.; Bodenhausen, G. *J. Biomol. NMR* **2013**, *56*, 85.
(260) Lewandowski, J. R.; Halse, M. E.; Blackledge, M.; Emsley, L. *Science* **2015**, *348*, 578.
(261) Hologne, M.; Chevelkov, V.; Reif, B. *Progress in Nuclear Magnetic Resonance Spectroscopy* **2006**, *48*, 211.
(262) Zhou, D. H.; Shah, G.; Cormos, M.; Mullen, C.; Sandoz, D.; Rienstra, C. M. *Journal of the American Chemical Society* **2007**, *129*, 11791.
(263) Asami, S.; Szekely, K.; Schanda, P.; Meier, B. H.; Reif, B. *Journal of Biomolecular NMR* **2012**, *54*, 155.
(264) Ward, M. E.; Wang, S. L.; Krishnamurthy, S.; Hutchins, H.; Fey, M.; Brown, L. S.; Ladizhansky, V. *Journal of Biomolecular NMR* **2014**, *58*, 37.
(265) Marchetti, A.; Jehle, S.; Felletti, M.; Knight, M. J.; Wang, Y.; Xu, Z. Q.; Park, A. Y.; Otting, G.; Lesage, A.; Emsley, L.; Dixon, N. E.; Pintacuda, G. *Angewandte Chemie International Edition* **2012**, *51*, 10756.
(266) Mainz, A.; Jehle, S.; van Rossum, B. J.; Oschkinat, H.; Reif, B. *J. Am. Chem. Soc.* **2009**, *131*, 15968.

(267) Carter, P. J. *Experimental Cell Research* **2011**, *317*, 1261.
(268) Stone, G. C.; Sjöbring, U.; Björck, L.; Sjöquist, J.; Barber, C. V.; Nardella, F. a. *Journal of Immunology* **1989**, *143*, 565.
(269) Derrick, J. P.; Wigley, D. B. *Nature* **1992**, *359*, 752.
(270) Gronenborn, A. M.; Clore, G. M. *Journal of Molecular Biology* **1993**, *233*, 331.
(271) Lian, L.-Y.; Barsukov, I. L.; Derrick, J. P.; Roberts, G. C. *Nature structural & molecular biology* **1994**, *1*, 355.
(272) Ishii, Y.; Tycko, R. *Journal of Magnetic Resonance* **2000**, *142*, 199.
(273) Wickramasinghe, N. P.; Parthasarathy, S.; Jones, C. R.; Bhardwaj, C.; Long, F.; Kotecha, M.; Mehboob, S.; Fung, L. W. M.; Past, J.; Samoson, A.; Ishii, Y. *Nature Methods* **2009**, *6*, 215.
(274) Kato, K.; Lian, L. Y.; Barsukov, I. L.; Derrick, J. P. *Structure* **1995**, *3*, 79.
(275) Sauer-Eriksson, A. E.; Kleywegt, G. J.; Uhlén, M.; Jones, T. A. *Structure* **1995**, *3*, 265.
(276) Lewandowski, J. R.; Sass, H. J.; Grzesiek, S.; Blackledge, M.; Emsley, L. *Journal of the American Chemical Society* **2011**, *133*, 16762.
(277) Kmiecik, S.; Kolinski, A. *Biophysical Journal* **2008**, *94*, 726.
(278) Harris, L. J.; Skaletsky, E.; McPherson, A. *Journal of Molecular Biology* **1998**, *275*, 861.
(279) Chevelkov, V.; Fink, U.; Reif, B. *Journal of the American Chemical Society* **2009**, *131*, 14018.
(280) Giraud, N.; Blackledge, M.; Goldman, M.; Böckmann, A.; Lesage, A.; Penin, F.; Emsley, L. *Journal of the American Chemical Society* **2005**, *127*, 18190.
(281) Franks, W. T.; Zhou, D. H.; Wylie, B. J.; Money, B. G.; Graesser, D. T.; Frericks, H. L.; Sahota, G.; Rienstra, C. M. *Journal of the American Chemical Society* **2005**, *127*, 12291.
(282) Cavanagh, J.; Fairbrother, W. J.; Palmer III, A. G.; Skelton, N. J. *Protein NMR Spectroscopy: Principles and Practice*; Academic Press, 1995.
(283) Gullion, T.; Schaefer, J. *Journal of Magnetic Resonance (1969)* **1989**, *81*, 196.
(284) Kotecha, M.; Wickramasinghe, N. P.; Ishii, Y. *Magnetic Resonance in Chemistry* **2007**, *45*, S221.
(285) Zorin, V. E.; Brown, S. P.; Hodgkinson, P. *The Journal of Chemical Physics* **2006**, *125*, 144508.
(286) Brown, S. P. *Solid State Nuclear Magnetic Resonance* **2012**, *41*, 1.
(287) Zheng, L.; Fishbein, K. W.; Griffin, R. G.; Herzfeld, J. *Journal of the American Chemical Society* **1993**, *115*, 6254.
(288) Gerstein, B. C.; Pembleton, R. G.; Wilson, R. C.; Ryan, L. M. *The Journal of Chemical Physics* **1977**, *66*, 361.
(289) Ryan, L. M.; Taylor, R. E.; Paff, A. J.; Gerstein, B. C. *The Journal of Chemical Physics* **1980**, *72*, 508.
(290) Lesage, A.; Duma, L.; Sakellariou, D.; Emsley, L. *Journal of the American Chemical Society* **2001**, *123*, 5747.
(291) Brown, S. P.; Lesage, A.; Elena, B.; Emsley, L. *Journal of the American Chemical Society* **2004**, *126*, 13230.
(292) Leskes, M.; Madhu, P. K.; Vega, S. *The Journal of Chemical Physics* **2008**, *128*, 052309.
(293) Leskes, M.; Steuernagel, S.; Schneider, D.; Madhu, P. K.; Vega, S. *Chemical Physics Letters* **2008**, *466*, 95.
(294) Paul, S.; Thakur, R. S.; Madhu, P. K. *Chemical Physics Letters* **2008**, *456*, 253.
(295) Amoureux, J.-P.; Hu, B.; Trébosc, J. *Journal of Magnetic Resonance* **2008**, *193*, 305.

(296) Salager, E.; Stein, R. S.; Steuernagel, S.; Lesage, A.; Elena, B.; Emsley, L. *Chemical Physics Letters* **2009**, *469*, 336.
(297) Paul, S.; Thakur, R. S.; Goswami, M.; Sauerwein, A. C.; Mamone, S.; Concistrè, M.; Förster, H.; Levitt, M. H.; Madhu, P. *Journal of Magnetic Resonance* **2009**, *197*, 14.
(298) Salager, E.; Dumez, J.-N.; Stein, R. S.; Steuernagel, S.; Lesage, A.; Elena-Herrmann, B.; Emsley, L. *Chemical Physics Letters* **2010**, *498*, 214.
(299) Paul, S.; Thakur, R. S.; Levitt, M. H.; Madhu, P. K. *Journal of Magnetic Resonance* **2010**, *205*, 269.
(300) Gan, Z.; Madhu, P. K.; Amoureux, J.-P.; Trébosc, J.; Lafon, O. *Chemical Physics Letters* **2011**, *503*, 167.
(301) Halse, M. E.; Emsley, L. *Physical Chemistry Chemical Physics* **2012**, *14*, 9121.
(302) Burum, D. P.; Linder, M.; Ernst, R. R. *Journal of Magnetic Resonance (1969)* **1981**, *44*, 173.
(303) Sakellariou, D.; Lesage, A.; Hodgkinson, P.; Emsley, L. *Chemical Physics Letters* **2000**, *319*, 253.
(304) Elena, B.; de Paëpe, G.; Emsley, L. *Chemical Physics Letters* **2004**, *398*, 532.
(305) Bertini, I.; Emsley, L.; Lelli, M.; Luchinat, C.; Mao, J.; Pintacuda, G. *Journal of the American Chemical Society* **2010**, *132*, 5558.
(306) Brunner, E.; Freude, D.; Gerstein, B.; Pfeifer, H. *Journal of Magnetic Resonance (1969)* **1990**, *90*, 90.
(307) Ray, S.; Vinogradov, E.; Boender, G.-J.; Vega, S. *Journal of Magnetic Resonance* **1998**, *135*, 418.
(308) Filip, C.; Hafner, S.; Schnell, I.; Demco, D. E.; Spiess, H. W. *The Journal of Chemical Physics* **1999**, *110*, 423.
(309) Zhou, D. H.; Graesser, D. T.; Franks, W. T.; Rienstra, C. M. *Journal of Magnetic Resonance* **2006**, *178*, 297.
(310) Ishii, Y.; Yesinowski, J. P.; Tycko, R. *Journal of the American Chemical Society* **2001**, *123*, 2921.
(311) Caravatti, P.; Bodenhausen, G.; Ernst, R. R. *Chemical Physics Letters* **1982**, *89*, 363.
(312) Caravatti, P.; Braunschweiler, L.; Ernst, R. R. *Chemical Physics Letters* **1983**, *100*, 305.
(313) van Rossum, B. J.; Förster, H.; De Groot, H. *Journal of Magnetic Resonance* **1997**, *124*, 516.
(314) Saalwächter, K.; Graf, R.; Spiess, H. W. *Journal of Magnetic Resonance* **1999**, *140*, 471.
(315) Lesage, A.; Sakellariou, D.; Steuernagel, S.; Emsley, L. *Journal of the American Chemical Society* **1998**, *120*, 13194.
(316) van Rossum, B. J.; De Groot, C. P.; Ladizhansky, V.; Vega, S.; De Groot, H. J. M. *Journal of the American Chemical Society* **2000**, *122*, 3465.
(317) Saalwächter, K.; Graf, R.; Spiess, H. W. *Journal of Magnetic Resonance* **2001**, *148*, 398.
(318) Demers, J.-P.; Chevelkov, V.; Lange, A. *Solid State Nuclear Magnetic Resonance* **2011**, *40*, 101.
(319) Sakellariou, D.; Le Goff, G.; Jacquinot, J. F. *Nature* **2007**, *447*, 694.
(320) Lesage, A.; Bardet, M.; Emsley, L. *Journal of the American Chemical Society* **1999**, *121*, 10987.
(321) Jarymowycz, V. A.; Stone, M. J. *Chemical Reviews* **2006**, *106*, 1624.
(322) Mittermaier, A.; Kay, L. E. *Science* **2006**, *312*, 224.
(323) DeAzevedo, E. R.; Hu, W.-G.; Bonagamba, T. J.; Schmidt-Rohr, K. *Journal of the American Chemical Society* **1999**, *121*, 8411.

(324) Andronesi, O. C.; Becker, S.; Seidel, K.; Heise, H.; Young, H. S.; Baldus, M. *Journal of the American Chemical Society* **2005**, *127*, 12965.
(325) Yang, J.; Tasayco, M. L.; Polenova, T. *Journal of the American Chemical Society* **2009**, *131*, 13690.
(326) Palmer III, A. G. *Chemical Reviews* **2004**, *104*, 3623.
(327) Gabel, F.; Bicout, D.; Lehnert, U.; Tehei, M.; Weik, M.; Zaccai, G. *Quarterly Reviews of Biophysics* **2002**, *35*, 327.
(328) Shaw, D. E.; Maragakis, P.; Lindorff-Larsen, K.; Piana, S.; Dror, R. O.; Eastwood, M. P.; Bank, J. A.; Jumper, J. M.; Salmon, J. K.; Shan, Y. *Science* **2010**, *330*, 341.
(329) Mollica, L.; Baias, M.; Lewandowski, J. z. R.; Wylie, B. J.; Sperling, L. J.; Rienstra, C. M.; Emsley, L.; Blackledge, M. *J Phys Chem Lett* **2012**, *3*, 3657.
(330) Chevelkov, V.; Xue, Y.; Linser, R.; Skrynnikov, N. R.; Reif, B. *Journal of the American Chemical Society* **2010**, *132*, 5015.
(331) Krushelnitsky, A.; Reichert, D. *Progress in Nuclear Magnetic Resonance Spectroscopy* **2005**, *47*, 1.
(332) Chevelkov, V.; Fink, U.; Reif, B. *J. Biomol. NMR* **2009**, *45*, 197.
(333) Tamura, A.; Matsushita, M.; Naito, A.; Kojima, S.; Miura, K. I.; Akasaka, K. *Protein Science* **1996**, *5*, 127.
(334) Chevelkov, V.; Diehl, A.; Reif, B. *Magnetic Resonance in Chemistry* **2007**, *45*, S156.
(335) Agarwal, V.; Xue, Y.; Reif, B.; Skrynnikov, N. R. *Journal of the American Chemical Society* **2008**, *130*, 16611.
(336) Lamley, J. M.; Öster, C.; Stevens, R. A.; Lewandowski, J. R. *Angewandte Chemie International Edition* **2015**.
(337) Alla, M.; Eckman, R.; Pines, A. *Chemical Physics Letters* **1980**, *71*, 148.
(338) Krushelnitsky, A.; Bräuniger, T.; Reichert, D. *Journal of Magnetic Resonance* **2006**, *182*, 339.
(339) Giraud, N.; Blackledge, M.; Böckmann, A.; Emsley, L. *Journal of Magnetic Resonance* **2007**, *184*, 51.
(340) Giraud, N.; Böckmann, A.; Lesage, A.; Penin, F.; Blackledge, M.; Emsley, L. *Journal of the American Chemical Society* **2004**, *126*, 11422.
(341) Chevelkov, V.; Diehl, A.; Reif, B. *The Journal of Chemical Physics* **2008**, *128*, 052316.
(342) Tollinger, M.; Sivertsen, A. C.; Meier, B. H.; Ernst, M.; Schanda, P. *J. Am. Chem. Soc.* **2012**, *134*, 14800.
(343) Krushelnitsky, A.; Kurbanov, R.; Reichert, D.; Hempel, G.; Schneider, H.; Fedotov, V. *Solid State Nuclear Magnetic Resonance* **2002**, *22*, 423.
(344) Quinn, C. M.; McDermott, A. E. *Journal of Magnetic Resonance* **2012**, *222*, 1.
(345) Good, D. B.; Wang, S.; Ward, M. E.; Struppe, J.; Brown, L. S.; Lewandowski, J. R.; Ladizhansky, V. *J. Am. Chem. Soc.* **2014**, *136*, 2833.
(346) Huster, D.; Xiao, L.; Hong, M. *Biochemistry* **2001**, *40*, 7662.
(347) Cady, S. D.; Hong, M. *Journal of Biomolecular NMR* **2009**, *45*, 185.
(348) Krushelnitsky, A.; Zinkevich, T.; Reichert, D.; Chevelkov, V.; Reif, B. *Journal of the American Chemical Society* **2010**, *132*, 11850.
(349) Krushelnitsky, A.; Zinkevich, T.; Reif, B.; Saalwächter, K. *Journal of Magnetic Resonance* **2014**, *148*, 8.
(350) Ma, P.; Haller, J. D.; Zajakala, J.; Macek, P.; Sivertsen, A. C.; Willbold, D.; Boisbouvier, J.; Schanda, P. *Angewandte Chemie International Edition* **2014**, *53*, 4312.
(351) Zinkevich, T.; Chevelkov, V.; Reif, B.; Saalwächter, K.; Krushelnitsky, A. *Journal of Biomolecular NMR* **2013**, *57*, 219.
(352) Parthasarathy, S.; Nishiyama, Y.; Ishii, Y. *Accounts of Chemical Research* **2013**, *46*, 2127.

(353) Bremi, T.; Brüschweiler, R. *Journal of the American Chemical Society* **1997**, *119*, 6672.
(354) Torchia, D. A.; Szabo, A. *Journal of Magnetic Resonance (1969)* **1982**, *49*, 107.
(355) Skrynnikov, N. R. *Magnetic Resonance in Chemistry* **2007**, *45*, S161.
(356) Schanda, P.; Meier, B. H.; Ernst, M. *Journal of the American Chemical Society* **2010**, *132*, 15957.
(357) Lamley, J. M.; Lougher, M. J.; Sass, H. J.; Rogowski, M.; Grzesiek, S.; Lewandowski, J. R. *Physical Chemistry Chemical Physics* **2015**, *17*, 21997.
(358) Clore, G. M.; Szabo, A.; Bax, A.; Kay, L. E.; Driscoll, P. C.; Gronenborn, A. M. *Journal of the American Chemical Society* **1990**, *112*, 4989.
(359) Chevelkov, V.; Zhuravleva, A. V.; Xue, Y.; Reif, B.; Skrynnikov, N. R. *Journal of the American Chemical Society* **2007**, *129*, 12594.
(360) Haller, J. D.; Schanda, P. *Journal of Biomolecular NMR* **2013**, *57*, 263.
(361) Goh, C.-S.; Milburn, D.; Gerstein, M. *Current Opinion in Structural Biology* **2004**, *14*, 104.
(362) Mittermaier, A. K.; Kay, L. E. *Trends in Biochemical Sciences* **2009**, *34*, 601.
(363) Baldwin, A. J.; Walsh, P.; Hansen, D. F.; Hilton, G. R.; Benesch, J. L.; Sharpe, S.; Kay, L. E. *Journal of the American Chemical Society* **2012**, *134*, 15343.
(364) Schanda, P.; Triboulet, S.; Laguri, C.; Bougault, C. M.; Ayala, I.; Callon, M.; Arthur, M.; Simorre, J.-P. *Journal of the American Chemical Society* **2014**, *136*, 17852.
(365) Lewandowski, J. R.; Sein, J.; Blackledge, M.; Emsley, L. *Journal of the American Chemical Society* **2010**, *132*, 1246.
(366) Wylie, B. J.; Sperling, L. J.; Nieuwkoop, A. J.; Franks, W. T.; Oldfield, E.; Rienstra, C. M. *Proceedings of the National Academy of Sciences* **2011**, *108*, 16974.
(367) Daviso, E.; Eddy, M. T.; Andreas, L. B.; Griffin, R. G.; Herzfeld, J. *Journal of Biomolecular NMR* **2013**, *55*, 257.
(368) Lewandowski, J. z. R. *Accounts of Chemical Research* **2013**, *46*, 2018.
(369) Good, D. B.; Wang, S.; Ward, M. E.; Struppe, J.; Brown, L. S.; Lewandowski, J. R.; Ladizhansky, V. *J. Am. Chem. Soc.* **2014**, *136*, 2833.
(370) Pettersen, E. F.; Goddard, T. D.; Huang, C. C.; Couch, G. S.; Greenblatt, D. M.; Meng, E. C.; Ferrin, T. E. *Journal of Computational Chemistry* **2004**, *25*, 1605.
(371) Barchi, J. J.; Grasberger, B.; Gronenborn, A. M.; Clore, G. M. *Protein Science* **1994**, *3*, 15.
(372) Bouvignies, G.; Bernado, P.; Meier, S.; Cho, K.; Grzesiek, S.; Brüschweiler, R.; Blackledge, M. *Proceedings of the National Academy of Sciences* **2005**, *102*, 13885.
(373) Yang, J.; Tasayco, M. L.; Polenova, T. *J. Am. Chem. Soc.* **2009**, *131*, 13690.
(374) Helmus, J. J.; Surewicz, K.; Surewicz, W. K.; Jaroniec, C. P. *Journal of the American Chemical Society* **2010**, *132*, 2393.
(375) Schmidt-Rohr, K.; Spiess, H. W. *Multidimensional Solid-State NMR and Polymers.*; Academic Press: London, 1994.
(376) Mollica, L.; Baias, M.; Lewandowski, J. R.; Wylie, B. J.; Sperling, L. J.; Rienstra, C. M.; Emsley, L.; Blackledge, M. *J Phys Chem Lett* **2012**, *3*, 3657.
(377) Yamazaki, T.; Muhandiram, R.; Kay, L. E. *Journal of the American Chemical Society* **1994**, *116*, 8266.
(378) Naito, A.; Ganapathy, S.; Akasaka, K.; Mcdowell, C. A. *Journal of Magnetic Resonance* **1983**, *54*, 226.
(379) Quinn, C. M.; McDermott, A. E. *Journal of Biomolecular NMR* **2009**, *45*, 5.
(380) Laage, S.; Lesage, A.; Emsley, L.; Bertini, I.; Felli, I. C.; Pierattelli, R.; Pintacuda, G. *Journal of the American Chemical Society* **2009**, *131*, 10816.
(381) Bertini, I.; Emsley, L.; Felli, I. C.; Laage, S.; Lesage, A.; Lewandowski, J. R.; Marchetti, A.; Pierattelli, R.; Pintacuda, G. *Chem Sci* **2011**, *2*, 345.

(382) Wylie, B. J.; Sperling, L. J.; Frericks, H. L.; Shah, G. J.; Franks, W. T.; Rienstra, C. M. *Journal of the American Chemical Society* **2007**, *129*, 5318.
(383) Chang, S. L.; Tjandra, N. *Journal of Magnetic Resonance* **2005**, *174*, 43.
(384) Idiyatullin, D.; Daragan, V. A.; Mayo, K. H. *Journal of Physical Chemistry B* **2003**, *107*, 2602.
(385) Charlier, C.; Khan, S. N.; Marquardsen, T.; Pelupessy, P.; Reiss, V.; Sakellariou, D.; Bodenhausen, G.; Engelke, F.; Ferrage, F. *Journal of the American Chemical Society* **2013**, *135*, 18665.
(386) Zinkevich, T.; Chevelkov, V.; Reif, B.; Saalwächter, K.; Krushelnitsky, A. *J. Biomol. NMR* **2013**, *57*, 219.
(387) Lienin, S. F.; Bremi, T.; Brutscher, B.; Bruschweiler, R.; Ernst, R. R. *Journal of the American Chemical Society* **1998**, *120*, 9870.
(388) Shapiro, Y. E.; Meirovitch, E. *Journal of Physical Chemistry B* **2012**, *116*, 4056.
(389) Derrick, J. P.; Wigley, D. B. *Journal of Molecular Biology* **1994**, *243*, 906.
(390) Frericks Schmidt, H. L.; Sperling, L. J.; Gao, Y. G.; Wylie, B. J.; Boettcher, J. M.; Wilson, S. R.; Rienstra, C. M. *Journal of Physical Chemistry B* **2007**, *111*, 14362.
(391) Ban, D.; Gossert, A. D.; Giller, K.; Becker, S.; Griesinger, C.; Lee, D. *Journal of Magnetic Resonance* **2012**, *221*, 1.
(392) Kmiecik, S.; Gront, D.; Kolinski, A. *Bmc Struct Biol* **2007**, *7*, 43.
(393) Allard, P.; Härd, T. *Journal of Magnetic Resonance* **1997**, *126*, 48.